Etching Kinetics and Surface Roughening of Polysilicon and Dielectric Materials in Inductively Coupled Plasma Beams

by

Yunpeng Yin

M. S., Chemical Engineering Practice
Massachusetts Institute of Technology, 2005

M. S., Chemical Engineering
Tsinghua University, 2002

B. E., Chemical Engineering
Tsinghua University, 1999

Submitted to the Department of Chemical Engineering
in Partial Fulfillment of the Requirements for the Degree of

Doctor of Philosophy in Chemical Engineering

at the

MASSACHUSETTS INSTITUTE OF TECHNOLOGY

June 2007

© Massachusetts Institute of Technology 2007. All rights reserved.

Author: ______________________________
Department of Chemical Engineering
May 18, 2007

Certified by: ______________________________
Prof. Herbert H. Sawin
Professor of Chemical Engineering and
Electrical Engineering & Computer Science
Thesis Supervisor

Accepted by: ______________________________
Prof. William M. Deen
Professor of Chemical Engineering
Chairman, Departmental Committee on Graduate Studies

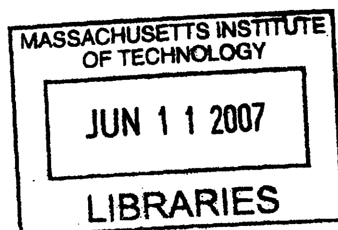

ARCHIVES

Etching Kinetics and Surface Roughening of Polysilicon and Dielectric Materials in Inductively Coupled Plasma Beams

by

Yunpeng Yin

M. S., Chemical Engineering Practice
Massachusetts Institute of Technology, 2005

M. S., Chemical Engineering
Tsinghua University, 2002

B. E., Chemical Engineering
Tsinghua University, 1999

Submitted to the Department of Chemical Engineering on May 18, 2007
in Partial Fulfillment of the Requirements for the Degree of
Doctor of Philosophy in Chemical Engineering

Abstract

Plasma etching processes often roughen the feature sidewalls forming anisotropic striations. A clear understanding of the origin and control of sidewall roughening is extremely desirable, particularly at the gate level where variations in line width can adversely impact the electrical performance of the device. In addition, at the back end, feature sidewall roughness of the dielectric materials might degrade the resolution of contacts, interfere with the deposition of conformal liner materials, and make the process integration challengeable.

In an inductively coupled plasma apparatus, the etching behavior on real feature sidewalls was simulated by etching blank films at grazing ion bombardment angles. The angular etching yields of polysilicon and dielectric materials in Ar, Cl_2/Ar, and C_4F_8/Ar plasma beams were studied as a function of ion bombardment energy, ion bombardment angle, etching time, plasma pressure, and plasma composition. Interestingly, the effective neutral-to-ion flux ratio was the primary factor influencing the etching yield. A typical sputtering angular yield curve, with a peak around 60° off-normal angle, was formed at non-saturated etching regime, while an ion-enhanced-etching angular yield curve peaked around 65° was observed in the saturated etching regime.

In Ar plasma, various films remained smooth after etching at normal angle but became rougher at grazing angles. Specifically, the striation structure formed at grazing angles could be either parallel or transverse to the beam impingement direction. Encouragingly, the sputtering caused roughening at different off-normal angles could be qualitatively explained by the corresponding angular dependent etching yield curve.

In fluorocarbon plasmas, the roughening of thermal silicon dioxide and low-k coral

films at grazing ion bombardment angles depended on both the etching kinetics and the etching chemistry. In particular, the surface roughened when the etching process was physical-sputtering like (at low neutral-to-ion flux ratios), even though the polymer deposition effect was trivial; when the etching kinetics was dominated by ion-enhanced etching (at high neutral-to-ion flux ratios), the roughening was mainly caused by the local polymer deposition effects. Moreover, surfaces could be etched without roughening at intermediate neutral-to-ion flux ratios and/or with the addition of oxygen to the discharge. The oxygen addition broadened the region over which etching without roughening can be performed. Additionally, the local-polymer-deposition effect can be used to explain the surface roughening of porous low-k films in fluorocarbon plasmas.

Last, it was shown that RMS roughness is not adequate to represent the surface roughness on etched surfaces, especially when anisotropic striations exist. Instead, statistical methods such as the power spectral density and geostatistical analysis are capable of measuring the surface roughening in both vertical and lateral dimensions. In this way, the spatial variation of the streaks formed during plasma etching can be characterized quantitatively.

Thesis Supervisor: Herbert H. Sawin
Professor of Chemical Engineering and Electrical Engineering & Computer Science

Acknowledgments

First of all, I would like to express my deep and sincere gratitude to my supervisor, Professor Herbert H. Sawin. His wide knowledge and his logical way of thinking have been of great value for me. His understanding, encouraging and personal guidance have provided an excellent basis for the present thesis. I am also grateful to my thesis committee members Professor Gleason and Professor Green for their thoughtful suggestions and advice.

I owe special thanks to the present and past members of the Sawin Lab at MIT. To Dr. Weidong Jin, thank you for showing me the first plasma glow I have ever seen so far and for teaching me how vacuum was maintained. To Dr. Stacy Rasgon, thank you for helping me set up the beam apparatus and for tutoring me on using AFM and ellipsometer. To Dr. Ohseung Kwon, thank you for teaching me for the first time how to use the XPS. To Dr. Bo Bai, thank you very much for letting me know how to work efficiently in the lab and those useful discussions on my projects. To Hiroyo Kawai, thank you for showing me your exciting 3-D simulation results. To Jujin An, thank you for maintaining the lab together with me in the past several years. To Wei Guo, thank you for reminding me that I am an expert on the beam experimental work.

I would also like to thank those helpful people out of the Sawin Lab at MIT. To the fellow students at Professor Gleason's Lab, especially, Long Hua Lee, thank you very much for your great help on accessing to the ellipsometer so conveniently. To Elisabeth L. Shaw, thank you very much for your critical help on the AFM. To Tim McClure, thank you very much for training me on how to use the profilometer. To the scientists at MTL, thank you very much for preparing wafers for me. To those technicians at the Edgerton center machine shop, thank you very much for showing me something new every time, and for helping me solve the transfer tube problem.

I would like to express my gratitude to Peter Romanow and Glori Collver-Jacobson for their assistance. Thank Texas Instruments and Novellus for supplying wafers for plasma etching experiments. Additionally, financial support from the Semiconductor Research Corporation (SRC) is gratefully acknowledged.

I wish to express my special thanks to my friends both at MIT and in China. To my friends at MIT, Minggang She, Wei Chai, Wenchao Sheng, Shuo Chen, Xiaoxia Dong, Huan Zhang, and all others whose name I can't remember right now, thank you. To my old friends in China and my former research advisor, Lan Xiang, at Tsinghua University, thank you. Your support, encouragement and friendship have made my journey at MIT more enjoyable.

Finally, I would like to give my deepest thanks to my family whose patience and love enabled me to complete this work. I am very fortunate that my parents, Xianting Yin and Qinglan Liu, my siblings, and my wife, Hong He, are always there for me, sharing both my exciting moments and bad times. Thank you so much!

Contents

Chapter 1. Background and Research Motivation 23
1.1 Integrated Circuits Manufacturing 23
1.2 Plasma Processing 23
1.3 Sidewall Roughening and Line-edge-roughening Effects 26
1.3.1 Sidewall Roughening as a Challenge 26
1.3.2 Top Line-edge-roughening Effects 27
1.3.3 Simulation Approach to Understand Sidewall Roughening 28
1.4 Surface Roughening on Blank Films in Plasma Etching 29
1.5 Impact of Etching Kinetics on Feature Surface Roughening 31
1.6 Scope and Objectives of This Work 32
1.7 References 33

Chapter 2. Apparatus and Plasma Beam Characterization 37
2.1 Apparatus 37
2.2 Matching Network 39
2.3 Inductive Coupling and Capacitive Coupling 41
2.4 Plasma Beam Characterization 43
2.4.1 Ion flux Analysis 43
2.4.1.1 Ion Flux Analyzer 43
2.4.1.2 Space Charge Neutralization 43
2.4.2 Ion Energy Analysis 46
2.4.3 Plasma Composition Analysis 49
2.5 Film Characterization 50
2.5.1 Etching Rate Measurement 50
2.5.2 X-Ray Photoelectron Spectroscopy (XPS) 51
2.5.3 Atomic Force Microscopy (AFM) 51
2.6 References 52

Chapter 3. The Angular Etching Yields of Polysilicon and Dielectric Materials in Cl_2/Ar and Fluorocarbon Plasmas 55
3.1 Introduction 55
3.2 Angular Etching Yields of Polysilicon in Cl_2/Ar Plasmas 57
3.3 Angular Etching Yields of Thermal SiO_2 in Fluorocarbon Plasmas 61
3.3.1 Angular Etching Yields in C4F8/Ar Plasmas 61
3.3.2 Angular Etching Yields in C2F6/Ar Plasmas 69
3.4 Impact of O_2 Addition on SiO_2 Angular Etching Yields 71
3.5 Angular Etching Yields of Low-k Coral Material in Fluorocarbon Plasmas. 79
3.6 Impact of Neutral-to-ion Flux Ratio 80
3.7 Polymer Deposition Effects 86
3.8 Conclusions 89
3.9 References 90

Chapter 4. Surface Roughening of Silicon, Thermal Silicon Dioxide and Low-k Dielectric Coral Films in Argon Plasma 95
4.1 Introduction 95
4.2 Ar Sputtering Kinetics 97

4.3 Spatial Frequency of Roughening 100
4.4 Ar Sputtering Caused Roughening 102
4.5 Discussion 111
4.6 Conclusions 116
4.7 References 116

Chapter 5. The Impact of Etching Kinetics on the Roughening of Thermal SiO_2 and Low-k Dielectric Coral Films in Fluorocarbon Plasmas 119
5.1 Introduction 119
5.2 Characterization of Unetched Films 121
5.3 Roughening at Grazing Ion Bombardment at Different Etching Regimes .. 122
5.4 Effects of O_2 Addition on Roughening with Grazing Ion Bombardment 129
5.5 References 133

Chapter 6. Surface Roughening of Low-k Films during Etching Using Fluorocarbon Plasma Beams 135
6.1 Introduction 135
6.2 Standard Etching Procedure 137
6.3 Characterization of Unetched Films 137
6.4 Surface Roughness Evolution with Etching Time 139
6.5 Effects of Ion Bombardment Energy on Surface Roughening and Etching Kinetics 142
6.6 Impact of Plasma Polymerizing Effects on Surface Roughening 145
6.7 Local Polymer Deposition Induced Micro-masking Roughening Mechanism.. 150
6.8 Surface Roughening during Etching at Grazing Angles 152
6.9 Conclusions 155
6.10 References 156

Chapter 7. Statistical Analysis of Plasma-etched Surfaces: Power Spectral Density and Geostatistical Methods 159
7.1 Introduction 159
7.2 Theory 161
7.2.1 Power Spectral Density Analysis 161
7.2.2 Geostatistical Analysis 162
7.3 Results and Discussion 167
7.3.1 Impact of Etching Time on the Striation Structure 167
7.3.2 Impact of Ion Bombardment Angle on the Striation Structure 175
7.4 Conclusions 178
7.5 References 179

Chapter 8. Conclusions and Recommendations for Future Work 181
8.1 Conclusions 181
8.2 Future Work 183
8.3 References 184

Appendix - Mechanical Drawings 185

List of Figures

1-1 The number of transistors on a chip is doubled every other 1.4 years. 24

1-2 Schematic diagram illustrating the chlorine ion-enhanced etching of photoresist patterned polysilicon. The major reactive species in plasma include energetic chlorine ions (Cl^+) and reactive neutrals (Cl, Cl_2, $SiCl_2$). 24

1-3 A couple of common artifacts in plasma etching process. 25

1-4 The AFM images of the feature sidewall at different processing steps. (a) After photoresist development but before plasma treatment; (b) after N_2-H_2 organic ARC open; (c) after 45 s oxide etch in fluorocarbon plasmas. 28

1-5 The schematic of how to measure the sidewall roughness using AFM technique. 30

1-6 Left-hand side shows the definition of the angle of ion impingement. Right-hand shows a sketch of how ions can reflect from sidewall of etching feature at small angles. 31

2-1 The schematic of a newly designed beam chamber system. The beam source locates at the upper part of the main chamber and the plasma is inductively coupled (ICP). This beam system has the flexibility to control the plasma chemistry, ion bombardment energy, and incident angle independently. 37

2-2 Schematic diagram of the integrated processing system that enables in situ sample transfer between process and analytic chambers. 39

2-3 Schematic diagram of the realistic plasma source. The inductively coupled plasma source consists of a stainless steel cylinder, a dielectric window, a three turn copper coil powered at 13.56 MHz (up to 1000 W) via a Matching Network. 39

2-4 The configuration of the matching network electronics. 40

2-5 RF power coupling transits from capacitive coupling to inductive coupling with the increase of the RF power. 42

2-6 The variation of ion flux at the sample surface as a function of the RF power level. 43

2-7 The contour plots of the ion current, which are measured by the ion flux analyzer and normalized to the ion current at the beam center, at DC bias level (a) 100 V and (b) 350 V for 10 mtorr Ar plasma with RF source power level at 350 W with the neutralization filament turned off. 45

2-8 The contour plots of the ion current, which is measured by the ion flux analyzer and normalized to the ion current at the beam center, at DC bias level (a) 100 V and (b) 350 V for 10 mtorr Ar plasma with RF source power level at 350 W with the neutralization filament turned on. 46

2-9 (a) I-V curve from ion energy analyzer from a 10 mtorr Ar plasma at 350 W RF power level. (b) Derivative of I-V characteristics give the ion-energy-distribution function (IEDF) at different DC bias levels. 47

2-10 The estimation of plasma sheath thickness as a function of DC bias level in 10 mtorr Ar plasma with RF source power level at 350 W. The horizontal line at 3.3 mm indicates the mean free path length for ion scattering. 49

2-11 A schematic showing how the AFM works. 52

3-1 The etching yield of PECVD polysilicon in Cl_2/Ar plasmas as a function of the square root of ion bombardment energy for different Cl_2 percentages at normal angle. For comparison, the sputtering rate of polysilicon was also shown in this figure. 59

3-2 The etching yield of PECVD polysilicon in Cl_2/Ar plasmas as a function of the effective neutral-to-ion flux ratio and ion bombardment energies at normal ion incidence angle. 59

3-3 Variation of polysilicon etching yields in chlorine plasmas with plasma composition. Cl^+/Cl data is from Chang et al.[30], and Cl^{2+}/Cl_2 data is taken from Balooch et al. [27]. The data points are experimental results, and the lines are linear fit of to our data. 60

3-4 The normalized angular etching yields of PECVD polysilicon in Cl_2/Ar plasmas under various plasma source pressures (5 mtorr, 8 mtorr, and 14 mtorr) and DC bias levels (150 V and 250 V). Solid and open symbols represent the results at DC bias levels 150 V and 250 V, respectively. The Cl_2 percentage in the feed gas mixture is: 7% Cl_2 at 5 mtorr, 25% Cl_2 at 8 mtorr, and 67% Cl_2 at 14 mtorr. All of the etching yields were normalized to the corresponding etching yields at normal angle. 61

3-5 The etching yield of thermal silicon dioxide in C_4F_8/Ar plasmas as a function of the ion bombardment energy for different C_4F_8 percentages at normal angle. For comparison, the sputtering rate of thermal silicon dioxide in argon plasma was also shown in this figure. 62

3-6 The normalized angular etching yields thermal silicon oxide in C_4F_8/Ar plasmas under various plasma source pressures and DC bias levels. All of the etching yields were normalized to the corresponding etching yields at normal angle. 63

3-7 The influence of ion incidence off-normal angle on the surface composition of etched thermal silicon dioxide in 10% C_4F_8/Ar plasma. The concentration of each species on the surface was characterized by XPS technique. The etching conditions are: DC 350 V, beam source pressure 4 mtorr, ion fluence reaching the surface 3.0×10^{17} ions/cm^2. 64

3-8 The influence of ion incidence off-normal angle on the surface composition of etched thermal silicon dioxide in 10% C_4F_8/Ar plasma. The concentration of each species on the surface was characterized by XPS technique. The etching conditions are: DC 350 V, beam source pressure 10 mtorr, ion fluence reaching the surface 2.0×10^{17} ions/cm^2. 65

3-9 The influence of ion incidence off-normal angle on the surface composition of etched thermal silicon dioxide in 15% C_4F_8/Ar plasma. The concentration of each species on the surface was characterized by XPS technique. The etching conditions are: DC 350 V, beam source pressure 13 mtorr, ion fluence reaching the surface 2.0×10^{17} ions/cm^2. 65

3-10 The impact of C_4F_8 percentage on the plasma neutral composition quantified using mass spectrometer. The plasma source pressure is between 4-6 mtorr. 66

3-11 The impact of C_4F_8 percentage on the plasma ion composition quantified using mass spectrometer. The plasma source pressure is between 4-6 mtorr. 66

3-12 The impact of plasma source pressure on the plasma ion composition quantified using mass spectrometer. The C_4F_8 percentage in the plasma feed gas mixture is 10% in all cases. 68

3-13 The impact of C_4F_8 percentage on the etching yields of thermal silicon oxide in C_4F_8/Ar plasmas at different ion energy levels at normal angle. The plasma source pressure is between 4-6 mtorr. For comparison, the sputtering rate of thermal silicon dioxide in argon plasma was also shown in this figure. 69

3-14 The impact of C_4F_8 percentage on the normalized angular etching yields of thermal silicon oxide in C_4F_8/Ar plasmas. The plasma source pressure is between 4-6 mtorr and the DC bias level is 350 V in all cases. All of the etching yields were normalized to the corresponding etching yields at normal angle. 69

3-15 The etching yield of thermal silicon dioxide in 20% C_2F_6/Ar plasmas as a function of ion bombardment energy for different plasma source pressures at normal angle. For comparison, the sputtering rate of thermal silicon dioxide in argon plasma was also shown in this figure. 70

3-16 The normalized angular etching yields of thermal silicon oxide in 20% C_2F_6/Ar plasmas at different plasma source pressures. The DC bias level is 350 V in all cases. All of the etching yields were normalized to the corresponding etching yields at normal angle. 71

3-17 The impact of O_2 addition on the plasma neutral composition in 20% C_4F_8/Ar plasma quantified using mass spectrometer. The plasma source pressure is between 10-13 mtorr. 72

3-18 The impact of O_2 addition on the plasma ion composition in 20% C_4F_8/Ar plasma quantified using mass spectrometer. The plasma source pressure is between 10-13 mtorr. 72

3-19 The impact of O_2 addition on the etching yields of thermal silicon oxide in 20% C_4F_8/Ar plasmas at different ion energy levels at normal angle. The plasma source pressure is 10 mtorr and 13 mtorr before and after O_2 addition, respectively. For comparison, the sputtering rate of thermal silicon dioxide in argon plasma was also shown in this figure. 73

3-20 The impact of O_2 addition on the angular etching yields of thermal silicon oxide in 20% C_4F_8/Ar plasmas. The plasma source pressures are 10 mtorr and 13 mtorr before and after O_2 addition, respectively. All of the etching yields were normalized to the corresponding etching yields at normal angle. 74

3-21 The surface carbon (C1s) XPS spectrums of etched SiO_2 films. The etching parameters are: (a) 0° off-normal angle, and (b) 75° off-normal angle in 20% C4F8/Ar plasmas at 10 mtorr; (c) 0° off-normal angle, and (d) 75° off-normal angle in 20% C_4F_8/20% O_2/Ar plasmas at 12 mtorr. In all cases, the ion fluence reaching the surface is 2.0×10^{17} ions/cm^2. 75

3-22 The impact of O_2 addition on the etching yields of thermal silicon oxide in 15% C_4F_8/Ar plasmas at different ion energy levels at normal angle. The plasma source pressure is 18 mtorr and 21 mtorr before and after O_2 addition, respectively. For comparison, the sputtering rate of thermal silicon dioxide in argon plasma was also shown in this figure. 76

3-23 The impact of O_2 addition on the normalized angular etching yields of thermal silicon oxide in 15% C_4F_8/Ar plasmas. The plasma source pressures are 18 mtorr and 21 mtorr before and after O_2 addition, respectively. All of the etching yields were normalized to the corresponding etching yields at normal angle. 77

3-24 The surface carbon (C1s) XPS spectrums of etched SiO_2 films. The etching parameters are: (a) 0° off-normal angle, and (b) 75° off-normal angle in 15% C_4F_8/Ar plasmas at 18 mtorr; (c) 0° off-normal angle, and (d) 75° off-normal angle in 15% C_4F_8/14% O_2/Ar plasmas at 20 mtorr. In all cases, the ion fluence reaching the surface is 2.0×10^{17} ions/cm^2. 78

3-25 The etching yield of low-k dielectric coral film in C_4F_8/Ar plasmas as a function of the ion bombardment energy for different C_4F_8 percentages (10% and 15%) and different plasma source pressures (4 mtorr and 21 mtorr) at normal angle. For comparison, the sputtering rate of thermal silicon dioxide in argon plasma was also shown in this figure. 80

3-26 The normalized angular etching yields of low-k dielectric coral in C_4F_8/Ar plasmas under various plasma source pressures and DC bias levels for different C_4F_8/Ar volumetric ratios. Both of the etching yields were normalized to the corresponding etching yields at normal angle. 80

3-27 The etching yield of thermal silicon dioxide in C_4F_8/Ar plasmas as a function of the effective neutral-to-ion flux ratio and ion bombardment energies at normal ion incidence angle. 82

3-28 The influence of XPS take-off angle on Cl(2p) and Si(2p) XPS spectrums of polysilicon after etching in 7% Cl_2/Ar plasmas under plasma pressure 5 mtorr. The ion fluence reaching the surface is 3.0×10^{17} ions/cm^2 and the ion bombardment off-normal angle is 60°. 84

3-29 Cl(2p) XPS signal intensity of etched polysilicon varies with the ion bombardment off-normal angle, the ion bombardment energy, and plasma chemistry. In all cases, the XPS take-off angle is 30°. 86

3-30 Average number of broken bonds per trajectory in the silicon substrate as a result of 500 eV Ar ions bombardment at the indicated off-normal angles. 89

4-1 The sputtering yield of polysilicon in Ar plasma as a function of the square root of ion bombardment energy. 97

4-2 (a) the sputtering yield of SiO2 and (b) the etching rate of coral per 10^{17} ions/cm^2 in argon plasma as a function of the square root of ion bombardment energy. For comparison, the etching rate of SiO_2 was also included in (b). 98

4-3 The normalized etching yield of polysilicon in Ar plasma as a function of off-normal angle. The curve followed the typical sputtering yield curve, with a maximum around 60° off-normal angle. 99

4-4 The normalized etching yield of SiO_2 and coral in Ar plasma as a function of off-normal angle. The curve followed the typical sputtering yield curve, with a maximum around 60-70° off-normal angle. 100

4-5 (a) The AFM image of SiO_2 after sputtering in Ar plasma at off-normal angle 75° at ion energy level 310 eV (total ion fluence is 3.5×10^{17} ions/cm^2). The arrow shows the ion beam impingement direction. (b) The corresponding cross section analysis of the surface in (a), shown as solid line; the dashed line is the cross section analysis of SiO_2 layer on the sidewall after plasma patterning (data collected from Ref. 2). Note that the spatial frequencies are comparable demonstrating that the beam measurements of roughening are of the same dimension as is encountered on sidewalls. 101

4-6 The AFM images of unetched (a) single crystal silicon, (b) SiO_2 and (b) low-k dielectric coral films. The vertical scale of all films is 10 nm and all of the images represent 1 μm×1 μm of the real sample surface. The RMS roughness of single crystal silicon, SiO_2 and coral films are 0.2 nm, 0.2 nm and 1.0 nm, respectively. 103

4-7 The surface topography of (a) single crystal silicon, (b) SiO_2 and (c) coral after sputtering in Ar plasma at normal angle using 310 eV ions. The vertical scale is 15 nm for all AFM images. (a) The dosage is 2×10^{18} ions/cm^2 and the RMS roughness is 0.3 nm after 160 nm film etched; (b) the dosage is 1.5×10^{18} ions/cm^2 and the RMS roughness is 0.1 nm after 115 nm film etched; (c) the dosage is 1.5×10^{18} ions/cm^2 and the RMS roughness is 0.5 nm after 288 nm film etched. 104

4-8 The surface topography of (a) single crystal silicon, (b) SiO_2 and (c) coral after sputtering in Ar plasma at 60° off-normal angle using 310 eV ions. The vertical scale is 30 nm for all AFM images. (a) The dosage is 6×10^{17} ions/cm^2 and the RMS roughness is 1.4 nm after 155 nm film etched; (b) the dosage is 7×10^{17} ions/cm^2 and the RMS roughness is 1.9 nm after 213 nm film etched; (c) the dosage is 7×10^{17} ions/cm^2 and the RMS roughness is 3.5 nm after 515 nm film etched. 106

4-9 The surface topography of (a) single crystal silicon, (b) SiO_2 and (c) coral after sputtering in Ar plasma at 75° off-normal angle using 310 eV ions. The vertical scale is 50 nm for all AFM images. In all cases, the ion fluence reaching the surface is 3.5×10^{17} ions/cm^2. (a) The RMS roughness is 4.0 nm after 84 nm film etched; (b) the RMS roughness is 1.5 nm after 115 nm film etched; (c) the RMS roughness is 8.6 nm after 221 nm film etched. 107

4-10 The surface roughness of (solid line) SiO_2 and (dashed line) coral after sputtering in argon plasma at various angles as a function of the thickness of material removed. SiO_2: (■) 60° and (□) 75°. Coral : (♦) 60° and (◊) 75°. 108

4-11 The surface roughness of (solid line) single crystal silicon and (dashed line) SiO_2 after sputtering in argon plasma at various angles as a function of the thickness of material removed. Single crystal silicon: (×) 0°; (♦) 60° and (◊) 75°. SiO_2: (+) 0°; (■) 60° and (□) 75°. 109

4-12 The surface topography of (a) single crystal silicon, (b) SiO_2 and (c) coral after sputtering in Ar plasma at 82° off-normal angle using 310 eV ions. The vertical scale of these AFM images is (a) 10 nm, (b) 10 nm and (c) 50 nm. In all cases, the ion fluence reaching the surface is 1.5×10^{17} ions/cm^2. (a) The RMS roughness is 0.1 nm after around 34 nm film etched; (b) the RMS roughness is 0.2 nm after 16 nm film etched; (c) the RMS roughness is 3.6 nm after 38 nm film etched. 110

4-13 The prediction of the ion scattering probability as a function of off-normal angle based upon the measurement of the angular dependence of the etching yield. The scattering probability is relative low when the off-normal angle is smaller than the peak angle and we can assume that all of the ion energy is transferred to the substrate; while the scattering probability is high when the off-normal angle is larger than the peak angle and we can assume that all of the ion energy is scattered away. 111

4-14 The prediction of surface roughness evolution during sputtering in Ar plasma at normal incidence angle. The arrows represent the ions bombarding the surface. (a) With initially large features, the surface will be smoothed out after etching because of the larger etching yield at faceting angles; (b) with initially smooth features, the surface will be roughened to low level because of the stochastic roughening due to the uniformity of the plasma beam at micro-scale. 112

4-15 With initially large features, the surface will be smoothed out after Ar sputtering at normal ion incidence angle. (a) Unetched polysilicon surface with a RMS roughness level of 3.6 nm and the vertical scale of the image is 40 nm. (b) Etched polysilicon surface after Ar sputtering at normal angle using 310 eV ions and the ion fluence received is 1.25×10^{18} ions/cm^2; the RMS roughness level is 1.3 nm and the vertical of the image is 10 nm. (c) The cross section analysis of the (solid line) unetched and the (dashed line) etched surfaces. 114

4-16 Dependence of the direction of the striation strurture on the beam incidence direction (adopted from Ref. 11). (a) When the off-normal angle is smaller than a threshold value, the striation formed is transverse to the beam direction. (b) At very high grazing angles, the striation is parallel to the beam direction because that the ion scattering effects are dominant and therefore the ion scattering caused channeling effect is important. 115

5-1 The AFM images and the corresponding surface carbon (C1s) XPS spectrums of (a) thermal SiO_2 and (b) low-k dielectric coral films before plasma etching. The vertical scale of both films is 15 nm and both of the images represent 1 μm × 1 μm of the real sample surface. The RMS roughness of SiO_2 and coral is 0.2 and 1.0 nm, respectively. 122

5-2 Surface AFM images and the corresponding surface carbon (C1s) XPS spectrums of thermal SiO_2 after etching in C_4F_8/Ar plasmas under various plasma source pressures and C_4F_8/Ar volumetric ratios. The vertical scale of all films is 15 nm and all of the images represent 1 μm × 1 μm of the real sample surface. The C_4F_8 percentage, beam source pressure level, and the ion fluence reach the surface are (a) 10%, 4 mtorr, and 3.0×10^{17} ions/cm^2; (b) 10%, 10 mtorr, and 1.5×10^{17} ions/cm^2; (c) 15%, 13 mtorr, and 2.0×10^{17} ions/cm^2; (d) 15%, 20 mtorr, and 1.3×10^{17} ions/cm^2, respectively. In all cases, the ions bombard the surface at 75° off-normal angle and the DC bias level is 350 V, and the ions reach the surface from the up-right direction. The RMS roughness and the film thickness etched are (a) RMS 2.5 nm and 82 nm etched; (b) RMS 0.15 nm and 58 nm etched; (c) RMS 1.5 nm and 61 nm etched; (d) RMS 1.4 nm and 31 nm etched, respectively. 124

5-3 Surface AFM images and the corresponding surface carbon (C1s) XPS spectrums of low-k dielectric coral film after etching in C_4F_8/Ar plasmas under various plasma source pressures and C_4F_8/Ar volumetric ratios. The vertical scale of all films is 15 nm and all of the images represent 1 μm × 1 μm of the real sample surface. The C_4F_8 percentage, beam source pressure level, and the ion fluence reach the surface are (a) 10%, 4 mtorr, and 3.0×10^{17} ions/cm^2; (b) 20%, 5 mtorr, and 3.0×10^{17} ions/cm^2; (c) 20%, 8 mtorr, and 2.0×10^{17} ions/cm^2; (d) 20%, 15 mtorr, and 1.75×10^{17} ions/cm^2, respectively. In all cases, the ions bombard the surface at 75° off-normal angle and the DC bias level is 350 V, and the ions reach the surface from the up-right direction. The RMS roughness and the film thickness etched are (a) RMS 1.4 nm and 199 nm etched; (b) RMS 0.57 nm and 211 nm etched; (c) RMS 0.81 nm and 195 nm etched; (d) 4.16 nm and 63 nm etched, respectively. 125

5-4 The impact of etching time on Surface roughness evolution of thermal SiO_2 after etching in 15% C_4F_8/Ar plasmas at 13 mtorr plasma source pressure level at 75° off-normal angles. The vertical scale of both films is 15 nm and both of the images represent 1 μm × 1 μm of the real sample surface. In both cases, the DC bias level is 350 V and the ions reach the surface from the up-right direction. The ion fluence reaching the surface, the film thickness etched and the RMS roughness level are (a) 1.0×10^{17} ions/cm^2, 32 nm, and 0.24 nm; (b) 2.0×10^{17} ions/cm^2, 61 nm, and 1.5 nm, respectively. 127

5-5 The impact of etching time on Surface roughness evolution of low-k dielectric coral film after etching in 20% C_4F_8/Ar plasmas at 15 mtorr plasma source pressure level at 75° off-normal angles. The vertical scale of both films is 15 nm and both of the images represent 1 μm × 1 μm of the real sample surface. In both cases, the DC bias level is 350 V and the ions reach the surface from the up-right direction. The ion fluence reaching the surface, the film thickness etched and the RMS roughness level are (a) 1.0×10^{17} ions/cm^2, 33 nm, and 1.42 nm; (b) 1.75×10^{17} ions/cm^2, 63 nm, and 4.16 nm, respectively. 128

5-6 The roughening of thermal SiO_2 after etching in $C_4F_8/Ar/O_2$ plasmas under various plasma source pressures and $C_4F_8/Ar/O_2$ volumetric ratios. The vertical scale of all films is 15 nm and all of the images represent 1 μm × 1 μm of the real sample surface. The C_4F_8 and O_2 percentages, beam source pressure level, and the ion fluence reach the surface are (a) 20% C_4F_8 and 10% O_2, 6 mtorr, and 2.0×10^{17} ions/cm^2; (b) 10% C_4F_8 and 5% O_2, 12 mtorr, and 2.0×10^{17} ions/cm^2; (c) 15% C_4F_8 and 15% O_2, 16 mtorr, and 2.0×10^{17} ions/cm^2, respectively. In all cases, the ions bombard the surface at 75° off-normal angle and the DC bias level is 350 V, and the ions reach the surface from the up-right direction. The RMS roughness and the film thickness etched are (a) RMS 0.17 nm and 113 nm etched; (b) RMS 0.16 nm and 79 nm etched; (c) RMS 0.15 nm and 80 nm etched, respectively. 131

5-7 The roughening of low-k dielectric coral film after etching in 20% C_4F_8/10% O_2/Ar plasmas under various plasma source pressures. The vertical scale of all films is 15 nm and all of the images represent 1 μm × 1 μm of the real sample surface. The beam source pressure level, and the ion fluence reach the surface are (a) 5 mtorr, and 3.0×10^{17} ions/cm^2; (b) 9 mtorr, and 2.0×10^{17} ions/cm^2; (c) 15 mtorr, and 1.75×10^{17} ions/cm^2, respectively. In all cases, the ions bombard the surface at 75° off-normal angle and the DC bias level is 350 V, and the ions reach the surface from the up-right direction. The RMS roughness and the film thickness etched are (a) RMS 0.39 nm and 175 nm etched; (b) RMS 0.49 nm and 170 nm etched; (c) RMS 0.58 nm and 101 nm etched, respectively. 132

6-1 The AFM images of unetched (a) OSG and (b) porous low-k films. The vertical scale of both films is 10 nm and both of the images represent 1 μm × 1 μm of the real sample surface. The RMS roughness of OSG and porous low-k films is 0.9 and 1.2 nm, respectively. 138

6-2 The surface composition of solid OSG and porous low-k films characterized by XPS before etching in C_2F_6/Ar plasma beams. 139

6-3 The evolution of surface roughness with the ion dosage reaching the porous low-k film during etching in 20% C_2F_6/Ar plasma beam at normal angle. Plasma etching conditions: total flow rate 5 sccm, beam source pressure 10 mtorr, RF source power of 350 W. 370 eV ions were used and the vertical scale is 50 nm for both AFM images. (a) The dosage is 2.0×10^{17} ions/cm^2 and the RMS roughness is 3.2 nm after 115 nm film was etched. (b) The dosage is 5.0×10^{17} ions/cm^2 and the RMS roughness is 9.0 nm after 300 nm film was etched. 140

6-4 The evolution of surface roughness with the ion dosage reaching solid OSG during etching in 20% C_2F_6/Ar plasma beam at normal angle. Plasma etching conditions: total flow rate 5 sccm, beam source pressure 10 mtorr, RF source power 350 W. 370 eV ions were used and the vertical scale is 10 nm for both AFM images. (a) The dosage is 2×10^{17} ions/cm^2 and the RMS roughness is 0.9 nm after 97 nm film was etched. (b) The dosage is 5×10^{17} ions/cm^2 and the RMS roughness is 1.1 nm after 238 nm film was etched. 140

6-5 XPS C(1s) signals of (a) OSG and (b) porous low-k films before and after etching in 20% C_2F_6 /Ar plasma at normal angle. Plasma etching conditions: total flow rate 5 sccm, beam source pressure 10 mtorr, RF source power 350 W, ion bombardment energy 370 eV. 142

6-6 The impact of ion bombardment energies (equivalently DC bias voltage) on (a) etching rate and (b) surface roughness after etching in 20% C_2F_6/Ar plasma at normal impingement angle. Plasma etching conditions: total flow rate 5 sccm, beam source pressure 10 mtorr, RF source power of 350 W, ion fluence 5.0×10^{17} ions/cm^2. 144

6-7 XPS C(1s) signals of (a) OSG and (b) porous low-k films before and after etching in 20% C_2F_6/Ar plasma using different ion bombardment energies levels at normal angle. Plasma etching conditions: total flow rate 5 sccm, beam source pressure 10 mtorr, RF source power of 350 W, ion fluence 5.0×10^{17} ions/cm^2. 145

6-8 The impact of plasma polymerization capability on (a) etching rate and (b) surface roughness after etching in C_2F_6/Ar plasma at normal impingement angle. Plasma etching conditions: total flow rate 5 sccm, beam source pressure 10 mtorr, RF source power 350 W, ion fluence 5.0×10^{17} ions/cm^2, and ion energy level 370 eV (equivalently, DC bias 350 V). 147

6-9 XPS C(1s) signals of (a) OSG and (b) porous low-k films before and after etching in C_2F_6/Ar plasma as a function of C_2F_6 molar percentage in the mixed feed gas at normal angle. Plasma etching conditions: total flow rate 5 sccm, beam source pressure 10 mtorr, RF source power 350 W, ion fluence 5.0×10^{17} ions/cm^2, and ion energy level 370 eV (equivalently, DC bias 350 V). 148

6-10 The plasma neutral spectrums of 10% C_2F_6/Ar and 20% C_2F_6/Ar plasmas. In both cases, the plasma running conditions are: total gas flow rate 5 sccm, beam source pressure ~10 mtorr, RF source power of 350 W. 149

6-11 Pore filling seeds micromask formation on porous low-k film. (a) The polymer fills into the pores; (b) Simultaneous etching of the porous low-k film forms polymer micromasks even under conditions of high ion bombardment; (c) Selectivity between the deposited polymer and the substrate roughens the surface. 150

6-12 The variation of surface roughness of (♦,◊) solid OSG and (■, □) porous low-k films after processing in 20% C_2F_6/Ar plasma at normal impingement angle. Plasma etching conditions: total flow rate 5 sccm, beam source pressure 10 mtorr, RF source power 350 W; ion fluence 5.0×10^{17} ions/cm^2 for close symbols and 2.0×10^{17} ions/cm^2 for open symbols. 152

6-13 The surface roughness of (a) porous low-k films and (b) solid OSG films after etching in 20% C_2F_6/Ar plasma beam at 75° off-normal angle. The beam direction is parallel to the striation structure and is from bottom to top. Plasma etching conditions: total flow rate 5 sccm, beam source pressure 10 mtorr, RF source power 350 W, ion energy is 340 eV. The vertical scale is 20 nm for both AFM images and RMS roughness is 2.7 nm for porous low-k and 0.5 nm for solid OSG film. The real ion fluence is 1.3×10^{17} ions/cm^2, which is measured at normal impingement angle and corrected to the view factor at 75° off-normal angle. 153

6-14 The schematic of "shadowed" sample area with near- glancing ions at 75°. Due to the very glancing angle formed by the beam ions, areas of the surface directly behind a protrusion receive no flux. This occurs when the angle formed by the surface normal and incident ion direction exceeds 90°. 154

6-15 The AFM image of porous low-k film after etching at grazing 75° off-normal angle in 20% C_2F_6/Ar plasma in the beam chamber system. 110 eV ions were used (DC bias level 100 V) and the vertical scale of the image is 10 nm. The surface topography after etching is very smooth and no striation structure is available. The RMS roughness is 0.8 nm. 155

6-16 The surface topography of porous low-k after sputtering in pure Ar chemistry at 75° off-normal angle with real ion fluence level 1.5×10^{17} ions/cm^2. The ion energy level is about 340 eV and the vertical scale is 20 nm. The RMS roughness after etching is 2.3 nm. 155

7-1 Ideal semivariogram on an isotropic surface where the sill (C) and the range (a) are shown. 165

7-2 Semivariogram of an anisotropic surface where a series of parallel streaks exist, taken in the direction across the streaks. The lag distance to the first minimum (mindist) can be interpreted as the average spacing of the ridges. 165

7-3 Comparison between the autocorrelation and semivariogram analysis on the sputtered coral film in Ar plasma at 75° ion bombardment off-normal angle. 166

7-4 The AFM images of coral film, after sputtering in argon plasma for different ion fluence levels at 75° ion bombardment off-normal angle. In all cases, the vertical range is 50 nm. The ion fluence levels are: (a) 1.0×10^{17}, (b) 2.0×10^{17}, and (c) 3.5×10^{17} ions/cm^2. 168

7-5 The PSD analysis of coral film, along the X direction perpendicular to the streaks, after sputtering in argon plasma for different ion fluence levels at 75° ion bombardment off-normal angle. 169

7-6 The impact of etching time on the semivariogram along the X direction, perpendicular to the striation structure, for coral film after sputtering in argon plasma for different ion fluence levels. 172

7-7 The impact of etching time on the average striation periodicity along the X direction, perpendicular to the striation structure, for coral film after sputtering in argon plasma for different ion fluence levels. 173

7-8 The impact of etching time on the semivariogram along the Y direction, parallel to the striation structure, for coral film after sputtering in argon plasma for different ion fluence levels. 173

7-9 The impact of etching time on the average striation length along the Y direction, parallel to the striation structure, for coral film after sputtering in argon plasma for different ion fluence levels. 174

7-10 The AFM images of coral film, after sputtering in argon plasma for two different ion bombardment off-normal angles. The vertical range is (a) 50 nm and (b) 30 nm. The ion bombardment off-normal angles are (a) 75°, and (b) 82°. 176

7-11 The impact of ion bombardment off-normal angle on the semivariogram along the X direction, perpendicular to the striation structure, for coral film after sputtering in argon plasma. 177

7-12 The impact of ion bombardment off-normal angle on the semivariogram along the Y direction, parallel to the striation structure, for coral film after sputtering in argon plasma. 177

List of Tables

3-1 Ion and neutral flux compositions in the Cl_2/Ar plasmas used in this study determined by mass spectrometry. 58

3-2 Comparison of Si(2p) and Cl(2p) XPS signal intensities at different ion bombardment angles, different etching chemistries, and different XPS take-off angles. The signal intensities have been corrected to their corresponding sensitivity factors. 85

7-1 Estimation of the critical spatial frequency beyond which the tip filtering effects exist. 171

7-2 The impact of ion bombardment off-normal angle on the average striation periodicity along the X direction, perpendicular to the striation structure, for coral film after sputtering in argon plasma. 178

7-3 The impact of ion bombardment off-normal angle on the average striation length along the Y direction, parallel to the striation structure, for coral film after sputtering in argon plasma. 178

Chapter 1. Background and Research Motivation

1.1 Integrated Circuits Manufacturing

Since its invention about 40 years ago, the Integrated Circuit (IC) has literally changed our world. To date, more and more complex circuits are built simply by making the individual components smaller which allows more of them to be integrated in a given area, and by making the overall size of chips larger. The higher levels of integration permitted by these smaller devices and bigger chips have made it possible to build progressively more complex, higher-performance, and more economical integrated systems as time passed. In IC technology, the component size is characterized by the minimum line width, which is defined as the smallest lateral feature size printed on the wafer surface during the fabrication process.

In Moore's law[1], it was predicted that the number of components on a chip would be doubled every 1.4 years, as shown in Figure 1-1. As the minimum feature size continues to shrink to sub 100 nm regime, however, semiconductor processing needs extremely strict requirements in terms of (a) selectivity with respect to mask and substrate or underlying material; (b) profile control of the pattern; (c) damage to the operating material; and (d) uniformity and rate of the etching. Plasma etching is one of the basic steps used in semiconductor processing for the fabrication of electronic devices because anisotropic etching allows high-fidelity pattern transfer and the processing can be performed at relatively low temperatures.

1.2 Plasma Processing

Plasma is a low pressure, partially ionized gas through which an electric current is passed to accelerate free electrons that in turn excite and dissociate molecules to form energetic ions and reactive neutrals. Figure 1-2 shows the schematic description of the plasma-surface interactions using chlorine etching of photoresist patterned polysilicon over a silicon dioxide film as an example.

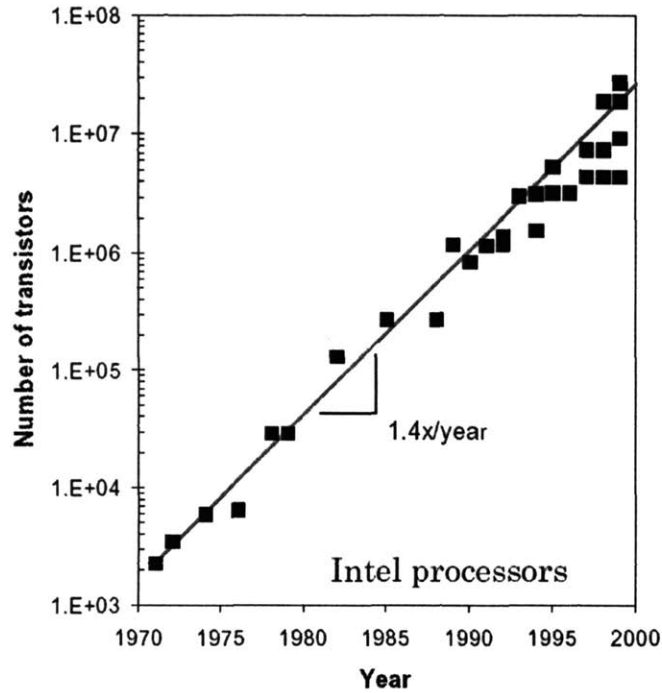

Figure 1-1 The number of transistors on a chip is doubled every other 1.4 years.

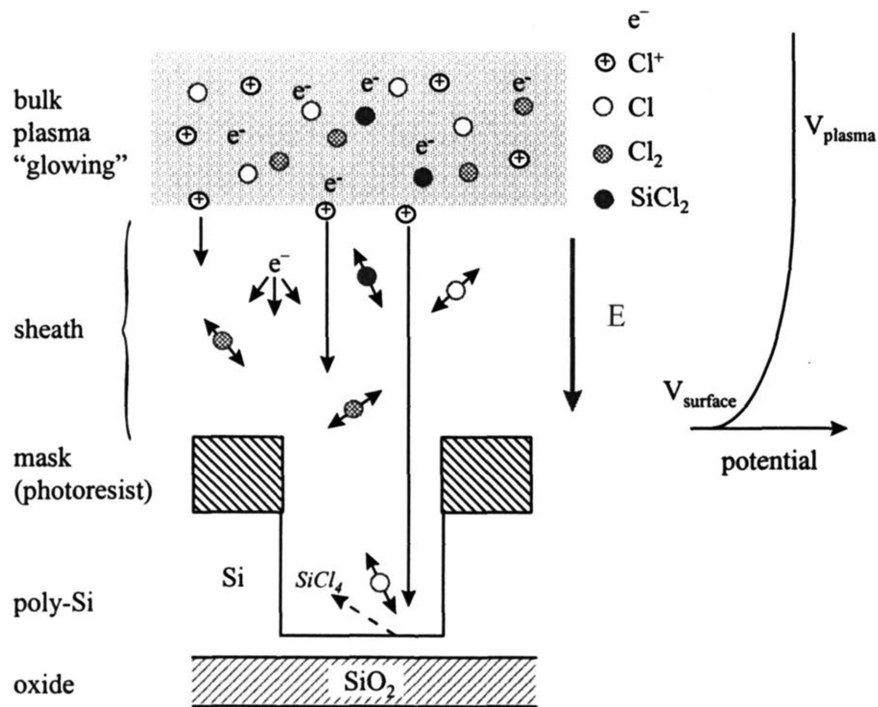

Figure 1-2 Schematic diagram illustrating the chlorine ion-enhanced etching of photoresist patterned polysilicon. The major reactive species in plasma include energetic chlorine ions (Cl^+) and reactive neutrals (Cl, Cl_2, $SiCl_2$).

An ideal plasma etching process requires perfect pattern transfer by anisotropic (directional) etching of polysilicon, and no etching of either photoresist or silicon dioxide upon ion bombardment (infinite selectivity). This typically requires highly directional ions and minimal spontaneous etching of polysilicon by reactive neutrals. However, in reality, various artifacts will appear in the etching process. Artifacts such as RIE lag[2] can be significantly reduced by moving to high density plasma sources, because of their less collisional plasma, however, various artifacts, such as sidewall bowing, bottom micro-trenching, undercutting, notching, will possibly be resulted[3-9]. Some common artifacts are shown schematically in Figure 1-3.

Bowing refers to the curvature of the sidewalls. Bowing can be caused by a variety of factors, such as non-directional ions, smaller etching yields for grazing angle ions[10] and sidewall deposition. Sidewall bowing affects the critical dimension of the feature and can cause micro-trenching at the feature bottom.

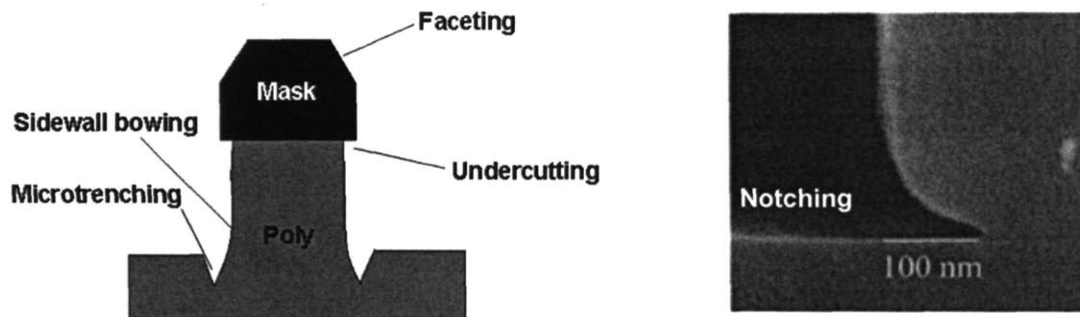

Figure 1-3 A couple of common artifacts in plasma etching process.

Micro-trenching is the enhanced etching at the foot of an etched sidewall. Micro-trenching is undesirable during the polysilicon etching step because the thin gate oxide can be broken through ion flux at the micro-trench locations damaging the Metal-Oxide-Semiconductor (MOS) transistor. Typically, it is caused by the increased flux of ions at the trenches due to reflection from tapered/bowed sidewalls or possible bending of ion trajectories because of charging effects[11,12]. Mahorowala et al.[8] found the etching recipe will also influence the formation of micro-trenching. By using two different recipes, they found that HBr or Br_2 chemistry removed the microtrenching, however it always existed when using chlorine chemistry. Vitale et al.[10] investigated the dependence of etching yield

on off-normal angle. Specifically, for Cl_2 based plasma, the etching yield decreased rapidly above 60°, and reached approximately 0 at 80°. However, in HBr plasmas, the ion enhanced etching yield decreased more gradually, and had relatively high etching yields even at nearly grazing incidence.

Undercutting refers to the lateral etching into a layer and can be considered as extreme sidewall bowing. Typically, undercutting occurs at the interface of two materials when one of them is resistant to the etching species. Generally, undercutting is attributed to the ion scattering off the neighboring hardmask[3,5,9]. Ion scattering off the hardmask at a constant angle would impact the sidewall of a neighboring feature. As the feature width shrinks, the ions impact higher on the neighboring sidewall, causing the observed undercutting.

Notching sometimes will be observed during overetching of conductive films, such as polysilicon, at its surface with an underlying insulating film like SiO_2. It has been attributed to the feature charging induced ion trajectory distortion and the subsequent etching of polysilicon by ion induced etching. However, Chang and Sawin[4] believed that surface charging solely could not explain the notching very well, because the gate oxide has already been caused surface leakage before the accumulated surface charge could distort the ions to the degree necessary to form notching. In addition, they proved that notching of polysilicon during the overetching step was in part induced by the stress enhanced spontaneous etching. The reason was that Si-Si bonds in the polysilicon were more susceptible to breakage.

1.3 Sidewall Roughening and Line-edge-roughening Effects

1.3.1 Sidewall Roughening as a Challenge

As the key dimension continues shrinking to sub-100 nm regime, it is critical to control the post-etch roughness on the feature sidewall. This sidewall roughness after plasma etching is undesired in microelectronics processing. For front end processing, the sidewall roughness presenting in the final etched gate can affect the implant profile of the source and drain regions of the transistor, and consequently change the effective gate length. Charge carrier mobility can also be degraded via electron scattering[13]. On the back

end, sidewall roughness will degrade the resolution of contacts, interfere with the deposition of conformal liner materials, and potentially lead to short circuits between adjacent metal lines or contacts[14,15].

1.3.2 Top Line-edge-roughening Effects

Many researchers explored the roughness evolution on photoresist sidewall during the development process and defined this sidewall roughness as the top line-edge-roughness (LER)[16-19]. This post-development LER on photoresist layer is due to many factors, including the structure of the resist, the roughness transferred from the mask features to the resist via the aerial image, statistical shot noise effects in the exposure process, variations in diffusion, and the reaction of photoacid generator (PAG) at the boundary between the polymer and developer in the development process. Reynolds et al.[20] showed that the most important contributions to the overall post-lithographic roughness appeared to be the development process and mask defect. However, they did not consider the influence of the resist properties. Several groups[21-25] have proven that the resist with lower molecular weight and narrow molecular weight distribution led to minimal sidewall roughness after the solution development. Shin et al.[26] also demonstrated that the sidewall roughness depended on the resist height (or the line to space ratio), they found that the sidewall roughness increased significantly with increasing resist height. This phenomenon can be explained from the mass transport perspective: for normal dissolution of bulk exposed resist, the developer solution has free access to the resist and may move in any direction parallel to or away form the surface, however, in the case of nested lines, the developer must penetrate into the exposed line between unexposed resist lines. As a result, the resist on the top surface will be in contact with the developer solution for longer time compared to the bottom.

It has been demonstrated that the top LER played a critical role on the sidewall roughness evolution of subsequently layers during plasma etching[17,27,28]. In particular, Goldfarb et al.[17] quantitatively studied this top LER effects for the etching of dielectric materials in fluorocarbon plasmas, as shown in Figure 1-4. Obviously, the resist sidewall roughness after development but before plasma etching was isotropic; during the anti-reflective coating (ARC) layer opening in plasma etching process, the photoresist layer

became striated and the top edge of the photoresist layer was faceted; the striation structure became much more significant and propagated down after etching of the subsequent SiO_2 layer.

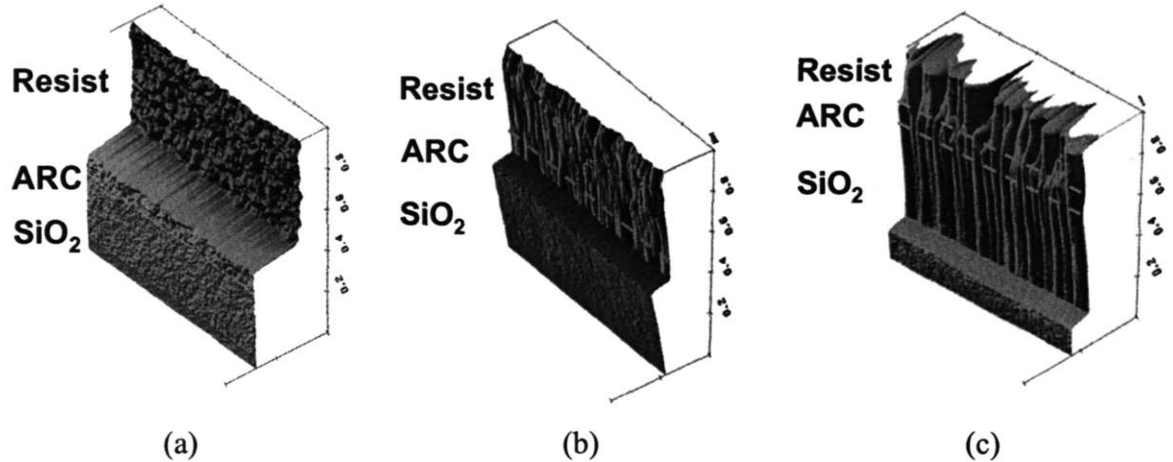

Figure 1-4 The AFM images of the feature sidewall at different processing steps. (a) After photoresist development but before plasma treatment; (b) after N_2-H_2 organic ARC open; (c) after 45 s oxide etch in fluorocarbon plasmas.

1.3.3 Simulation Approach to Understand Sidewall Roughening

Different feature profile simulators[5,29-33] have been developed to understand various artifacts seen in the real processing conditions, such as microtrenching, sidewall bowing, undercut, and sidewall roughening discussed above. Among them, however, most efforts have been focused on simulating the sidewall roughening of photoresist during its development. For instance, Patsis et al.[18,21,34-37] simulated the surface roughness and LER during the solution development based on a three dimensional square lattice model. Using this model, it was possible to predict the change of roughness with dose, development time, acid diffusion length, photoacid generator (PAG) concentration, and polymer structure. Willson et al.[16,38] performed the simulation using a similar three dimensional lattice model. However, they allowed polymer blended so that the effects of poly-dispersity could be investigated. Additionally, a portion of the polymer matrix was set aside as void space. Void cells automatically converted to developed cells whenever one of their neighboring cells developed. It was demonstrated that polymers with a lower degree of polymerization, narrower poly-dispersity, and greater void fraction produced less surface roughness.

Recently, based on existed 2D simulator[5,12,32,39,40], Kawai, Jin, and Sawin[41] have developed a 3-Dimensional Monte Carlo simulator to improve the fundamental understanding of feature profile evolution and surface roughness transfer on the feature sidewall in plasma etching. Besides the capability of modeling the top LER effects on the sidewall roughening, it is the first and only simulator that models the transition of surface roughening from ion bombardment, including both transverse and longitudinal orientation, on blank film in pure physical sputtering etching kinetics.

Besides the 3-Dimensional profile, a robust simulator must incorporate realistic surface kinetics that can model both deposition as well as etching. The modeling of polymer deposition is critical to contact hole etching in that it greatly affect the ultimate hole dimension as well as the roughness of the sidewall. For example, scattering within a hole in 3D can lead to increasing assymmetry forming oval rather than circular holes due to focusing effects. Kwon, Bai, Guo and Sawin[42-44] have developed a numerical model that used a well mixed translating film to describe the etching and deposition kinetics during plasma etching. This generic surface kinetics model allows reactions to be developed using numerical techniques with their approximate rate coefficients, and incorporated directly into a 3-Dimensional simulator. This approach made the development of the reactions and corresponding rates for any system of interest rapid.

Without a complete set of experimental data, however, both the 3-Dimensional feature profile simulator and the generic surface kinetics model mentioned above are difficult to produce results with solid physical meaning. These critical experimental data include the plasma composition and the etching yields at various plasma conditions and ion bombardment off-normal angles, and more importantly, the surface composition and surface topography on etched surfaces, etc.

1.4 Surface Roughening on Blank Films in Plasma Etching

The sidewall roughness can be measured using Atomic Force Microscopy (AFM) based techniques[17,20,45,46]. In this method, the wafer is cleaved parallel to the line-and-space patterns one is interested in, as shown in Figure 1-5. The sample is then rotated so that the AFM tip can graze the sidewall. The AFM tip scans the desired length of the sidewall and traverses laterally to scan the entire sidewall. As a result, sidewall roughness

variation as a function of feature depth can be studied. In this way, the sidewall roughness is the root mean square roughness and is defined as[20]:

$$rms = \left[\frac{1}{n}\sum_{1}^{n}(z_i - z)^2\right]^{1/2}, \tag{1-1}$$

where z is the average height of the image, z_i is the height of each datum in the image, and n is the total number of data points.

However, this new technique is limited by the diameter of the AFM tip and higher roughness frequencies are difficult to capture. And the AFM tip might not reach the valley of a roughness related feature and the roughness might be underestimated[17].

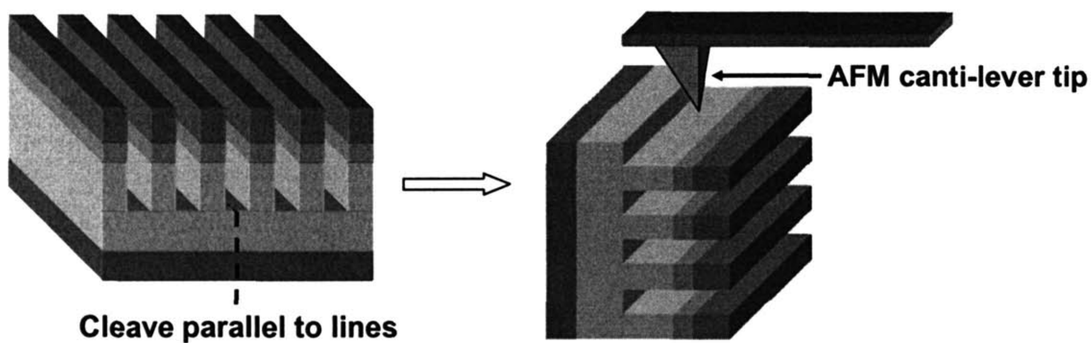

Figure 1-5 The schematic of how to measure the sidewall roughness using AFM technique.

Alternatively, it is sometimes assumed that the top surface of the resist/substrate will have a similar roughness to that of the sidewall surface. By varying the off-normal angle of ion impingement onto blank substrates, the etching kinetics and surface roughening various ion bombardment off-normal angles can be characterized conveniently. In particular, the etching kinetics and roughening on the real feature sidewall can be mimicked. The schematic of this method is shown in Figure 1-6.

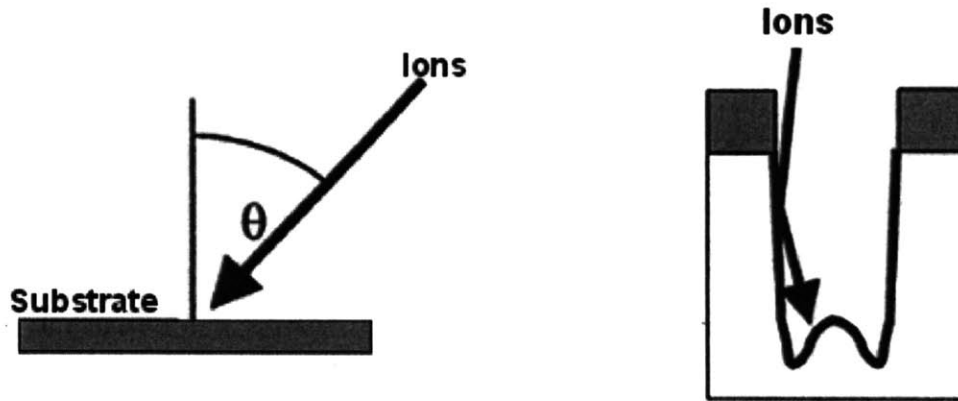

Figure 1-6 Left-hand side shows the definition of the angle of ion impingement. Right-hand shows a sketch of how ions can reflect from sidewall of etching feature at small angles.

1.5 Impact of Etching Kinetics on Feature Surface Roughening

Although minimal sidewall roughness is always desired on etched features in microelectronics processing, the mechanism of the sidewall roughness evolution in plasma etching has not been fully understood. The following questions have to be answered in order to have a better understanding of the mechanism of sidewall roughening. Besides the top LER effects discussed previously, will various materials be roughened in plasma etching? In particular, what is the influence of etching kinetics and etching chemistry on feature surface roughening? Additionally, will the etching kinetics be manipulated by changing plasma parameters?

Indeed, it has been demonstrated in the literature that the etching kinetics, especially the angular etching yields, varied with the plasma etching conditions. Blom et al.[47,48] measured the normalized angular etching yields during the etching of silicon nitride in fluorocarbon plasmas, and found that the angular etching yield curve was manipulated by changing the plasma pressure. More specifically, the angular etching yield curve was sputtering like at low plasma pressure level, while ion-enhanced-etching-like at high plasma pressure levels. Different researchers[49,50] have tried to understand why the angular etching yields changed with etching parameters, such as the plasma pressure. Kwon et al.[50] proposed an ion-enhanced polymer deposition mechanism to explain the evolution of angular etching yields during the etching of SiO_2 in fluorocarbon plasmas. However, this

proposed polymer deposition effect could not explain why the angular etching yields sometimes peaked around 65° off-normal angles.

In order to have a better understanding of the impact of plasma conditions on angular etching yields, as well as the relation between etching kinetics and feature surface roughening, an apparatus with the flexibility to control the plasma chemistry, ion bombardment energy, and incident angle independently is designed. A detailed description of this plasma beam reactor will be discussed in Chapter 2.

1.6 Scope and Objectives of This Work

The scope of this work is to experimentally characterize the etching kinetics and surface roughening of polysilicon and dielectric materials in various etching conditions so that a complete set of experimental data is available for the 3-Dimensional feature profile simulator that includes roughening and the generic surface kinetics modeling.

The first objective was to design and construct an inductively coupled plasma beam apparatus that can control the plasma composition, ion energy, and ion bombardment angle separately. This plasma beam reactor will be described in Chapter 2. The ion energy distribution, ion beam uniformity, ion flux stability, and the space charge effects on the ion beam were carefully characterized. Additionally, the ion flux variation with the ion bombardment off-normal angle was measured experimentally and the variation follows the cosine distribution. Encouragingly, my plasma beam apparatus was adequate for quantifying the etching kinetics and surface roughening of different materials under various etching conditions.

The second objective was to study the impact of etching parameters on the angular etching yields. In particular, I need to understand why physical-sputtering like angular etching yields are often formed at low plasma pressures, while in most cases high plasma pressures result in ion-enhanced-etching like angular etching yields. Chapter 3 summarized the experimental results on the measurement of angular etching yields of polysilicon and dielectric films in Cl_2/Ar and fluorocarbon plasmas. Most importantly, it was found that the neutral-to-ion flux ratio was an important factor to determine the angular etching yields. Specifically, physical-sputtering like angular etching yield curves

were often formed at low ratios; while high ratios led to ion-enhanced-etching like angular yields in most cases.

The third objective was to characterize the impact of etching kinetics on surface roughening of different materials in plasma etching. First of all, the surface roughness evolution of various blank films in pure physical sputtering kinetics was studied and summarized in Chapter 4. Most importantly, the surface roughening at grazing ion bombardment angles was believed to be due to the ion-scattering-caused-channeling effects. Second, the impact of etching kinetics on dielectric materials roughening at grazing ion bombardment angles in fluorocarbon plasmas was characterized and reported in Chapter 5. In particular, at low neutral-to-ion flux ratios the roughening was mainly due to the ion scattering caused channeling effects; at high ratios, the roughening was mainly caused by local-polymer-deposition-caused micro-masking mechanism. Third, this local polymer deposition effects were applied to explain the roughening of low-k dielectric materials in fluorocarbon plasmas, which was discussed in Chapter 6.

The fourth objective was to introduce statistical data analysis methods to the characterization of surface roughness on etched surfaces. In particular, the Power Spectral Density (PSD) and geostatistical Semivariogram methods were discussed in Chapter 7. It was shown that these two methods were capable to capture the surface roughness on both vertical and lateral dimensions. Specifically, the spatial variation of the streaks formed during plasma etching can be quantitative measured by applying these two methods.

1.7 References

1. G. E. Moore, Electronics 38 (1965).
2. J. W. Coburn and H. F. Winters, Applied Physics Letters 55, 2730-2732 (1989).
3. H. Abe, Japanese Journal of Applied Physics 14, 1825-1826 (1975).
4. J. P. Chang and H. H. Sawin, Journal of Vacuum Science & Technology B 19, 1870-1873 (2001).
5. W. D. Jin and H. H. Sawin, Journal of Vacuum Science & Technology A 21, 911-921 (2003).
6. T. Kinoshita, M. Hane, and J. P. McVittie, Journal of Vacuum Science & Technology B 14, 560-565 (1996).

[7] J. M. Lane, F. P. Klemens, K. H. A. Bogart, M. V. Malyshev, and J. T. C. Lee, Journal of Vacuum Science & Technology a-Vacuum Surfaces and Films 18, 188-196 (2000).

[8] A. P. Mahorowala, H. H. Sawin, R. Jones, and A. H. Labun, Journal of Vacuum Science & Technology B 20, 1055-1063 (2002).

[9] M. Oda and K. Hirata, Japanese Journal of Applied Physics 19, L405-L408 (1980).

[10] S. A. Vitale, H. Chae, and H. H. Sawin, Journal of Vacuum Science & Technology a-an International Journal Devoted to Vacuum Surfaces and Films 19, 2197-2206 (2001).

[11] J. C. Arnold and H. H. Sawin, Journal of Applied Physics 70, 5314-5317 (1991).

[12] A. P. Mahorowala and H. H. Sawin, Journal of Vacuum Science & Technology B 20, 1084-1095 (2002).

[13] A. Pirovano, A. L. Lacaita, G. Ghidini, and G. Tallarida, Ieee Electron Device Letters 21, 34-36 (2000).

[14] A. E. Kaloyeros and E. Eisenbraun, Annual Review of Materials Science 30, 363-385 (2000).

[15] B. Z. Li, T. D. Sullivan, T. C. Lee, and D. Badami, Microelectronics Reliability 44, 365-380 (2004).

[16] L. W. Flanagin, V. K. Singh, and C. G. Willson, Journal of Vacuum Science & Technology B 17, 1371-1379 (1999).

[17] D. L. Goldfarb, A. P. Mahorowala, G. M. Gallatin, K. E. Petrillo, K. Temple, M. Angelopoulos, S. Rasgon, H. H. Sawin, S. D. Allen, M. C. Lawson, and R. W. Kwong, Journal of Vacuum Science & Technology B 22, 647-653 (2004).

[18] G. P. Patsis, V. Constantoudis, and E. Gogolides, Microelectronic Engineering 75, 297-308 (2004).

[19] E. Gogolides, V. Constantoudis, G. P. Patsis, and A. Tserepi, Microelectronic Engineering 83, 1067-1072 (2006).

[20] G. W. Reynolds and J. W. Taylor, Journal of Vacuum Science & Technology B 17, 334-344 (1999).

[21] G. P. Patsis and E. Gogolides, Microelectronic Engineering 83, 1078-1081 (2006).

[22] A. Tserepi, G. Cordoyiannis, G. P. Patsis, V. Constantoudis, E. Gogolides, E. S. Valamontes, D. Eon, M. C. Peignon, G. Cartry, C. Cardinaud, and G. Turban, Journal of Vacuum Science & Technology B 21, 174-182 (2003).

[23] A. Tserepi, E. S. Valamontes, E. Tegou, I. Raptis, and E. Gogolides, Microelectronic Engineering 57-8, 547-554 (2001).

[24] T. Yoshimura, H. Shiraishi, J. Yamamoto, and S. Okazaki, Japanese Journal of Applied Physics Part 1-Regular Papers Short Notes & Review Papers 32, 6065-6070 (1993).

[25] T. Yamaguchi, K. Yamazaki, and H. Namatsu, Journal of Vacuum Science & Technology B 22, 2604-2610 (2004).

[26] J. Shin, Y. Ma, and F. Cerrina, Journal of Vacuum Science & Technology B 20, 2927-2931 (2002).

[27] A. P. Mahorowala, K. Babich, Q. Lin, D. R. Medeiros, K. Petrillo, J. Simons, M. Angelopoulos, R. Sooriyakumaran, D. Hofer, G. W. Reynolds, and J. W. Taylor, Journal of Vacuum Science & Technology a-Vacuum Surfaces and Films 18, 1411-1419 (2000).

[28] P. Bhatnagara, S. Panda, N. L. Edleman, S. D. Allen, R. Wise, and A. Mahorowala, Applied Physics Letters 88 (2006).

[29] J. P. Chang, A. P. Mahorowala, and H. H. Sawin, Journal of Vacuum Science & Technology a-Vacuum Surfaces and Films 16, 217-224 (1998).

[30] D. B. Graves and M. J. Kushner, Journal of Vacuum Science & Technology A 21, S152-S156 (2003).

[31] G. Kokkoris, A. Tserepi, A. G. Boudouvis, and E. Gogolides, Journal of Vacuum Science & Technology A 22, 1896-1902 (2004).

[32] A. P. Mahorowala and H. H. Sawin, Journal of Vacuum Science & Technology B 20, 1064-1076 (2002).

[33] A. Sankaran and M. J. Kushner, Applied Physics Letters 82, 1824-1826 (2003).

[34] G. P. Patsis and E. Gogolides, Journal of Vacuum Science & Technology B 23, 1371-1375 (2005).

[35] G. P. Patsis, N. Glezos, and E. Gogolides, Journal of Vacuum Science & Technology B 21, 254-266 (2003).

[36] V. Constandoudis, E. Gogolides, G. P. Patsis, A. Tserepi, and E. S. Valamontes, Journal of Vacuum Science & Technology B 19, 2694-2698 (2001).

[37] G. P. Patsis, A. Tserepi, I. Raptis, N. Glezos, E. Gogolides, and E. S. Valamontes, Journal of Vacuum Science & Technology B 18, 3292-3296 (2000).

[38] L. W. Flanagin, V. K. Singh, and C. G. Willson, Journal of Polymer Science Part B-Polymer Physics 37, 2103-2113 (1999).

[39] W. D. Jin and H. H. Sawin, Journal of the Electrochemical Society 150, G711-G717 (2003).

[40] W. D. Jin, S. A. Vitale, and H. H. Sawin, Journal of Vacuum Science & Technology a-Vacuum Surfaces and Films 20, 2106-2114 (2002).

[41] H. Kawai, Jin, W. D., Sawin, H. H., (unpublished).

[42] O. Kwon and H. H. Sawin, Journal of Vacuum Science & Technology A 24, 1906-1913 (2006).

[43] O. Kwon and H. H. Sawin, Journal of Vacuum Science & Technology A 24, 1914-1919 (2006).

[44] O. Kwon, B. Bai, and H. H. Sawin, Journal of Vacuum Science & Technology A 24, 1920-1927 (2006).

[45] G. W. Reynolds and J. W. Taylor, Journal of Vacuum Science & Technology B 17, 2723-2729 (1999).

[46] G. W. Reynolds, J. W. Taylor, and C. J. Brooks, Journal of Vacuum Science & Technology B 17, 3420-3425 (1999).

[47] A. M. Barklund and H. O. Blom, Journal of Vacuum Science & Technology a-Vacuum Surfaces and Films 11, 1226-1229 (1993).

[48] A. M. Barklund and H. O. Blom, Journal of Vacuum Science & Technology a-Vacuum Surfaces and Films 10, 1212-1216 (1992).

[49] B. O. Cho, S. W. Hwang, G. R. Lee, and S. H. Moon, Journal of Vacuum Science & Technology A 18, 2791-2798 (2000).

[50] O. Kwon, W. D. Jin, and H. H. Sawin, Applied Physics Letters 88 (2006).

Chapter 2. Apparatus and Plasma Beam Characterization

2.1 Apparatus

Commercialized and home-designed plasma etchers have been extensively used to characterize the etching kinetics of low dielectric constant materials, as well as other films in various etching chemistries[1-10]. These plasma etchers, however, lack the flexibility to control the plasma chemistry, ion bombardment energy, and incident angle independently, which is necessary in order to fully understand the origin and evolution of the surface roughness during plasma etching. Therefore, a new dedicated plasma beam apparatus with the abilities mentioned above has been designed to characterize the etching kinetics and roughening of semiconductor materials. The schematic of this newly designed beam chamber is shown in Figure 2-1.

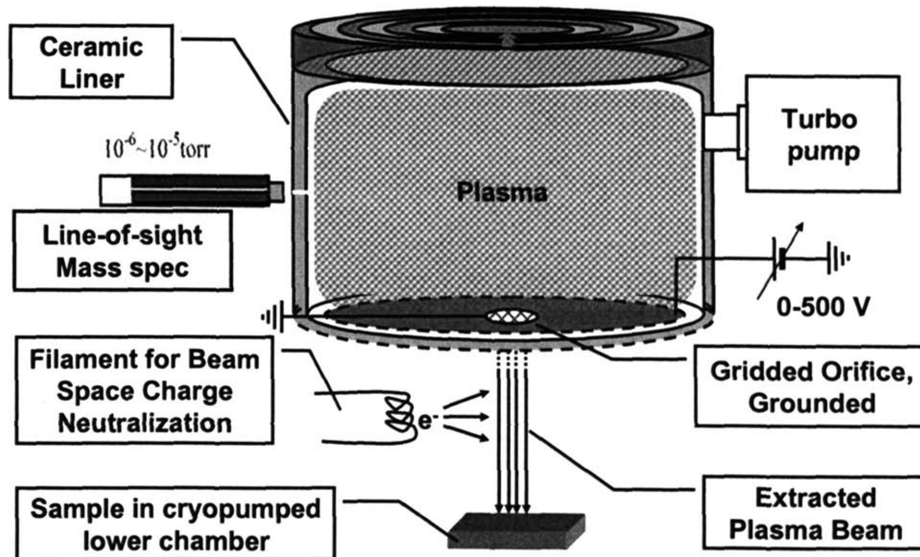

Figure 2-1 The schematic of a newly designed beam chamber system. The beam source locates at the upper part of the main chamber and the plasma is inductively coupled (ICP). This beam system has the flexibility to control the plasma chemistry, ion bombardment energy, and incident angle independently.

The beam source is located at the upper part of the main chamber, with the plasma powered by inductively coupling through a ceramic/quartz window located on the top of the chamber. A ceramic/quartz liner is used to isolate the plasma from the wall, which enables the plasma to be DC biased up to 500 V by using a metal electrode placed on the

interior of the beam source. The plasma potential relative to ground is the sum of the DC bias applied to the metal electrode and the plasma self-biased potential, which is typically 5-20 eV when the plasma density is sufficiently high so that the power is primarily coupled inductively. The pressure in the beam source can be controlled by throttling the flow to a turbo-molecular pump (Leybold TMP 361). The lower chamber is evacuated by a 4000 l/s cryogenic pump (CTI Cryogenics Cryo-torr 8) to maintain a base pressure of 10^{-8} torr and a pressure of $\sim 1.0 \times 10^{-4}$ torr during processing, thus ensure an adequately long mean free path for beam scattering. The plasma beam is extracted from the beam source to the lower part of the main chamber through a grounded gridded orifice. A tungsten filament (0.004 inch in diameter) emits low-energy electrons into the emerging beam in order to minimize the beam spreading due to space charge and to prevent charging of insulated samples. The lower chamber holds a sample stage (for about 0.5 inch wafer chips), an ion energy analyzer (to characterize the ion bombardment energy of the ions in the beam), and an ion flux analyzer (to characterize the ion current/flux from the beam). All three items are mounted on linear motions, rotatable or z axis feedthroughs, and can be backed away from the chamber center when not in use.

The sample stage can be rotated around its axis to change the beam impingement angle to the substrate surface. Sidewall roughening during plasma etching was investigated by etching blank films at glancing angles. One of the advantages of this method is that it is much more convenient to characterize the surface roughness on blank samples using the AFM technique.

The beam apparatus is connected to an ultrahigh vacuum transfer tube running at 10^{-9} torr. XPS chamber and other processing chambers are also connected to the transfer tube as shown in Figure 2-2. Sample was transferred through this transfer tube for surface analysis or other processing if necessary. Contamination of sample during transfer can be minimized thanks to the ultrahigh vacuum environment of the transfer tube. All the chambers connected to the ultrahigh vacuum transfer tube were designed for 4" wafer. ICP etcher and XPS analysis chamber were used for this study.

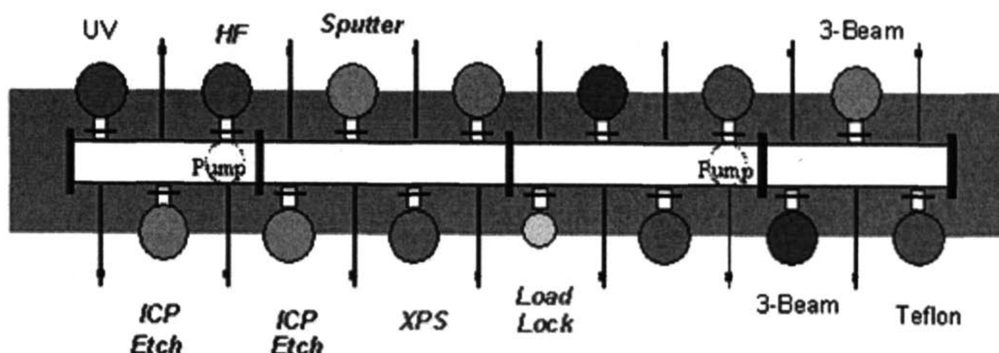

Figure 2-2 Schematic diagram of the integrated processing system that enables *in situ* sample transfer between process and analytic chambers.

2.2 Matching Network

RF power can be coupled to plasma by capacitive, inductive, or electromagnetic means. In each way, the impedance of the power source must match to that of the plasma for efficient power transfer. For this reason, a matching network is necessary for the best possible energy transfer efficiency. The schematic diagram of the realistic plasma source used in this work is shown in Figure 2-3. The inductively coupled plasma source consists of a stainless steel cylinder, a dielectric window (quartz or alumina), a three turn copper coil powered at 13.56 MHz (up to 1000 W) via a matching network.

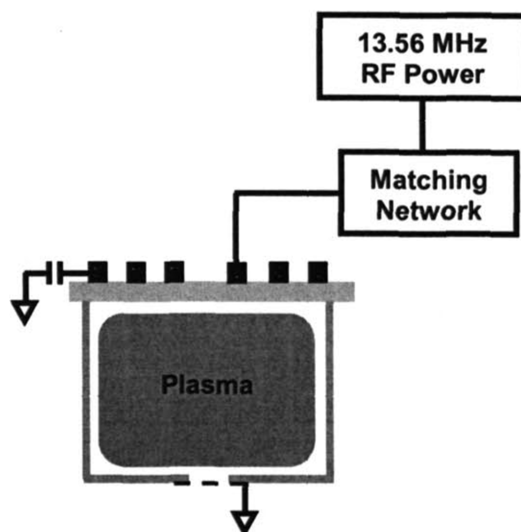

Figure 2-3 Schematic diagram of the realistic plasma source. The inductively coupled plasma source consists of a stainless steel cylinder, a dielectric window, a three turn copper coil powered at 13.56 MHz (up to 1000 W) via a Matching Network.

A typical RF matching network with L configuration is shown Figure 2-4. It is tuned by two variable capacitors (load capacitor C_1 and tune capacitor C_2) and an inductor (L_1) to create a resonance oscillation at the power supply frequency (e.g. 13.56 MHz). L_2 represents the total inductance of the 3-turn copper coil and the RF coaxial cable connecting the matching network and the copper coil. C_3 is a capacitor with fixed value between the outside end of the 3-turn copper coil and the ground. By manipulating the value of C_3, the AC voltage potential of the 3-turn copper coil can be adjusted, consequently, the amount of capacitive coupling to the plasma can be controlled, which will be discussed in next section. The energy oscillates between the inductor and capacitor at the RF power frequency. Assuming the resistive power losses are negligible, the following relationship must be satisfied at resonance frequency ω_0:

$$\omega_0 C_1 = \frac{1}{\omega_0 L_1 + \omega_0 L_2 - \frac{1}{\omega_0 C_2} - \frac{1}{\omega_0 C_3}}. \quad (2\text{-}1)$$

In current work, ω_0 is 13.56 MHz. In order to make the matching network have the highest possible power coupling efficiency, the numerical values of C_1, C_2, C_3, L_1, and L_2 have to be adjusted properly to meet the criteria in equation (2-1).

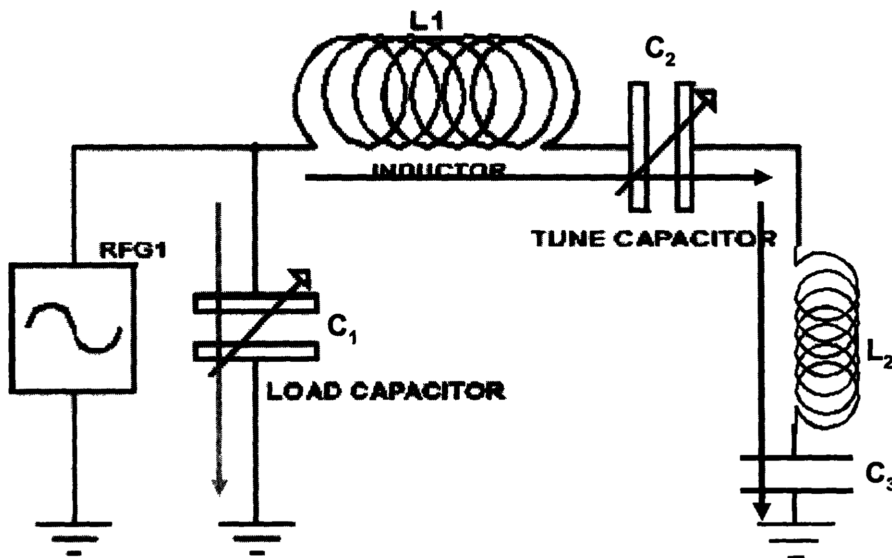

Figure 2-4 The configuration of the matching network electronics.

2.3 Inductive Coupling and Capacitive Coupling

Primarily, there are two different power coupling methods in RF plasmas: inductively coupled plasma (ICP) and capacitively coupled plasma (CCP)[11]. In capacitively coupled plasma, the applied electric field can be described capacitively. The electrons respond to the applied electric fields by accelerating. In inductively coupled plasmas, the power is coupled through an oscillating magnetic field. The oscillating magnetic field induces a current in the plasma that opposes the magnetic field by creating an equal current flowing in the opposite direction. The magnetic field of the primary (copper coil) is cancelled by the opposing magnetic field of the plasma. Consequently, power is coupled to the plasma.

In capacitively coupled plasma, a large fraction of the RF power is dissipated in the plasma sheath region to accelerate ions. On the other hand, most of the RF power is coupled to the plasma bulk phase in inductively coupled plasmas. Therefore, at a given RF input power level, the plasma density in capacitively coupled plasmas is lower than that in inductively coupled plasmas. Indeed, in realistic plasma etchers, the plasma density is controlled by a RF power source through inductive coupling, while the ion bombardment energy can be manipulated independently through capacitive coupling using a secondary RF power source.

In my plasma beam apparatus, inductively coupled plasma was desired so that the plasma density in the bulk phase was closer to the realistic plasma densities in real industrial etchers. Additionally, the ion bombardment energy was controlled using DC bias method. In general, at low RF power levels, the fraction of power dissipated in the sheath region is large so that capacitive coupling is dominating. In contrast, at high RF power levels, the fraction of power dissipated in the sheath region becomes less and the majority of power is coupled to the plasma bulk region so that the plasma is denser. At intermediate RF power, there is a transition regime where the plasma changes between capacitive coupling and inductive coupling and therefore plasma density can change sharply at this transition regime, as shown in Figure 2-5.

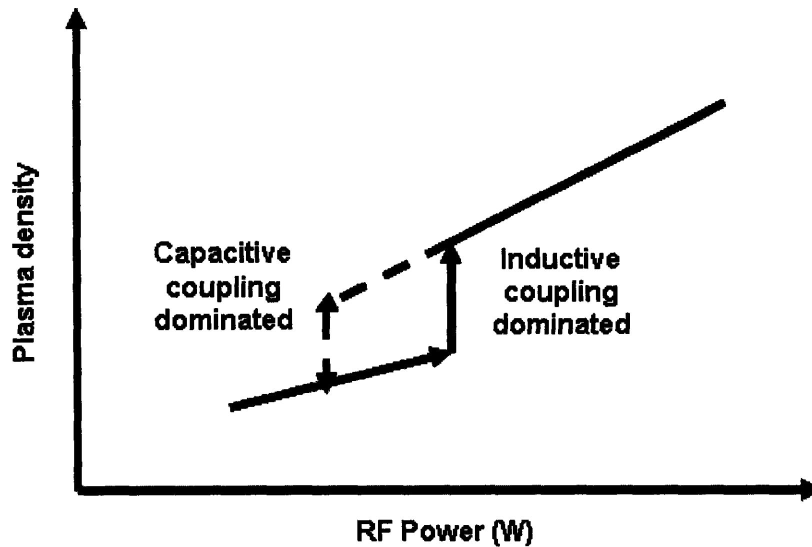

Figure 2-5 RF power coupling transits from capacitive coupling to inductive coupling with the increase of the RF power.

In the current apparatus, it was expected that the ion flux at the sample surface was a reflection of the plasma density in the bulk phase. Figure 2-6 shows the ion flux current measured by the ion flux analyzer as a function of RF power level. Unlike the trend described in Figure 2-5, the flux current has a local maximum around RF power 80W, then it increases monotonically with RF power. This inconsistency was due to the position where the ion flux was measured. In current work, the ions were always extracted from the bottom of the plasma bulk phase. At low RF power (before the local maximum), capacitive coupling dominated so that the plasma was relatively denser around the sheath region. At the local maximum, the plasma changed from capacitively coupled to inductively coupled. In inductively coupled plasma, the plasma was the densest at the top region around the 3-turn copper coil and the density decreased from the top region to the bottom region. Therefore, the plasma density at the bottom region decreased sharply at this critical RF power (the local maximum). For this reason, the ion flux current measured by the flux analyzer decreases quickly after the local maximum. With the increase of the RF power, the plasma density is recovered gradually and increases monotonically.

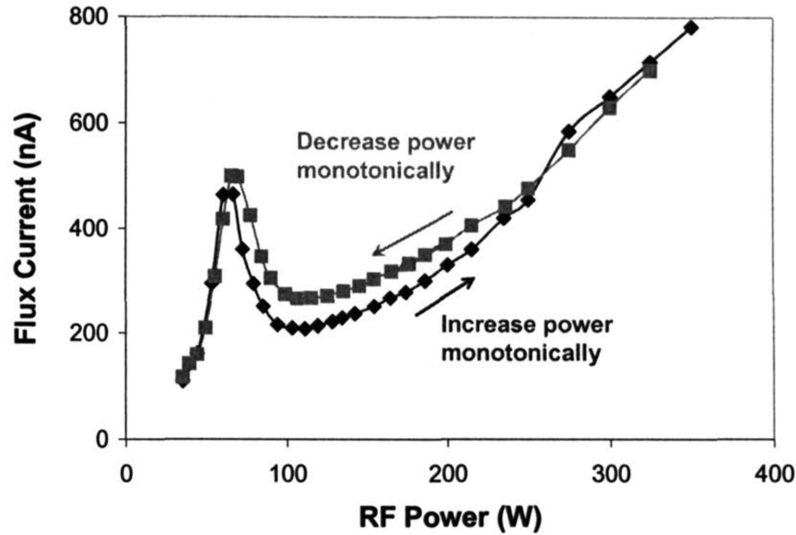

Figure 2-6 The variation of ion flux at the sample surface as a function of the RF power level.

2.4 Plasma Beam Characterization

2.4.1 Ion flux Analysis

2.4.1.1 Ion Flux Analyzer

A detailed review of the ion flux analyzer (IFA) used in this work has been demonstrated previous[12]. Essentially, it consisted of a grounded stainless top plate with a 1 mm of orifice, and collector plate that was electronically isolated from the IFA via ceramic washers and nylon 0-80 screws. The entire assembly was housed in a grounded aluminum cap shield to prevent ion flux from the sides to be measured at the collector. Furthermore, the electric field between the grounded top plate and the collector was not influenced significantly since the orifice on the top plate was only 1 mm in diameter. In addition, the electric field leakage from the top plate orifice was not important so that the impact of ions attraction effects around the orifice on ion flux measurement could be neglected.

2.4.1.2 Space Charge Neutralization

Well controlled plasma beam uniformity is desired in order to achieve accurate etching kinetics on various substrates by *ex situ* film thickness measurements. Over the entire range of my measurements, the variation of the normalized ion current across the

sample was less than 20%. In this newly designed plasma beam chamber system, the uniformity of the plasma beam extracted from the grounded orifice was controlled by neutralizing the space charge using low-energy electron emission from the tungsten filament.

Figure 2-7 shows the contour plots of the normalized ion current collected by the ion flux analyzer at DC bias of 100 V and 350 V along the beam center for 10 mtorr Ar plasma with RF source power of 350 W. The plasma beam uniformity was poor when the space charge neutralization filament was turned off. Specifically, the beam uniformity was even worse at high DC bias. Consequently, a small misalignment during the film thickness characterization might result in a large error of the corresponding etching rate measurements when using this beam. However, the plasma beam uniformity is well controlled using the tungsten filament with a filament current of ~1.4 A, as shown in Figure 2-8 The variation of the ion current is less than 20% over the sample center diameter of 0.3 inch when the DC bias level is 100 V. The beam uniformity is enhanced by increasing the DC bias.

(a)

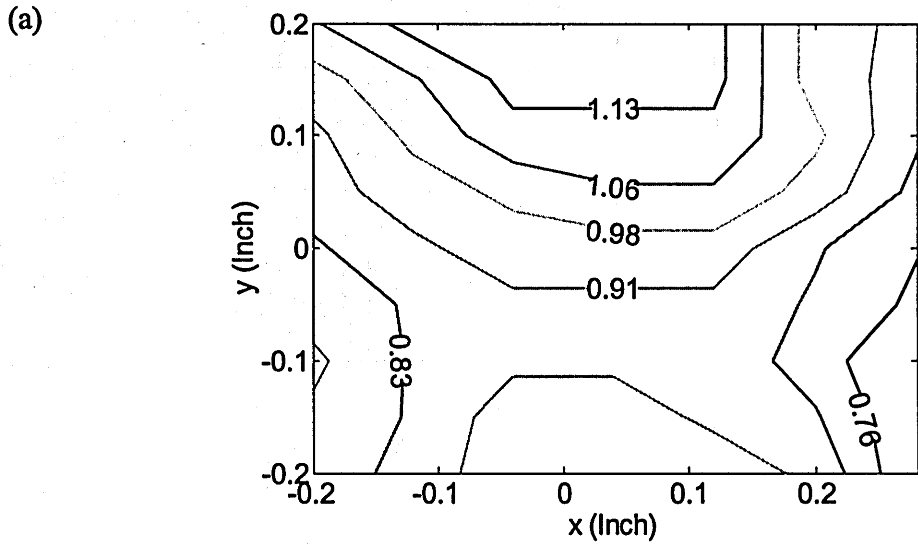

(b)

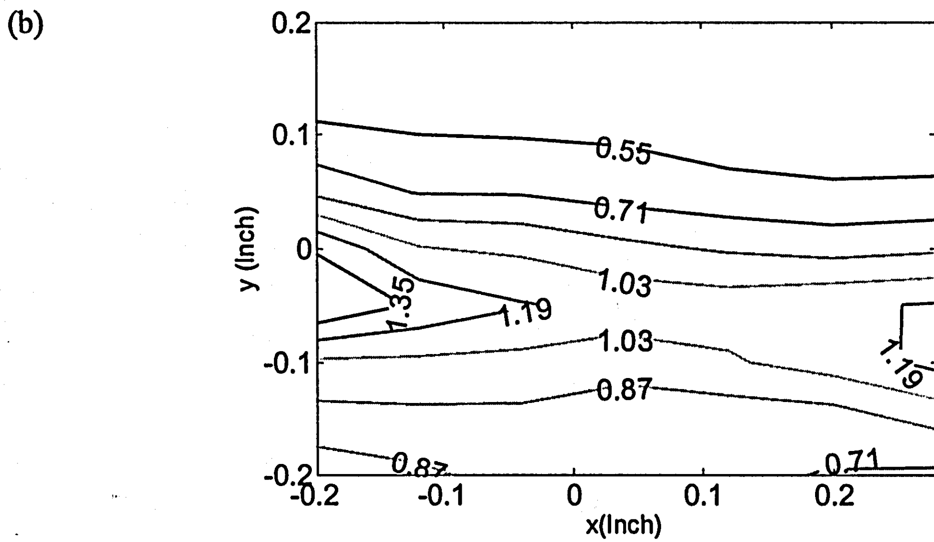

Figure 2-7 The contour plots of the ion current, which are measured by the ion flux analyzer and normalized to the ion current at the beam center, at DC bias level (a) 100 V and (b) 350 V for 10 mtorr Ar plasma with RF source power level at 350 W with the neutralization filament turned off.

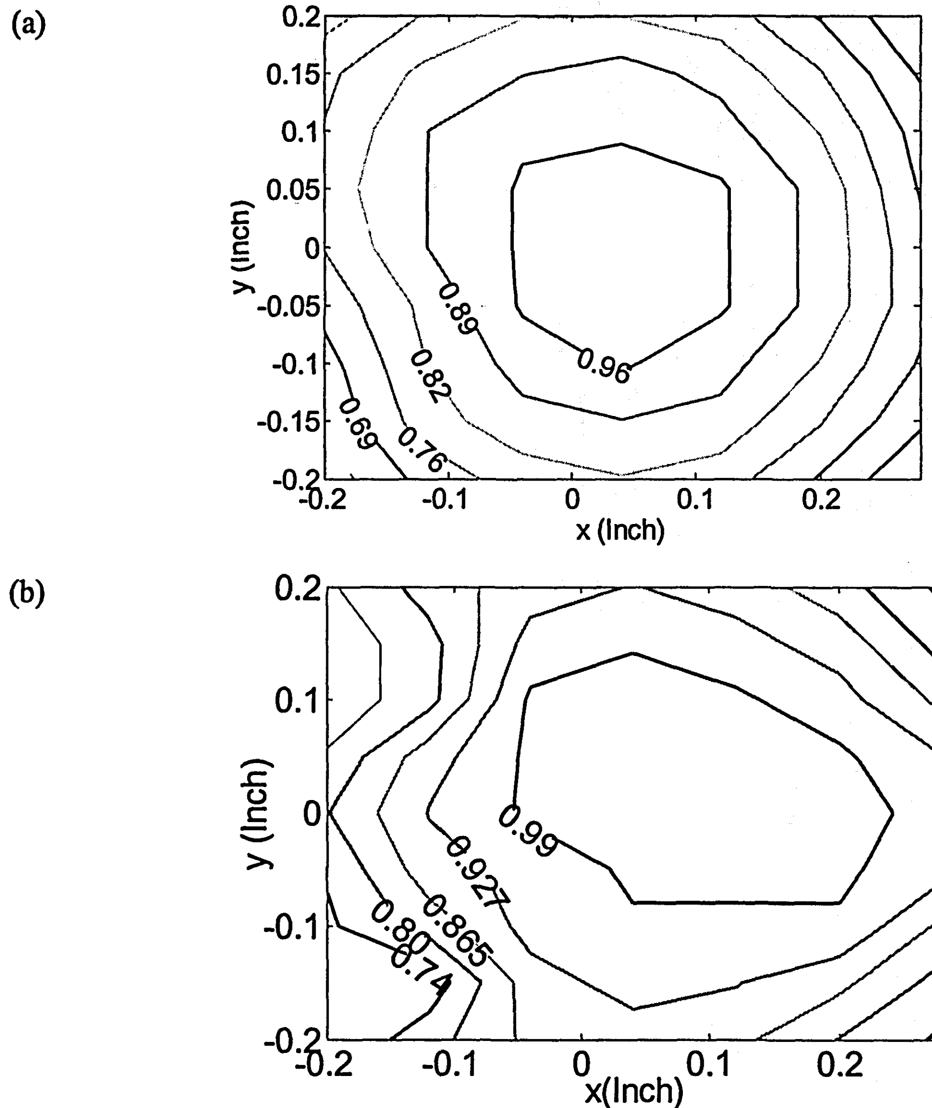

Figure 2-8 The contour plots of the ion current, which is measured by the ion flux analyzer and normalized to the ion current at the beam center, at DC bias level (a) 100 V and (b) 350 V for 10 mtorr Ar plasma with RF source power level at 350 W with the neutralization filament turned on.

2.4.2 Ion Energy Analysis

A gridded "retarding field" energy analyzer[13-18] was used to analyze the ion energy distributions levels in the plasma beam chamber system. A detailed schematic of the design has been shown elsewhere[14,17]. The assembly was mounted inside a grounded aluminum housing. The pressure inside the system was around 1.0×10^{-4} Torr or less during operation so that the collisions of ions inside the system would not distort the measurements. Figure 2-9 gives typical I-V curves and ion energy distribution function

(IEDF) measured by this ion energy analyzer. The averaged ion energy level scales very well with the DC bias voltage applied and the difference between these two reflects the plasma self-bias potential, which is about 5-20 eV in inductive coupling mode.

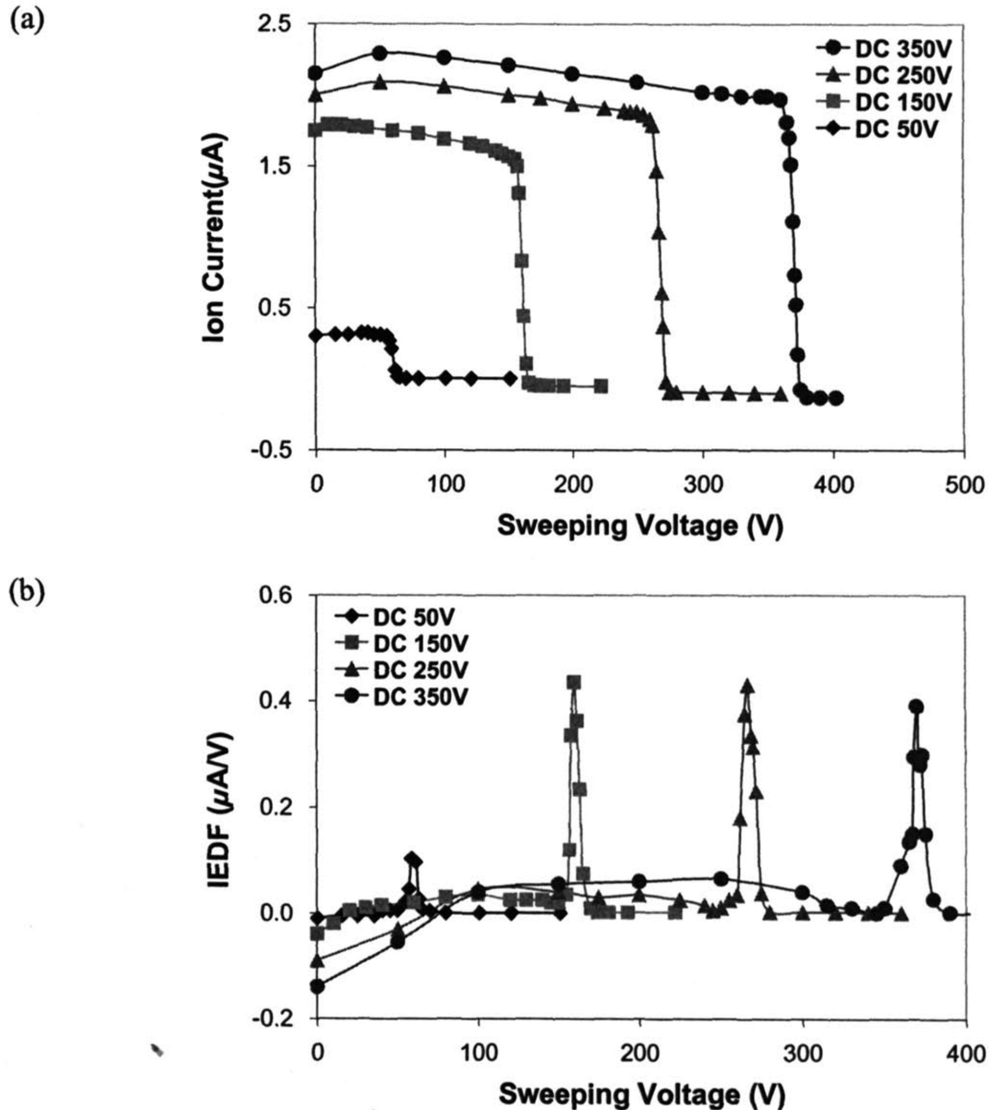

Figure 2-9 (a) I-V curve from ion energy analyzer from a 10 mtorr Ar plasma at 350 W RF power level. (b) Derivative of I-V characteristics give the ion-energy-distribution function (IEDF) at different DC bias levels.

The low energy tail of the IEDFs shown in Figure 2-9 (b) may be related to the collisions of ions in the plasma sheath, since the sheath becomes more collisional as the sheath thickens with increasing DC bias voltage. For colllisionless sheaths in low pressures, the Child-Langmuir sheath kinetics predicts the sheath thickness as[11,19]

$$d = \sqrt{\frac{4\varepsilon_0}{9}\left(\frac{2e}{m}\right)^{0.5}\frac{V^{3/2}}{j}}\,, \tag{2-2}$$

where ε_0 is the dielectric constant, e is the elementary electric charge, m is the ion mass, j is the ion current density at the plasma-sheath boundary, and V is the voltage drop across the sheath. V is equal to the summation of the DC bias level and the plasma self-bias potential at the center of the grounded orifice. For the collisional sheath in which the ions movement is mobility limited[11], the sheath thickness is given by

$$d = \left(\frac{9\varepsilon_0}{8}\frac{V^2}{j}\right)^{1/3}. \tag{2-3}$$

For Ar plasma at 10 mtorr with radio frequency source power level at 350 W, the ion current density j at the plasma-sheath boundary was estimated to be ~130 μA/cm^2, and was a very weak function of DC bias voltage level. The mean free path λ_i was about 3.3 mm under these plasma running conditions. The plasma sheath was collisionless when the sheath thickness estimated by equation (2-2) is smaller than the mean free path (~3.3 mm for Ar at 10 mtorr; otherwise the plasma sheath was collisional and the thickness could be estimated by equation (2-3). The estimated plasma sheath thickness is shown in Figure 2-10 as a function of DC bias voltage level. The plasma sheath is collisionless when the DC bias is low enough and there are trivial ion collisions in the sheath region. This can explain why there is almost no low energy tail on the IEDF at the DC bias level of 100 V in Figure 2-9 (b). On the contrary, the plasma sheath is collisional when the DC bias level is high enough (DC bias level of 150 V or more), which leads to the significant low energy tails of the IEDFs at the corresponding DC bias levels.

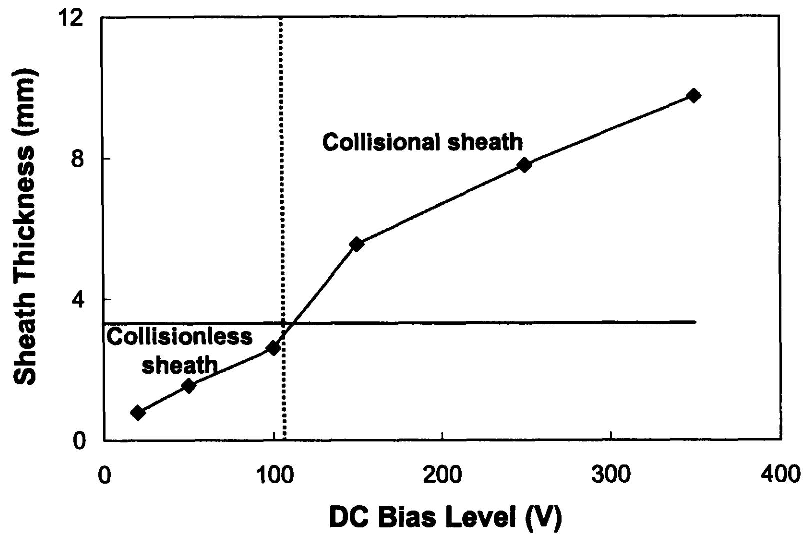

Figure 2-10 The estimation of plasma sheath thickness as a function of DC bias level in 10 mtorr Ar plasma with RF source power level at 350 W. The horizontal line at 3.3 mm indicates the mean free path length for ion scattering.

2.4.3 Plasma Composition Analysis

Mass spectrometers use the difference in mass-to-charge ratio (m/e) of ionized atoms or molecules to separate them from each other. Mass spectrometry is therefore useful for quantitative analysis of atoms or molecules and also for determining chemical and structural information about molecules.

In current work, a UTI 100C quadrupole line-of-sight mass spectrometer was used to analyze the ion and neutral compositions of various plasmas under different processing conditions. It consisted of three major components of ionizer, quadrupole mass filter, and detector. The ionization efficiency, the quadrupole transmission efficiency, and the electron multiplier gain (G) of various ions have been explored previously[1,17,20], and were adopted here for semi-quantitative plasma composition analyses. In particular, the ionization efficiency was a function of the cross-section for electron removal and the ease of bond breaking. The transmission (T) of any ion through the quadrupole filter was dependent on the AMU approximately. The transmission of the standard UTI Model 100C could be considered nearly 100% from AMU 1-40, then decreased roughly one magnitude per 150 AMU. The muitiplier gain under some conditions was considered to be a function

of the ion mass (AMU), and proportional to $(AMU)^{-1/2}$ approximately. Electron impact energy of 30-40 V was used to avoid fragmentation of neutrals in the ionizer.

2.5 Film Characterization

2.5.1 Etching Rate Measurement

Ellipsometry useing polarized light is a very sensitive surface and thin film measurement technique. It measures the change in polarization state of light reflected from the surface of a sample. Polarised light is shone on to a sample surface at an oblique angle of incidence. The plane of incidence of the light is the plane that contains both incident and reflected beams. The polarisation of light reflected parallel (p) and perpendicular (s) to the plane of incidence is measured. This allows the relative phase change ( ) and relative amplitude change (Ψ) from the reflected surface to be determined. Ellipsometry can be used to measure film thicknesses, and with variable wavelength, dielectric properties can also be estimated. In this work, a variable angle specroscopic ellipsometer (J.A. Woollam M-2000) was used to determine the film thicknesses of polysilicon and thermal silicon dioxide before and after plasma etching. This system consisted of a light source, monochromator, collimating optics, polarizer, sample stage, rotating analyzer, and a detector. The data were collected with wavelength from 315 nm to 800 nm at 2 nm intervals, at 65, 70 and 75 incident angles.

A Tencor P-10 profilometer was used to measure the thicknesses of pre and post-etch porous low-k film and the PECVD low-k coral films because the optical constants (e.g. the reflective index) of these films were not available. Profilometer is a laboratory measuring instrument that uses a diamond stylus to measure a feature's length or depth, usually in the micrometer or nanometer level. A diamond stylus is moved vertically in contact with a sample and then moved laterally across the sample for a specified distance and specified contact force. A profilometer can measure small surface variations in vertical stylus displacement as a function of position. A typical profilometer can measure small vertical features ranging in height from 10 to 65,000 nm.

2.5.2 X-Ray Photoelectron Spectroscopy (XPS)

The mechanism of XPS is based on the photoelectric effect where photons are used to excite electrons and emit photoelectrons from a surface when photons impinge upon it. Al Kα (1486.6eV) or Mg Kα (1253.6eV) are the typical choices of the photon energy. The XPS technique is highly surface specific (several nm) due to the short range of the photoelectrons that are excited from the solid. The energy of the photoelectrons leaving the sample is determined using a Concentric Hemispherical Analyser (CHA) which provides a spectrum with a series of photoelectron peaks. The binding energy of these peaks are characteristic of each element. The peak areas can be used to determine the composition of the materials surface, after correction to appropriate sensitivity factors. The shape of each peak and the binding energy can be slightly altered by the chemical state of the emitting atom. For this reason, XPS can provide chemical bonding information as well. XPS is not sensitive to hydrogen or helium, but can detect all other elements.

An *in situ* x-ray photoelectron spectroscopy (XPS) with Al Kα was used to characterize the near surface composition before and after plasma etching of polysilicon and dielectric materials. Both the XPS chamber and the plasma beam chamber were integrated with an ultrahigh vacuum transfer tube as shown in Figure 2-2, which enabled *in vacu* sample transfer between the process and analytic chambers so that the surface composition of the etched samples could be characterized *in situ*.

2.5.3 Atomic Force Microscopy (AFM)

The atomic force microscopy (AFM) was applied in this work to characterize the surface topography on pre- and post-etched sample surfaces. The principle of AFM is very simple, as shown in Figure 2-11. An atomically sharp tip is scanned over a surface with feedback mechanisms that enable the piezo-electric scanners to maintain the tip at a constant force (to obtain height information), or height (to obtain force information) above the sample surface. The AFM head employs an optical detection system in which the tip is attached to the underside of a reflective cantilever. A diode laser is focused onto the back of a reflective cantilever. As the tip scans the surface of the sample, moving up and down with the contour of the surface, the laser beam is deflected off the attached cantilever into a dual element photodiode. The photodetector measures the difference in light intensities

between the upper and lower photodetectors, then converts to voltage. Feedback from the photodiode difference signal, through software control from the computer, enables the tip to maintain either a constant force or constant height above the sample.

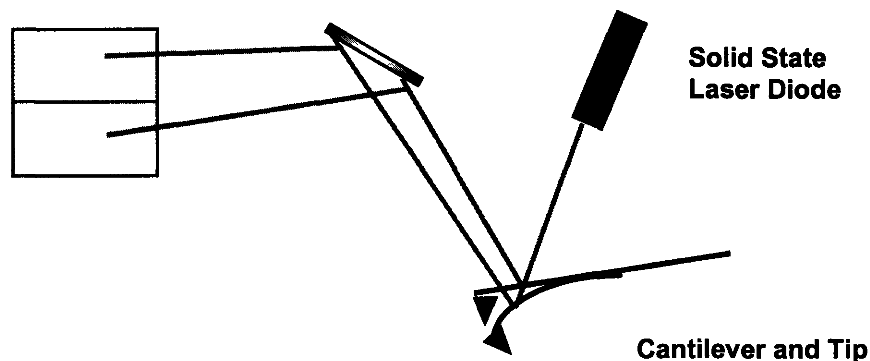

Figure 2-11 A schematic showing how the AFM works.

Typically, there are three different operation modes: Contact Mode, Non-contact and Tapping Mode. At contact mode, the AFM tip is scanned across the sample while a feedback loop maintains a constant cantilever deflection. At non-contact mode, the cantilever is oscillated slightly above its resonant frequency. At tapping mode, the cantilever with attached tip is oscillated at its resonant frequency and scanned across the sample surface. In current research, tapping mode was used since it could result in higher lateral resolution on most samples (1-5 nm) while lower forces and less damage to soft samples imaged in air. Additionally, lateral forces are virtually eliminated so there was no scraping.

A Digital Instruments 3100 atomic force microscope (AFM) in tapping mode was used in this work. Standard tapping-mode etched silicon probes (TESP) tips were used to image the surfaces. Root-mean squared (RMS) roughness of each image was calculated after correcting any residual line-to-line offsets. All images were 1 μm × 1 μm, 256 linescans with 256 pixels/linescan.

2.6 References

1 H. Chae, S. A. Vitale, and H. H. Sawin, Journal of Vacuum Science & Technology A 21, 381-387 (2003).

[2] G. Cunge, R. L. Inglebert, O. Joubert, L. Vallier, and N. Sadeghi, Journal of Vacuum Science & Technology B 20, 2137-2148 (2002).

[3] N. R. Rueger, M. F. Doemling, M. Schaepkens, J. J. Beulens, T. Standaert, and G. S. Oehrlein, Journal of Vacuum Science & Technology a-Vacuum Surfaces and Films 17, 2492-2502 (1999).

[4] M. Schaepkens and G. S. Oehrlein, Journal of the Electrochemical Society 148, C211-C221 (2001).

[5] M. Schaepkens, T. Standaert, N. R. Rueger, P. G. M. Sebel, G. S. Oehrlein, and J. M. Cook, Journal of Vacuum Science & Technology a-Vacuum Surfaces and Films 17, 26-37 (1999).

[6] M. Sekine, Applied Surface Science 192, 270-298 (2002).

[7] M. J. Sowa, M. E. Littau, V. Pohray, and J. L. Cecchi, Journal of Vacuum Science & Technology a-Vacuum Surfaces and Films 18, 2122-2129 (2000).

[8] T. Standaert, C. Hedlund, E. A. Joseph, G. S. Oehrlein, and T. J. Dalton, Journal of Vacuum Science & Technology A 22, 53-60 (2004).

[9] T. Standaert, M. Schaepkens, N. R. Rueger, P. G. M. Sebel, G. S. Oehrlein, and J. M. Cook, Journal of Vacuum Science & Technology A 16, 239-249 (1998).

[10] S. A. Vitale, H. Chae, and H. H. Sawin, Journal of Vacuum Science & Technology a-an International Journal Devoted to Vacuum Surfaces and Films 19, 2197-2206 (2001).

[11] H. H. Sawin, (unpublished).

[12] S. A. Rasgon, Ph.D. Thesis, Massachusetts Institute of Technology, 2005.

[13] G. W. Gibson, H. H. Sawin, I. Tepermeister, D. E. Ibbotson, and J. T. C. Lee, Journal of Vacuum Science & Technology B 12, 2333-2341 (1994).

[14] B. Lipschultz, I. Hutchinson, B. Labombard, and A. Wan, Journal of Vacuum Science & Technology a-Vacuum Surfaces and Films 4, 1810-1816 (1986).

[15] J. Liu, G. L. Huppert, and H. H. Sawin, Journal of Applied Physics 68, 3916-3934 (1990).

[16] B. E. Thompson, K. D. Allen, A. D. Richards, and H. H. Sawin, Journal of Applied Physics 59, 1890-1903 (1986).

[17] S. A. Vitale, Ph.D. Thesis, Massachusetts Institute of Technology, 2001.

[18] J. R. Woodworth, M. E. Riley, D. C. Meister, B. P. Aragon, M. S. Le, and H. H. Sawin, Journal of Applied Physics 80, 1304-1311 (1996).

[19] N. Mutsukura, K. Kobayashi, and Y. Machi, Journal of Applied Physics 68, 2657-2660 (1990).

[20] O. Kwon, Sc.D. Thesis, Massachusetts Institute of Technology, 2004.

Chapter 3. The Angular Etching Yields of Polysilicon and Dielectric Materials in Cl_2/Ar and Fluorocarbon Plasmas

The angular etching yields of polysilicon in Cl_2/Ar plasmas, and dielectric materials (thermal silicon dioxide and low-k dielectric coral) in fluorocarbon plasmas, have been characterized in an inductively coupled plasma beam apparatus. The impacts of ion energy, feed gas composition, and plasma source pressure are studied. My experimental results showed that these etching parameters had significant impact on the resulting angular etching yield curve. In particular, the angular etching yield curve was more sputtering-like at low plasma source pressure and/or low effective gas percentage (Cl_2, C_4F_8, or C_2F_6), with a peak around 60-70° off-normal ion incident angle. In contrast, ion-enhanced-etching like angular curves, which dropped gradually with off-normal angle, were formed at high plasma source pressure and/or high effective gas percentage. Further analysis indicated that the effective neutral-to-ion flux ratio reaching the surface was the primary factor to influence the angular etching yield curve. More specifically, the angular etching yield curve had physical sputtering characteristics at low neutral-to-ion flux ratios; while etching process was really dominated by ion enhanced etching at high ratios and the angular curve was ion-enhanced-etching like. The polymer deposition effects are also discussed in this Chapter.

3.1 Introduction

It is more and more challenging to keep the fidelity of pattern transfer during plasma etching as the key feature size keeps shrinking below100 nm regimes. One of the major difficulties is due to the feature side-wall roughening introduced by plasma etching. A heavy load of research interests have been focused on understanding the origin and mechanism of side-wall roughening since it is crucial to minimize the sidewall roughness in order to improve the device performance[1-14]. Many researchers found that the top line-edge roughness (LER) of the photoresist layer during development process acted as the origin of the sidewall roughening during plasma etching[3,5,6,8,11,14]. In particular, Goldfarb et al. reported that this top LER played an important role for the sidewall roughening of oxide patterning in fluorocarbon chemistries[5].

Different profile feature modeling tools have also been developed to understand the key effects causing the artifacts during feature patterning, such as sidewall bowing, microtrenching, under-cut, notching, and sidewall roughening[15-20]. However, a complete set of experimental database is necessary in order to make these modeling tools meaningful. Among them the angular etching yields are one of the most important parameters need to be collected.

It has been demonstrated that a minor change of the angular etching yield curves had significant impact on the feature profile evolution[16,21]. For instance, the feature profile during polysilicon gate etch is influenced by the etching chemistries, which alters the angular etching yield curves. For pure Cl_2 plasmas, the etching yield remains constant with the off-normal ion bombardment angle up to 45°, while the etching yield starts dropping even with small off-normal angles in HBr plasmas. Lane et al.[21] has experimentally showed that this slight difference of angular yields between HBr and Cl_2 resulted in very different etched feature profiles. In particular, micro-trenches were formed at the bottom in Cl_2 chemistry, while the feature bottom remained flat in HBr plasmas. Using Monte Carlo simulation approach, Jin et al.[16] also reported similar results.

Previously, people have already observed that plasma etching parameters might change what the etching yields looked like. Mayer et al.[22] found that the angular etching yields of polysilicon and SiO_2 could be manipulated by ion bombardment energy and plasma beam pressure. In particular, the etching yield curves could be physical-sputtering like with a peak around 60-70°, or ion-enhanced-etching like where the etching yield dropped off gradually with ion bombardment off-normal angle. Similar results have also been reported by Blom et al.[23,24] during the etching of silicon nitride in fluorocarbon plasmas, in which they found that the angular etching yield curve was manipulated by changing the plasma pressure. More specifically, the angular etching yield curve was sputtering like at low plasma pressure level, while ion-enhanced-etching-like at high plasma pressure levels.

In the literature[25,26], different researchers have tried to understand why the angular etching yields changed with etching parameters, such as the plasma pressure. Kwon et al.[26] proposed an ion-enhanced polymer deposition mechanism to explain the evolution of

angular etching yields during the etching of SiO_2 in fluorocarbon plasmas. However, this proposed polymer deposition effect could not explain why the angular etching yields sometimes peaked around 65° off-normal angles, which has already been reported in the literature[23,24] and is also shown in this Chapter.

In this Chapter, the angular etching yields of polysilicon in Cl_2/Ar plasmas, and dielectric materials in fluorocarbon plasmas, are experimentally quantified using an inductively coupled plasma beam apparatus. In the case of polysilicon etch in Cl_2/Ar plasmas, the impact of ion energy, Cl_2 percentage in the feed gas, and the plasma source pressure were studied. For the etching of dielectric films in fluorocarbon plasmas, I mainly focused on thermal SiO_2 etch in C_4F_8/Ar plasmas, where the effects of ion energy, C_4F_8 feed gas percentage, and plasma source pressure were investigated. In addition, the angular etching yields of low dielectric constant coral film in C_4F_8/Ar plasmas were also studied. My objective was to have a clear understanding of the impact of etching parameters on the angular etching yields.

3.2 Angular Etching Yields of Polysilicon in Cl_2/Ar Plasmas

The etching yields of polysilicon in chlorine chemistry has been measured previously using reactive ion beams[27-30] or real plasma beams[31] that consisted of Cl and Cl_2 neutrals and ions. In the present work, polysilicon was etched in Cl_2/Ar plasma beams. Ar gas was added to the plasma since Ar neutral did not contribute to the etching process so that the plasma composition could be modulated. The ion and neutral flux compositions in the plasma beam at different Cl_2/Ar gas mixing ratios are summarized in Table 3-1. At a fixed RF power level, with the increase of Cl_2 percentage in the feed gas mixture, the fraction of effective neutrals including both Cl and Cl_2 increases. In addition, Cl/Cl_2 ratio also decreases with increasing Cl_2 percentage in the feed gas. In terms of ions in the plasma, both of the Cl^+/Cl_2^+ ratio and Ar^+ fraction decrease when increasing the Cl_2 percentage in the feed gas. In particular, only about 5% of ions or less contribute to Ar ions if the percentage of Cl_2 is higher than 60%. This is because Ar ionization (15.6 eV) is higher than Cl ionization (13 eV)[32]. For this reason, at high Cl_2 percentages, Ar acts mainly as a dilution gas in the plasma.

Table 3-1 Ion and neutral flux compositions in the Cl_2/Ar plasmas used in this study determined by mass spectrometry.

Plasma	Plasma pressure (mtorr)	Ion flux (%)			Neutral flux (%)	
		Cl^+	Cl_2^+	Ar^+	Cl	Cl_2
7% Cl_2	4-5	39.6	8.2	52.2	19.4	11.4
10% Cl_2	6-7	50.7	8.4	40.9	22.3	13.5
20% Cl_2	5-6	61.1	10.4	28.5	28.9	22.0
25% Cl_2	8-9	69.3	13.9	16.8	26.0	29.2
50% Cl_2	8-9	69.7	20.5	9.8	27.2	45.8
60% Cl_2	10-11	68.9	25.7	5.4	23.5	55.2
67% Cl_2	14	54.4	41.4	4.2	18.3	63.0

Figure 3-1 shows the polysilicon etching yield at normal ion incident angle as a function of ion bombardment energy and Cl_2/Ar gas mixing ratios. Obviously, the etching yields scales with the square root of ion energy under each gas mixing ratio, which is consistent with the literature. In addition, the etching yields at each ion energy level increase gradually with the Cl_2 percentage in the feed gas mixture. Further analysis indicates that the polysilicon etching yields in the present work follows the typical ion enhanced etching kinetics described previously: initially the etching yields increase linearly with the effective neutral-to-ion flux ratios, then a saturated etching regime is reached at high ratios. These observations are plotted in Figure 3-2 at different ion energies. The method that the neutral-to-ion flux ratio was estimated has already been described in detail previously[31].

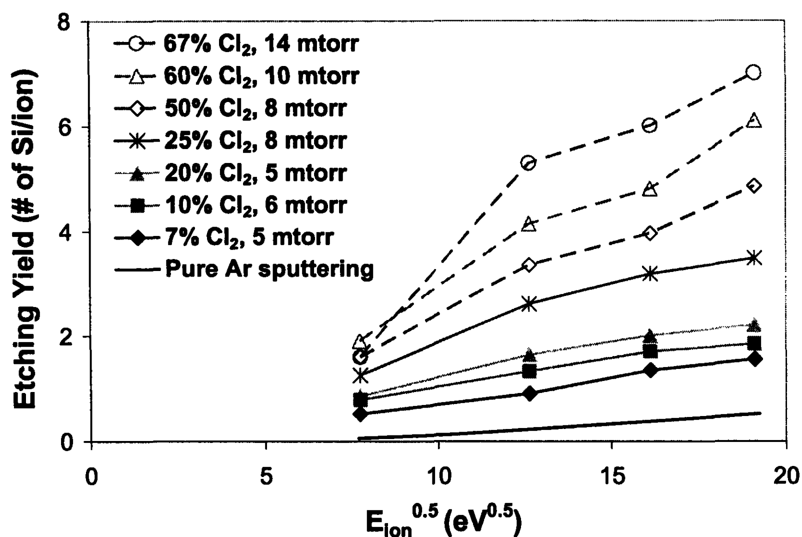

Figure 3-1 The etching yield of PECVD polysilicon in Cl_2/Ar plasmas as a function of the square root of ion bombardment energy for different Cl_2 percentages at normal angle. For comparison, the sputtering rate of polysilicon was also shown in this figure.

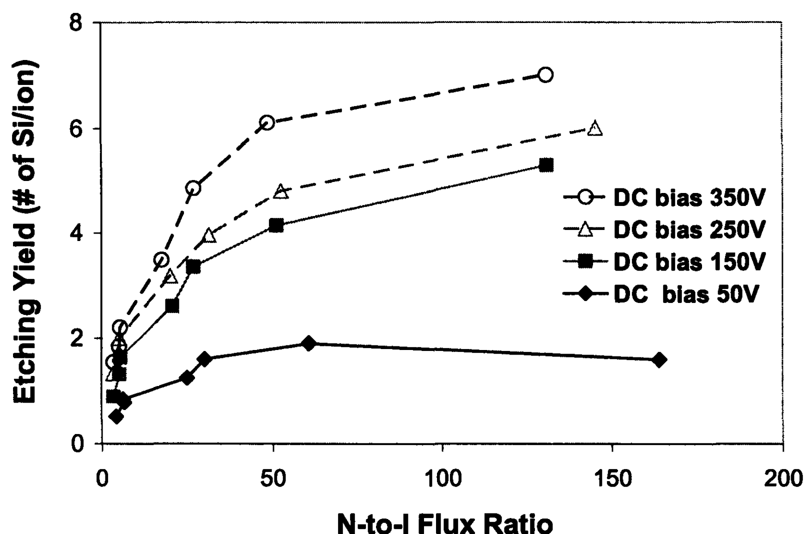

Figure 3-2 The etching yield of PECVD polysilicon in Cl_2/Ar plasmas as a function of the effective neutral-to-ion flux ratio and ion bombardment energies at normal ion incidence angle.

It is important to notice that plasma composition influences silicon etching yield in Cl_2 plasma beams. Figure 3-3 compares the etching yields in the present work (67% Cl_2, plasma source pressure of 14 mtorr, and effective neutral-to-ion flux ratio of 130-160) and previous work in Cl_2 plasma beam reported by Vitale et al.[31] at saturated etching regime.

For comparison, the saturated etching yield data from Cl^+/Cl[30] and Cl_2^+/Cl_2[27] beam studies are also plotted in Figure 3-3. Silicon etching yields in Cl^+/Cl beams are higher than those in Cl_2^+/Cl_2 beams at a given ion energy level. Since real Cl_2 plasma beams are a mixture of Cl and Cl_2 ions and neutrals, the etching yields are in the range between those two extreme cases. In addition, higher etching yields would be resulted in Cl_2 plasmas with higher Cl^+/Cl_2^+ and/or Cl/Cl_2 ratios. In Vitale's work, the ratios of Cl^+/Cl_2^+ and Cl/Cl_2 were 0.43 and 0.11, respectively. In the present work, for the plasma beam of 67% Cl_2 at 14 mtorr, the ratios of Cl^+/Cl_2^+ and Cl/Cl_2 were 1.31 and 0.29, respectively. Therefore, the etching yields in the present work are higher than those in Vitale's work at a given ion energy level, although the effective neutral-to-ion flux ratios are 130-160 in the 67% Cl_2 plasma beam at 14 mtorr, which has not completed fallen in the saturated etching regime.

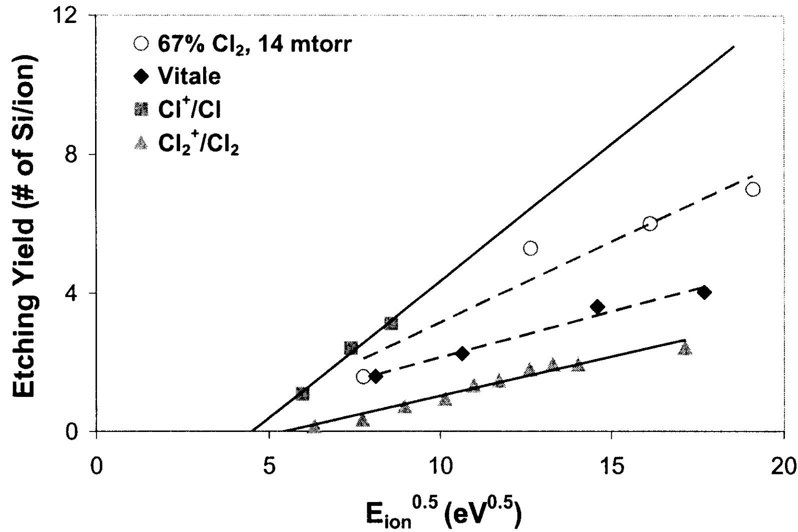

Figure 3-3 Variation of polysilicon etching yields in chlorine plasmas with plasma composition. Cl^+/Cl data is from Chang et al.[30], and Cl_2^+/Cl_2 data is taken from Balooch et al.[27]. The data points are experimental results, and the lines are linear fit of to my data.

Figure 3-4 reports the normalized angular etching yields of polysilicon in three different plasma conditions (both the Cl_2 feed gas percentage and the plasma source pressure) and two different ion energies (DC 150 V and DC 250 V, or equivalently, 160 eV and 260 eV)). At low Cl_2 gas percentage (7%) and low plasma source pressure (5 mtorr), the angular yields at both ion energy levels exhibit sputtering characteristics, with a peak around 60° off-normal angle. In contrast, the angular yields at high Cl_2 gas percentage (67%) and high plasma source pressure (14 mtorr) demonstrates ion-enhanced-

etching-like curves. For comparison, the angular yields at saturated etching regime from previous studies[30,31] are also plotted. Clearly, the angular yields at high Cl_2 percentage and plasma pressure, which lead to high neutral-to-ion flux ratio and push the etching kinetics to the saturated regime, are consistent with the data reported earlier.

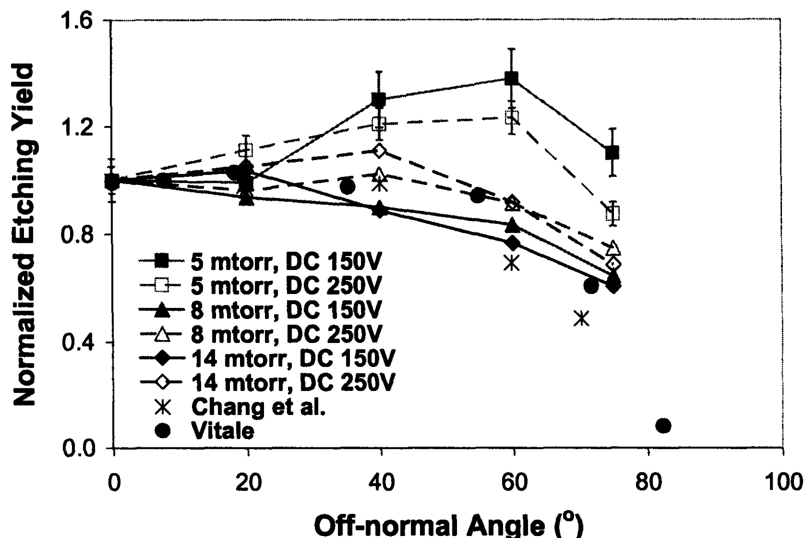

Figure 3-4 The normalized angular etching yields of PECVD polysilicon in Cl_2/Ar plasmas under various plasma source pressures (5 mtorr, 8 mtorr, and 14 mtorr) and DC bias levels (150 V and 250 V). Solid and open symbols represent the results at DC bias levels 150 V and 250 V, respectively. The Cl_2 percentage in the feed gas mixture is: 7% Cl_2 at 5 mtorr, 25% Cl_2 at 8 mtorr, and 67% Cl_2 at 14 mtorr. All of the etching yields were normalized to the corresponding etching yields at normal angle.

3.3 Angular Etching Yields of Thermal SiO_2 in Fluorocarbon Plasmas

3.3.1 Angular Etching Yields in C_4F_8/Ar Plasmas

The etching yields of thermal silicon dioxide as a function of ion energy for various C_4F_8/Ar feed gas ratios and plasma source pressures are shown in Figure 3-5. For comparison, SiO_2 sputtering yields in pure Ar plasmas are also plotted in this figure. The etching yields increase with ion bombardment energy for all conditions, which is consistent with the previous data in the literature[33-36]. Moreover, the etching behavior is influenced by the C_4F_8 percentage and/or the plasma pressure in the feed gas mixture. At low beam source pressure level (10 mtorr) and low C_4F_8 percentage (10%), the etching is dominated by net etching over the ion energy range investigated in this work, while net deposition happens at low ion bombardment energies with high plasma source pressure

and/or C_4F_8 percentages. Here, net deposition at low ion energies occurs due to two different reasons. First, the plasma becomes more electronegative with more C_4F_8 addition to the feed gas mixture for a given RF power, therefore, the electron density decreases partially due to the electron attachments, which consequently makes the ion density lower. At the same time, effective neutral concentration becomes higher since more C_4F_8 is added in the plasma mixture. Second, the electron temperature decreases with the increase of the plasma pressure. For this reason, the ionization efficiency is less at higher plasma source pressures, and consequently the ion density decreases. Due to these two reasons, at high plasma source pressure and/or C_4F_8 percentages, the ion flux reaching the surface is less while neutral flux becomes higher. Consequently, net deposition happens at low ion bombardment energies.

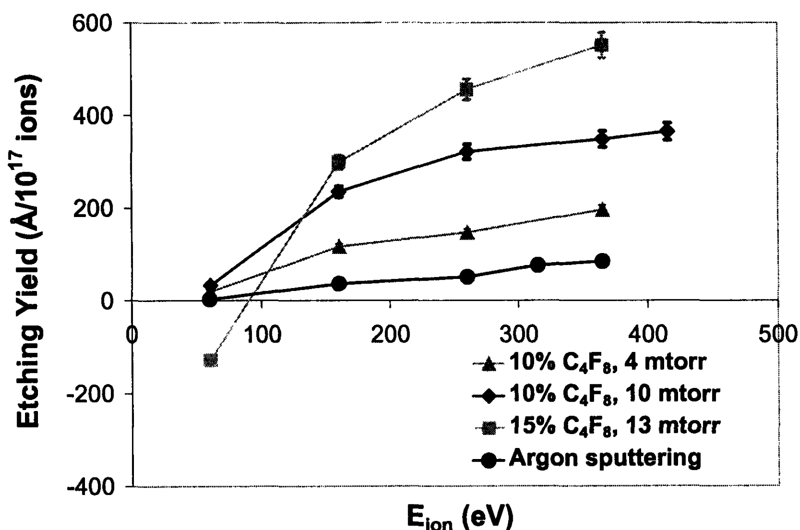

Figure 3-5 The etching yield of thermal silicon dioxide in C_4F_8/Ar plasmas as a function of the ion bombardment energy for different C_4F_8 percentages at normal angle. For comparison, the sputtering rate of thermal silicon dioxide in argon plasma was also shown in this figure.

The corresponding normalized angular etching yields under these plasma conditions in Figure 3-5 are characterized at several ion energy levels, as shown in Figure 3-6. Most importantly, the shape of the angular etching yields is influenced by the etching parameters, as has already been mentioned in Section 3.2. At low plasma source pressure (4 mtorr) and low C_4F_8 percentage (10%), the resulting angular etching yield curve is sputtering like. On the other hand, the measured etching yields demonstrate ion-enhanced-

etching characteristics at high plasma source pressure (13 mtorr) and high C_4F_8 percentage (15%). In addition, ion bombardment energy might also affect the angular etching yields. Specifically, higher ion bombardment energy seems to results in angular etching yields with more sputtering characteristics. For instance, during the etching in 10% C_4F_8 at 10 mtorr, the etching yield curve at DC bias 420 V is more sputtering-like compared to that at DC bias 250 V.

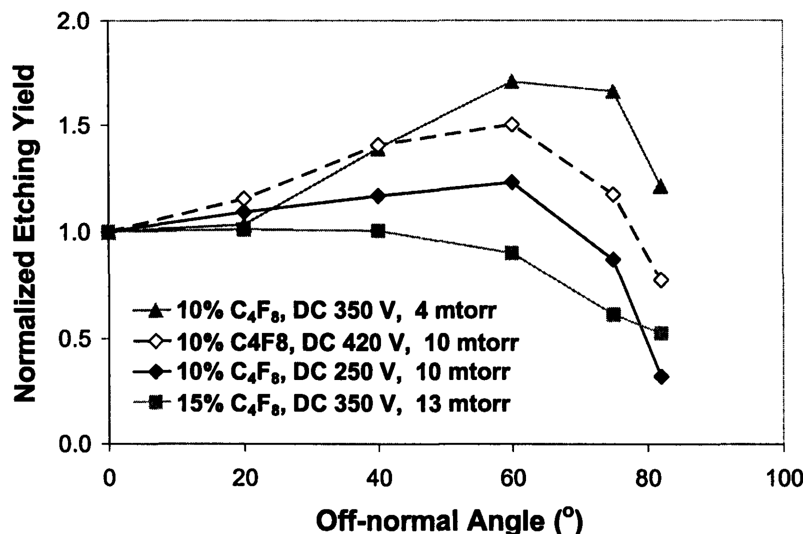

Figure 3-6 The normalized angular etching yields thermal silicon oxide in C_4F_8/Ar plasmas under various plasma source pressures and DC bias levels. All of the etching yields were normalized to the corresponding etching yields at normal angle.

Figure 3-7, Figure 3-8, and Figure 3-9 show the influence of ion incidence off-normal angle on the surface elemental composition of etched thermal silicon dioxide under those plasma conditions (plasma pressure and C_4F_8 percentage) described in Figure 3-5 at DC bias 350 V. In particular, Figure 3-7 reports the results at low plasma pressure (4 mtorr) and C_4F_8 percentage (10%), while Figure 3-9 shows the elemental compositions for high plasma pressure (13 mtorr) and C_4F_8 percentage (15%). The elemental fraction of each species was calculated based upon its XPS spectrums and corrected to its corresponding XPS sensitivity factors[37]. By comparison of these three figures, one can see that the surface carbon and fluorocarbon fractions roughly increase while silicon and oxygen decrease by increasing the plasma source pressure and C_4F_8 percentage. This is because at high pressure and/or high C_4F_8 percentages, there are more sticky reactive neutrals available but with less ion flux reaching the surface. As a result, local

fluorocarbon deposition becomes more significant. In addition, roughly speaking, the fraction of each species does not change much with the ion bombardment off-normal angle, and there is no obvious evidence to show that ion-enhanced polymer deposition effects are important at least over the range explored in this work. Additionally, the carbon and fluorine fractions at 75° off-normal angle after etched in the plasma beam at high pressure and C_4F_8 percentage are slightly lower than those at lower off-normal angles. This might be because that the ion penetration depth becomes smaller at grazing angles at a given ion energy, therefore, the XPS signal intensities are attenuated more by the bulk SiO_2 in the substrate than at lower off-normal angles.

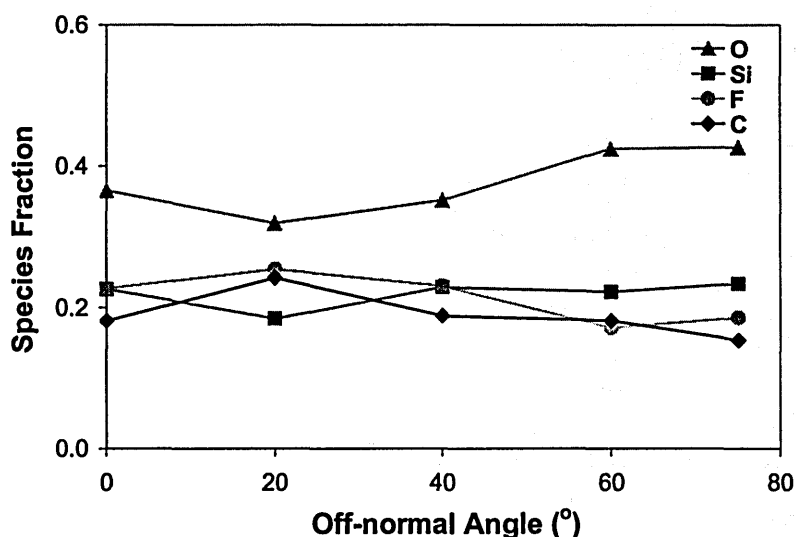

Figure 3-7 The influence of ion incidence off-normal angle on the surface composition of etched thermal silicon dioxide in 10% C_4F_8/Ar plasma. The concentration of each species on the surface was characterized by XPS technique. The etching conditions are: DC 350 V, beam source pressure 4 mtorr, ion fluence reaching the surface 3.0×10^{17} ions/cm^2.

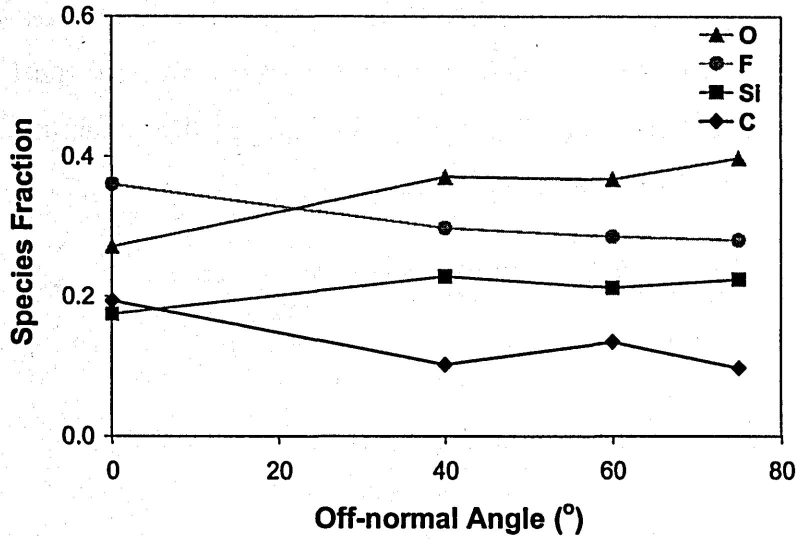

Figure 3-8 The influence of ion incidence off-normal angle on the surface composition of etched thermal silicon dioxide in 10% C_4F_8/Ar plasma. The concentration of each species on the surface was characterized by XPS technique. The etching conditions are: DC 350 V, beam source pressure 10 mtorr, ion fluence reaching the surface 2.0×10^{17} ions/cm^2.

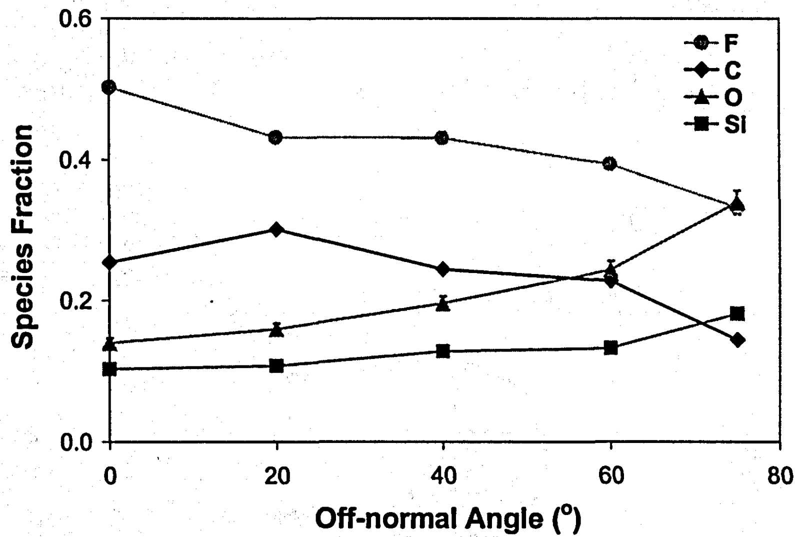

Figure 3-9 The influence of ion incidence off-normal angle on the surface composition of etched thermal silicon dioxide in 15% C_4F_8/Ar plasma. The concentration of each species on the surface was characterized by XPS technique. The etching conditions are: DC 350 V, beam source pressure 13 mtorr, ion fluence reaching the surface 2.0×10^{17} ions/cm^2.

At an approximately fixed plasma pressure (4-6 mtorr), the effects of C_4F_8 percentage (10%, 20%, and 33%) in the feed gas on the plasma composition were studied. The plasma neutral and ion compositions analyzed by mass spectrometry are shown in

Figure 3-10 and Figure 3-11, respectively. The ionization efficiency, quadrupole transmission efficiency, and electron multiplier gain of various species have been considered when calculating the concentrations based upon their peak intensities. These sensitivity factors are adopted from previous studies[38].

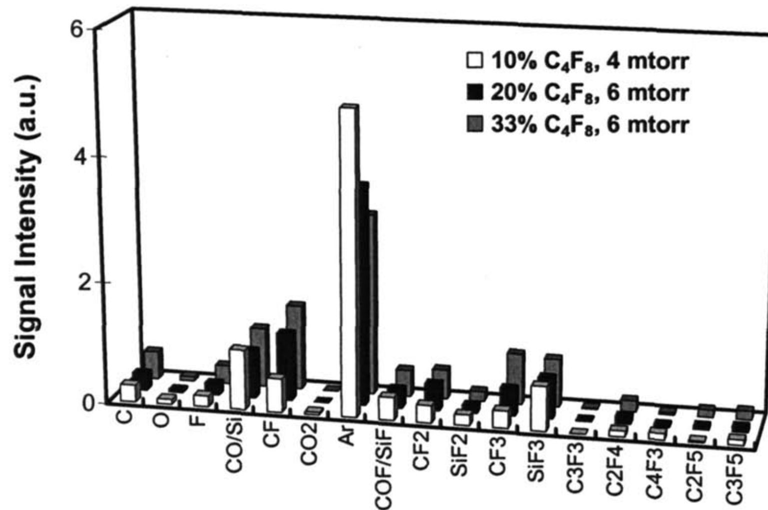

Figure 3-10 The impact of C_4F_8 percentage on the plasma neutral composition quantified using mass spectrometer. The plasma source pressure is between 4-6 mtorr.

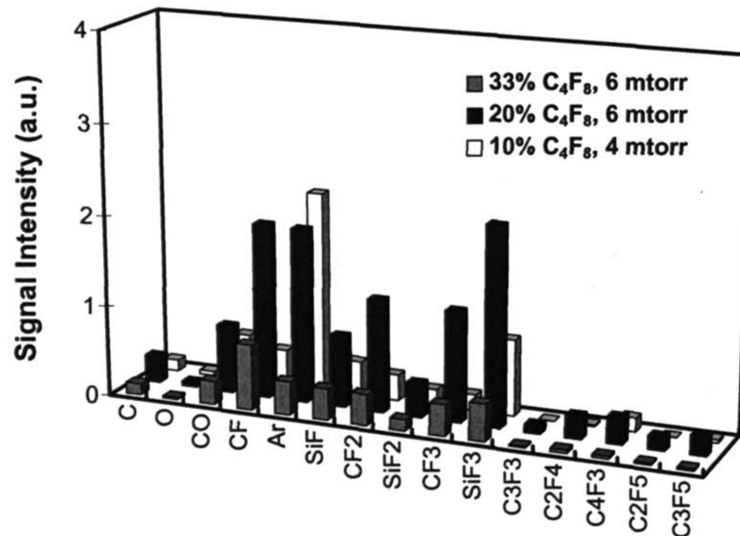

Figure 3-11 The impact of C_4F_8 percentage on the plasma ion composition quantified using mass spectrometer. The plasma source pressure is between 4-6 mtorr.

In plasma neutrals, with the increase of C_4F_8 percentage in the gas mixture, the intensities of most of C and F related species such as C, CF, CF_2, and CF_3 increase, while the intensity of Ar decreases. In plasma ions, the situation is a little complicated. The intensity of Ar ion decreases with the increase of C_4F_8 percentage, which is consistent with my previous analysis since the plasma becomes more negative with more C_4F_8 addition. For C and F related ion species, their intensities increase first, then drop off. Actually, the same phenomena was also observed for 10% C_4F_8/Ar plasmas with various plasma source pressures (5 mtorr, 9 mtorr, and 15 mtorr) and the results are shown in Figure 3-12. A possible explanation is related to the method of maintaining the inductively coupled plasma. The plasma is inductively coupled and the mass spectrometer locates on the sidewall of the beam source and is closer to the top. When the beam source pressure is pretty low, the high density region is larger and I am sampling the plasma from this denser region. When increasing the beam source pressure, the volume of this denser region is smaller, which means the ion density in this denser region might become higher since the RF used to produce the plasma is constant. If the mass spectrometer is sampling the plasma from the denser region in this scenario, the signal intensity would be higher. When increasing the beam source pressure furthermore, the denser region shrinks furthermore. Finally, it is possible to sample the plasma from outside of the denser region, then the signal intensity would drop off. Since I only care about the fractions of each ion species reaching the sample surfaces and the absolute ion flux bombarding the sample surface can be quantified by an ion flux analyzer[39], this modulation of plasma ion composition with plasma source pressure has no significant negative impact on the current research.

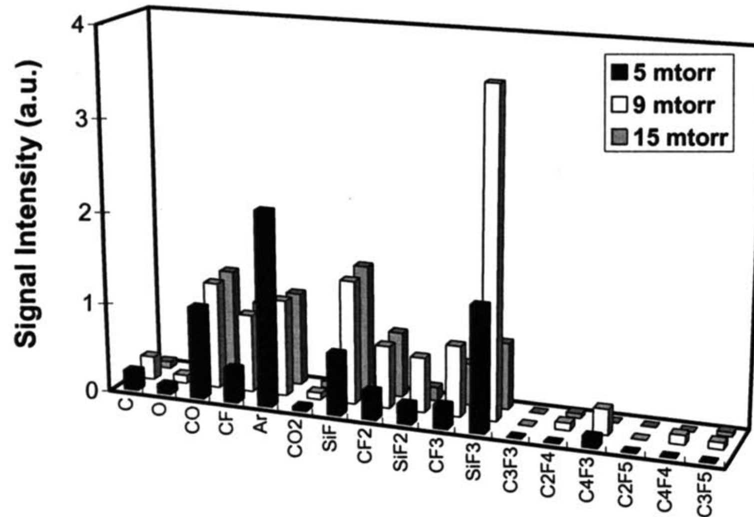

Figure 3-12 The impact of plasma source pressure on the plasma ion composition quantified using mass spectrometer. The C_4F_8 percentage in the plasma feed gas mixture is 10% in all cases.

The etching yields at normal ion incident angle are shown in Figure 3-13 as a function of the square root of ion energy at these three different C_4F_8 percentages (10%, 20%, and 33%). Similarly, with the increase of C_4F_8 percentage, the etching yields at high ion energies(e.g. DC bias 350 V) increases while decreases and even falls into the net deposition regime at very low ion energy level (DC bias 50 V) when the C_4F_8 percentage is high (20% and 33%). The corresponding normalized angular etching yields at DC bias 350 V for these three C_4F_8 percentages are summarized in Figure 3-14. Consistently, at low C_4F_8 percentage (10%) the angular etching curve is physical-sputtering like; at high C_4F_8 percentage (33%) ion-enhanced-etching like angular yield curve is formed. The angular etching yield curve at 20% C_4F_8 percentage is between these two extremes.

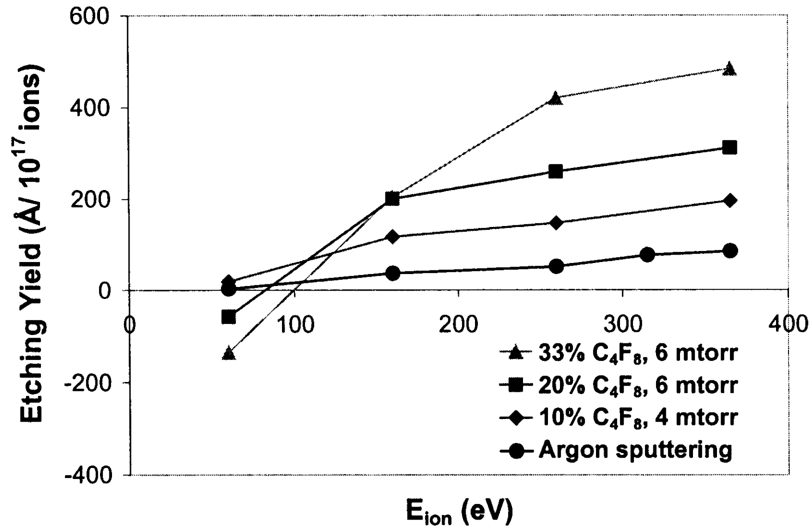

Figure 3-13 The impact of C_4F_8 percentage on the etching yields of thermal silicon oxide in C_4F_8/Ar plasmas at different ion energy levels at normal angle. The plasma source pressure is between 4-6 mtorr. For comparison, the sputtering rate of thermal silicon dioxide in argon plasma was also shown in this figure.

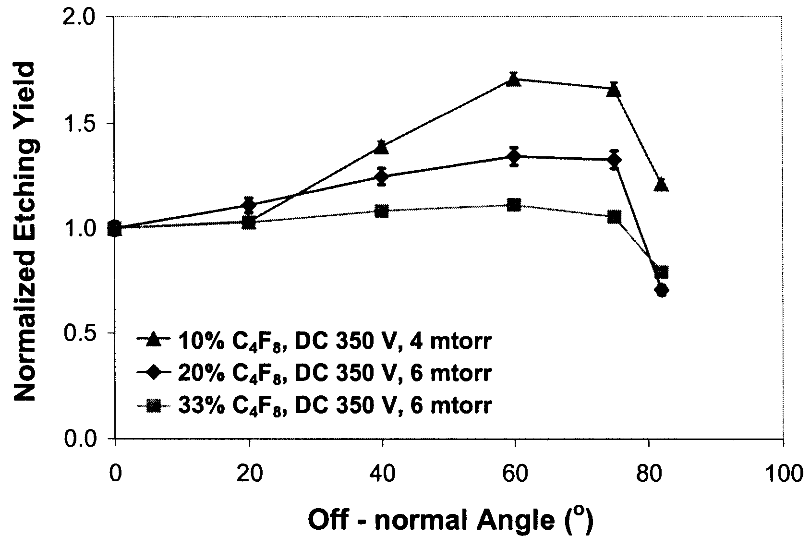

Figure 3-14 The impact of C_4F_8 percentage on the normalized angular etching yields of thermal silicon oxide in C_4F_8/Ar plasmas. The plasma source pressure is between 4-6 mtorr and the DC bias level is 350 V in all cases. All of the etching yields were normalized to the corresponding etching yields at normal angle.

3.3.2 Angular Etching Yields in C_2F_6/Ar Plasmas

Thermal silicon dioxide etching yields were also measured in 20% C_2F_6/Ar plasma at different plasma source pressures (6 mtorr, 13 mtorr, and 21 mtorr). The evolution of

the angular etching yield curves in C_2F_6/Ar plasmas with plasma pressure is similar with the trends I have discussed in C_4F_8/Ar plasmas. Figure 3-15 shows the etching yields of SiO_2 at normal angle as a function of ion energy. The normalized angular etching yields in these three different beam source pressures at DC bias 350 V are summarized in Figure 3-16. With the increases of plasma source pressure, more reactive neutrals and less ions reach the plasma sample surface, consequently, the etching yields at a given ion bombardment energy increases gradually. Consistently, the angular etching yields at low plasma source pressure (6 mtorr) have typical physical sputtering behavior. One the contrary, the resulting angular etching yield curve is ion-enhanced-etching-like at high plasma source pressure (21 mtorr). At 13 mtorr, the angular etching yield curve is between these two extremes.

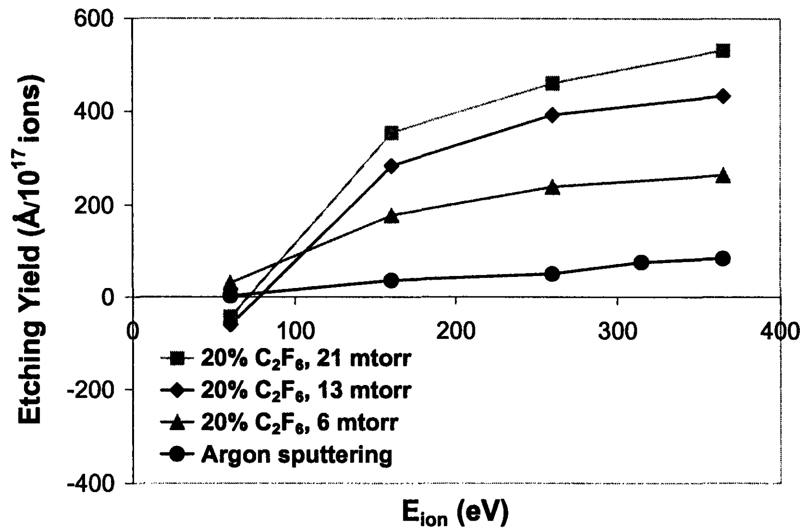

Figure 3-15 The etching yield of thermal silicon dioxide in 20% C_2F_6/Ar plasmas as a function of ion bombardment energy for different plasma source pressures at normal angle. For comparison, the sputtering rate of thermal silicon dioxide in argon plasma was also shown in this figure.

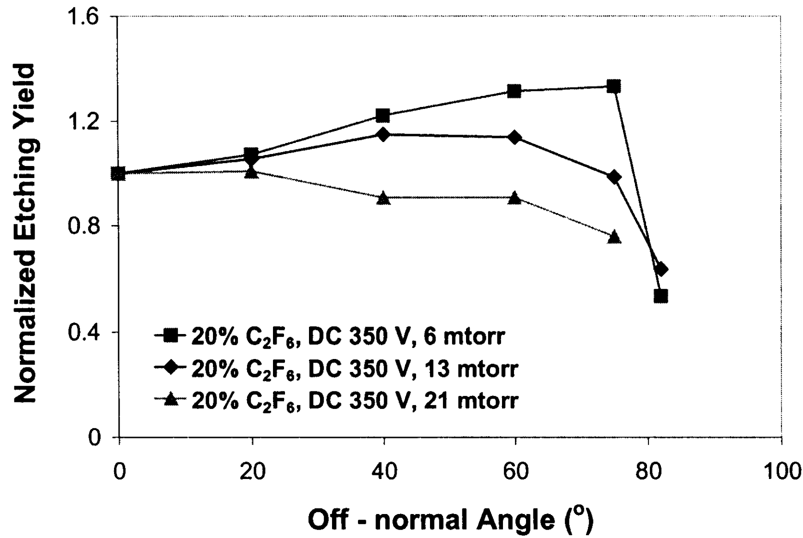

Figure 3-16 The normalized angular etching yields of thermal silicon oxide in 20% C_2F_6/Ar plasmas at different plasma source pressures. The DC bias level is 350 V in all cases. All of the etching yields were normalized to the corresponding etching yields at normal angle.

3.4 Impact of O_2 Addition on SiO_2 Angular Etching Yields

The fluorocarbon thin film formed during the dielectric materials etching in fluorocarbon plasmas had obvious influence on the etching kinetics[34,36,40,41] and surface roughening evolution[42]. Experimentally, people have shown that the thickness of this fluorocarbon thin film can be altered by changing the etching parameters, such as the ion bombardment energy, etching time, and more importantly the etching chemistry[34,40,41]. Oxygen addition to the plasma will change the plasma composition, both the neutrals and ions, therefore, the plasma polymer deposition capability is manipulated. In particular, more O_2 addition makes the plasma less polymerizing.

Figure 3-17 and Figure 3-18 show the plasma neutral and ion compositions variation with O_2 addition in 20% C_4F_8/Ar plasmas at 10-13 mtorr, respectively. In plasma neutrals (Figure 3-17), the concentration of CF neutral decreases significantly with oxygen addition, which makes the plasma less polymerizing. In addition, CO concentration also jumps up with oxygen addition. In plasma ions, the intensities of all species decreases due to two separated effects. First, oxygen is electronegative and the electron density in the resulting plasma decreases because of electron attachments. Second, the plasma pressure

increases from 10 to 13 mtorr after oxygen addition. This pressure increase makes the electron temperature lower, which leads to a lower ionization efficiency.

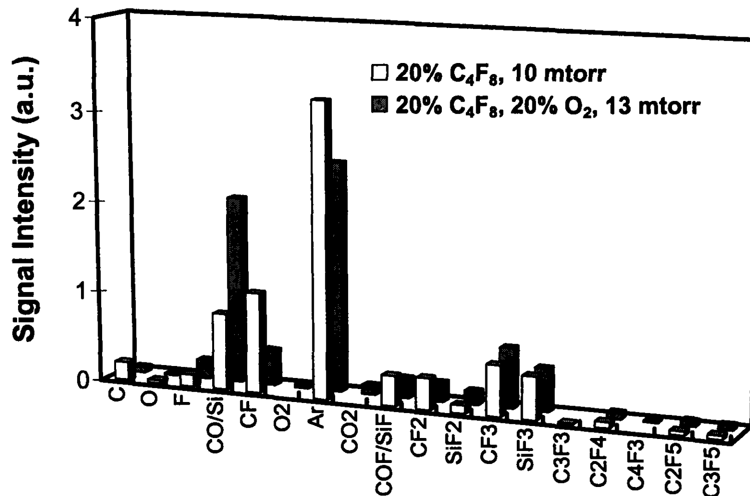

Figure 3-17 The impact of O_2 addition on the plasma neutral composition in 20% C_4F_8/Ar plasma quantified using mass spectrometer. The plasma source pressure is between 10-13 mtorr.

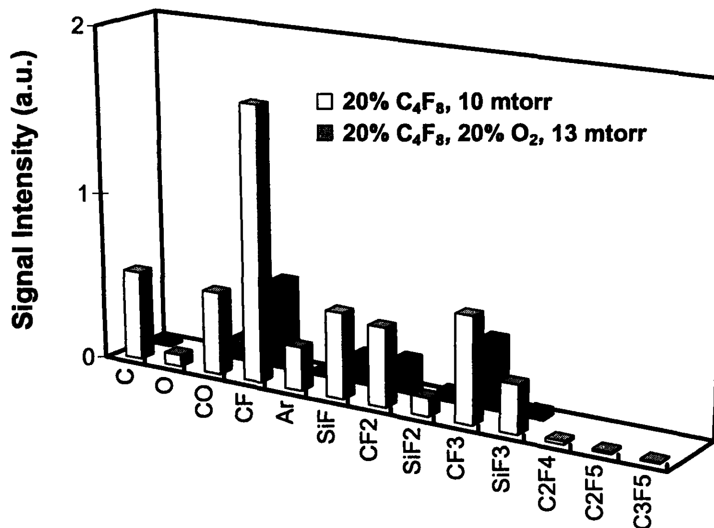

Figure 3-18 The impact of O_2 addition on the plasma ion composition in 20% C_4F_8/Ar plasma quantified using mass spectrometer. The plasma source pressure is between 10-13 mtorr.

In the net etching regime in the present work, the effect of oxygen addition to the plasma on the angular etching yield evolution was studied. Figure 3-19 indicates the impact of oxygen addition on the etching yields at normal ion incident angle for 20% C_4F_8/Ar plasmas. It can be seen that oxygen addition has no obvious effect on the etching yields at high ion energies (e.g. DC bias 350 V). In contrast, the etching behavior is quite different at low ion energy levels. In particular, at dc bias 50 V, the etching is in net deposition regime before oxygen addition, while it is in net etching regime after oxygen addition. These experimental observations are consistent with the plasma composition analysis with oxygen addition. Since oxygen addition makes the plasma less polymerizing, the polymer formed on the surface even at very low ion energy level (DC bias 50 V) is very thin and the etching process is still in net etching regime. On the other hand, at high ion energies the polymer layer formed can also be relatively thin because of the high ion bombardment energy even without oxygen addition; therefore, the etching kinetics is not influenced significantly by the oxygen addition.

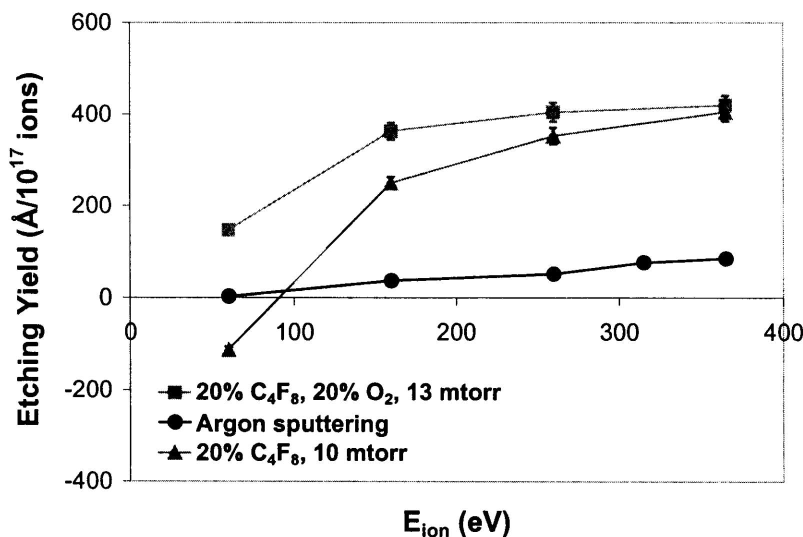

Figure 3-19 The impact of O_2 addition on the etching yields of thermal silicon oxide in 20% C_4F_8/Ar plasmas at different ion energy levels at normal angle. The plasma source pressure is 10 mtorr and 13 mtorr before and after O_2 addition, respectively. For comparison, the sputtering rate of thermal silicon dioxide in argon plasma was also shown in this figure.

Figure 3-20 shows the resulting angular etching yield curves at DC bias 350 V before and after oxygen addition. Intriguingly, oxygen addition has no obvious impact on

the angular etching yields under this specific situation. In both cases, the angular etching yield curves have similar trends. In particular, the etching yields almost keep constant up to 60° off-normal angles, and then drop off with the off-normal angle.

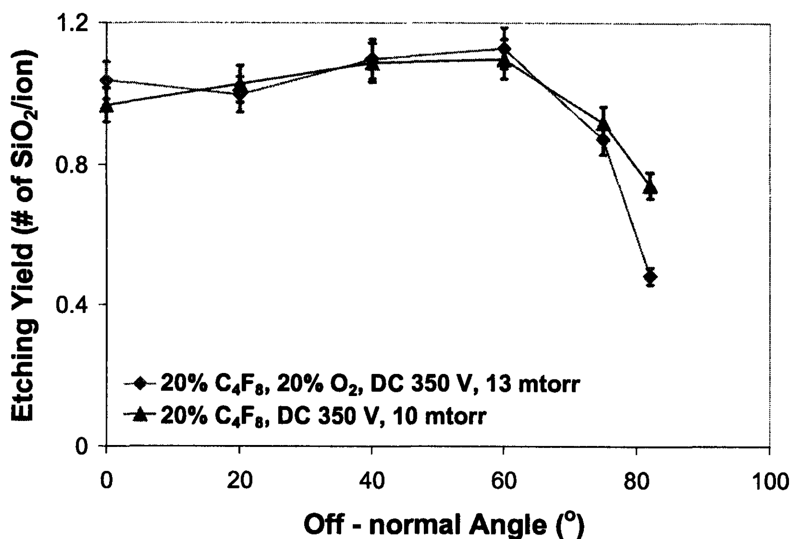

Figure 3-20 The impact of O_2 addition on the angular etching yields of thermal silicon oxide in 20% C_4F_8/Ar plasmas. The plasma source pressures are 10 mtorr and 13 mtorr before and after O_2 addition, respectively. All of the etching yields were normalized to the corresponding etching yields at normal angle.

The surface carbon (C1s) XPS spectrums at 0° and 75° off normal angles of SiO_2 surfaces are shown in Figure 3-21 after etching in 20% C_4F_8/Ar plasmas with and without oxygen addition. Various peaks including C-Si, C-C, and CFx (x = 1, 2, 3) are founded on the etching surfaces without oxygen addition; while mainly C-Si peak is detected after oxygen addition to the plasma. I believe that the Carbon (C1s) XPS signal is a reflection of the content of fluorocarbon deposition on the substrate surface. Consistently, the fluorocarbon content on the etched surface is higher in plasmas without oxygen addition at both normal and 75° off normal angles. On the contrary, O_2 addition leads to an etching kinetics with lower fluorocarbon content on the etched surface because of less polymerizing capability after O_2 addition. Based upon the angular etching yield curves in Figure 3-20 and the XPS analysis results above, it is concluded that the polymer deposition effects on the angular etching yields evolution are not obvious under this specific scenario.

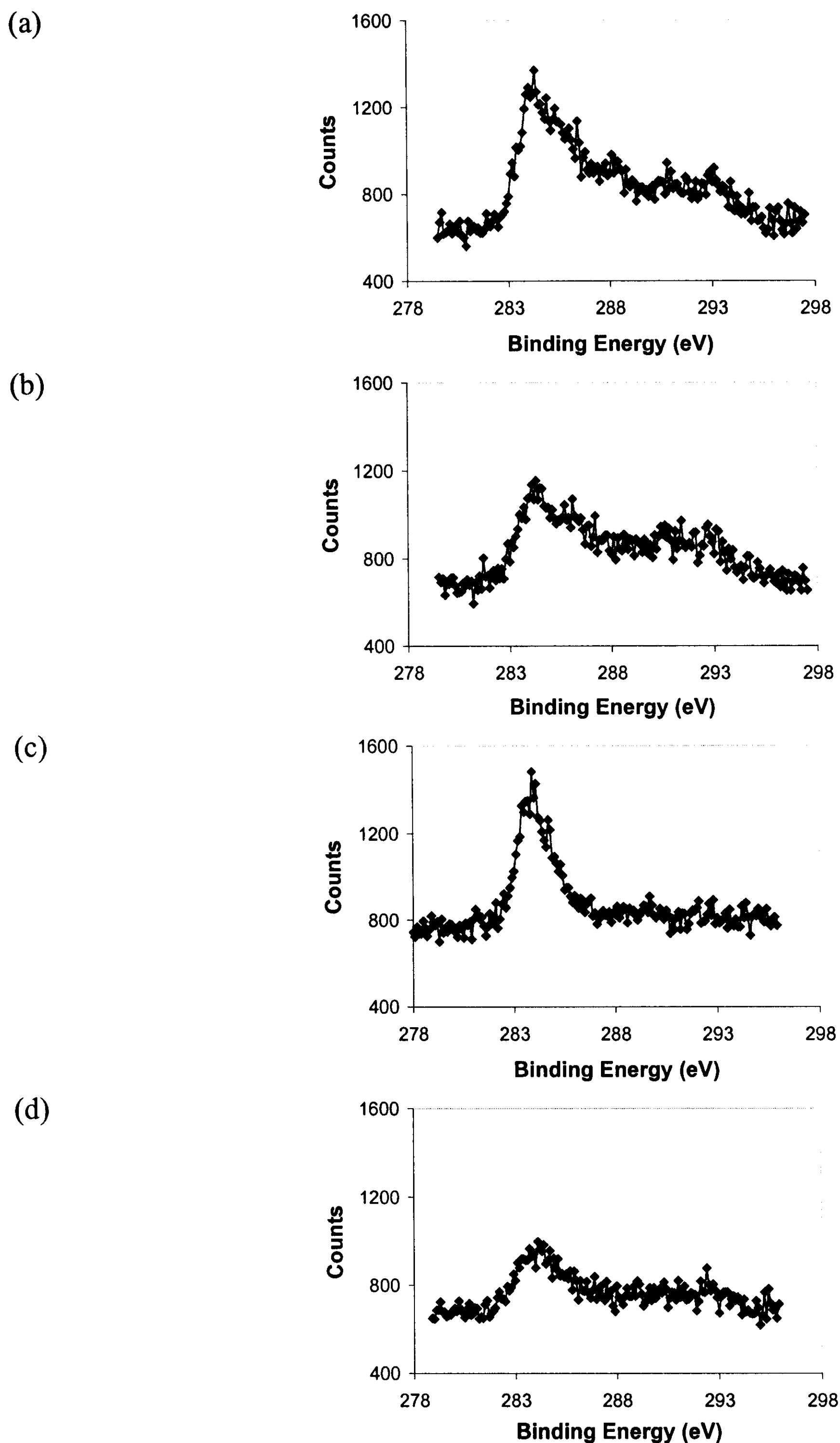

Figure 3-21 The surface carbon (C1s) XPS spectrums of etched SiO_2 films. The etching parameters are: (a) 0° off-normal angle, and (b) 75° off-normal angle in 20% C_4F_8/Ar plasmas at 10 mtorr; (c) 0° off-normal angle, and (d) 75° off-normal angle in 20% C_4F_8/20% O_2/Ar plasmas at 12 mtorr. In all cases, the ion fluence reaching the surface is 2.0×10^{17} ions/cm^2.

In order to have a better understanding of the polymer deposition effects, thermal SiO_2 was etched in plasmas with slightly higher polymer deposition capability: 15% C_4F_8/Ar plasmas before and after oxygen addition at plasma pressure 18-20 mtorr. Figure 3-22 reports the etching yields at normal ion incident angle and Figure 3-23 shows the resulting normalized etching yield curves at DC bias 350 V. Figure 3-24 summarizes the surface carbon (C1s) XPS spectrums at 0° and 75° off normal angles of SiO_2 surfaces after etching in 15% C_4F_8/Ar plasmas with and without oxygen addition. Similarly, oxygen addition to the plasma leads to less polymer deposition, therefore, weaker C(1s) signals in the XPS analysis for both 0° and 75° off normal angles.

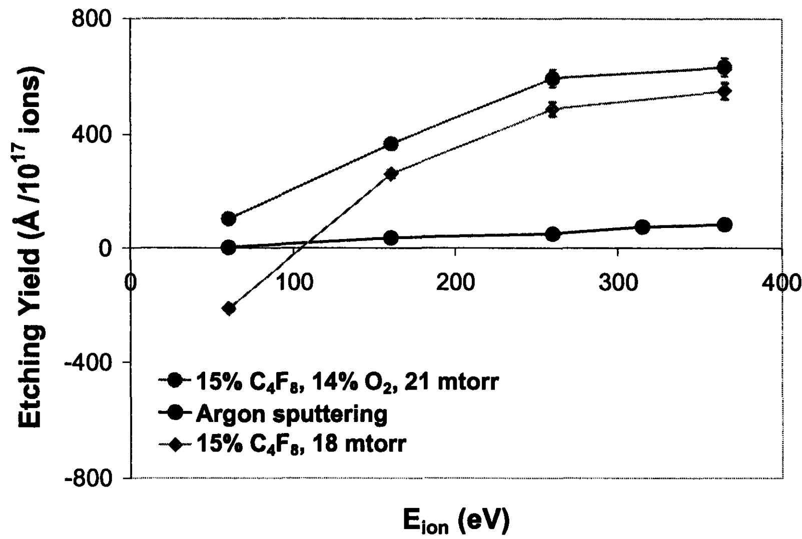

Figure 3-22 The impact of O_2 addition on the etching yields of thermal silicon oxide in 15% C_4F_8/Ar plasmas at different ion energy levels at normal angle. The plasma source pressure is 18 mtorr and 21 mtorr before and after O_2 addition, respectively. For comparison, the sputtering rate of thermal silicon dioxide in argon plasma was also shown in this figure.

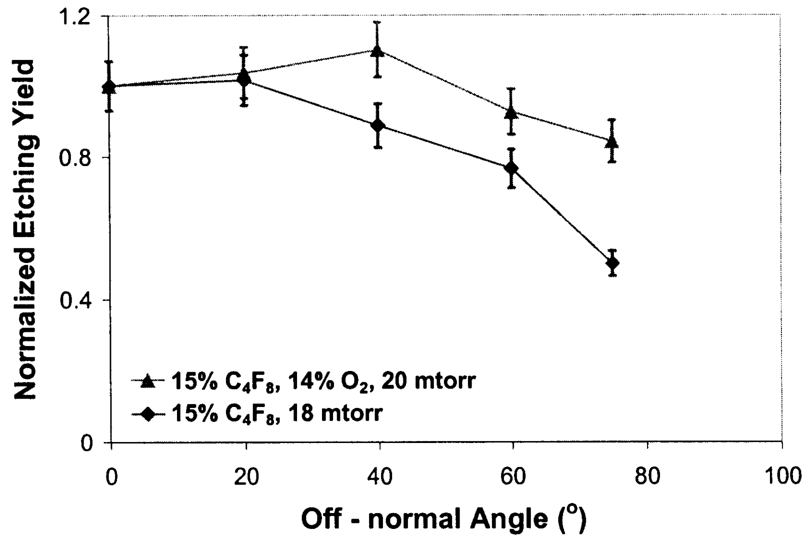

Figure 3-23 The impact of O_2 addition on the normalized angular etching yields of thermal silicon oxide in 15% C_4F_8/Ar plasmas. The plasma source pressures are 18 mtorr and 21 mtorr before and after O_2 addition, respectively. All of the etching yields were normalized to the corresponding etching yields at normal angle.

Consistently, in 15% C_4F_8/Ar plasmas at 18-20 mtorr, oxygen addition has more significant impact on the etching kinetics at low ion bombardment energies, where oxygen addition helps to push the etching kinetics from net deposition to net etching. At high ion energy level (DC 350 V), the etching yields at normal angle are slight different. At this high energy level (DC 350 V), however, oxygen addition has obvious impact on the angular etching yields. In particular, the angular etching yields decrease more quickly without oxygen addition. I believe that this angular etching yields difference is mainly caused by the difference of fluorocarbon deposition layer thickness. Further discussion of polymer deposition effects on angular etching yield curves will be performed in Section 3.7.

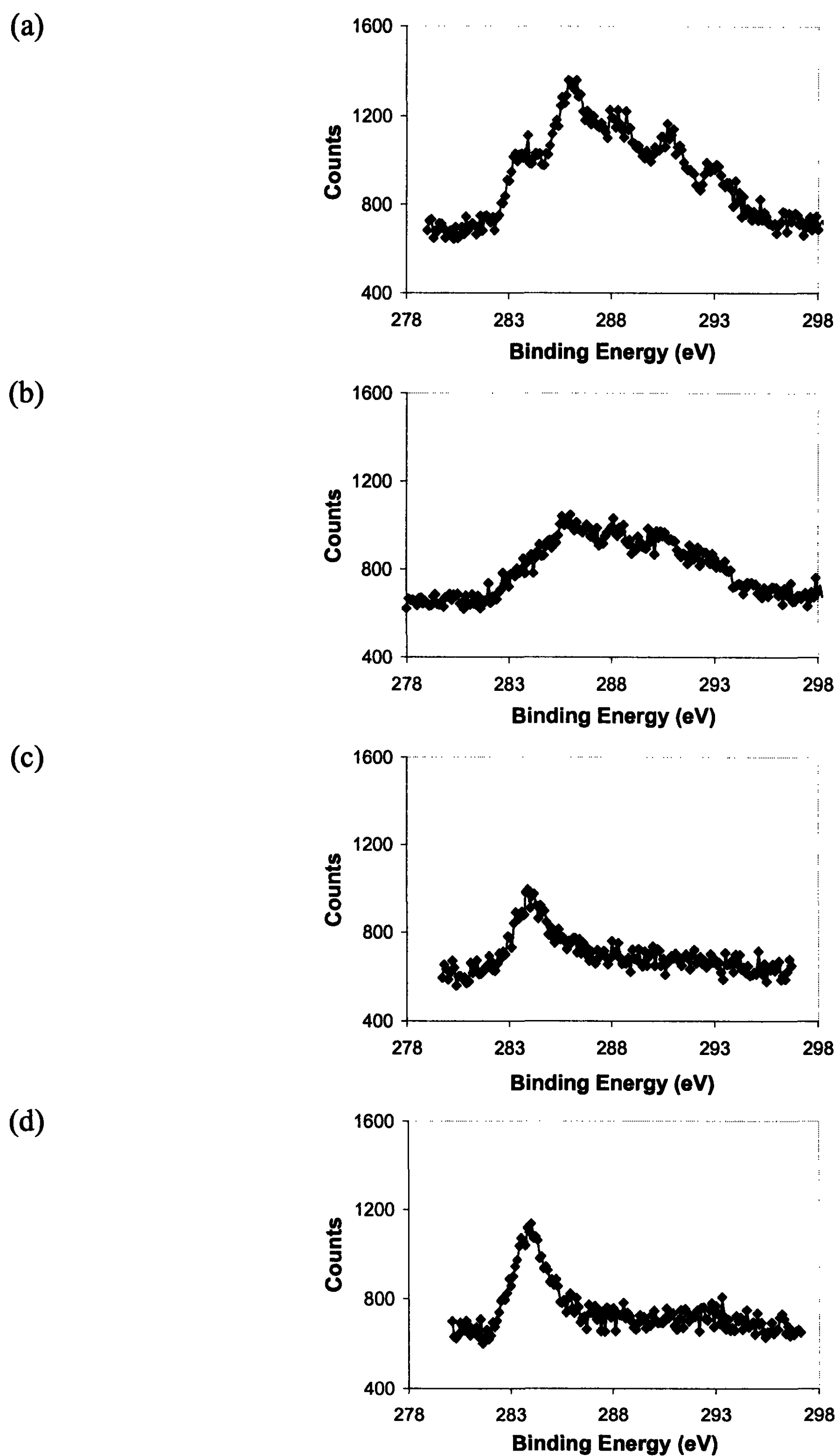

Figure 3-24 The surface carbon (C1s) XPS spectrums of etched SiO_2 films. The etching parameters are: (a) 0° off-normal angle, and (b) 75° off-normal angle in 15% C_4F_8/Ar plasmas at 18 mtorr; (c) 0° off-normal angle, and (d) 75° off-normal angle in 15% C_4F_8/14% O_2/Ar plasmas at 20 mtorr. In all cases, the ion fluence reaching the surface is 2.0×10^{17} ions/cm^2.

3.5 Angular Etching Yields of Low-k Coral Material in Fluorocarbon Plasmas

Low-k dielectric materials etching in plasmas, especially in fluorocarbon plasmas, has attracted the interests of many researcher since low-k material is promising to lower signal delay between copper interconnects[43-47]. However, the angular etching kinetics of low-k materials has seldom been addressed in the literature although it is one of the most important parameters that must be experimentally characterized. In this section, the angular etching yield of low-k dielectric coral material was studied in C_4F_8/Ar plasmas.

Figure 3-25 shows the etching yields of coral material at normal ion incident angle for two different plasma conditions: low plasma pressure (4 mtorr) and C_4F_8 percentage (10%), and high plasma pressure (21 mtorr) and C_4F_8 percentage (15%). Ion bombardment energy has obvious effects on the etching behavior, as has already been addressed for oxide etching in C_4F_8/Ar plasmas. The etching kinetics transits from net deposition regime to net etching with the increase of ion energy. In addition, the threshold energy needed to have net etching is higher than that for SiO_2 etching. This might be related to the difference between coral and thermal silicon dioxide since there are doped ethyl- groups in coral film. These ethyl groups in the pre-etched coral film might enhance the local fluorocarbon deposition in fluorocarbon plasmas; therefore, net deposition might happen at relatively high ion bombardment energy compared to SiO_2 etching.

In fluorocarbon plasmas, the angular etching yields of coral demonstrate similar trends with SiO_2 materials etching discussed previously in this article. Figure 3-26 shows the normalized angular etching yield curves of coral in C_4F_8/Ar plasmas described in Figure 3-25 at DC bias 350 V. At low plasma pressure (4 mtorr) and C_4F_8 percentage (10%), the resulting angular etching yield curve is physical sputtering like. On the other hand, ion-enhanced-etching-like angular etching yield curve is resulted at high plasma pressure (21 mtorr) and C_4F_8 percentage (15%).

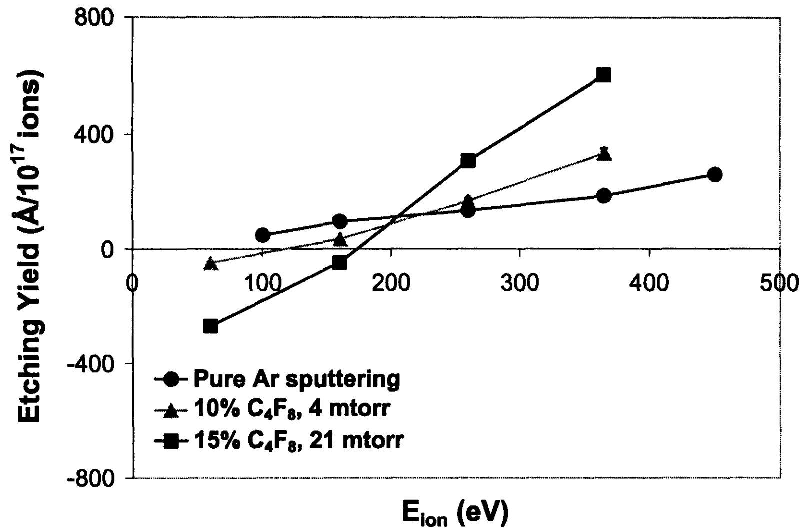

Figure 3-25 The etching yield of low-k dielectric coral film in C_4F_8/Ar plasmas as a function of the ion bombardment energy for different C_4F_8 percentages (10% and 15%) and different plasma source pressures (4 mtorr and 21 mtorr) at normal angle. For comparison, the sputtering rate of thermal silicon dioxide in argon plasma was also shown in this figure.

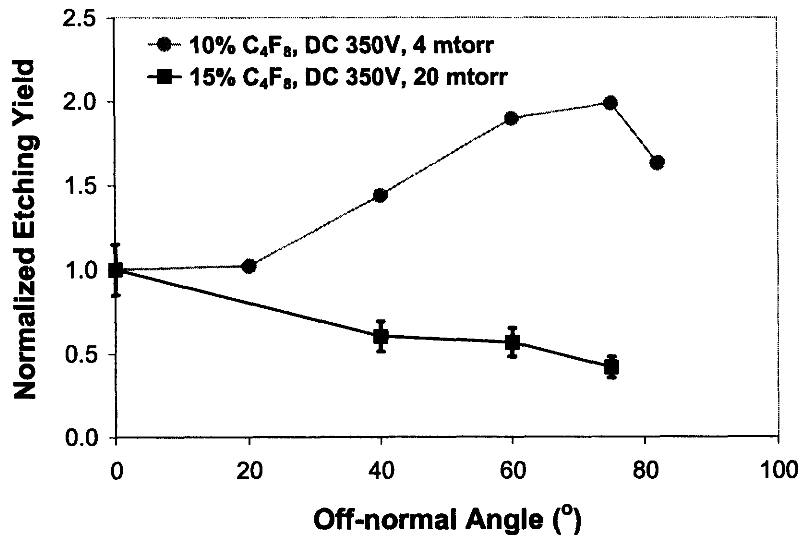

Figure 3-26 The normalized angular etching yields of low-k dielectric coral in C_4F_8/Ar plasmas under various plasma source pressures and DC bias levels for different C_4F_8/Ar volumetric ratios. Both of the etching yields were normalized to the corresponding etching yields at normal angle.

3.6 Impact of Neutral-to-ion Flux Ratio

So far, it has been demonstrated in my experiments that etching parameters have obvious impact on the evolution of angular etching yields. In particular, it seems that

physical- sputtering-like angular curves are formed at low plasma source pressure and/or low effective reactive gas percentage (Cl_2 or fluorocarbon gas), while ion-enhanced-etching-like angular etching kinetics is resulted with high plasma source pressure and/or high effective reactive gas percentages. In addition, plasma source pressure and effective reactive gas percentage essentially affect the effective neutral-to-ion flux ratio, which is a key factor to determine the etching behavior. At low plasma pressure and/or reactive gas percentage, low neutral-to-ion flux ratio is resulted, where the etching process is limited by the reactive neutrals on the etching surface. In contrast, high plasma pressure and/or reactive gas percentage lead to high neutral-to-ion flux ratio, where enough reactive neutrals are available on the sample surface and the etching reaction is generally ion flux limited.

It has already been demonstrated that there are two etching regimes with changing the effective neutral-to-ion flux ratios for silicon etching in Cl_2/Ar chemistries, which has already been shown in Figure 3-2. They were defined as non-saturated and saturated etching regimes, respectively. In the non saturated etching regime, the neutral-to-ion flux ratio is very low and the etching yield increases almost linearly with increasing the neutral-to-ion flux ratio. At the saturated etching regime (high flux ratios), the etching yield only increases moderately with increasing flux ratio. Similar trends are also found from silicon dioxide etching in C_4F_8/Ar plasmas. Figure 3-27 summarizes SiO_2 etching yield variation with the effective neutral-to-ion flux ratio at different ion bombardment energies. Consistently, at low flux ratios non saturated etching kinetics is resulted, while high flux ratios push the etching to saturated etching regime.

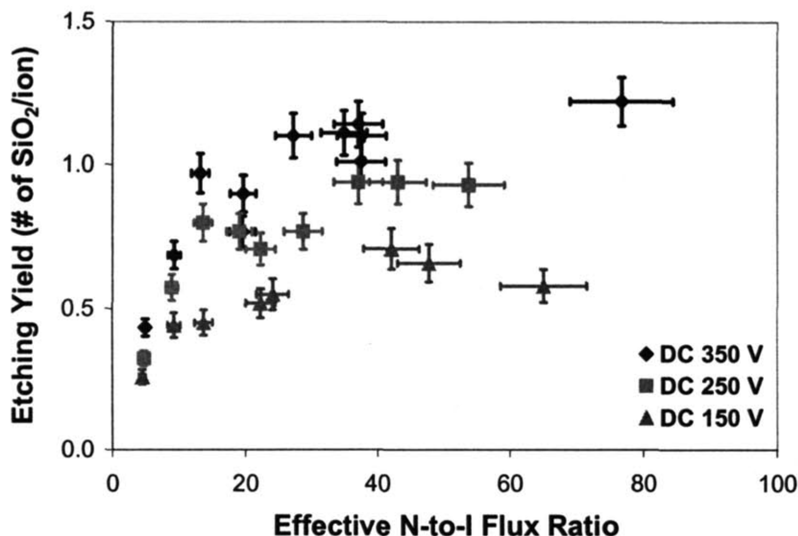

Figure 3-27 The etching yield of thermal silicon dioxide in C_4F_8/Ar plasmas as a function of the effective neutral-to-ion flux ratio and ion bombardment energies at normal ion incidence angle.

Intriguingly, it is found that physical-sputtering-like angular etching yield curves are resulted at the non-saturated etching regime (low effective neutral-to-ion flux ratios). On the other hand, the angular etching kinetics is ion-enhanced-etching-like at the saturated etching regime (high neutral-to-ion flux ratios). Actually, these experimental observations are reasonable. In the non-saturated regime, the etching surface is limited by reactive neutrals, and therefore, ion-enhanced-etching is not dominating the etching kinetics and physical sputtering kinetics is important. Consequently, the overall angular kinetics has physical-sputtering behavior, with a peak around 60-70° off-normal angle. In the saturated etching regime, the etching surface is highly saturated with reactive neutrals, and ion-enhanced-etching is much more important compared to physical sputtering kinetics. As a result, the resulted angular etching yield curves are ion-enhanced-etching-like.

The argument mentioned above is supported by the etching yield date at normal ion incident angle, which have been shown multiple times in previous sections. An example is the thermal SiO_2 etching yields at different C_4F_8 percentages shown in Figure 3-13. At very low neutral-to-ion flux ratio (10% C_4F_8, 4 mtorr), the etching yield at a given ion energy is only doubled compared to the pure physical sputtering yield. Roughly speaking, this means the ion-enhanced etching component is comparable to the physical sputtering

component. Since the ion-enhanced etching is not dominating, the resulting angular etching yield curve has physical sputtering characteristics. On the other hand, at high neutral-to-ion flux ratio (33% C_4F_8, 6 mtorr), the overall etching yield is much higher than the pure sputtering yield at DC bias 350 V, which means that the physical sputtering kinetics is trivial in the overall etching kinetics. Therefore, ion-enhanced-etching like angular etching yields are formed in this high neutral-to-ion flux ratio.

In order to have a further understanding of the impact of neutral-to-ion flux ratio on the angular etching kinetics, XPS analysis of etched polysilicon surface in Cl_2/Ar plasmas was performed at different ion bombardment angles and different plasma conditions. Figure 3-28 illustrates the signal intensity variation as the XPS take-off angle is changed on an etched polysilicon surface. The Cl(2p) signal intensity does not change obviously with the take-off angle, which suggests that chlorine is mainly confined to the top surface with a layer thickness less than the mean free path of the photoelectrons. On the other hand, Th Si(2p) signal intensity increases significantly when the take-off angle increases from 30° to 80° because the XPS can sample deeper into the substrate at higher take-off angles.

Table 3-2 summaries the effect of XPS take-off angle on Si(2p) and Cl(2p) intensities at different plasma process conditions. Consistently, the intensity of Cl(2p) is almost independent of the take-off angle, while Si(2p) intensity increases with increasing XPS take-off angle. Similar observations have also been reported by Chang et al.[48]. Since chlorine is mainly confined to the top surface within the XPS penetration depth, the amount of chlorine introduced to the substrate during plasma etching can be estimated by measuring the Cl(2p) intensity at XPS take-off angle 30°.

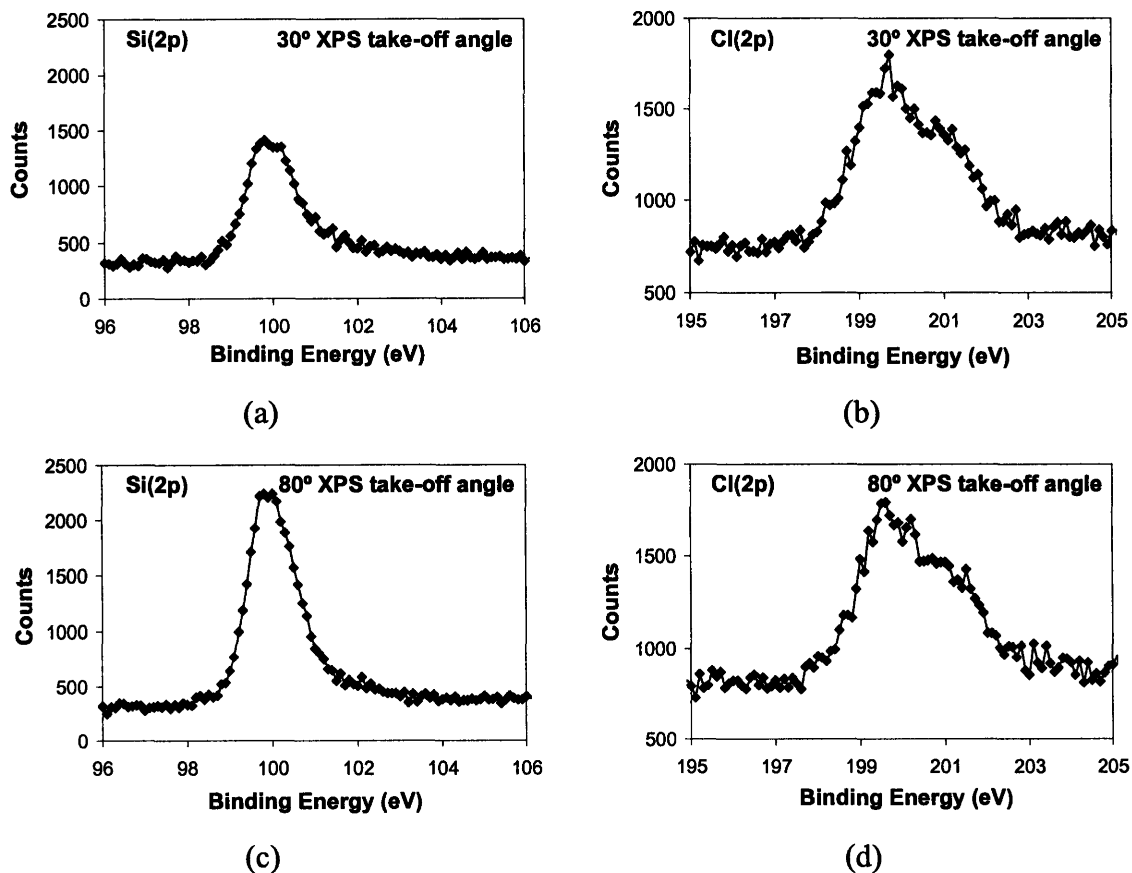

Figure 3-28 The influence of XPS take-off angle on Cl(2p) and Si(2p) XPS spectrums of polysilicon after etching in 7% Cl_2/Ar plasmas under plasma pressure 5 mtorr. The ion fluence reaching the surface is 3.0×10^{17} ions/cm^2 and the ion bombardment off-normal angle is 60°.

Table 3-2 Comparison of Si(2p) and Cl(2p) XPS signal intensities at different ion bombardment angles, different etching chemistries, and different XPS take-off angles. The signal intensities have been corrected to their corresponding sensitivity factors.

Plasma condition	ion incident off-normal angle (°)	XPS take off angle	Signal intensity		Elemental fraction	
			Si(2p)	Cl(2p)	Si(2p)	Cl(2p)
7% Cl_2/Ar 5 mtorr DC 250 V	20	30	1875	1314	0.59	0.41
		80	3340	1207	0.73	0.27
	60	30	2175	918	0.70	0.30
		80	3646	918	0.80	0.20
67% Cl_2/Ar 14 mtorr DC 250 V	20	30	1804	1815	0.50	0.50
		80	2958	1907	0.61	0.39
	60	30	2269	1765	0.56	0.44
		80	3674	1645	0.69	0.31

The amount of chlorine incorporated into the substrate surface is strongly influenced by the processing conditions, such as the ion bombardment off-normal angle, ion energy, and neutral-to-ion flux ratio. Figure 3-29 shows the Cl(2p) photoemission intensity as a function of ion bombardment off-normal angle at different neutral-to-ion flux ratios and ion energies. Interestingly, the evolution of Cl(2p) intensity with off-normal angle at low flux ratio (7% Cl_2, 5 mtorr) is quite different from that at high flux ratios (67% Cl_2, 14 mtorr). At low flux ratios (7% Cl_2, 5 mtorr), the Cl(2p) signal intensity is maximized at normal ion bombardment angle and then decreases obviously with increasing the off-normal angle. On the other hand, the Cl(2p) signal intensity remains relatively constant at different off-normal angles at high flux ratios (67% Cl_2, 14 mtorr).

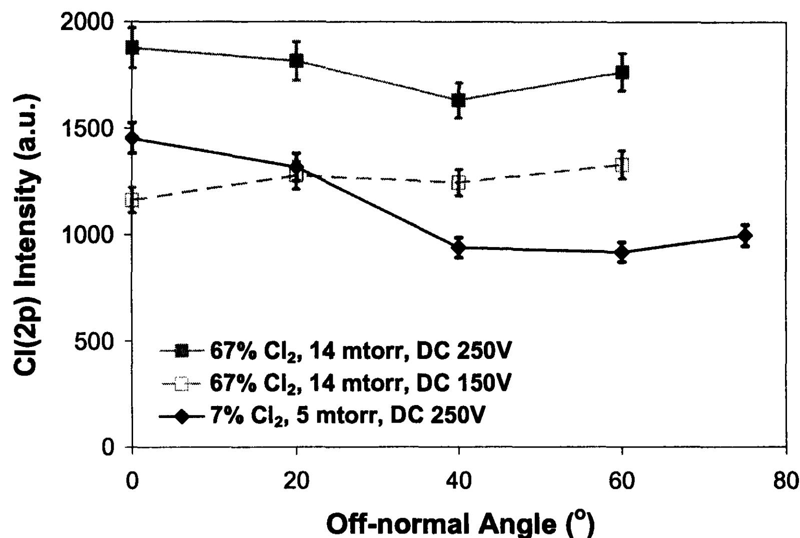

Figure 3-29 Cl(2p) XPS signal intensity of etched polysilicon varies with the ion bombardment off-normal angle, the ion bombardment energy, and plasma chemistry. In all cases, the XPS take-off angle is 30°.

A possible explanation is related to the ion incorporation efficiency at different ion bombardment off-normal angles and the neutral-to-ion flux ratio. At low neutral-to-ion flux ratio (7% Cl_2, 5 mtorr), the surface reaction is limited by the reactive neutrals on the surface, and reactive neutral adsorption has trivial contribution to the surface chlorine concentration. Therefore, reactive ion incorporation mainly contributes to the chlorine on the top surface detected by XPS. Since the ion incorporation efficiency becomes lower at high off-normal angles compared to that at near normal angles[49,50], the overall amount of Cl(2p) photoemission intensity decreases as I increase the ion bombardment off-normal angle. At high neutral-to-flux ratio (67% Cl_2, 14 mtorr), the etching is mainly limited by ions bombarding the surface. As a result, reactive neutral adsorption on the surface is more important and reactive ion incorporation becomes relatively trivial. Since the reactive neutral adsorption has weaker dependence on the ion incident off-normal angle compared to ion incorporation, the overall Si(2p) photoemission intensity remains relatively constant at different ion bombardment off-normal angles.

3.7 Polymer Deposition Effects

The apparatus used in this work, cannot run plasmas with high fluorocarbon gas percentage in the feed gas. This is because polymer deposition becomes very significant

on the mesh between the plasma source chamber and the processing chamber when the plasma becomes very polymerizing. Consequently, positive charge is accumulated on this polymer insulating layer since I use DC bias method to accelerate the ions across the plasma sheath. This positive charge on polymer insulating layer repels the ions coming from the plasma bulk and causes ion flux instabilities reaching the etching surface. As a result, the etching process is not stable and the resulting etching kinetics are not believable. For this reason, my experimental data at high ion bombardment energies (e.g. DC 350 V) always fall into the net etching regime. Therefore, the resulting angular etching yield curves in my current research always remain in the net etching regime even at grazing ion bombardment off-normal angles. In the literature, however, many researchers have reported that net deposition happened when etching dielectric materials in fluorocarbon plasmas at grazing angles. For instance, Chae et al.[33] reported the angular dependence of oxide etching yield with C_4F_8 and C_4F_8/O_2 plasma. When pure C_4F_8 plasma was used, the angular etching yield decreased quickly with increasing the off-normal ion incident angle, and the etching was in net deposition regime when the off-normal angle is beyond 50°. On the other hand, with 60% C_4F_8/O_2, the plasma was less polymerizing and the angular etching yield over the experimental range remained in the net etching regime.

People have argued that the fluorocarbon thin film formed on the etching surface of dielectric materials in fluorocarbon plasmas has significant impact on the etching kinetics and surface roughness development[34,35,40,41]. In particular, this fluorocarbon thin film was believed to play a key role on the resulting angular etching yield curve. Blom et al.[23,24] proposed that the difference of polymer deposition rate at different ion bombardment off-normal angles was the main reason of forming physical-sputtering-like angular etching yield curve. In particular, it was proposed that the surface coverage of polymer at small off-normal angles was higher than that at high off-normal angles (above 60°). At low pressures, Blom et al. believed that polymer formed at grazing angles could be neglected. Since the physical part of polymer etching process seemed to be dominant, the etching rate was higher at high off-normal angles (e.g. 60°). With the increase of plasma pressure, polymer was also formed at grazing angles; therefore, the peak in the etching rate at around 60° was depressed. Thus, the overall angular etching yield curve would be ion-enhanced-etching like.

Kwon et al.[26], however, suggested a different polymer deposition related mechanism to explain the variation of the angular etching yields under different processing conditions in fluorocarbon plasmas. It was proposed that an ion-induced polymer deposition mechanism was the main reason why the angular yield decreases gradually with off-normal angle or even falls in the net deposition regime at grazing angles, as reported by Chae et al. In this proposed ion-induced deposition process, ions strike the surface and deliver kinetic energy to the surface to generate active sites, which then react with fluorocarbon radicals from the plasma. Since the overall angular deposition curve of this proposed ion-induced deposition mechanism is similar to the physical sputtering angular curve, with a peak around 60° off-normal angle, the amount of energy dissipated at the surface (the number of active sites created for deposition) should qualitatively have a shape of sputtering angular curve too.

Experimentally, it is hard to argue whether the active sites generation on the surface under ion bombardment follows the shape of sputtering angular curve. Fortunately, a couple of simulation efforts have been focused on this problem. Based upon the calculation using software "*The Stopping and Range of Ions in Solids*"(SRIM) developed by Ziegler et al.[51], Guo and Sawin[52] estimated the number of vacancies generated per ion bombarding the surface as a function of ion bombardment off-normal angle, as shown in Figure 3-30. Clearly, the vacancy generation (or equivalently, the active site creation) curve does not peak around 60° off-normal angle, unlike the prediction by Kwon et al. Using classical molecular dynamics approach, Jang et al.[53] found the number of bonds broken per ion bombardment (reactive ion $C_3H_5^+$, 50 eV) also decreases gradually with the increase of ion bombardment off-normal angle. Since both the simulation results seem to be inconsistent with the prediction by Kwon et al., in the future it might be necessary to find a way to experimentally characterize fluorocarbon polymer deposition rate as a function of ion bombardment off-normal angle in fluorocarbon plasma in order to verify the ion-induced polymer deposition mechanism.

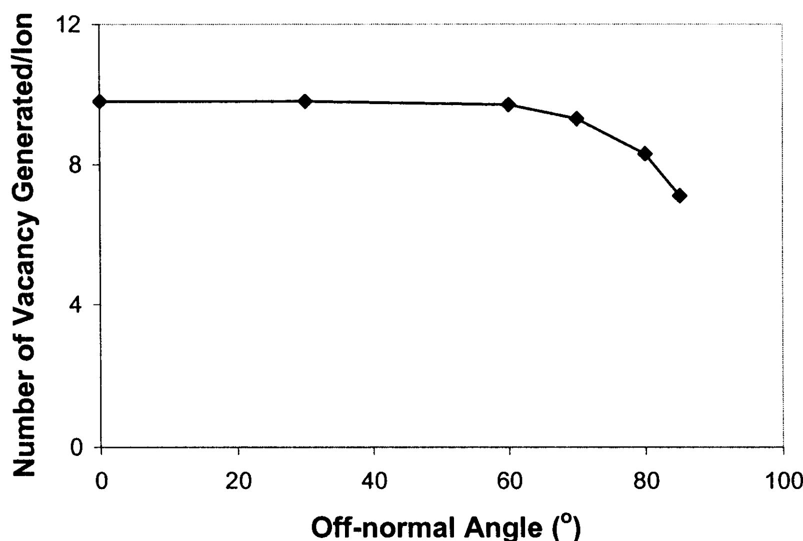

Figure 3-30 Average number of broken bonds per trajectory in the silicon substrate as a result of 500 eV Ar ions bombardment at the indicated off-normal angles.

In the current work, where the etching is always in the net etching regime, however, polymer deposition effects are not the primary reason for the angular etching yield development. In particular, the thickness of the fluorocarbon polymer layer remained relatively thin since the plasma is not extremely polymerizing. In addition, the surface elemental composition analysis with ion bombardment off-normal angle shown in Figure 3-7, Figure 3-8, and Figure 3-9 indicates that fluorocarbon deposition rate is not influenced obviously by the off-normal angle although the thickness of the thin fluorocarbon layer, which is not necessarily continuous, varies with the plasma conditions. The ion enhanced polymer deposition effects proposed by Kwon et al., if they exist, are not important in the present work since the polymer thickness depends weakly on the ion bombardment off-normal angle.

3.8 Conclusions

It has been demonstrated in an inductively coupled plasma beam reactor that the angular etching yields can be manipulated by changing the plasma processing conditions, such as the plasma source pressure, reactive feed gas percentage, and ion bombardment energy. The angular etching yield curve was more sputtering-like at low plasma source pressure and/or low effective gas percentage (Cl_2, C_4F_8, or C_2F_6), with a peak around 60-70° off-normal ion incident angle. In contrast, ion-enhanced-etching like angular curves,

which dropped gradually with off-normal angle, were formed at high plasma source pressure and/or high effective gas percentage. These observations have meaningful impact on processing side of the integrated circuits. In particular, the surface roughening in plasma processing can be altered by manipulating the angular etching yield curves, which has been addressed in detail elsewhere[54]. Further analysis indicated that the effective neutral-to-ion flux ratio reaching the surface was the primary factor to influence the angular etching yield curve. At low flux ratios, the etching process was limited by the reactive neutrals on the etching surface. Therefore, the overall etching process had physical sputtering characteristics since the ion-enhanced-etching was not dominantly important. For this reason, the overall angular etching yield curve had physical sputtering characteristics at low flux ratios. At high flux ratios, enough neutrals were available on the etching surface and the overall etching process was limited by ion flux. Therefore, the overall etching process was really dominated by ion enhanced etching and the resulting angular etching yield curve was ion-enhanced-etching-like. Although polymer deposition effects might have obvious impact on the angular etching yield curves, it only had trivial influence over the experimental range explored in the present work since the fluorocarbon plasmas involved in this work were not very polymerizing.

3.9 References

1 M. Y. Ali, N. P. Hung, B. K. A. Ngoi, and S. Yuan, Surface Engineering 19, 97-103 (2003).

2 M. Y. Ali, N. P. Hung, B. K. A. Ngoi, and S. Yuan, Surface Engineering 19, 104-108 (2003).

3 L. W. Flanagin, V. K. Singh, and C. G. Willson, Journal of Vacuum Science & Technology B 17, 1371-1379 (1999).

4 E. Gogolides, V. Constantoudis, G. P. Patsis, and A. Tserepi, Microelectronic Engineering 83, 1067-1072 (2006).

5 D. L. Goldfarb, A. P. Mahorowala, G. M. Gallatin, K. E. Petrillo, K. Temple, M. Angelopoulos, S. Rasgon, H. H. Sawin, S. D. Allen, M. C. Lawson, and R. W. Kwong, Journal of Vacuum Science & Technology B 22, 647-653 (2004).

6 D. He and F. Cerrina, Journal of Vacuum Science & Technology B 16, 3748-3751 (1998).

7 J. H. Jang, W. Zhao, J. W. Bae, I. Adesida, A. Lepore, M. Kwakernaak, and J. H. Abeles, Journal of Vacuum Science & Technology B 22, 2538-2541 (2004).

[8] G. P. Patsis, V. Constantoudis, A. Tserepi, E. Gogolides, and G. Grozev, Journal of Vacuum Science & Technology B 21, 1008-1018 (2003).

[9] G. W. Reynolds and J. W. Taylor, Journal of Vacuum Science & Technology B 17, 2723-2729 (1999).

[10] G. W. Reynolds, J. W. Taylor, and C. J. Brooks, Journal of Vacuum Science & Technology B 17, 3420-3425 (1999).

[11] J. Shin, G. Han, Y. Ma, K. Moloni, and F. Cerrina, Journal of Vacuum Science & Technology B 19, 2890-2895 (2001).

[12] J. Thiault, J. Foucher, J. H. Tortai, O. Joubert, S. Landis, and S. Pauliac, Journal of Vacuum Science & Technology B 23, 3075-3079 (2005).

[13] T. Yamaguchi, K. Yamazaki, M. Nagase, and H. Namatsu, Japanese Journal of Applied Physics Part 1-Regular Papers Short Notes & Review Papers 42, 3755-3762 (2003).

[14] T. Yamaguchi, K. Yamazaki, and H. Namatsu, Journal of Vacuum Science & Technology B 22, 2604-2610 (2004).

[15] W. D. Jin and H. H. Sawin, Journal of the Electrochemical Society 150, G711-G717 (2003).

[16] W. D. Jin and H. H. Sawin, Journal of Vacuum Science & Technology A 21, 911-921 (2003).

[17] W. D. Jin, S. A. Vitale, and H. H. Sawin, Journal of Vacuum Science & Technology a-Vacuum Surfaces and Films 20, 2106-2114 (2002).

[18] A. P. Mahorowala and H. H. Sawin, Journal of Vacuum Science & Technology B 20, 1064-1076 (2002).

[19] A. P. Mahorowala and H. H. Sawin, Journal of Vacuum Science & Technology B 20, 1084-1095 (2002).

[20] A. Sankaran and M. J. Kushner, Applied Physics Letters 82, 1824-1826 (2003).

[21] J. M. Lane, F. P. Klemens, K. H. A. Bogart, M. V. Malyshev, and J. T. C. Lee, Journal of Vacuum Science & Technology a-Vacuum Surfaces and Films 18, 188-196 (2000).

[22] T. M. Mayer, R. A. Barker, and L. J. Whitman, Journal of Vacuum Science & Technology 18, 349-352 (1981).

[23] A. M. Barklund and H. O. Blom, Journal of Vacuum Science & Technology a-Vacuum Surfaces and Films 11, 1226-1229 (1993).

[24] A. M. Barklund and H. O. Blom, Journal of Vacuum Science & Technology a-Vacuum Surfaces and Films 10, 1212-1216 (1992).

[25] B. O. Cho, S. W. Hwang, G. R. Lee, and S. H. Moon, Journal of Vacuum Science & Technology A 18, 2791-2798 (2000).

[26] O. Kwon, W. D. Jin, and H. H. Sawin, Applied Physics Letters 88 (2006).

[27] M. Balooch, M. Moalem, W. E. Wang, and A. V. Hamza, Journal of Vacuum Science & Technology a-Vacuum Surfaces and Films 14, 229-233 (1996).

[28] J. P. Chang, J. C. Arnold, G. C. H. Zau, H. S. Shin, and H. H. Sawin, Journal of Vacuum Science & Technology a-Vacuum Surfaces and Films 15, 1853-1863 (1997).

[29] J. P. Chang, A. P. Mahorowala, and H. H. Sawin, Journal of Vacuum Science & Technology a-Vacuum Surfaces and Films 16, 217-224 (1998).

[30] J. P. Chang and H. H. Sawin, Journal of Vacuum Science & Technology a-Vacuum Surfaces and Films 15, 610-615 (1997).

[31] S. A. Vitale, H. Chae, and H. H. Sawin, Journal of Vacuum Science & Technology a-an International Journal Devoted to Vacuum Surfaces and Films 19, 2197-2206 (2001).

[32] C. R. Eddy, D. Leonhardt, S. R. Douglass, B. D. Thoms, V. A. Shamamian, and J. E. Butler, Journal of Vacuum Science & Technology a-Vacuum Surfaces and Films 17, 38-51 (1999).

[33] H. Chae, S. A. Vitale, and H. H. Sawin, Journal of Vacuum Science & Technology A 21, 381-387 (2003).

[34] M. Schaepkens and G. S. Oehrlein, Journal of the Electrochemical Society 148, C211-C221 (2001).

[35] M. Schaepkens, G. S. Oehrlein, C. Hedlund, L. B. Jonsson, and H. O. Blom, Journal of Vacuum Science & Technology a-Vacuum Surfaces and Films 16, 3281-3286 (1998).

[36] M. Schaepkens, T. Standaert, N. R. Rueger, P. G. M. Sebel, G. S. Oehrlein, and J. M. Cook, Journal of Vacuum Science & Technology a-Vacuum Surfaces and Films 17, 26-37 (1999).

[37] J. H. Scofield, Journal of Electron Spectroscopy and Related Phenomena 8, 129-137 (1976).

[38] S. A. Vitale, Ph.D. Thesis, Massachusetts Institute of Technology, 2001.

[39] S. A. Rasgon, Ph.D. Thesis, Massachusetts Institute of Technology, 2005.

[40] T. Standaert, C. Hedlund, E. A. Joseph, G. S. Oehrlein, and T. J. Dalton, Journal of Vacuum Science & Technology A 22, 53-60 (2004).

[41] N. R. Rueger, J. J. Beulens, M. Schaepkens, M. F. Doemling, J. M. Mirza, T. Standaert, and G. S. Oehrlein, Journal of Vacuum Science & Technology a-Vacuum Surfaces and Films 15, 1881-1889 (1997).

[42] Y. P. Yin, S. Rasgon, and H. H. Sawin, Journal of Vacuum Science & Technology B 24, 2360-2371 (2006).

[43] R. H. Havemann and J. A. Hutchby, Proceedings of the Ieee 89, 586-601 (2001).

[44] A. Jain, S. Rogojevic, S. Ponoth, N. Agarwal, I. Matthew, W. N. Gill, P. Persans, M. Tomozawa, J. L. Plawsky, and E. Simonyi, Thin Solid Films 398, 513-522 (2001).

[45] K. Maex, M. R. Baklanov, D. Shamiryan, F. Iacopi, S. H. Brongersma, and Z. S. Yanovitskaya, Journal of Applied Physics 93, 8793-8841 (2003).

[46] A. Grill, Journal of Applied Physics 93, 1785-1790 (2003).

[47] M. Morgen, E. T. Ryan, J. H. Zhao, C. Hu, T. H. Cho, and P. S. Ho, Annual Review of Materials Science 30, 645-680 (2000).

[48] J. P. Chang and H. H. Sawin, Journal of Vacuum Science & Technology B 19, 1319-1327 (2001).

[49] C. F. Abrams and D. B. Graves, Journal of Vacuum Science & Technology A 16, 3006-3019 (1998).

[50] B. A. Helmer and D. B. Graves, Journal of Vacuum Science & Technology a-Vacuum Surfaces and Films 16, 3502-3514 (1998).

[51] J. F. Ziegler, J. P. Biersack, and U. Littmark, *The stopping and range of ions in solids* (Pergamon, New York, 1985).

[52] W. Guo, Sawin, H. H., (unpublished).

[53] I. Jang, B. Ni, and S. B. Sinnott, Journal of Vacuum Science & Technology a-Vacuum Surfaces and Films 20, 564-568 (2002).

[54] Y. P. Yin and H. H. Sawin, to be submitted.

Chapter 4. Surface Roughening of Silicon, Thermal Silicon Dioxide and Low-k Dielectric Coral Films in Argon Plasma

The surface roughness evolution of single crystal silicon, thermal silicon dioxide (SiO_2) and low dielectric constant film coral in argon plasma have been measured by atomic force microscopy (AFM) as a function of ion bombardment energy, ion impingement angle and etching time in an inductively coupled plasma beam chamber in which the plasma chemistry, ion energy, ion flux and ion incident angle can be adjusted independently. The sputtering yield (or etching rate) scales linearly with the square root of ion energy at normal impingement angle; additionally, the angular dependence of the etching yield of all films in argon plasma followed the typical sputtering yield curve, with a maximum around 60-70° off-normal angle. All films stayed smooth after etching at normal angle but typically became rougher at grazing angles. In particular, at grazing angles the RMS roughness level of all films increased if more material was removed; additionally, the striation structure formed at grazing angles can be either parallel or transverse to the beam impingement direction, which depends upon the off-normal angle. More interestingly, the sputtering caused roughness evolution at different off-normal angles can be qualitatively explained by the corresponding angular dependent etching yield curve. In addition, the roughening at grazing angles is a strong function of the type of surface; specifically, coral suffers greater roughening compared to thermal silicon dioxide.

4.1 Introduction

The sidewall roughening developed during plasma etching process becomes crucial as the feature sizes have been continuously scaling down in order to maximize the transistor density. A trivial impact in the past has now become a significant contributor to the off-state leakage budget and short-channel effect (SCE) control for sub-100 nm gate length devices[1]. As shown in the literature[2,3], top line-edge roughness (LER) play a very important role for the sidewall roughening of oxide patterning during etching in fluorocarbon chemistries. It was found that the resist sidewall roughness after development but before plasma etching was isotropic; during the anti-reflective coating (ARC) layer opening in plasma etching process, the photoresist layer became striated and

the top edge of the photoresist layer was faceted; the striation structure became much more significant and propagated down after etching of the subsequent SiO_2 layer.

The surface roughening of different films, such as dielectric oxide material[4,5], may occur during plasma etching in addition to the top LER effects on sidewall roughness evolution. Consequently, it is crucial to fully understand the mechanisms of the inherent surface roughening before I can optimize the plasma etching conditions to minimize the surface roughness level after etching. The following questions should be answered before I can propose a plausible mechanism for surface roughening during plasma etching process: What is the impact of ion bombardment on surface topography evolution? Is the roughening related to the etching chemistry? Will film properties influence the roughness evolution?

Some modeling effects aiming to understand the feature profile evolution and sidewall roughening in plasma etching have already been addressed in the literature[6-10]. Among them, Kawai and Sawin[10] have developed a 3-D simulator to simulate the plasma-surface interactions at nano-scale using Monte Carlo simulation. Specifically, a cellular representation of the substrate surface is used. In this 3-D simulator, the sidewall roughening as well as inherent roughening of different films can be simulated. However, there are very limited the experimental results on roughness evolution during plasma etching in literature which can be used to test the fidelity of the 3-D simulator.

In this Chapter, I address the surface roughening of three different initially smooth films (single crystal silicon, thermal SiO_2 and low-k dielectric coral) during etching in Ar plasma beam. The objective is to have a better understanding of the impact of ion sputtering on surface roughening evolution and provide an experimental data base for the 3-D profile simulation. In the literature[11-20], many researchers have already characterized the surface morphology evolution of silicon and SiO_2 films during pure Ar ion sputtering. What they found is that Ar sputtering might roughen the substrates depending on the ion energy level, ion bombardment angle and some other factors. Unfortunately, most of the work focused on high incident ion energy level typically larger than 1000 eV despite that ion energies around several hundred eV are normally used in industrial plasma-based processes. My focus in this paper is on the surface roughness produced by ions less than

500 eV. Additionally, rather than using Kaufman-type ion beam sources to produce Ar ions, my Ar plasma beam is extracted from an inductively coupled plasma source through a grounded orifice. By this means, the plasma beam has a better representation of the plasmas used in industrial processes.

4.2 Ar Sputtering Kinetics

The sputtering yields in argon plasma beam scale linearly with the square root of the ion bombardment energy and are consistent with data in the literature[21-28], which verifies that my ion flux measurement at normal angle and the etching rates characterized by ellipsometer/profilometer are reasonable. Figure 4-1 and Figure 4-2 give the sputtering yields of polysilicon, coral and SiO_2 as a function of square root of ion energy. Interestingly, the sputtering threshold energies of these films are all about 50 eV, consistent with pure physical sputtering. Additionally, the sputtering yield of coral is higher than SiO_2 for the same ion energy level. This might be due to the different inherent film properties of different films. One possible reason is that PECVD low-k dielectric coral is less dense compared with thermal SiO_2.

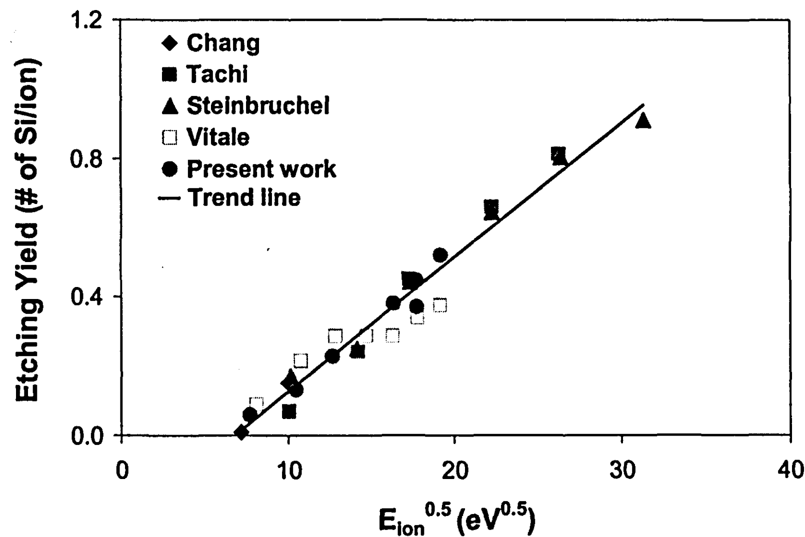

Figure 4-1 The sputtering yield of polysilicon in Ar plasma as a function of the square root of ion bombardment energy.

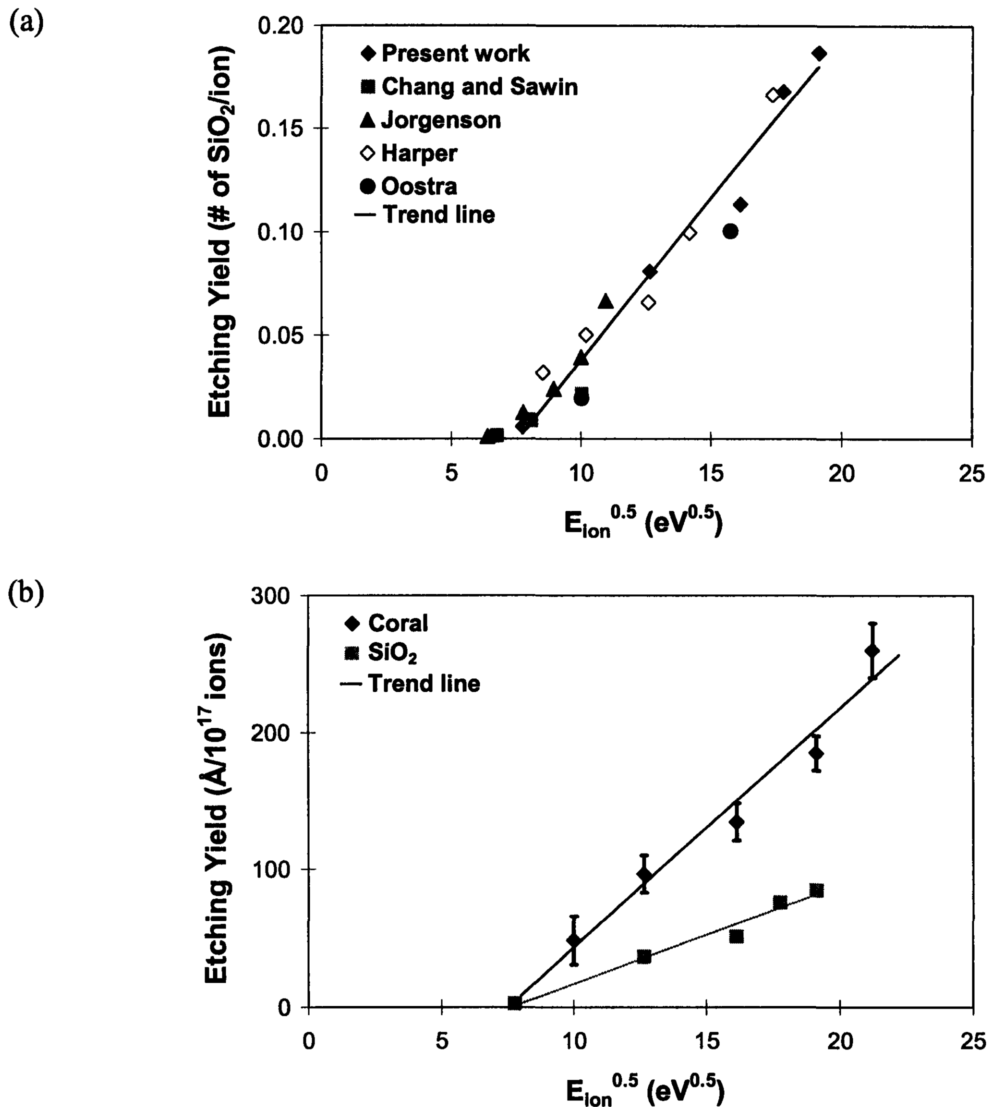

Figure 4-2 (a) the sputtering yield of SiO_2 and (b) the etching rate of coral per 10^{17} ions/cm^2 in argon plasma as a function of the square root of ion bombardment energy. For comparison, the etching rate of SiO_2 was also included in (b).

It is crucial to have adequate and comprehensive experimental database in order to develop a detailed model of plasma-surface interaction which can capture fine details happened during real plasma patterning conditions, such as the mirco-trenching and sidewall bowing effects[29]. One of the most important experimental parameters required is the relative etching yield as a function of ion bombardment angle. A better understanding of sidewall scattering effects is not possible without a solid quantification of the angular dependence of the etching yield. Figure 4-3 and Figure 4-4 show the normalized etching yield as a function of off-normal angle for polysilicon, SiO_2 and coral. Note that all of the

etching yields are normalized to the corresponding yields at normal angle for each material. Obviously, the etching yield of all films in argon plasma followed the typical sputtering yield curve, with a maximum around 60-70° off-normal angle. This suggests that my angular measurements of the ion flux are reliable. More specifically, the oxide and coral have the maximum yield shifted about 5-10° toward more grazing angles compared to polysilicon. Additionally, the relative shape of the angular etching yield curve is almost independent of the the ion energies in the scope of less than 500 eV, which can be seen in Figure 4-3.

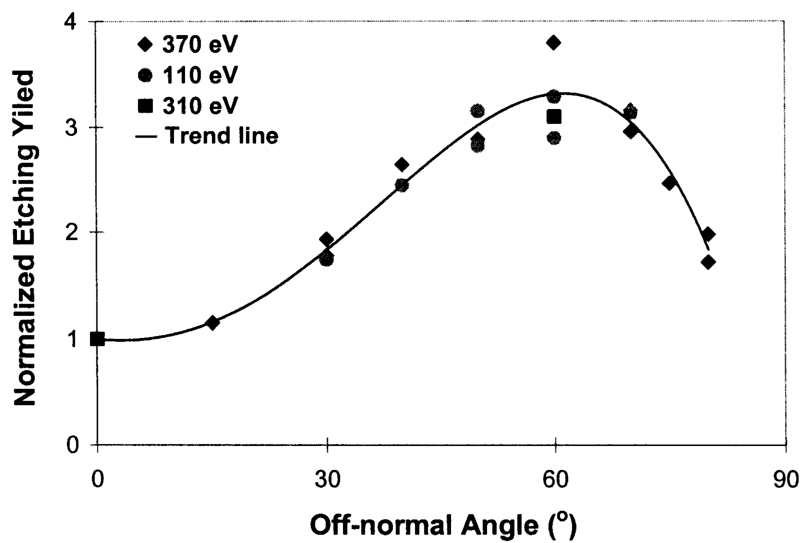

Figure 4-3 The normalized etching yield of polysilicon in Ar plasma as a function of off-normal angle. The curve followed the typical sputtering yield curve, with a maximum around 60° off-normal angle.

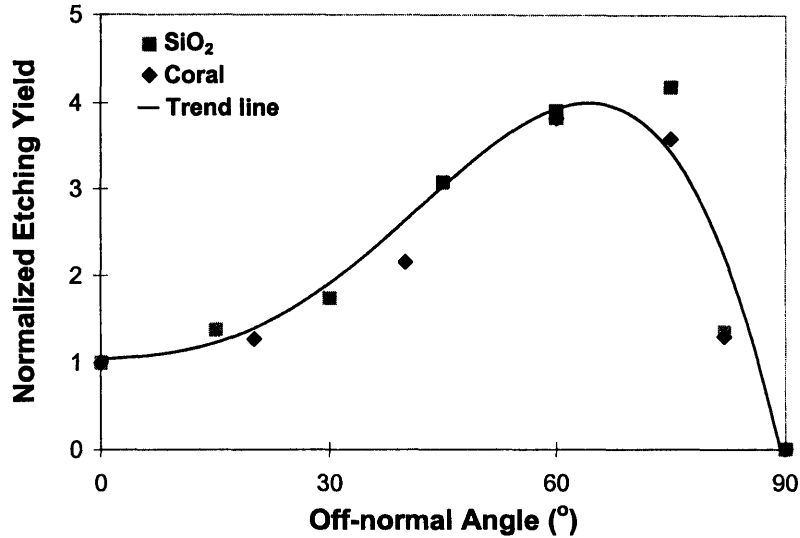

Figure 4-4 The normalized etching yield of SiO_2 and coral in Ar plasma as a function of off-normal angle. The curve followed the typical sputtering yield curve, with a maximum around 60-70° off-normal angle.

4.3 Spatial Frequency of Roughening

It is extremely promising that I can investigate real sidewall roughening based upon the etching of blank films at grazing angles in current plasma beam chamber since the characterization of roughening on real sidewall using AFM is complicated. One of the biggest concerns, however, is that if the beam measurements of roughening on blank films are of the same dimension as is encountered on real sidewalls. The spatial frequency of sidewall roughening was measured by cleaving patterned samples and using AFM analysis[2]. Specifically, the roughening in general decreases in amplitude with depth and is correlated as it emanates from the mask. In Figure 4-5(b), the dashed line demonstrates the cross section analysis of the oxide surface, 150 nm from ARC/oxide interface (Line c in Figure 4 of Ref. 2). In particular, the spatial frequency of the striation structure is about tens of nanometers.

(a)

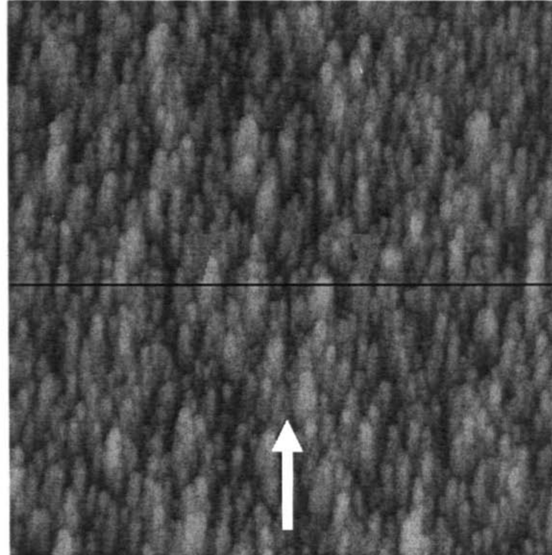

(b)

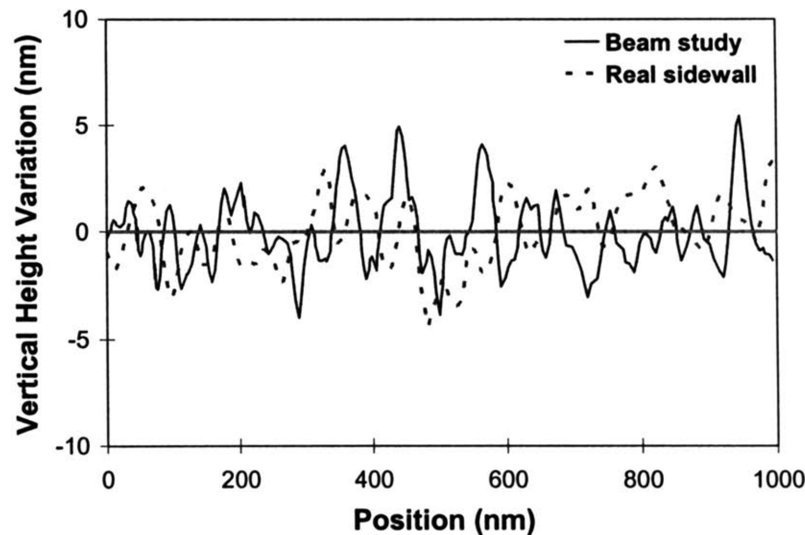

Figure 4-5 (a) The AFM image of SiO_2 after sputtering in Ar plasma at off-normal angle 75° at ion energy level 310 eV (total ion fluence is 3.5×10^{17} ions/cm^2). The arrow shows the ion beam impingement direction. (b) The corresponding cross section analysis of the surface in (a), shown as solid line; the dashed line is the cross section analysis of SiO_2 layer on the sidewall after plasma patterning (data collected from Ref. 2). Note that the spatial frequencies are comparable demonstrating that the beam measurements of roughening are of the same dimension as is encountered on sidewalls.

Figure 4-5 (a) gives one example of the surface topography of initially planar SiO_2 film after etching in Ar plasma at 75° off-normal angle using 310 eV ion energies, and the corresponding cross section analysis of this etched surface is shown as the solid line in Figure 4-5 (b). It is straightforward to conclude that the spatial frequencies of the roughness captured by my plasma beam study and by real sidewall roughening

characterization are comparable to each other, and both have a characteristic length around tens of nanometers. Therefore, my plasma beam chamber is capable to replicate the roughness on real sidewall during plasma patterning by etching planar films at grazing angles using plasma beams.

4.4 Ar Sputtering Caused Roughening

The low-k dielectric coral film prepared by plasma enhanced chemical vapor deposition method (PECVD) is supplied by Novellus. Specifically, the dielectric constant k of this coral film is around 2.85. The un-etched films were characterized using AFM and the images are shown in Figure 4-6. The vertical scales of all films are 10 nm. The RMS roughness level is about 0.2 nm for single crystal silicon and thermal SiO_2, while 0.9 nm for coral film. In addition, the surfaces of all pre-etched films are isotropic without any specific orientation.

Figure 4-7 shows the AFM images after sputtering in Ar plasma at normal angle using 310 eV ions. Compared to the surface before etching, the RMS roughness level of single crystal silicon and SiO_2 remains almost the same after sputtering. Coral, on the other hand, becomes smoother after sputtering and the RMS roughness is 0.5 nm. These different roughness evolution trends are believed to be due to different initial surface roughness, which will be discussed further later on. Additionally, all of the surfaces remain isotropic after sputtering at normal angle.

(a)

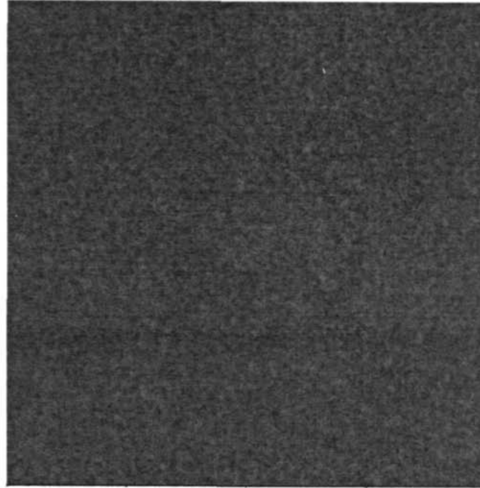

(b)

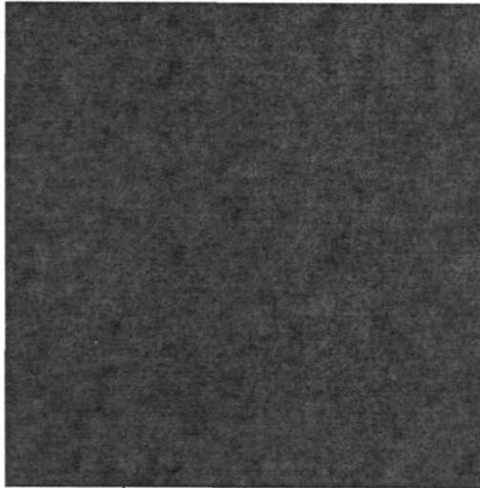

(c)

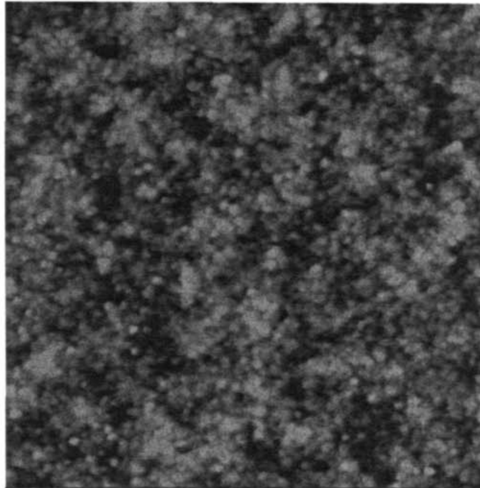

Figure 4-6 The AFM images of unetched (a) single crystal silicon, (b) SiO_2 and (b) low-k dielectric coral films. The vertical scale of all films is 10 nm and all of the images represent 1 μm×1 μm of the real sample surface. The RMS roughness of single crystal silicon, SiO_2 and coral films are 0.2 nm, 0.2 nm and 1.0 nm, respectively.

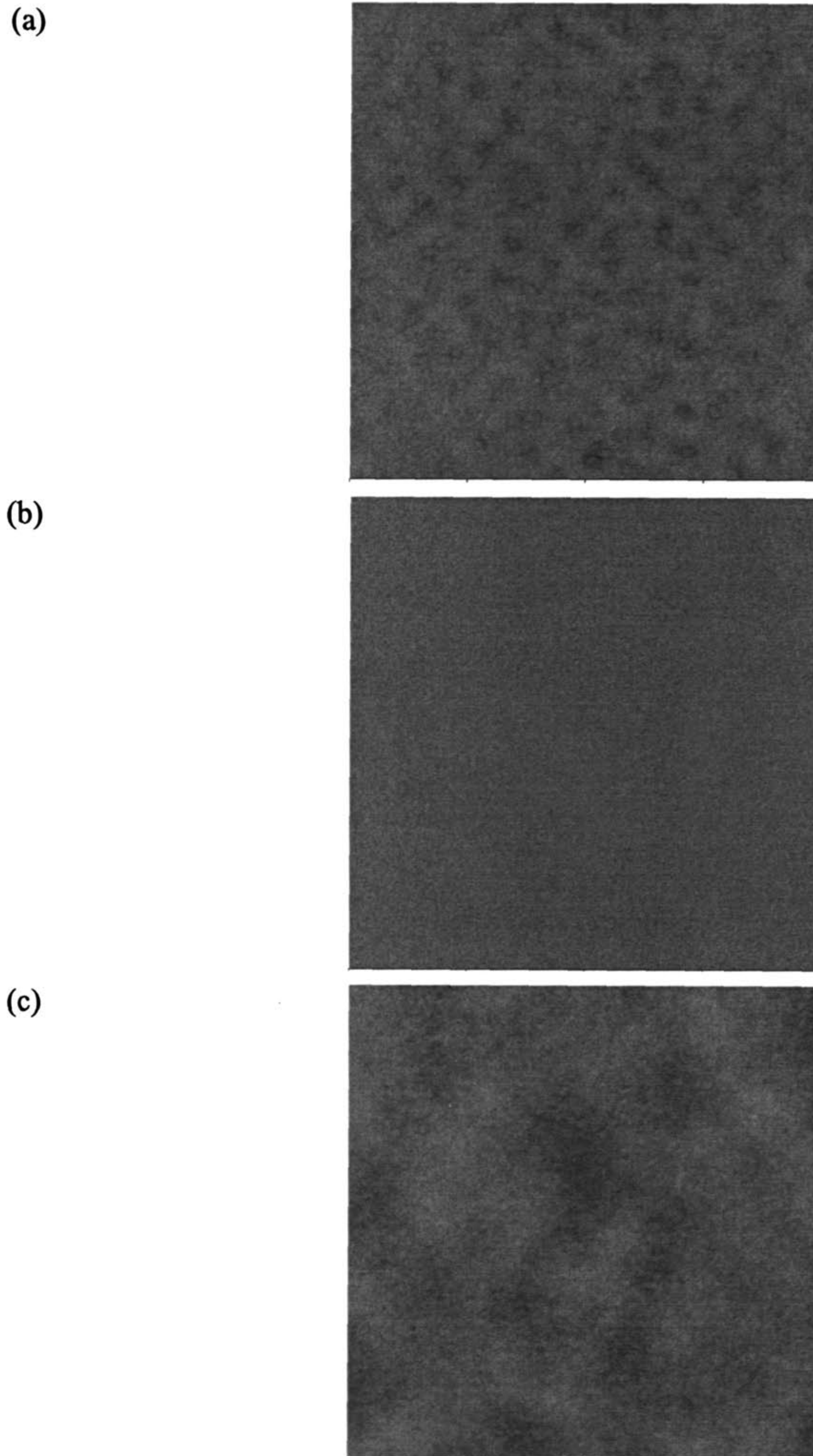

Figure 4-7 The surface topography of (a) single crystal silicon, (b) SiO_2 and (c) coral after sputtering in Ar plasma at normal angle using 310 eV ions. The vertical scale is 15 nm for all AFM images. (a) The dosage is 2×10^{18} ions/cm^2 and the RMS roughness is 0.3 nm after 160 nm film etched; (b) the dosage is 1.5×10^{18} ions/cm^2 and the RMS roughness is 0.1 nm after 115nm film etched; (c) the dosage is 1.5×10^{18} ions/cm^2 and the RMS roughness is 0.5 nm after 288 nm film etched.

The AFM images of these three film after sputtering in Ar plasma at 60° off-normal angle using 310 eV ions are shown Figure 4-8. Obviously, the roughness evolution of each film is totally different from what it is at normal ion incidence angle. Most importantly, all of these three films get roughened and form striation structure at 60° off-normal angle. Specifically, the silicon and oxide samples show spatial waves transverse to the beam while coral forms waves that are parallel with the beam.

Similarly, all of these films are also roughened and form striation structure on the surface after sputtering in Ar plasma at 75° off-normal angle using 310 eV ions, which can be seen from Figure 4-9. One significant difference, however, is the direction of the striation structure for a given beam impingement direction. Specifically, all surfaces form spatial waves that are aligned with the ion beam at 75° while the striation can be parallel or transverse to the beam at 60°.

Another Intriguing thing is that coral shows higher roughening potential compared to SiO_2 for a given ion fluence reaching the surface at both 60° and 75° off-normal angles. This can be observed by comparing (b) and (c) in Figure 4-8 or Figure 4-9. For instance, after both receiving 3.5×10^{17} ions/cm^2 at 75° off-normal angle, the RMS roughness level for SiO_2 and coral is 1.5 nm and 8.6 nm, respectively. One part of the reason why coral has higher roughening propensity is due to the faster etching rate of coral than SiO_2. Unfortunately, it is very straightforward to see from Figure 4-10 that the etching rate difference solely can not fully explain the higher roughening capability of coral. For instance, for the same amount of film removed at 75° off-normal angle, coral has much higher RMS roughness level compared to SiO_2. Another reason caused this difference might be related to the inherent different film properties of different films. One possibility is that coral material has some density inhomogeneities in the film since it is prepared by PECVD method while SiO_2 film is prepared by thermal oxidation method and the density variation is trivial.

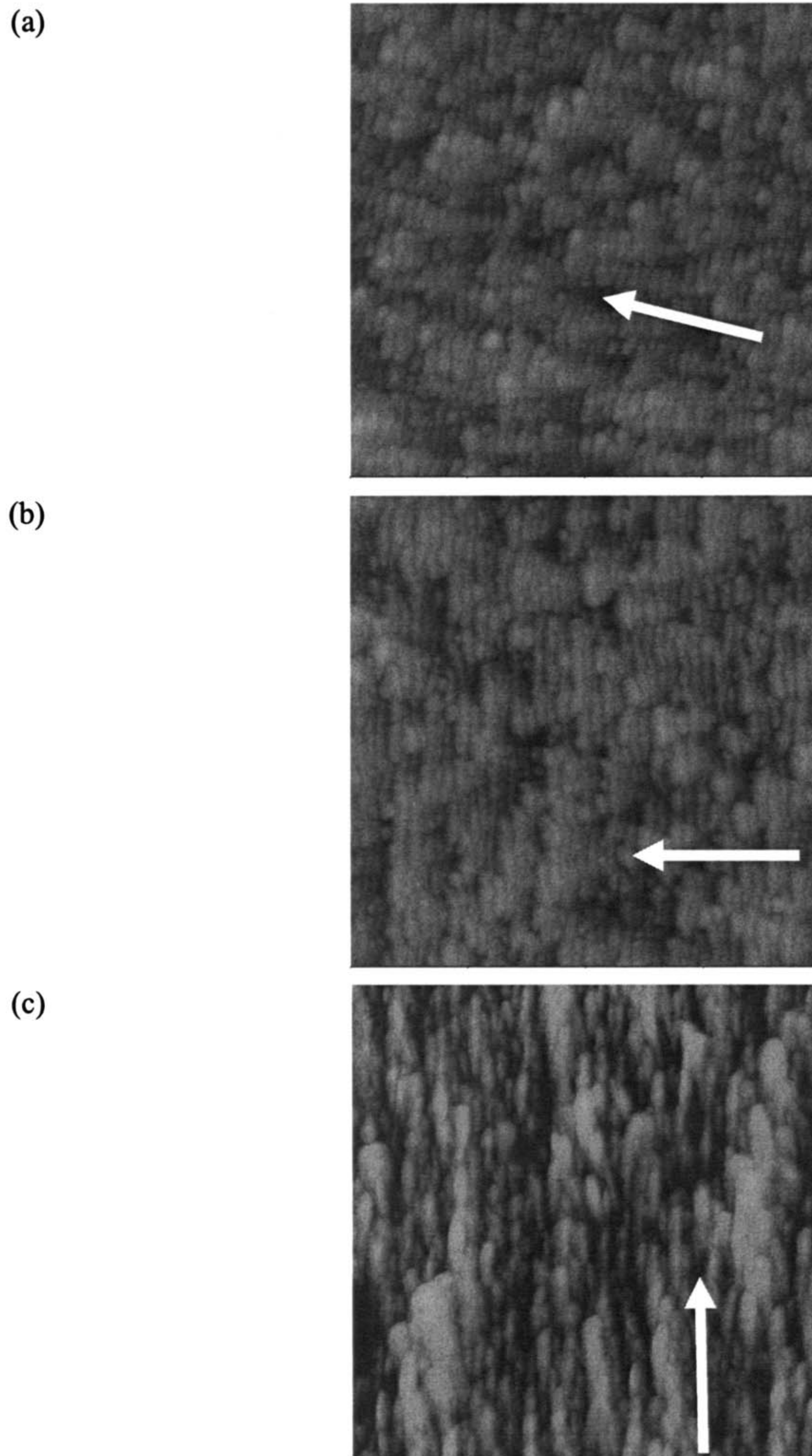

Figure 4-8 The surface topography of (a) single crystal silicon, (b) SiO_2 and (c) coral after sputtering in Ar plasma at 60° off-normal angle using 310 eV ions. The vertical scale is 30 nm for all AFM images. (a) The dosage is 6×10^{17} ions/cm^2 and the RMS roughness is 1.4 nm after 155 nm film etched; (b) the dosage is 7×10^{17} ions/cm^2 and the RMS roughness is 1.9 nm after 213 nm film etched; (c) the dosage is 7×10^{17} ions/cm^2 and the RMS roughness is 3.5 nm after 515 nm film etched.

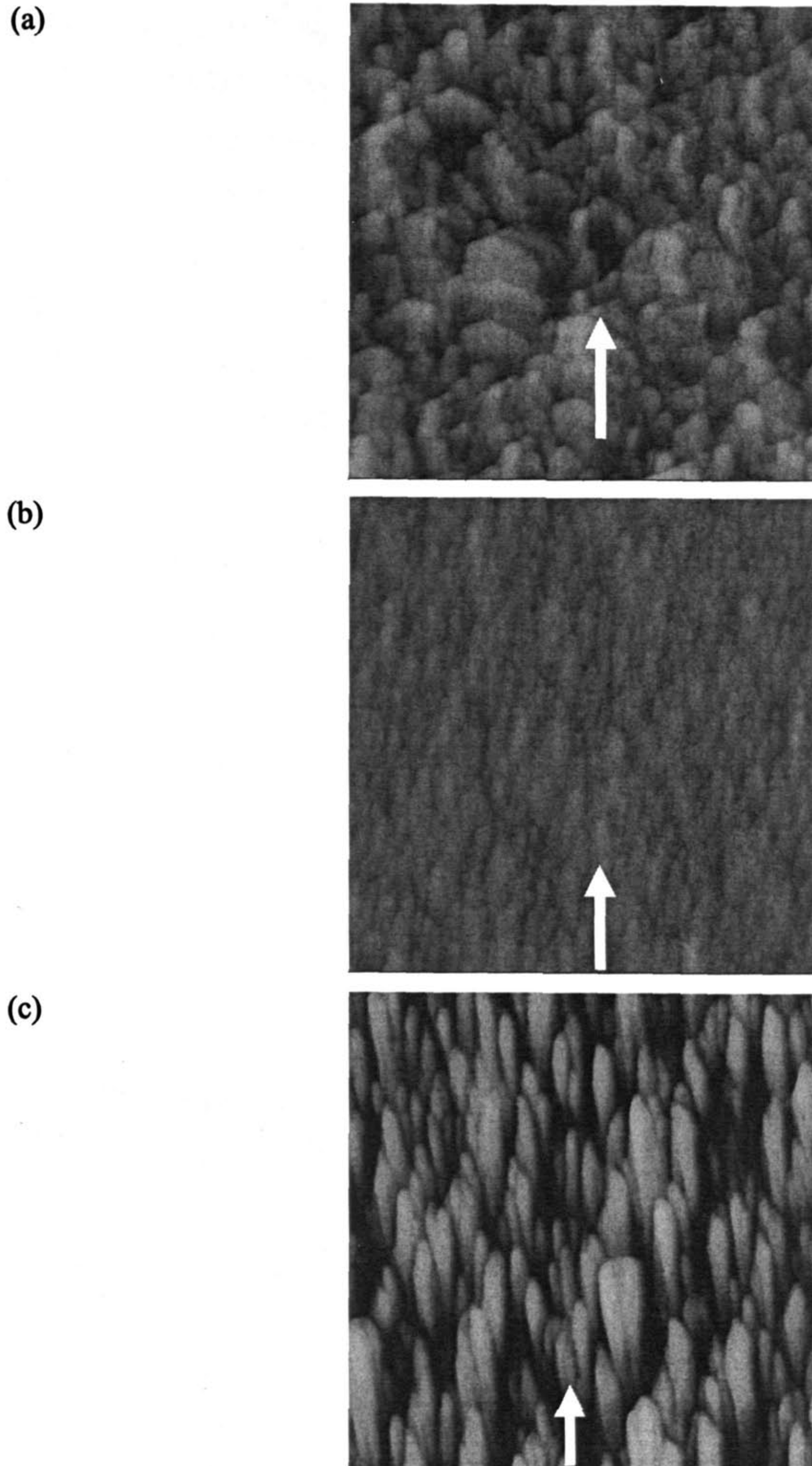

Figure 4-9 The surface topography of (a) single crystal silicon, (b) SiO_2 and (c) coral after sputtering in Ar plasma at 75° off-normal angle using 310 eV ions. The vertical scale is 50 nm for all AFM images. In all cases, the ion fluence reaching the surface is 3.5×10^{17} ions/cm^2. (a) The RMS roughness is 4.0 nm after 84 nm film etched; (b) the RMS roughness is 1.5 nm after 115 nm film etched; (c) the RMS roughness is 8.6 nm after 221 nm film etched.

The surface roughness of each film after sputtering at grazing angles (60° or 75°) increases with the amount of material etched, unlike the roughening trends at normal ion incidence angle that does not change with exposure after reaching its steady state. The results are summarized in Figure 4-10 and Figure 4-11. As shown in Figure 4-11, the roughness of single crystal and SiO_2 is almost independent of the material etched at normal angle; at grazing angles, however, the roughness increases when more material is removed. More specifically, all of these three films have higher roughening potential at 75° than at 60° off-normal angle for a given amount of material removed. In particular, the results of coral and single crystal silicon are more obvious than SiO_2.

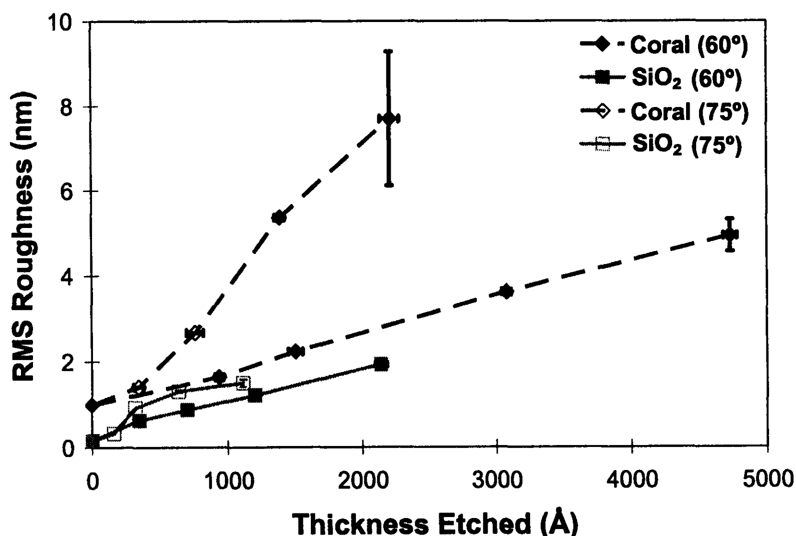

Figure 4-10 The surface roughness of (solid line) SiO_2 and (dashed line) coral after sputtering in argon plasma at various angles as a function of the thickness of material removed. SiO_2: (■) 60° and (□) 75°. Coral : (♦) 60° and (◊) 75°.

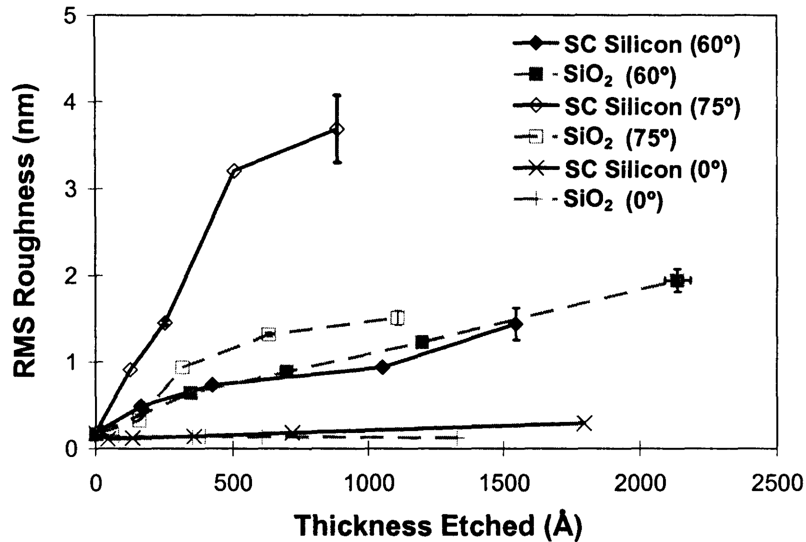

Figure 4-11 The surface roughness of (solid line) single crystal silicon and (dashed line) SiO_2 after sputtering in argon plasma at various angles as a function of the thickness of material removed. Single crystal silicon: (×) 0°; (♦) 60° and (◊) 75°. SiO_2: (+) 0°; (■) 60° and (□) 75°.

At more grazing 82° off-normal angle, single crystal silicon and SiO_2 remain smooth but coral roughens despite a much smaller amount of material being removed compared to the situation at less grazing angles such as 75°. The AFM images of these etched films are given in Figure 4-12. Moreover, for coral, the spatial frequency of the striation increases and the streak length becomes much longer compared to the previous results at 60° or 75° off-normal angles.

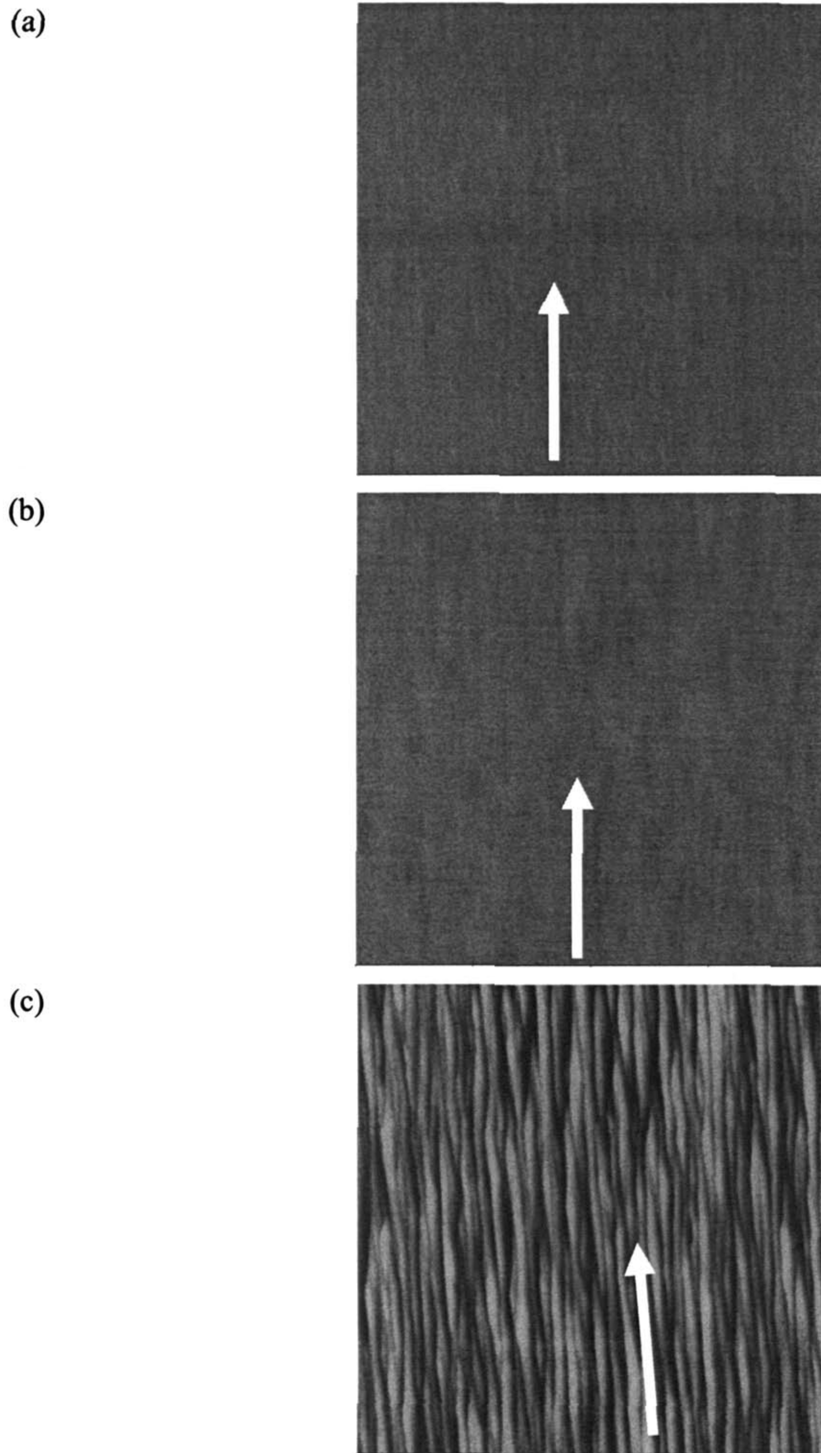

Figure 4-12 The surface topography of (a) single crystal silicon, (b) SiO_2 and (c) coral after sputtering in Ar plasma at 82° off-normal angle using 310 eV ions. The vertical scale of these AFM images is (a) 10 nm, (b) 10 nm and (c) 50 nm. In all cases, the ion fluence reaching the surface is 1.5×10^{17} ions/cm^2. (a) The RMS roughness is 0.1 nm after around 34 nm film etched; (b) the RMS roughness is 0.2 nm after 16 nm film etched; (c) the RMS roughness is 3.6 nm after 38 nm film etched.

4.5 Discussion

It is crucial to have a deep understanding of how ions impact the substrates in Ar plasma in order to understand the mechanism of roughness evolution data shown in the previous section. For a typical ion sputtering process, Graves et. al.[30,31] studied the way that the ions interact with the substrate surface based upon molecular dynamics simulation. They found that the scattering probability of normal incidence ions is very low and the fraction of reflected ion energy is small even if an ion is scattered away from the surface; on the contrary, the reflection probabilities were larger than 90% for incident angles larger than 75° from the surface normal. Additionally, I know that the etching yield peaks around 60-75° off-normal angle θ_{peak} for a typical sputtering process because the energy transfer efficiency at this range is optimal. As a result, I can assume that the ion scattering probability is almost zero when the ion incident angle is less than θ_{peak}, while the ion scattering probability becomes high if the ion incident angle is larger than θ_{peak}. This assumption is shown schematically in Figure 4-13.

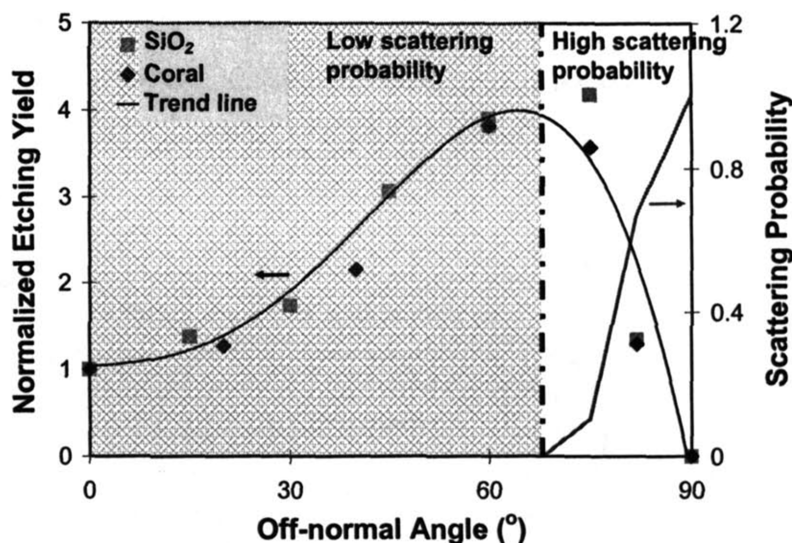

Figure 4-13 The prediction of the ion scattering probability as a function of off-normal angle based upon the measurement of the angular dependence of the etching yield. The scattering probability is relative low when the off-normal angle is smaller than the peak angle and I can assume that all of the ion energy is transferred to the substrate; while the scattering probability is high when the off-normal angle is larger than the peak angle and I can assume that all of the ion energy is scattered away.

At normal ion incidence angle, the ion scattering effects are trivial and the surface smoothing phenomena shown in Figure 4-7 (especially for coral) can be explained qualitatively by the sputtering yield curve. Figure 4-14 demonstrates two possible scenarios: initially smooth surface and surface with initial large features. For surfaces with initially large features, the surface will be smoothed out after etching because of the larger etching yield at faceting angles. Specifically, the small features, if exist, typically have facet angles around or less than 10 degrees during the sputtering process. This can be observed in the cross section analysis results given in Figure 4-5 (b). It is worth noting that the cross section analysis is not in scale and the vertical scale is much less than the horizontal scale. For films with initially smooth features, on the other hand, the surface will be roughened to low level because of the stochastic roughening due to the uniformity of the plasma beam at atomistic-scale.

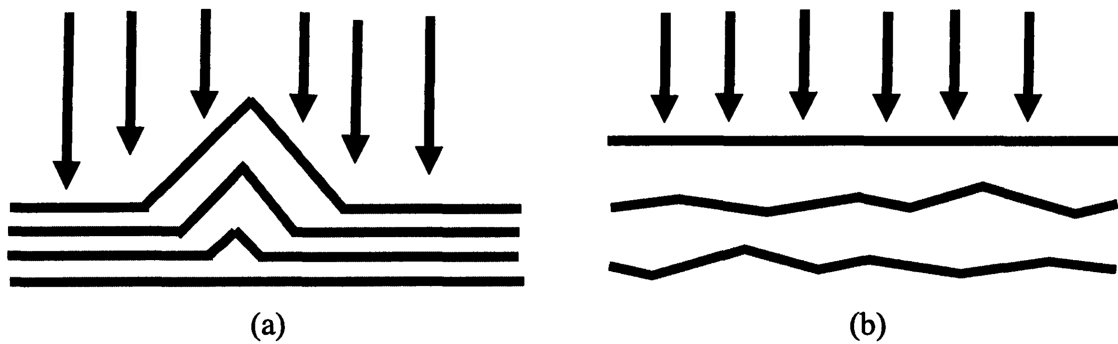

Figure 4-14 The prediction of surface roughness evolution during sputtering in Ar plasma at normal incidence angle. The arrows represent the ions bombarding the surface. (a) With initially large features, the surface will be smoothed out after etching because of the larger etching yield at faceting angles; (b) with initially smooth features, the surface will be roughened to low level because of the stochastic roughening due to the uniformity of the plasma beam at micro-scale.

At normal ion incidence angle, the surface roughness evolution of polysilicon film prepared by low pressure chemical vapor deposition method (LPCVD), further confirms my previous analysis. The surfaces before and after sputtering as well as the corresponding cross section analyses are shown in Figure 4-15. In particular, the RMS roughness level of this unetched polysilicon film is about 3.6 nm, which is much higher than unetched single crystal silicon (0.2 nm). Due to relatively higher etching yield at facet angles, the surface after sputtering becomes much smoother and the RMS roughness

level is 1.3 nm after receiving 1.25×10^{18} ions/cm^2. Consistently, according to the cross section analyses, those features on the unetched surface (shown as the solid line) are removed after sputtering (shown as dashed line).

In previous studies[11-19], it has been observed that off-normal incidence ion bombardment, typically ion energies at keV range, often roughens the surface and produces striation parallel or transverse to the beam direction. In particular, Bradley and Harper[11] developed a theoretical model where they believe that the striation formation is caused by a surface instability caused by the competition between roughening (curvature dependent sputtering) and smoothing (surface diffusion) processes. Moreover, the resulting striation direction depends on the incidence angle of ions. Specifically, the striation structure is perpendicular to the component of the ion beam in the surface plane when incidence angles are less than a critical off-normal angle θ_c (Figure 4-16(a)), while the striation is parallel to the beam direction for incidence angles close to grazing.

As has been addressed by Bradley and Harper, however, the model they proposed did not account for the ion scattering effects. Consequently, the theory is not valid for ion incidence angles larger than θ_{peak} where the sputtering yield peaks due to the significant ion scattering effects. Additionally, the predictions of Bradley and Harper model concerning the changes in the striation orientation apply only to materials in which the critical angle θ_c is less than θ_{peak}.

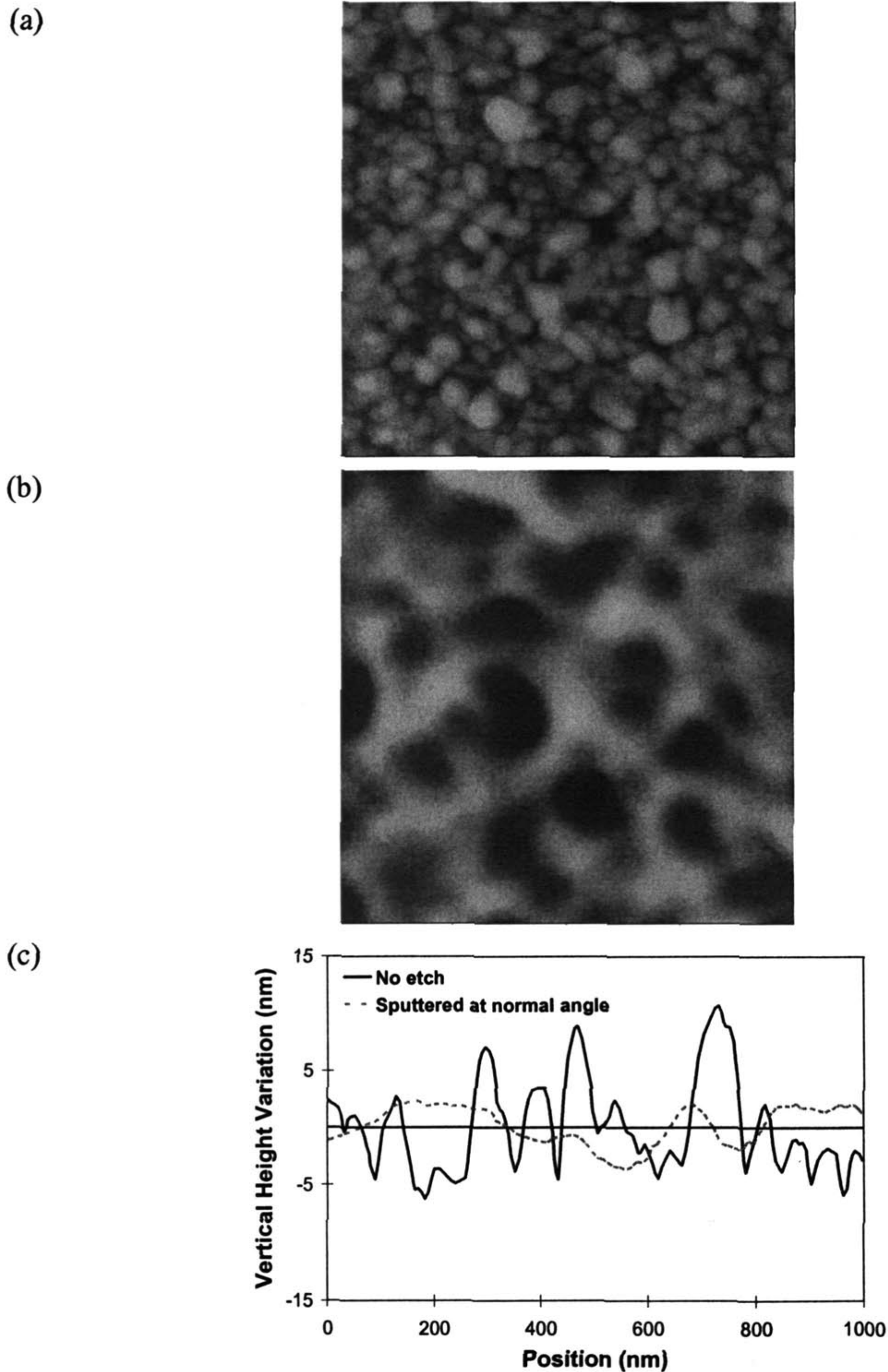

Figure 4-15 With initially large features, the surface will be smoothed out after Ar sputtering at normal ion incidence angle. (a) Unetched polysilicon surface with a RMS roughness level of 3.6 nm and the vertical scale of the image is 40 nm. (b) Etched polysilicon surface after Ar sputtering at normal angle using 310 eV ions and the ion fluence received is 1.25×10^{18} ions/cm^2; the RMS roughness level is 1.3 nm and the vertical of the image is 10 nm. (c) The cross section analysis of the (solid line) unetched and the (dashed line) etched surfaces.

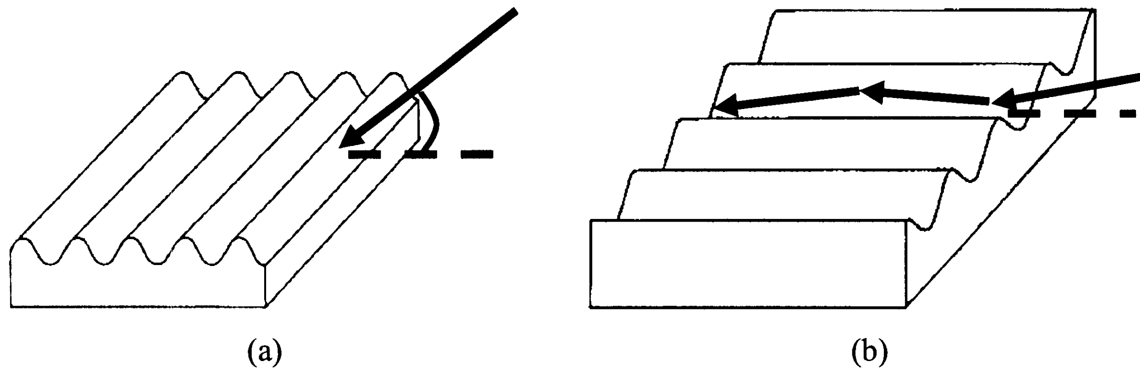

Figure 4-16 Dependence of the direction of the striation strurture on the beam incidence direction (adopted from Ref. 11). (a) When the off-normal angle is smaller than a threshold value, the striation formed is transverse to the beam direction. (b) At very high grazing angles, the striation is parallel to the beam direction because that the ion scattering effects are dominant and therefore the ion scattering caused channeling effect is important.

Bradley and Harper model can be used to partially explain the roughness evolution at 60° off-normal angle. As mentioned previously in Figure 4-8, the striation is transverse to the ion beam direction for single crystal silicon and SiO_2, while parallel to the ion beam for coral. In addition, the maximal sputtering yield happens around 60-70° off-normal angle for all of the films. Therefore, the ion sputtering effects are not very significant at 60° off-normal angle and Bradley and Harper model is suitable to explain the striation formation. The difference of surface striation direction between coral and SiO_2/single crystal silicon is not clear, but it might be caused by the corresponding different film properties.

At more grazing angles, however, Bradley and Harper model is not applicable any more. I believe that the striation structure is mainly caused by the ion scattering effects. With these grazing angles (75° and 82°), scattering of ions are dominant. In particular, the scattered ions might be bounced around the surface along the beam direction and cause ion channeling effects, which is shown schematically in Figure 4-16(b). Consequently, striation structure parallel to the beam impingement direction forms due to this ion channeling effects. Additionally, the ion scattering effects is more significant at 82° than at 75° off-normal angle. As an impact, the striation length is more elongated and the spatial frequency of the waves increases at more grazing angles, which has already been shown in Figure 4-12(c).

One last thing I have to admit is that I still don't fully understand why coral and SiO_2 display very different roughness evolution trends in many cases shown previously although they demonstrate similar etching kinetics. Intriguingly, coral often has more roughening capability at grazing angles. For instance, SiO_2 remain smooth while coral roughens after sputtering at 82° off-normal angle. One possibility might be due to the inherent film properties difference between coral and SiO_2. Specifically, coral is prepared using PECVD method and there are some doped methyl- or ethyl- groups in the substrate. These doped groups introduce inherent inhomogeneity to coral film, therefore, the roughening trend of coral film might be different compared to thermal SiO2/singal crystal silicon.

4.6 Conclusions

I have successfully demonstrated that the inductively plasma beam chamber can be used to quantify surface roughening of different films. Specifically, the beam measurements of roughening are of the same dimension as is encountered on sidewalls. Moreover, the sputtering caused surface roughening can be explained by the angular dependence of the etching yield curve. At normal ion incidence angles, surfaces with initial large features are smoothed out due to the relative higher etching yield at facet angles, while initially smooth surface will be roughened to a low level due to stochastic roughening. At intermediate off-normal angles (60° in this paper), the roughness evolution can be partially explained by Bradley and Harper model where the roughening and striation formation are caused by the surface instability due to the competition between curvature dependent sputtering caused roughening and surface diffusion caused smoothing. At high grazing angles (75° and 82° in this paper), the striation development on the etched surface is mainly due to the ion scattering caused ion channeling effects. Additionally, coral often displays higher roughening potential in many cases compared to SiO_2 but the mechanism has not been fully understood yet.

4.7 References

1 C. H. Diaz, H. J. Tao, Y. C. Ku, A. Yen, and K. Young, Ieee Electron Device Letters 22, 287-289 (2001).

[2] D. L. Goldfarb, A. P. Mahorowala, G. M. Gallatin, K. E. Petrillo, K. Temple, M. Angelopoulos, S. Rasgon, H. H. Sawin, S. D. Allen, M. C. Lawson, and R. W. Kwong, Journal of Vacuum Science & Technology B 22, 647-653 (2004).

[3] S. A. Rasgon, Ph.D. Thesis, Massachusetts Institute of Technology, 2005.

[4] P. Lazzeri, X. Hua, G. S. Oehrlein, M. Barozzi, E. Iacob, and M. Anderle, Journal of Vacuum Science & Technology B 23, 1491-1498 (2005).

[5] Y. P. Yin, S. Rasgon, and H. H. Sawin, Journal of Vacuum Science & Technology B 24, 2360-2371 (2006).

[6] A. Sankaran and M. J. Kushner, Journal of Vacuum Science & Technology A 22, 1242-1259 (2004).

[7] A. Sankaran and M. J. Kushner, Journal of Vacuum Science & Technology A 22, 1260-1274 (2004).

[8] A. Sankaran and M. J. Kushner, Applied Physics Letters 82, 1824-1826 (2003).

[9] Y. Osano and K. Ono, Japanese Journal of Applied Physics Part 1-Regular Papers Brief Communications & Review Papers 44, 8650-8660 (2005).

[10] H. Kawai, Bai, O, Sawin, H. H. , (unpublished).

[11] R. M. Bradley and J. M. E. Harper, Journal of Vacuum Science & Technology a-Vacuum Surfaces and Films 6, 2390-2395 (1988).

[12] T. M. Mayer, E. Chason, and A. J. Howard, Journal of Applied Physics 76, 1633-1643 (1994).

[13] D. W. Moon and K. J. Kim, Journal of Vacuum Science & Technology A 14, 2744-2756 (1996).

[14] J. Erlebacher, M. J. Aziz, E. Chason, M. B. Sinclair, and J. A. Floro, Journal of Vacuum Science & Technology A 18, 115-120 (2000).

[15] J. Erlebacher, M. J. Aziz, E. Chason, M. B. Sinclair, and J. A. Floro, Physical Review Letters 82, 2330-2333 (1999).

[16] R. Gago, L. Vazquez, R. Cuerno, M. Varela, C. Ballesteros, and J. M. Albella, Applied Physics Letters 78, 3316-3318 (2001).

[17] D. Flamm, F. Frost, and D. Hirsch, Applied Surface Science 179, 95-101 (2001).

[18] F. Ludwig, C. R. Eddy, O. Malis, and R. L. Headrick, Applied Physics Letters 81, 2770-2772 (2002).

[19] T. K. Chini, F. Okuyama, M. Tanemura, and K. Nordlund, Physical Review B 67 (2003).

[20] F. Frost, B. Ziberi, T. Hoche, and B. Rauschenbach, Nuclear Instruments & Methods in Physics Research Section B-Beam Interactions with Materials and Atoms 216, 9-19 (2004).

[21] S. Tachi and S. Okudaira, Journal of Vacuum Science & Technology B 4, 459-467 (1986).

[22] C. Steinbruchel, Applied Physics Letters 55, 1960-1962 (1989).

[23] J. P. Chang, J. C. Arnold, G. C. H. Zau, H. S. Shin, and H. H. Sawin, Journal of Vacuum Science & Technology a-Vacuum Surfaces and Films 15, 1853-1863 (1997).

[24] S. A. Vitale, H. Chae, and H. H. Sawin, Journal of Vacuum Science & Technology a-an International Journal Devoted to Vacuum Surfaces and Films 19, 2197-2206 (2001).

[25] G. V. Jorgenson, Wehner, G. K. , Journal of Applied Physics 36, 2672-2674 (1965).

[26] J. M. E. Harper, J. J. Cuomo, P. A. Leary, G. M. Summa, H. R. Kaufman, and F. J. Bresnock, Journal of the Electrochemical Society 128, 1077-1083 (1981).

[27] D. J. Oostra, R. P. Vaningen, A. Haring, A. E. Devries, and G. N. A. Vanveen, Applied Physics Letters 50, 1506-1508 (1987).

[28] J. P. Chang and H. H. Sawin, Journal of Vacuum Science & Technology B 19, 1319-1327 (2001).

[29] J. M. Lane, F. P. Klemens, K. H. A. Bogart, M. V. Malyshev, and J. T. C. Lee, Journal of Vacuum Science & Technology a-Vacuum Surfaces and Films 18, 188-196 (2000).

[30] C. F. Abrams and D. B. Graves, Journal of Vacuum Science & Technology A 16, 3006-3019 (1998).

[31] B. A. Helmer and D. B. Graves, Journal of Vacuum Science & Technology a-Vacuum Surfaces and Films 16, 3502-3514 (1998).

Chapter 5. The Impact of Etching Kinetics on the Roughening of Thermal SiO_2 and Low-k Dielectric Coral Films in Fluorocarbon Plasmas

The impact of etching kinetics and etching chemistries on surface roughening was investigated by etching thermal silicon dioxide and low-k dielectric coral materials in C_4F_8/Ar plasma beams in an inductive coupled plasma beam reactor. The etching kinetics, especially the angular etching yield curves, was measured by changing the plasma pressure and the feed gas composition which influence the effective neutral-to-ion flux ratio during etching. At low neutral-to-ion flux ratios, the angular etching yield curves are sputtering like, with a peak around 60-70° off-normal angles; the surface at grazing ion incidence angles becomes roughened due to ion scattering related ion channeling effects. At high neutral-to-ion flux ratios, ion enhanced etching dominates and surface roughening at grazing angles is mainly caused by the local fluorocarbon deposition induced micro-masking mechanism. Interestingly, the etched surfaces at grazing angles remain smooth for both films at intermediate neutral-to-ion flux ratio regime. Furthermore, the oxygen addition broadens the region over which the etching without roughening can be performed.

5.1 Introduction

As the feature sizes have been continuously scaling down in order to maximize the transistor density, the interconnect signal delay becomes increasingly important. With copper as a common metallization material, lowering signal delay by replacing SiO_2 with low-k dielectrics is a very promising choice[1-3]. However, the application of these materials is often hampered by the lack of process compatibility with damascene process as scaling feature sizes continues[4]. One of the major difficulties is related to the sidewall roughening produced in plasma etching process during the formation of vias and trenches for the fabrication of multilevel interconnects[5,6].

The etching kinetics of SiO_2 and SiO_2-like low dielectric materials in fluorocarbon plasmas has been investigated extensively partially because of their ability to etch certain films selectively with respect to other films[7-12]. From roughening perspective, however,

many fewer experimental observations have been reported and the mechanism causing surface roughening during plasma etching process is still vague.

As shown in the literature[6,13,14], top line-edge roughness (LER) played a very important role for the sidewall roughening of feature patterning in various etching chemistries. The top LER is defined as the roughness on the photoresist sidewall, and it is primarily formed during the development process of photoresist layer. In particular, Goldfarb et al.[6] found that the resist sidewall roughness after development but before plasma etching was isotropic; during the anti-reflective coating (ARC) layer opening in plasma etching process, the photoresist layer became striated and the top edge of the photoresist layer was faceted; the striation structure became much more significant and propagated down after etching of the subsequent SiO_2 layer.

The surface roughening of low-k films may occur during etching in fluorocarbon plasmas in addition to the top LER effects on sidewall roughness evolution mentioned above. Consequently, it is crucial to fully understand the mechanisms of the inherent surface roughening before I can optimize the plasma etching conditions to minimize the surface roughness level after etching. The following questions should be answered before I can propose a plausible mechanism for surface roughening during plasma etching process. Is the roughening related to the etching chemistry and etching kinetics? Do film properties influence the roughness evolution?

In Chapter 4, the surface roughening of various films in Ar plasma has been studied in detail. The sputtering caused surface roughening can be partially explained by the angular dependence of the etching yield curve. At normal ion incidence angles, surfaces with initial large features are smoothed out due to the relative higher etching yield at large off-normal surface facet angles. At intermediate off-normal angles, the roughness evolution can be partially explained by Bradley and Harper model where the roughening and striation formation are caused by the surface instability due to the competition between curvature dependent sputtering caused roughening and surface diffusion caused smoothing. At high grazing angles (75° and 82° in this paper), the striation development on the etched surface is mainly due to the ion-scattering caused channeling effects.

In this Chapter, the impact of etching chemistry and etching kinetics, especially the angular etching yield dependence, on surface roughening of thermal SiO_2 and low-k dielectric coral materials have been investigated in C_4F_8/Ar plasmas. I found that the surface roughness evolution of these films is influenced by the etching conditions such as the etching chemistry and etching kinetics. It is shown in this paper that the major cause of surface roughening at grazing impingement angles associated with LER is the angular dependence of the etching yield. At low neutral-to-ion flux ratios, the etching yield curve becomes physical with a peak in yield at about 65 degree. Under these conditions the surface is roughened because of the sputtering like kinetics of the oxide etching. At high neutral-to-ion ratios, the greater polymerization potential (even without the formation of fluorocarbon deposition) can lead to roughening of the surface as well. Surfaces can be etched without roughening at intermediate ratios and/or with the addition of oxygen to the discharge. More interestingly, the oxygen addition broadens the region over which etching without roughening can be performed.

5.2 Characterization of Unetched Films

The RMS surface roughness level of un-etched thermal silicon dioxide and low-k dielectric coral materials are 0.2 nm and 1.0 nm, respectively. The XPS carbon (C1s) analysis suggests that there is no carbon on thermal SiO_2 surface; while the carbon (C1s) peaks in coral material indicate that carbon exists as C-H and C-Si. The results discussed above are summarized in Figure 5-1.

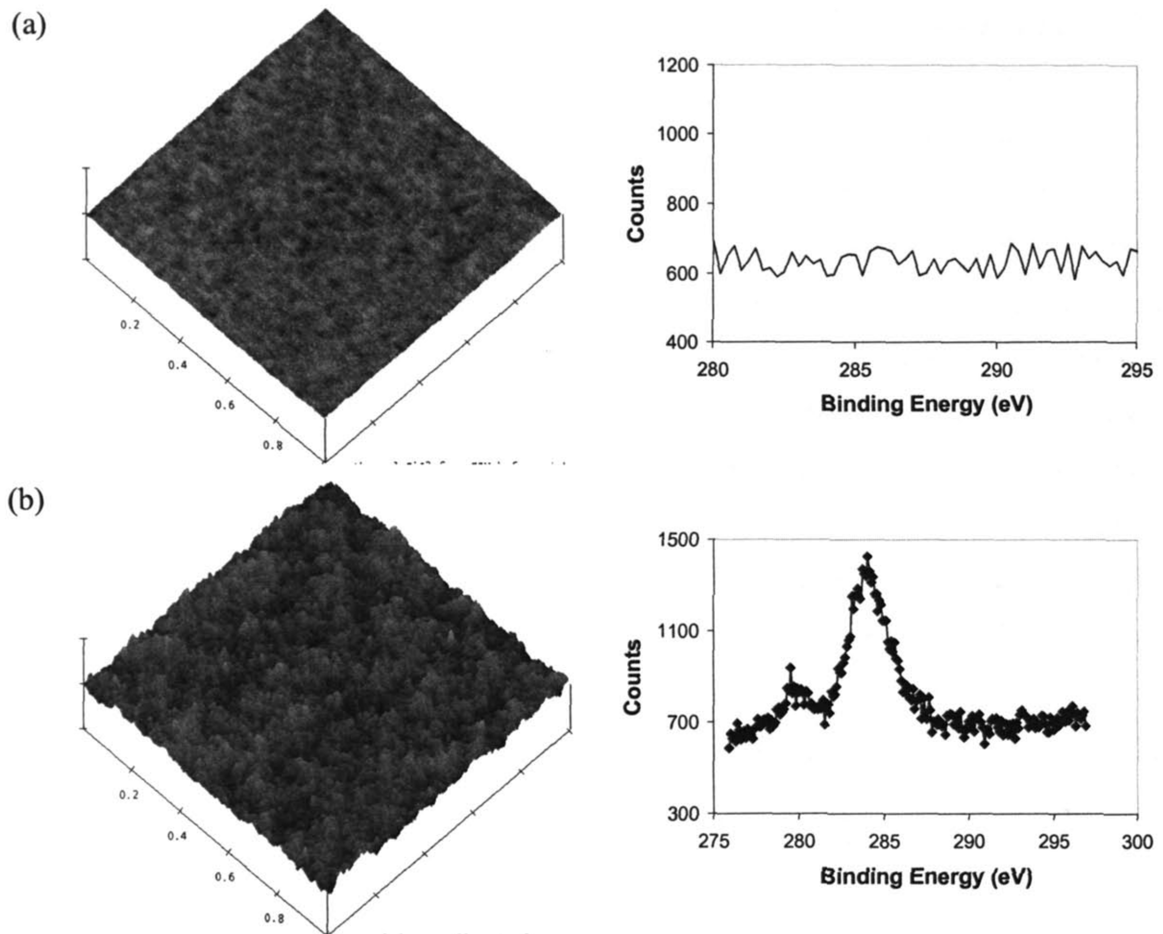

Figure 5-1 The AFM images and the corresponding surface carbon (C1s) XPS spectrums of (a) thermal SiO_2 and (b) low-k dielectric coral films before plasma etching. The vertical scale of both films is 15 nm and both of the images represent 1 μm × 1 μm of the real sample surface. The RMS roughness of SiO_2 and coral is 0.2 and 1.0 nm, respectively.

5.3 Roughening at Grazing Ion Bombardment at Different Etching Regimes

As mentioned earlier, the etching kinetics, especially the angular etching yields, have significant impact on the roughening of thermal SiO_2 and coral films at grazing angles in C_4F_8/Ar plasmas. Figure 5-2 and Figure 5-3 show the variation of the surface roughness of SiO_2 and coral films with the plasma pressure and the C_4F_8/Ar volumetric ratios. In particular, from left-hand side to right-hand side, the neutral-to-ion flux ratio increases gradually with increasing plasma pressure and C_4F_8/Ar ratio. As can be seen from both films, the surfaces are roughened at low neutral-to-ion flux ratios (left-hand side), then become smooth at intermediate neutral-to-ion flux ratios, and are roughened again at high neutral-to-ion flux ratios (right-hand side). The corresponding surface carbon

(C1s) XPS spectra under different etching conditions are also shown in Figure 5-2 and Figure 5-3. As reported previously in the literature[12,15-20], a thin layer of fluorocarbon layer, which is not necessarily continuous, was often formed during the etching of dielectric materials in fluorocarbon chemistries. I believe that the Carbon (C1s) XPS signal is a reflection of the content of fluorocarbon deposition on the substrate surface. As demonstrated in both figures, the Carbon (C1s) XPS signal becomes stronger with the increase of the neutral-to-ion flux ratios (from left-hand side to right-hand side). This means that the local fluorocarbon deposition becomes more significant as the neutral-to-ion flux ratio increases. In addition, the carbon (C1s) peak around 280 eV for coral film corresponds to C-H signal, which also roughly becomes weaker when the neutral-to-ion flux ratio increases because the fluorocarbon content on the surface becomes stronger and C-H signal is attenuated.

The roughening of these two films at low neutral-to-ion flux ratios (Figure 5-2(a) and Figure 5-3(a)) is mainly due to ion-sputtering caused ion scattering effects[21,22] rather than the local polymer deposition effects[23]. The carbon (C1s) XPS spectrums at this low neutral-to-ion regime indicate that the carbon on the surface mainly exists in the form of C-Si, and no obvious CFx ($x = 1, 2, 3$) related signal was detected. This suggests that local polymer deposition related effects are not important in terms of the surface roughness evolution. In contrast, as discussed earlier, the angular etching yield curves are sputtering-like in this low neutral-to-ion ratio regime. Therefore, the ion-scattering caused ion-channeling effects along the ion bombardment direction become important. As a result, the surface becomes roughened and sometimes striations parallel to the beam impingement direction are formed, which can be clearly seen in Figure 5-3 (a).

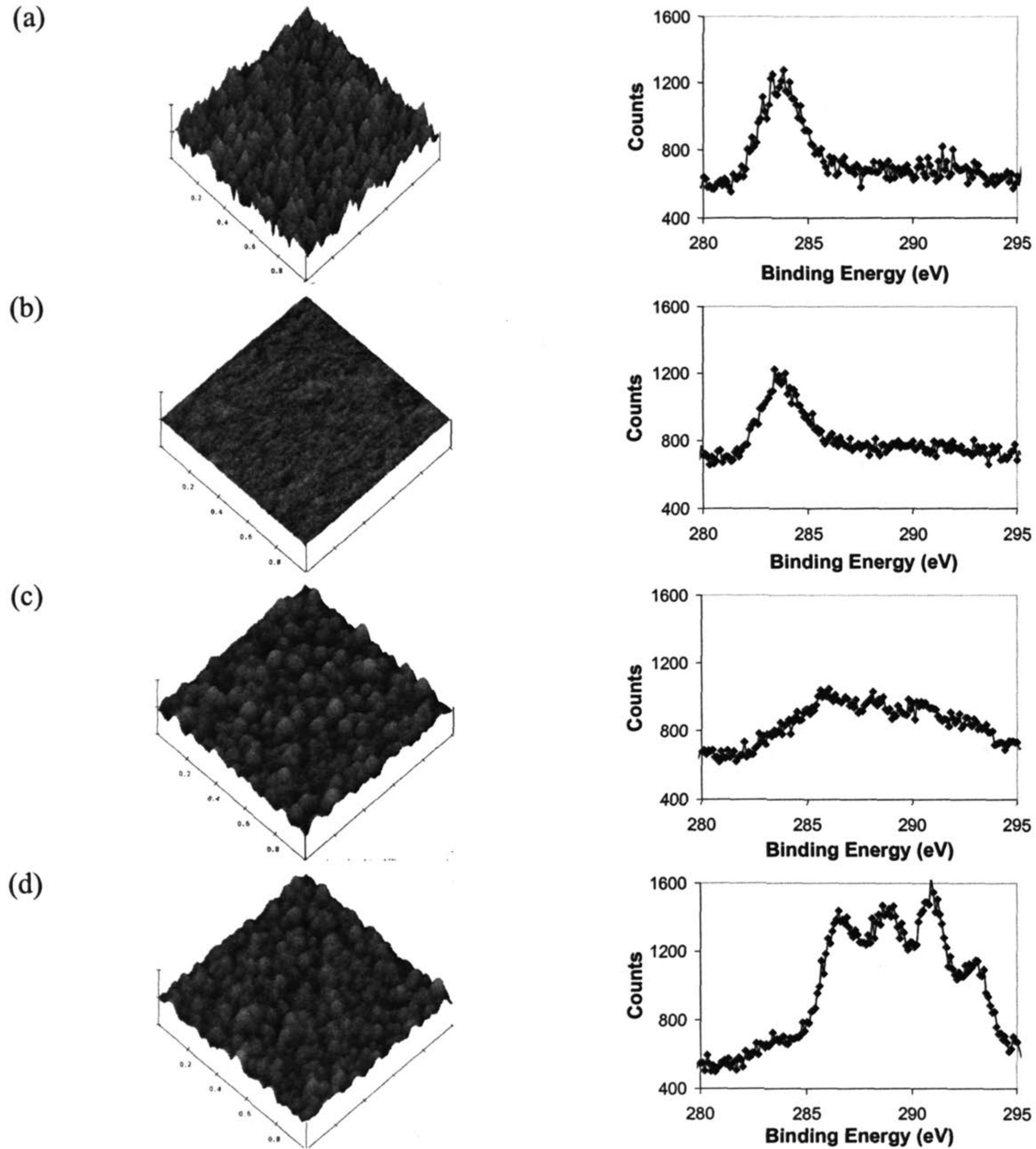

Figure 5-2 Surface AFM images and the corresponding surface carbon (C1s) XPS spectrums of thermal SiO_2 after etching in C_4F_8/Ar plasmas under various plasma source pressures and C_4F_8/Ar volumetric ratios. The vertical scale of all films is 15 nm and all of the images represent 1 μm × 1 μm of the real sample surface. The C_4F_8 percentage, beam source pressure level, and the ion fluence reach the surface are (a) 10%, 4 mtorr, and 3.0×10^{17} ions/cm^2; (b) 10%, 10 mtorr, and 1.5×10^{17} ions/cm^2; (c) 15%, 13 mtorr, and 2.0×10^{17} ions/cm^2; (d) 15%, 20 mtorr, and 1.3×10^{17} ions/cm^2, respectively. In all cases, the ions bombard the surface at 75° off-normal angle and the DC bias level is 350 V, and the ions reach the surface from the up-right direction. The RMS roughness and the film thickness etched are (a) RMS 2.5 nm and 82 nm etched; (b) RMS 0.15 nm and 58 nm etched; (c) RMS 1.5 nm and 61 nm etched; (d) RMS 1.4 nm and 31 nm etched, respectively.

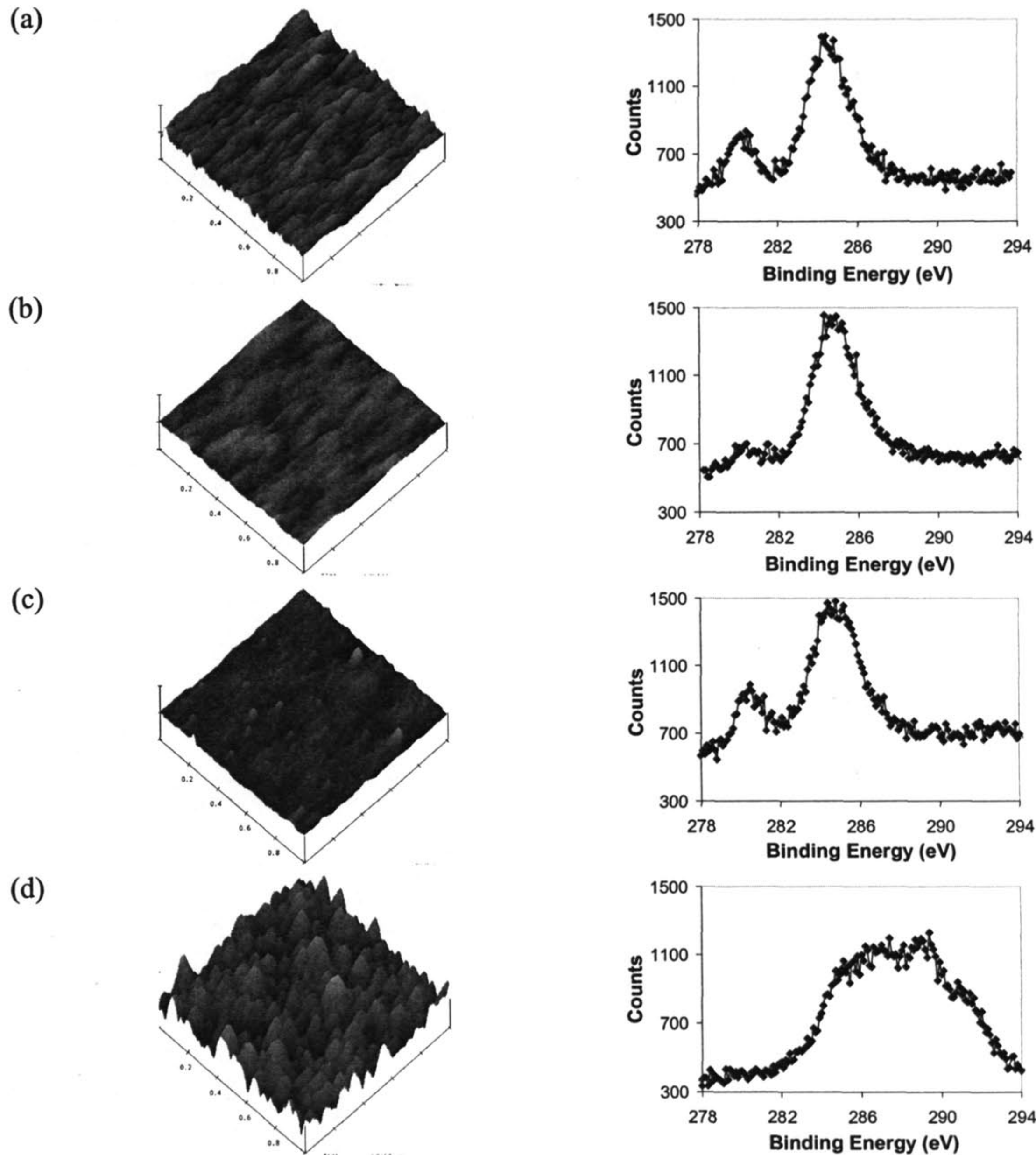

Figure 5-3 Surface AFM images and the corresponding surface carbon (C1s) XPS spectrums of low-k dielectric coral film after etching in C_4F_8/Ar plasmas under various plasma source pressures and C_4F_8/Ar volumetric ratios. The vertical scale of all films is 15 nm and all of the images represent 1 μm × 1 μm of the real sample surface. The C_4F_8 percentage, beam source pressure level, and the ion fluence reach the surface are (a) 10%, 4 mtorr, and 3.0×10^{17} ions/cm^2; (b) 20%, 5 mtorr, and 3.0×10^{17} ions/cm^2; (c) 20%, 8 mtorr, and 2.0×10^{17} ions/cm^2; (d) 20%, 15 mtorr, and 1.75×10^{17} ions/cm^2, respectively. In all cases, the ions bombard the surface at 75° off-normal angle and the DC bias level is 350 V, and the ions reach the surface from the up-right direction. The RMS roughness and the film thickness etched are (a) RMS 1.4 nm and 199 nm etched; (b) RMS 0.57 nm and 211 nm etched; (c) RMS 0.81 nm and 195 nm etched; (d) 4.16 nm and 63 nm etched, respectively.

On the other hand, the surface roughening of these two films at high neutral-to-ion ratios is mainly related to local fluorocarbon deposition induced micro-masking effects that has been discussed in detail previously[23]. As shown in Figure 5-2 (d) and Figure 5-3 (d), the surface carbon (C1s) XPS signals at this high neutral-to-ion ratios regime indicate that carbon on the surface mainly exists in the form of C-C and CFx (x = 1, 2, 3) rather than C-Si. This makes sense because the surface can see more reactive fluorocarbon neutrals per ion bombardment; therefore, the surface fluorocarbon content is much higher than that at low neutral-to-ion ratios. As proposed in my previous studies of porous low-k materials roughening in fluorocarbon chemistries[23], this local fluorocarbon deposition introduces inhomogeneity on the substrate surface and leads to surface roughening. It is commonly observed that fluorocarbon rich surfaces are etched more slowly than oxide rich surfaces during exposure to the same plasma fluxes. Under the condition of high selectivity, it has been observed that polymer is deposited on the fluorocarbon surfaces while etching occurs on the oxide surfaces. Under these particular conditions, it is believed that that the polymer-rich regions grow while the oxide-rich regions etch. This process continues with time, and the polymer-rich regions form micro-masks that induce roughening.

The evolution of the roughness with etching time of these two materials at high neutral-to-ion flux ratio regime is shown in Figure 5-4 and Figure 5-5. In general, the surface roughness level increases with increasing etching time for both films. For instance, the roughness level of coral increases from 1.42 nm to 4.16 nm when the ion fluence reaching the surface changed from 1.0×10^{17} ions/cm^2 to 1.75×10^{17} ions/cm^2. The typical dosage during an etching process is of order 10^{17}-10^{18} ions/cm^2 on surface facets parallel to the macroscopic wafer surface and much less for facets nearly perpendicular to the macroscopic surface. Moreover, the surface carbon (C1s) XPS signal becomes stronger when the etching time increases. Specifically, C-Si signal becomes weaker while CFx (x = 1, 2, 3) signal stronger. Consistently, the intensity of C-H peak in coral C1s spectrum decreases with etching time since more fluorocarbon deposition forms on the surface.

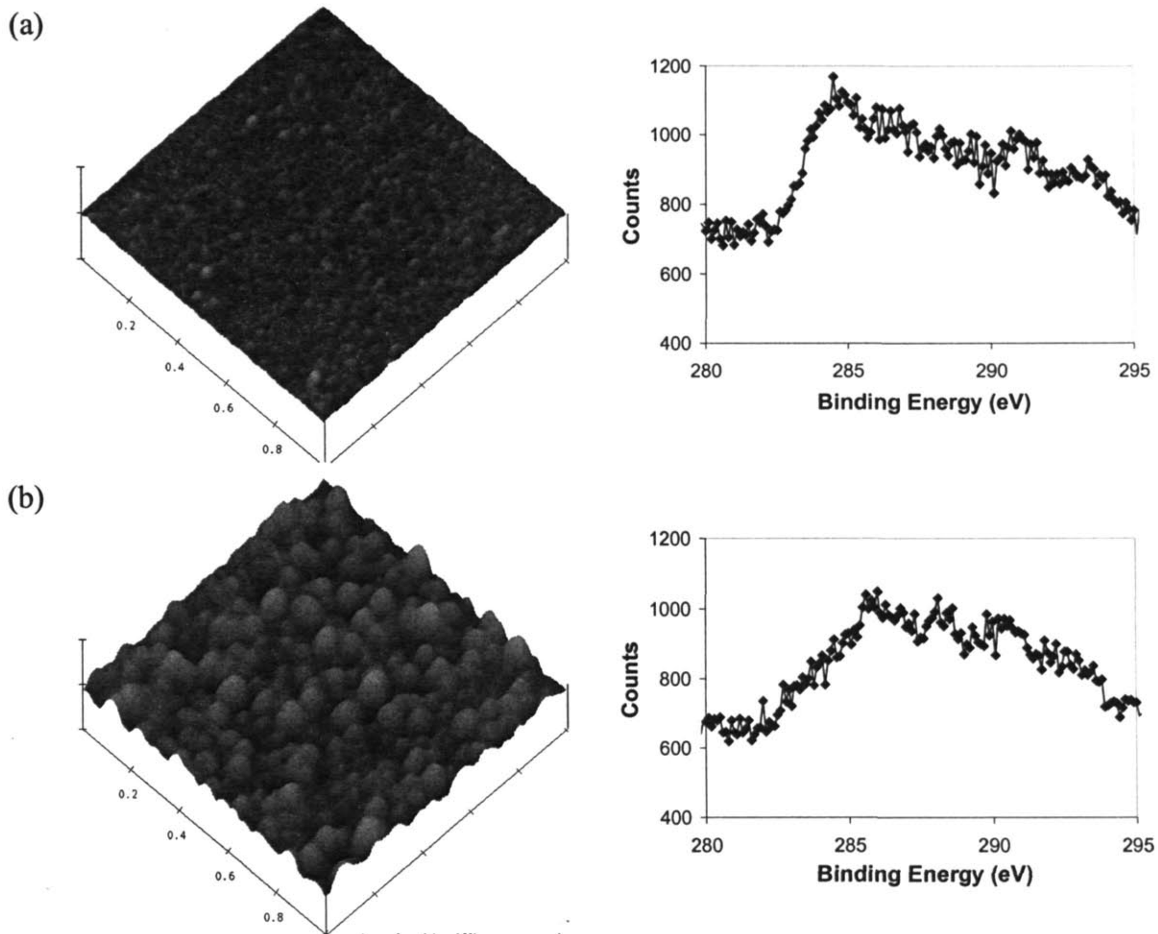

Figure 5-4 The impact of etching time on Surface roughness evolution of thermal SiO_2 after etching in 15% C_4F_8/Ar plasmas at 13 mtorr plasma source pressure level at 75° off-normal angles. The vertical scale of both films is 15 nm and both of the images represent 1 μm × 1 μm of the real sample surface. In both cases, the DC bias level is 350 V and the ions reach the surface from the up-right direction. The ion fluence reaching the surface, the film thickness etched and the RMS roughness level are (a) 1.0×10^{17} ions/cm^2, 32 nm, and 0.24 nm; (b) 2.0×10^{17} ions/cm^2, 61 nm, and 1.5 nm, respectively.

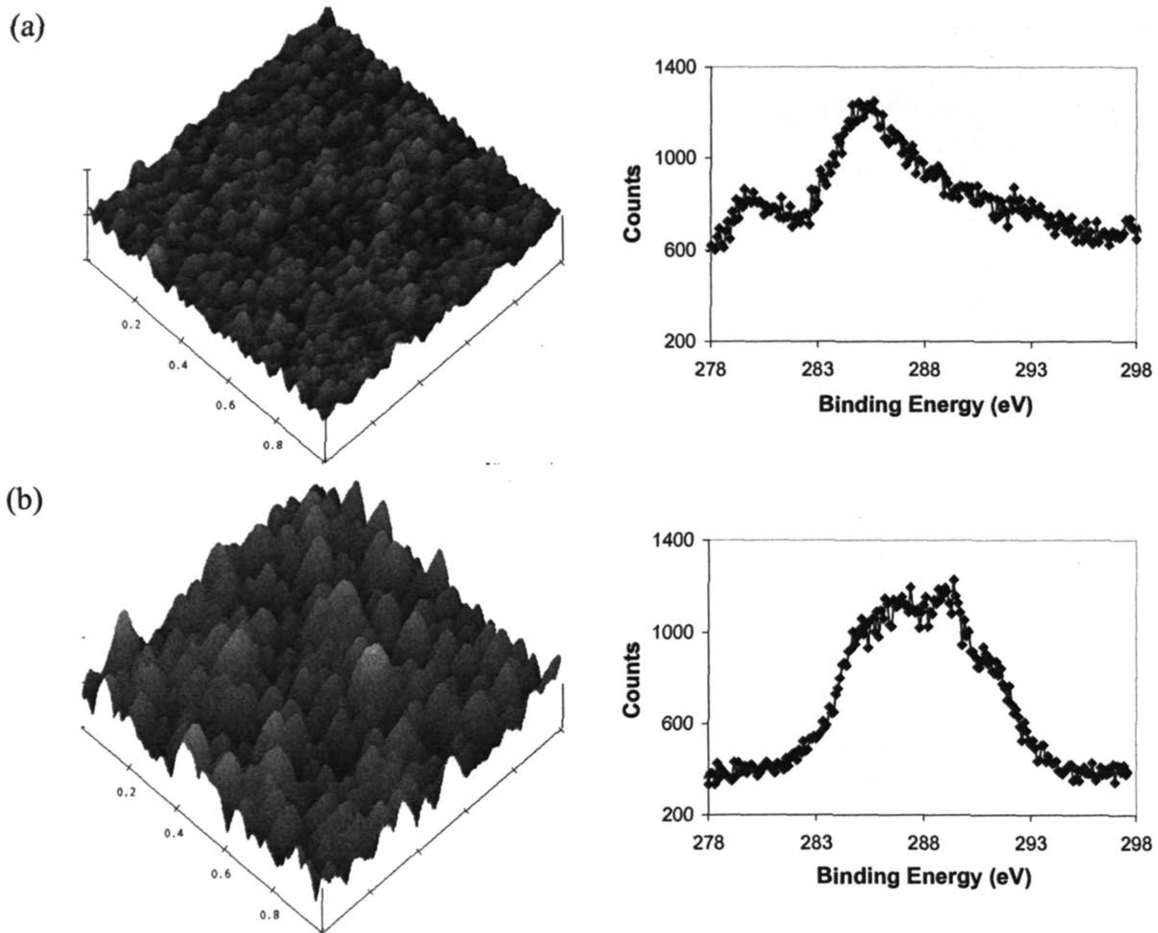

Figure 5-5 The impact of etching time on Surface roughness evolution of low-k dielectric coral film after etching in 20% C_4F_8/Ar plasmas at 15 mtorr plasma source pressure level at 75° off-normal angles. The vertical scale of both films is 15 nm and both of the images represent 1 μm × 1 μm of the real sample surface. In both cases, the DC bias level is 350 V and the ions reach the surface from the up-right direction. The ion fluence reaching the surface, the film thickness etched and the RMS roughness level are (a) 1.0×10^{17} ions/cm^2, 33 nm, and 1.42 nm; (b) 1.75×10^{17} ions/cm^2, 63 nm, and 4.16 nm, respectively.

The results of roughness evolution with etching time at high neutral-to-ion flux ratio regime discussed above are consistent with the proposed local-polymer-deposition induced micro-masking mechanism. Since it is commonly observed that fluorocarbon rich surfaces are etched more slowly than oxide rich surfaces during exposure to the same plasma fluxes. Under the condition of high selectivity, it has been observed that polymer is deposited on the fluorocarbon surfaces while etching occurs on the dielectric surfaces. Consequently, fluorocarbon local deposition is more significant with the increase of etching time, which has already been confirmed by the C1s XPS spectrums shown in

Figure 5-4 and Figure 5-5. Therefore, the inhomogeneity introduced by the fluorocarbon local deposition becomes more significant when the etching time is longer. As a result, the surface roughness level increases with etching time.

The surface roughness of both films after etching is minimized at intermediate neutral-to-ion flux ratios and the results are shown in Figure 5-2(b) and Figure 5-3(b)-(c). Consistently, the C1s XPS spectrums indicate that carbon on the surface is mainly bonded to Si to form C-Si. Again the C1s peak around 280 eV in coral film is due to the contribution of C-H bonds. Since the local fluorocarbon deposition on the surface is minimized, the inhomogeneity introduced to the surface is trivial. For this reason, the surfaces remain smooth after etching at this intermediate neutral-to-ion flux ratio regime.

5.4 Effects of O_2 Addition on Roughening with Grazing Ion Bombardment

It is very intriguing that the etched surfaces remain smooth for both films at intermediate neutral-to-ion flux ratio regime. Furthermore, the oxygen addition broadens the region over which etching without roughening can be performed. The results shown in Figure 5-6 and Figure 5-7 display the roughening of these two films at different neutral-to-ion flux ratios with oxygen addition to the plasma. Obviously, the surface roughness level is comparable or lower than that before plasma etch. In particular, coral film becomes slightly smoother (RMS roughness level 0.4-0.6 nm) after etch, compared to the RMS roughness level of 1.0 nm on un-etched surface. Moreover, the C1s XPS analyses show that carbon on the surface is mainly C-Si for SiO_2, and C-H and C-Si for coral; while CFx(x = 1, 2, 3) peaks are not obvious. This suggests that the plasma fluorocarbon deposition propensity is decreased by the oxygen addition. As a result, the surface fluorocarbon content is much lower compared to that without oxygen addition to the plasma. Therefore, the surface after etch remains smooth since the local polymer deposition induced micro-masking is not important.

The impact of ion-scattering caused channeling effects at intermediate and high neutral-to-ion flux regimes has not been discussed so far. In fact, ion scattering is important in terms of roughness evolution when the angular etching yield curves are sputtering-like. However, this ion scattering effects becomes trivial when ion enhanced etching becomes more important during etching. Rasgon[24] has demonstrated that during

the etching of single-crystal silicon and polysilicon materials at grazing angles in HBr plasmas, where the plasma has almost no polymer deposition capability on the substrate surface and the angular etching yield curves are ion-enhanced etching like, surfaces remained smooth if there is no obvious initial roughness on the un-etched films. The roughness evolution of thermal silicon dioxide and coral materials at intermediate neutral-to-ion flux ratios, where the ion enhanced etching becomes important and the local fluorocarbon deposition induced roughening is minimal, also suggests that the ion scattering effects are not important to develop surface roughness in ion enhanced etching kinetics.

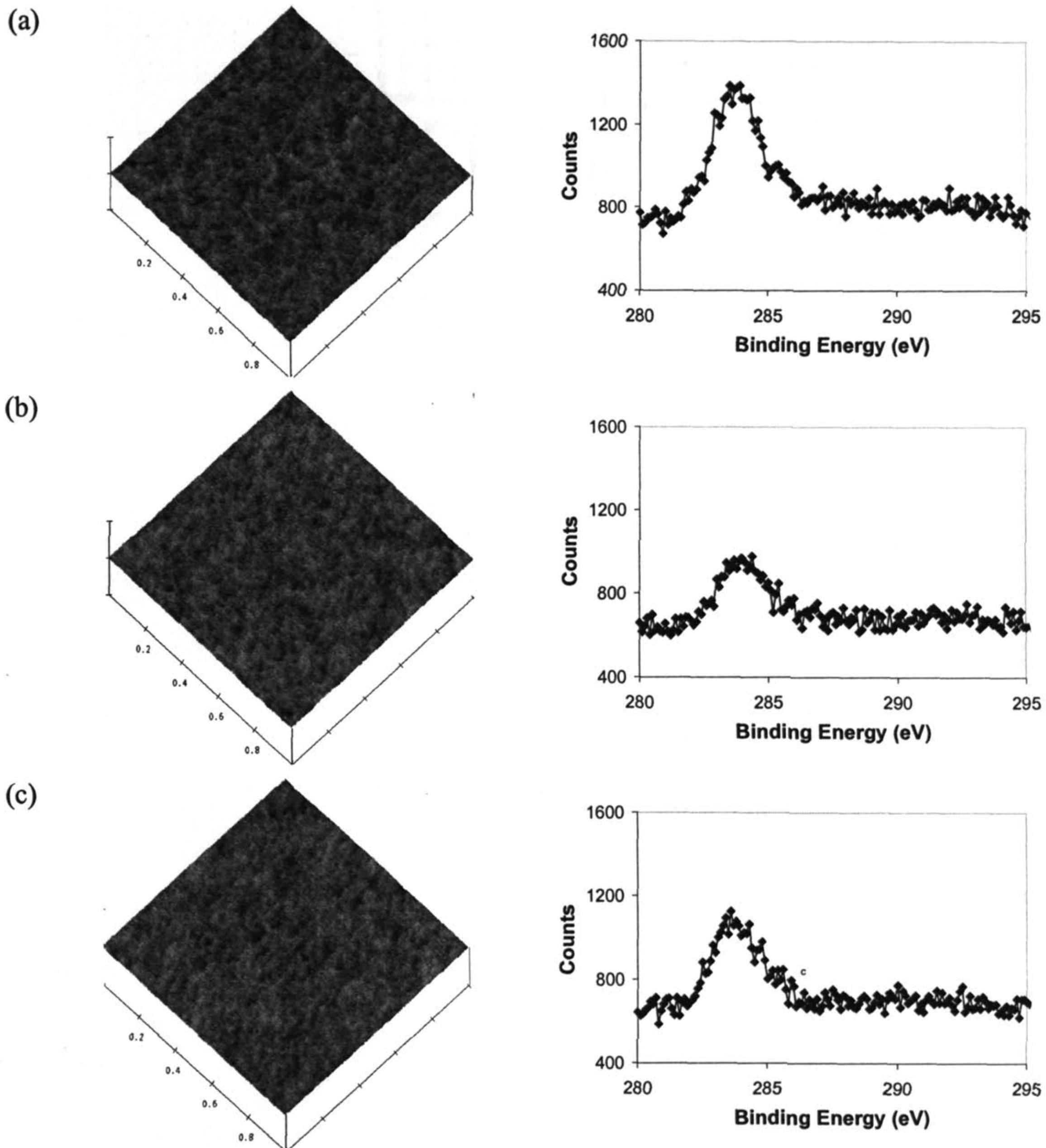

Figure 5-6 The roughening of thermal SiO_2 after etching in $C_4F_8/Ar/O_2$ plasmas under various plasma source pressures and $C_4F_8/Ar/O_2$ volumetric ratios. The vertical scale of all films is 15 nm and all of the images represent 1 μm × 1 μm of the real sample surface. The C_4F_8 and O_2 percentages, beam source pressure level, and the ion fluence reach the surface are (a) 20% C_4F_8 and 10% O_2, 6 mtorr, and 2.0×10^{17} ions/cm^2; (b) 10% C_4F_8 and 5% O_2, 12 mtorr, and 2.0×10^{17} ions/cm^2; (c) 15% C_4F_8 and 15% O_2, 16 mtorr, and 2.0×10^{17} ions/cm^2, respectively. In all cases, the ions bombard the surface at 75° off-normal angle and the DC bias level is 350 V, and the ions reach the surface from the up-right direction. The RMS roughness and the film thickness etched are (a) RMS 0.17 nm and 113 nm etched; (b) RMS 0.16 nm and 79 nm etched; (c) RMS 0.15 nm and 80 nm etched, respectively.

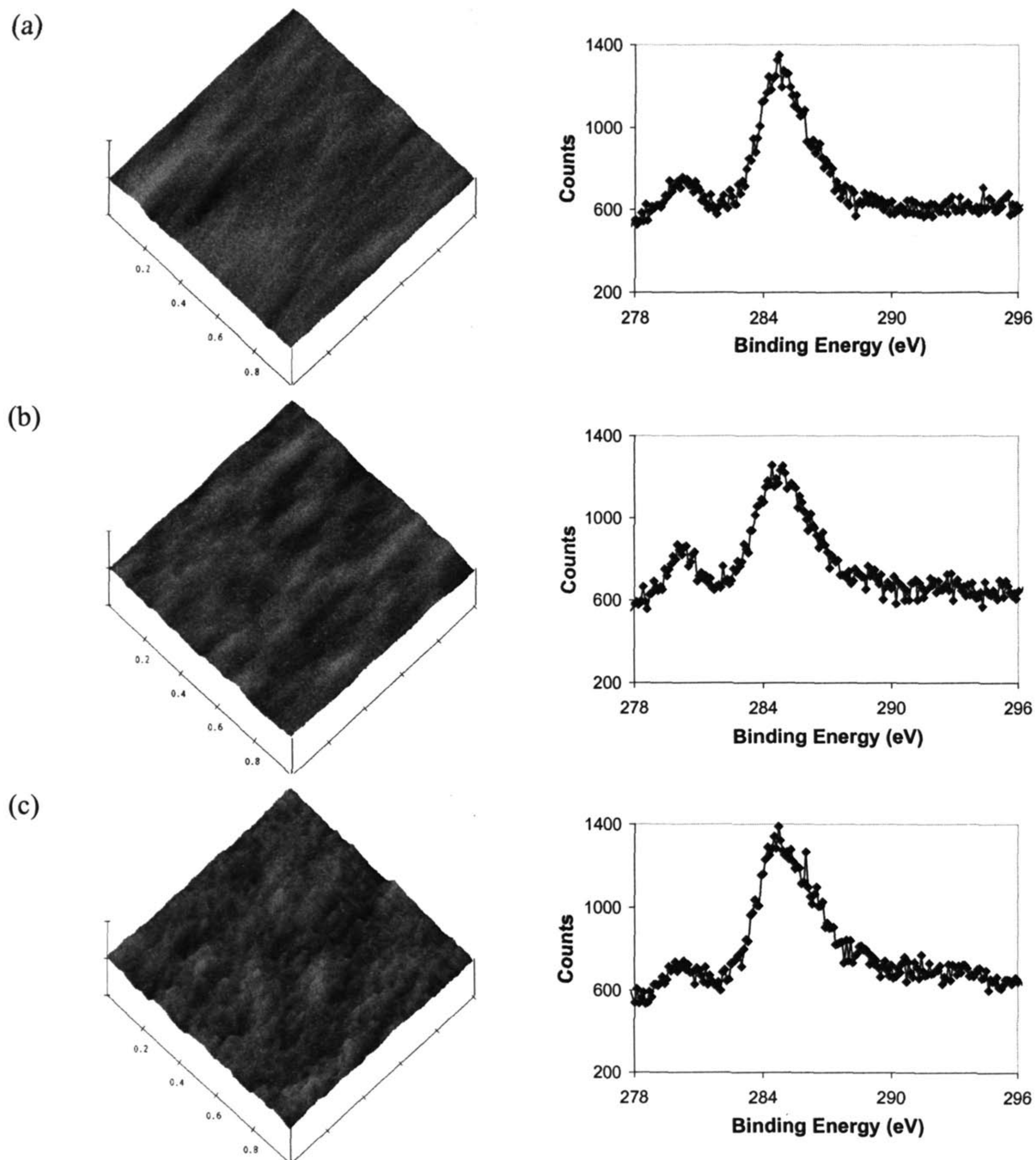

Figure 5-7 The roughening of low-k dielectric coral film after etching in 20% C_4F_8/10% O_2/Ar plasmas under various plasma source pressures. The vertical scale of all films is 15 nm and all of the images represent 1 μm × 1 μm of the real sample surface. The beam source pressure level, and the ion fluence reach the surface are (a) 5 mtorr, and 3.0×10^{17} ions/cm^2; (b) 9 mtorr, and 2.0×10^{17} ions/cm^2; (c) 15 mtorr, and 1.75×10^{17} ions/cm^2, respectively. In all cases, the ions bombard the surface at 75° off-normal angle and the DC bias level is 350 V, and the ions reach the surface from the up-right direction. The RMS roughness and the film thickness etched are (a) RMS 0.39 nm and 175 nm etched; (b) RMS 0.49 nm and 170 nm etched; (c) RMS 0.58 nm and 101 nm etched, respectively.

5.5 References

[1] R. H. Havemann and J. A. Hutchby, Proceedings of the Ieee 89, 586-601 (2001).

[2] A. Jain, S. Rogojevic, S. Ponoth, N. Agarwal, I. Matthew, W. N. Gill, P. Persans, M. Tomozawa, J. L. Plawsky, and E. Simonyi, Thin Solid Films 398, 513-522 (2001).

[3] K. Maex, M. R. Baklanov, D. Shamiryan, F. Iacopi, S. H. Brongersma, and Z. S. Yanovitskaya, Journal of Applied Physics 93, 8793-8841 (2003).

[4] M. Morgen, E. T. Ryan, J. H. Zhao, C. Hu, T. H. Cho, and P. S. Ho, Annual Review of Materials Science 30, 645-680 (2000).

[5] Z. Chen, K. Prasad, C. Y. Li, P. W. Lu, S. S. Su, L. J. Tang, D. Gui, S. Balakumar, R. Shu, and R. Kumar, Applied Physics Letters 84, 2442-2444 (2004).

[6] D. L. Goldfarb, A. P. Mahorowala, G. M. Gallatin, K. E. Petrillo, K. Temple, M. Angelopoulos, S. Rasgon, H. H. Sawin, S. D. Allen, M. C. Lawson, and R. W. Kwong, Journal of Vacuum Science & Technology B 22, 647-653 (2004).

[7] A. Sankaran and M. J. Kushner, Applied Physics Letters 82, 1824-1826 (2003).

[8] M. Sekine, Applied Surface Science 192, 270-298 (2002).

[9] S. A. Vitale and H. H. Sawin, Journal of Vacuum Science & Technology a-Vacuum Surfaces and Films 20, 651-660 (2002).

[10] H. Nagai, S. Takashima, M. Hiramatsu, M. Hori, and T. Goto, Journal of Applied Physics 91, 2615-2621 (2002).

[11] S. A. Vitale, H. Chae, and H. H. Sawin, Journal of Vacuum Science & Technology A 18, 2770-2778 (2000).

[12] T. Standaert, P. J. Matsuo, S. D. Allen, G. S. Oehrlein, and T. J. Dalton, Journal of Vacuum Science & Technology A 17, 741-748 (1999).

[13] L. W. Flanagin, V. K. Singh, and C. G. Willson, Journal of Vacuum Science & Technology B 17, 1371-1379 (1999).

[14] G. P. Patsis, V. Constantoudis, and E. Gogolides, Microelectronic Engineering 75, 297-308 (2004).

[15] M. Schaepkens and G. S. Oehrlein, Journal of the Electrochemical Society 148, C211-C221 (2001).

[16] B. E. E. Kastenmeier, P. J. Matsuo, G. S. Oehrlein, R. E. Ellefson, and L. C. Frees, Journal of Vacuum Science & Technology a-Vacuum Surfaces and Films 19, 25-30 (2001).

[17] T. Standaert, E. A. Joseph, G. S. Oehrlein, A. Jain, W. N. Gill, P. C. Wayner, and J. L. Plawsky, Journal of Vacuum Science & Technology a-Vacuum Surfaces and Films 18, 2742-2748 (2000).

[18] B. E. E. Kastenmeier, G. S. Oehrlein, J. G. Langan, and W. R. Entley, Journal of Vacuum Science & Technology a-Vacuum Surfaces and Films 18, 2102-2107 (2000).

[19] N. R. Rueger, M. F. Doemling, M. Schaepkens, J. J. Beulens, T. Standaert, and G. S. Oehrlein, Journal of Vacuum Science & Technology a-Vacuum Surfaces and Films 17, 2492-2502 (1999).

[20] M. Schaepkens, T. Standaert, N. R. Rueger, P. G. M. Sebel, G. S. Oehrlein, and J. M. Cook, Journal of Vacuum Science & Technology a-Vacuum Surfaces and Films 17, 26-37 (1999).

[21] B. A. Helmer and D. B. Graves, Journal of Vacuum Science & Technology a-Vacuum Surfaces and Films 16, 3502-3514 (1998).

[22] C. F. Abrams and D. B. Graves, Journal of Vacuum Science & Technology A 16, 3006-3019 (1998).

[23] Y. P. Yin, S. Rasgon, and H. H. Sawin, Journal of Vacuum Science & Technology B 24, 2360-2371 (2006).

[24] S. A. Rasgon, Ph.D. Thesis, Massachusetts Institute of Technology, 2005.

Chapter 6. Surface Roughening of Low-k Films during Etching Using Fluorocarbon Plasma Beams

The surface roughness evolution of solid organosilicate glass (OSG) and methylsilsesquioxane (MSQ) spin-on porous low-k films after etching in C_2F_6/Ar plasmas was characterized as a function of ion bombardment energy, ion fluence reaching the surface (or, equivalently, the etching time), ion impingement angle, and plasma polymerization propensity in a newly designed plasma beam system in which the plasma chemistry, ion energy, ion flux, and ion incident angle can be adjusted independently. A polymerization-induced micro-masking mechanism was proposed to explain the surface roughening of these low-k films. The porous structure in the substrate plays a critical role in the film roughening evolution. This effect can be understood using the concept of pore filling with polymeric deposits that etch more slowly under fluorocarbon plasma exposure. Upon exposure to etching, the polymer forms micro-masks that induce roughening. Under the same etching conditions, the solid OSG film remains smooth during etching because only a fairly thin and uniform layer of polymer deposits on the surface of solid OSG substrates during the etching in C_2F_6/Ar plasmas. Consequently, the inhomogeneity caused by the polymer deposition is not sufficient to induce micro-masking in the absence of surface inhomogeneities. Additionally, the roughness level of porous low-k film etched in C_2F_6/Ar plasma is primarily related to the film thickness removed, although it also increases with the ion bombardment energy; no similar trend was observed on non-porous OSG films under the same etching conditions. Striations formed when etching porous low-k films at grazing angles. The striation formation is mainly due to shadowing effects, although conditions of net polymer deposition quenched the striation formation.

6.1 Introduction

For the patterning of sub-100 nm features, a clear understanding of the origin and control of line-edge roughness (LER) is extremely desirable, both from a fundamental and a manufacturing perspective. Plasma etching processes often roughen the feature sidewalls, leading to the formation of anisotropic striations. It is this post-etch sidewall roughness which ultimately affects device performance and yield[1-4].

When the device key dimensions shrink to the deep sub-micrometer regime, the interconnect resistance-capacitance (RC) delay can become dominant over intrinsic gate delay[5,6]. Dielectric materials with low dielectric constants become advantageous in order to further reduce interconnect delay and enable higher device speeds. For instance, solid OSG and MSQ spin-on porous low-k films are attractive candidates[6-13]. Specifically, the etching kinetics of various promising low-k films in fluorocarbon plasmas and other etching chemistries have been reported[14-21]. However, the integration of low-k films as low-k interlayer dielectrics presents new challenges from a roughening standpoint, particularly when using highly polymerizing fluorocarbon plasma chemistries typical of oxide etching. The first consequence of the sidewall roughening of low-k film is the copper interconnect resistance increase related to the deposition of thicker conformal liner/barrier layers to avoid gaps that would allow the diffusion of Cu into the pores of the low-k materials[10,22,23]. Because of the sidewall roughness after plasma processing, a thicker layer of barrier layer has to be deposited in order to get good coverage. Consequently, the space for subsequent copper line filling is limited, which leads to the increase of the copper interconnect resistance. In addition, the post-etching cleaning of low k film surfaces before the deposition of the liner layer becomes difficult due to the sidewall roughness, especially for the cleaning of porous low-k films because of the retaining of fluorocarbons in the pores. Roughening can also lead to a short between contacts, causing device failure.

As shown in the literature[24,25], top LER (or equivalent templating effects) plays a very important role for the sidewall roughening of oxide patterning during etching in fluorocarbon chemistries. It was found that the resist sidewall roughness after development (but before plasma etching) was isotropic; during the anti-reflective coating (ARC) layer opening in the plasma etching process, the photoresist layer became striated and the top edge of the photoresist layer was faceted. The striation structure became much more significant and propagated down after etching of the subsequent SiO_2 layer.

The surface roughening of low-k films may occur during etching in fluorocarbon plasmas, in addition to the templating effects on sidewall roughness evolution mentioned above. Consequently, it is crucial to fully understand the mechanisms of the inherent

surface roughening before I can optimize the plasma etching conditions to minimize the surface roughness level after etching.

In this Chapter, the inherent roughening of low-k films during plasma etching was investigated in the fluorocarbon plasma chemistries. The roughening was characterized as a function of ion bombardment energy, ion fluence, ion impingement angle, and plasma polymerization propensity of C_2F_6/Ar plasma beams. My objective is to explore the inherent roughening mechanism of low-k films during plasma etching.

6.2 Standard Etching Procedure

Polymer was gradually deposited on the liner interior when the fluorocarbon plasma run, which gradually modified the chamber conditions. Consequently, the plasma composition in the gas phase was also influenced by the chamber history. A standard etching procedure was developed to minimize the historical effects. Before each sample etching experiment, the chamber was cleaned and warmed up in Ar/O_2 plasma for about 15 minutes, followed by 4 minutes of running with identical running conditions to the sample etching experiments.

6.3 Characterization of Unetched Films

Solid OSG and MSQ spin-on porous low-k films supplied by Texas Instruments Corporation were used in this work. Specifically, both the OSG and the porous low-k film were spun-on coated on single crystal silicon wafers. The dielectric constant of the solid OSG film was about 2.8. The porous low-k film had a solid phase composition similar to the OSG, with approximately 30% porosity and a dielectric constant of ~2.2.

The unetched OSG and porous low-k films were characterized using AFM. The images are shown in Figure 6-1. The vertical scale of both films is 10 nm. The RMS roughnesses of OSG and porous low-k films are 0.9 and 1.2 nm, respectively. Compared with the etched samples, which will be discussed later on, both the pre-etched films are very smooth, although porous low-k film was slightly rougher than the solid OSG. This might be due to the porous structure of the porous low-k film, although the radius of curvature of the AFM tip is actually likely too large to capture the pore structure in the

images[24]. In addition, the roughness of both pre-etched films is isotropic, with no specific orientation.

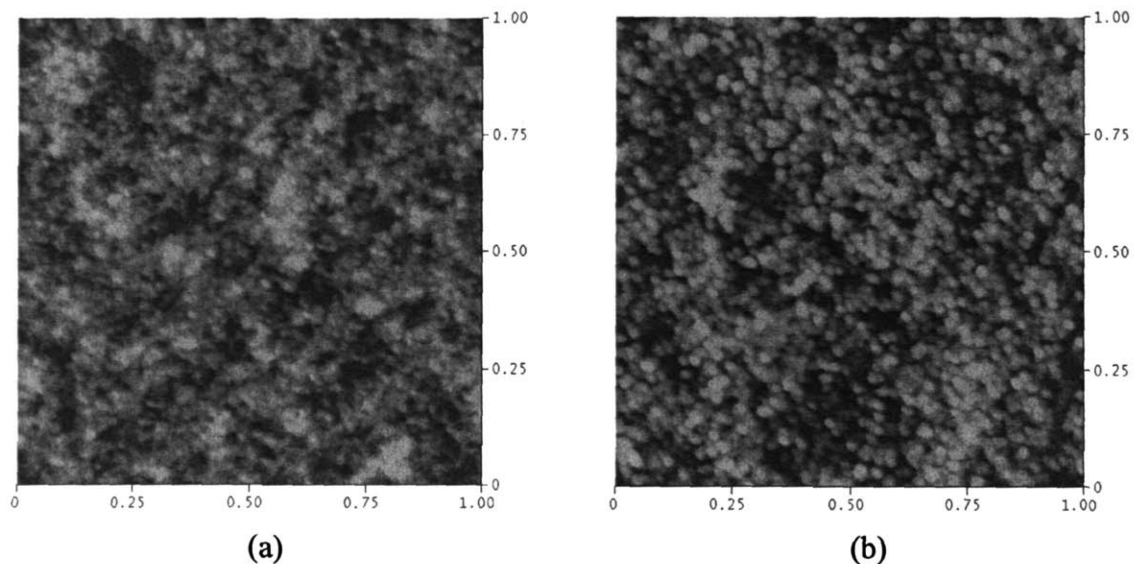

Figure 6-1 The AFM images of unetched (a) OSG and (b) porous low-k films. The vertical scale of both films is 10 nm and both of the images represent 1 μm × 1 μm of the real sample surface. The RMS roughness of OSG and porous low-k films is 0.9 and 1.2 nm, respectively.

The near surface elemental compositions of these two low-k films were characterized by XPS and summarized in Figure 6-2. The surface atom fractions are based upon the signal intensities of each element after correction of the corresponding XPS sensitivity factors:[26] $S_{Si(2p)} = 0.817$, $S_{C(1s)} = 1.00$, $S_{O(1s)} = 2.93$, $S_{F(1s)} = 4.43$. As shown in Figure 6-2, no fluorine species was detected on both the low-k films by XPS before processing in fluorocarbon plasma beams. The XPS result indicates that the OSG and the porous low-k have similar chemical composition, except that there is a bit more carbon in OSG film.

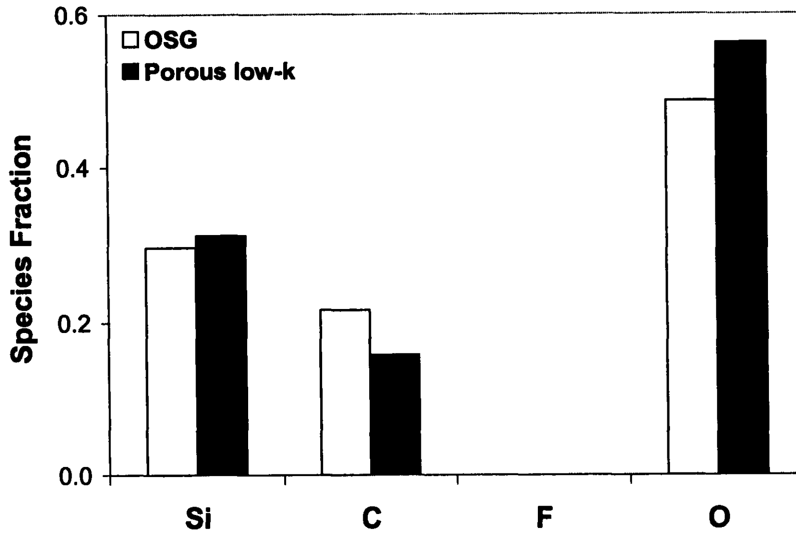

Figure 6-2 The surface composition of solid OSG and porous low-k films characterized by XPS before etching in C_2F_6/Ar plasma beams.

6.4 Surface Roughness Evolution with Etching Time

The surface roughness of solid OSG and porous low-k films after processing in 20% C_2F_6/Ar plasma is shown in Figure 6-3 and Figure 6-4 as a function of ion fluence reaching the sample surface at the normal angle. The plasma etching conditions are: total flow rate 5 sccm, beam source pressure 10 mtorr, radio frequency source power 350 W, and ion bombardment energy 370 eV, which corresponds to DC bias voltage of 350 V. The porous low-k films became significantly roughened after etching and became even rougher with the increasing ion fluence. In particular, the porous low-k film roughening increased, with the RMS roughness value going from 3.2 nm to 9.0 nm, as shown in Figure 6-4. In contrast, the solid OSG films remained smooth after processing under identical plasma etching conditions. The roughness of OSG appeared to approach a constant at RMS value 1.0 nm for both of the ion fluences of 2.0×10^{17} and 5.0×10^{17} ions/cm^2.

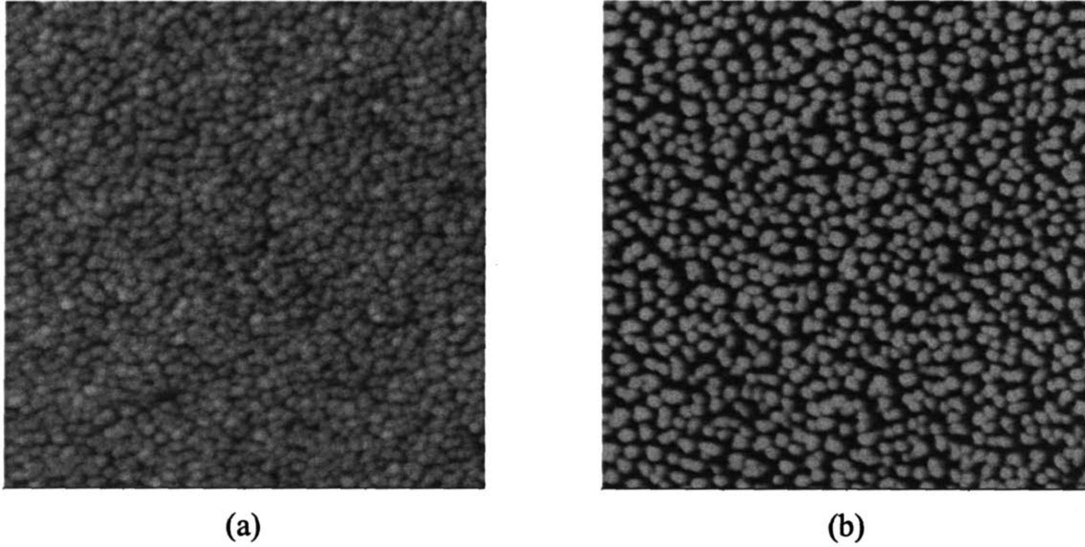

Figure 6-3 The evolution of surface roughness with the ion dosage reaching the porous low-k film during etching in 20% C_2F_6/Ar plasma beam at normal angle. Plasma etching conditions: total flow rate 5 sccm, beam source pressure 10 mtorr, RF source power of 350 W. 370 eV ions were used and the vertical scale is 50 nm for both AFM images. (a) The dosage is 2.0×10^{17} ions/cm^2 and the RMS roughness is 3.2 nm after 115 nm film was etched. (b) The dosage is 5.0×10^{17} ions/cm^2 and the RMS roughness is 9.0 nm after 300 nm film was etched.

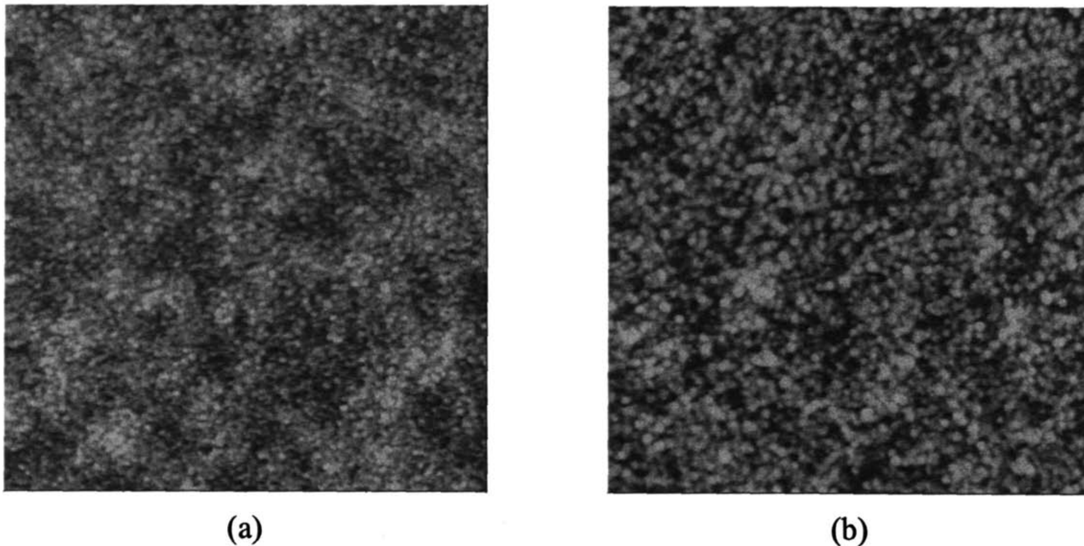

Figure 6-4 The evolution of surface roughness with the ion dosage reaching solid OSG during etching in 20% C_2F_6/Ar plasma beam at normal angle. Plasma etching conditions: total flow rate 5 sccm, beam source pressure 10 mtorr, RF source power 350 W. 370 eV ions were used and the vertical scale is 10 nm for both AFM images. (a) The dosage is 2×10^{17} ions/cm^2 and the RMS roughness is 0.9 nm after 97 nm film was etched. (b) The dosage is 5×10^{17} ions/cm^2 and the RMS roughness is 1.1 nm after 238 nm film was etched.

The XPS C(1s) signal before and after processing in 20% C_2F_6/Ar plasma for both solid OSG and porous low-k films is shown in Figure 6-5. The C(1s) signal loses its symmetry after processing in fluorocarbon plasma. The high energy tail is caused by the CF, CF_2, and CF_3 peaks of the thin fluorocarbon films deposited on the surface of the substrates during processing in fluorocarbon plasmas. Similar XPS characterization results have been reported in the literature[27-29]. The polymer layer deposited on the surface of OSG after processing is very thin according to the XPS C(1s) shown in Figure 6-5(a). Additionally, the polymer film thickness doesn't vary greatly with the increase of etching time. The polymer thickness on the porous low-k film is also thin when the processing time is short (ion fluence level 2.0×10^{17} ions/cm^2). However, the polymer layer becomes thicker when the processing time is longer (corresponding to 5×10^{17} ions/cm^2), which results in a relatively stronger CF_x (x = 1, 2, 3) peak intensities at the high energy tail in C(1s) signal. This trend is believed to be related to the porous structure in porous low-k films, which retains fluorocarbon chain structures during etching in fluorocarbon plasmas. These polymer chains retained in the pores enable further polymer deposition and make the polymer layer thicker.

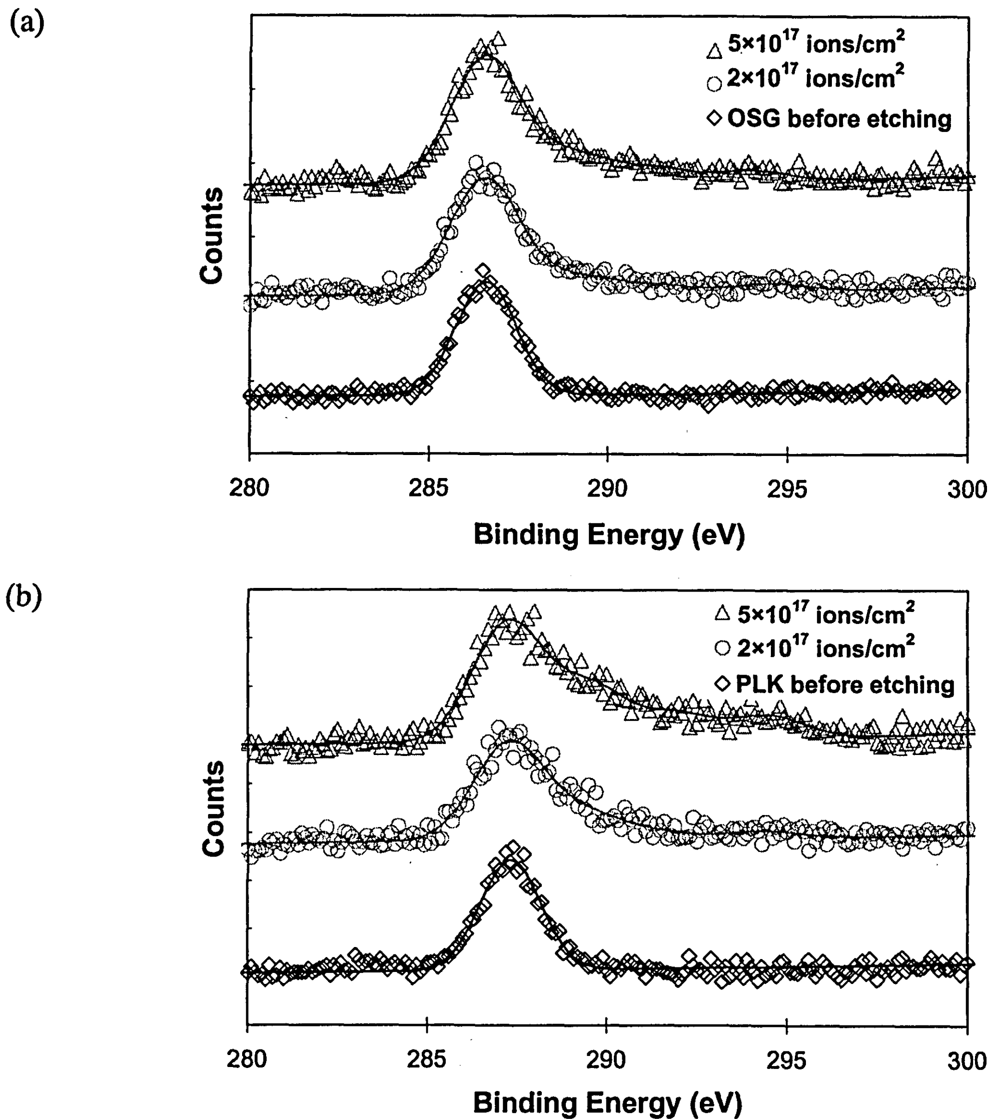

Figure 6-5 XPS C(1s) signals of (a) OSG and (b) porous low-k films before and after etching in 20% C_2F_6 /Ar plasma at normal angle. Plasma etching conditions: total flow rate 5 sccm, beam source pressure 10 mtorr, RF source power 350 W, ion bombardment energy 370 eV.

6.5 Effects of Ion Bombardment Energy on Surface Roughening and Etching Kinetics

Figure 6-6 gives the etching rate and surface roughness of solid OSG and porous low-k films after etching in 20% C_2F_6/Ar plasma. The plasma running conditions are: total flow rate 5 sccm, beam source pressure 10 mtorr, RF source power 350 W, and ion fluence 5.0×10^{17} ions/cm^2. The etching rate of both films increases when the ion bombardment energy level is higher, as shown in Figure 6-6(a). Additionally, porous low-

k film etches faster than solid OSG film because the porous structure in the film makes the substrate less dense. With the increase of the ion bombardment energy, porous low-k film becomes rougher, while the roughness of solid OSG is almost constant and identical to the RMS roughness value 1.0 nm before etching, which can be seen in Figure 6-6(b).

XPS analysis result suggests that the thickness of the fluorocarbon film is thicker at low ion bombardment energies for both the solid OSG and porous low-k films, which can be seen in Figure 6-7. Additionally, the signal intensities of CF_x ($x = 1, 2, 3$) at the high binding energy tail become weaker as the ion bombardment energy grows higher, which indicates that the fluorocarbon layer on the surface becomes thinner with the increase of the ion energies. My observation is consistent with the results in the literature. Oehrlein et al.[28] argue that the etching rates of SiO_2 in fluorocarbon plasma are significantly influenced by the thin fluorocarbon film deposited on the substrate film during plasma processing. More specifically, a higher etching rate is typically accompanied by thinner fluorocarbon film. Through the molecular dynamics simulation approach, Graves et al.[30] also found that the etching yield of silicon in fluorocarbon and Ar plasmas is inversely related to the fluorocarbon film content on the substrate surface.

(a)

(b)

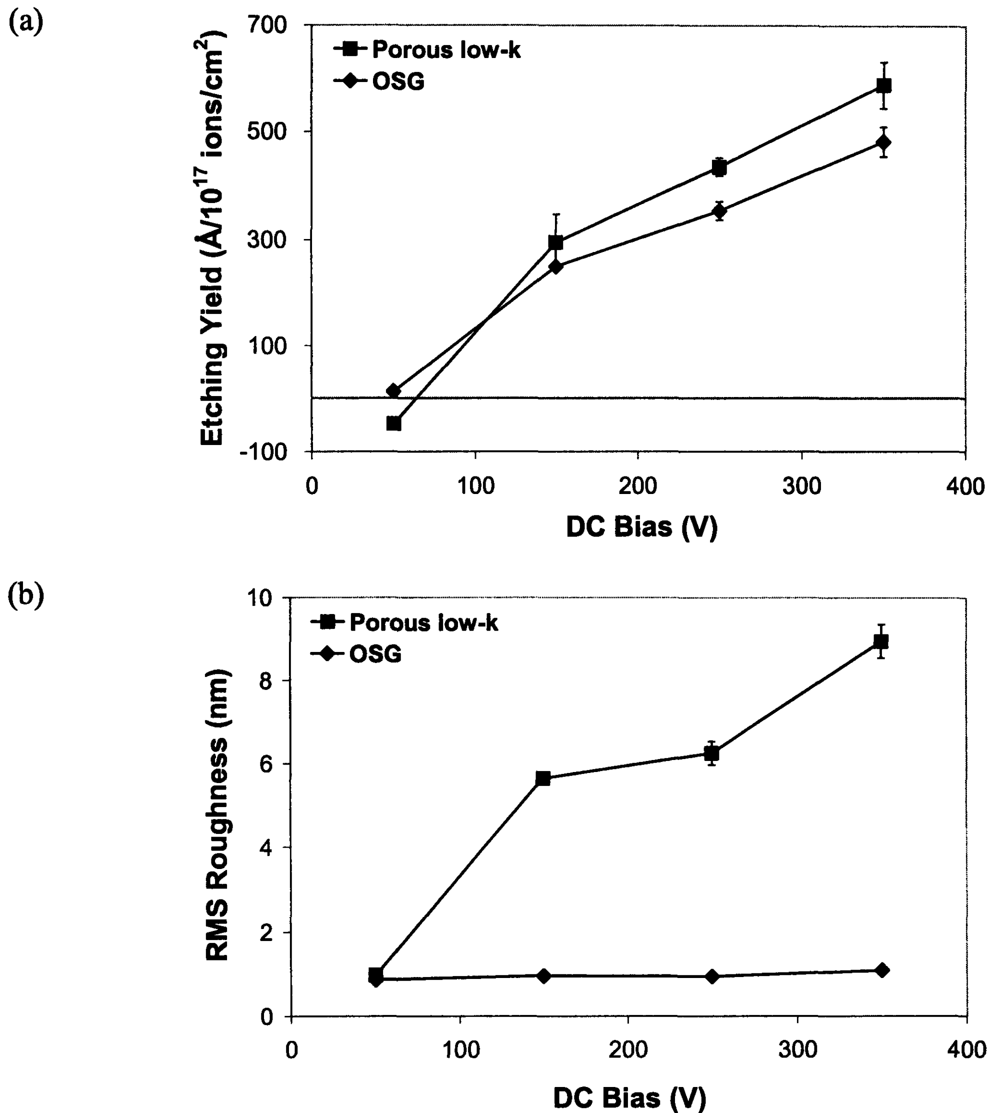

Figure 6-6 The impact of ion bombardment energies (equivalently DC bias voltage) on (a) etching rate and (b) surface roughness after etching in 20% C_2F_6/Ar plasma at normal impingement angle. Plasma etching conditions: total flow rate 5 sccm, beam source pressure 10 mtorr, RF source power of 350 W, ion fluence 5.0×10^{17} ions/cm^2.

The XPS results also confirm that the porous structure in porous low-k films enhances the fluorocarbon polymer thin film deposition. For instance, the porous low-k substrate surface is covered by a relatively thick layer of fluorocarbon film when the DC bias level is 50 V; the XPS signal of other species, including O(1s) and Si(1s) (XPS spectrum not shown here), cannot be detected below this ion energy level since the polymer layer is thick. Consequently, net deposition occurs under this condition, as shown in Figure 6-6(a). However, the fluorocarbon film is not thick enough to stop the etching

process for solid OSG film at the DC bias level 50 V because of the absence of porous structure in solid OSG film.

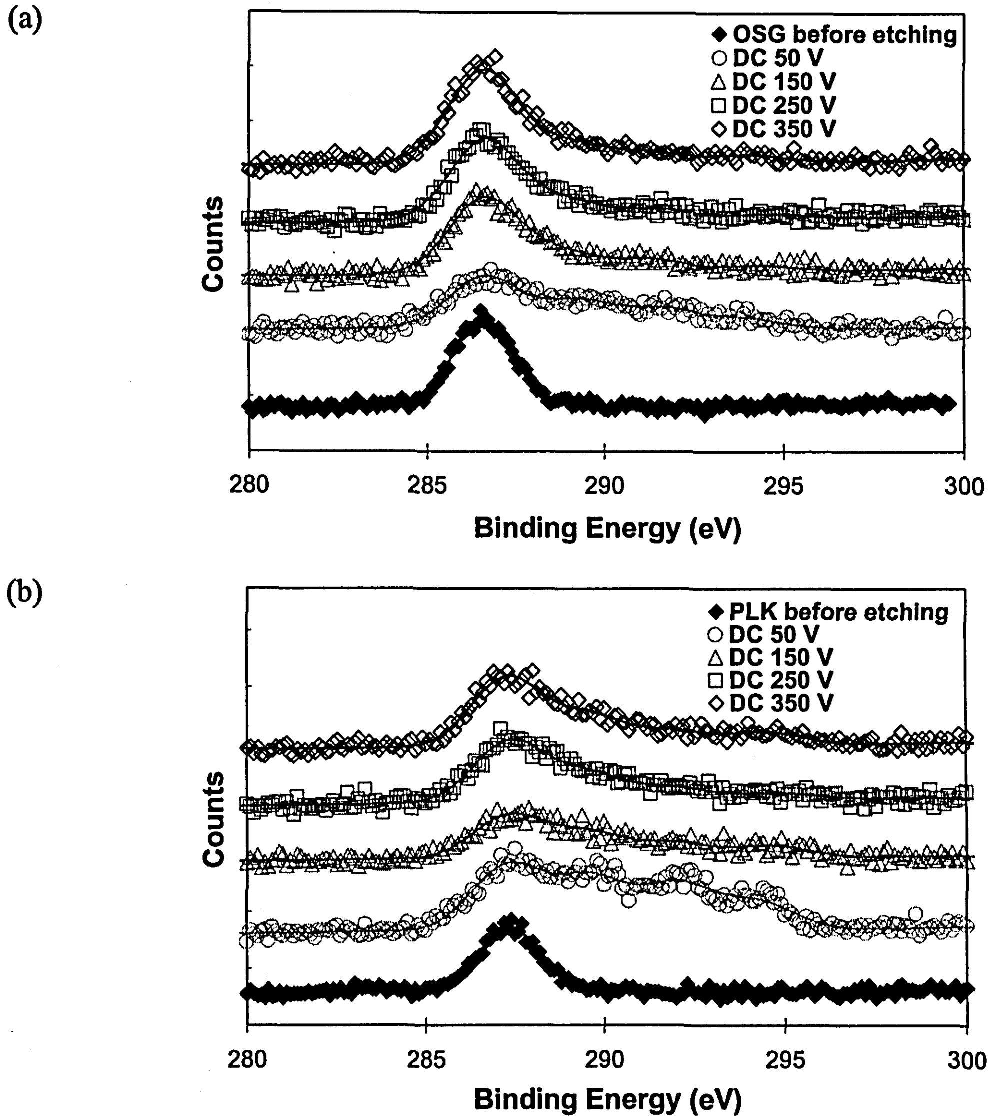

Figure 6-7 *XPS C(1s) signals of* (a) OSG and (b) porous low-k films before and after etching in 20% C_2F_6/Ar plasma using different ion bombardment energies levels at normal angle. Plasma etching conditions: total flow rate 5 sccm, beam source pressure 10 mtorr, RF source power of 350 W, ion fluence 5.0×10^{17} ions/cm^2.

6.6 Impact of Plasma Polymerizing Effects on Surface Roughening

The etching kinetics of solid OSG and porous low-k films is significantly influenced by the plasma polymerization capability. Figure 6-8 shows the etching rate and surface roughness of both films after processing as a function of C_2F_6 molar percentage in

the feed gas. The plasma running conditions are a total gas flow rate of 5 sccm, a beam source pressure of 10 mtorr, an RF source power of 350 W, an ion fluence of 5×10^{17} ions/cm^2, and an ion energy level of 370 eV (equivalently, DC bias of 350 V). Net etching occurs when the C_2F_6 percentage is low while net deposition occurs when C_2F_6 percentage is high, as indicated in Figure 6-8(a). Consistently, net deposition is always accompanied by a fairly thick fluorocarbon film, which corresponds to strong CF_x signal intensities at the high binding energy tail shown in Figure 6-9.

The etching rate variation with C_2F_6 percentage in C_2F_6/Ar is partially related to the modulation of ion flux by the addition of Ar. Specifically, the direct ion penetration into the substrate surface is enhanced when the ion flux is high and the ion-bombardment-induced mixing mechanism contributes more to the etching. It was found in this work that the ion flux reaching the sample surface was enhanced by the addition of Ar. Pure C_2F_6 plasma under these plasma running conditions is not stable, which can be seen under visual observation in terms of luminosity difference. It is believed that negative ions are formed by electron attachment in fluorocarbon plasma, which can cause fluctuation of electron density and consequently leads to plasma instability. In contrast, Ar is electropositive and the addition of Ar to the fluorocarbon gas increases the electron density and energy of the plasma, thereby stabilizing the plasma, which consequently results in the increase of the ion density according to the ambipolar diffusion assumption[31]. Therefore, the ion flux extracted from the grounded gridded orifice is also enhanced. This ion flux enhancement is not significant until the Ar percentage exceeds some threshold value related to the fraction required to increase the electron energy. Since the ionization energy for Ar atoms is about 15.68 eV[32], which is higher than most ionization processes for fluorocarbons and the fluorocarbon dissociation products, the addition of Ar does not initially change the electron energy. As a result, Ar only acts as a dilution gas when the molar percentage of it is lower than the threshold value. With greater dilution, Ar is ionized as the electron energy increases. The modulation of ion flux in fluorocarbon plasmas by the addition of Ar has also been reported in the literature and is consistent with my observations[33,34].

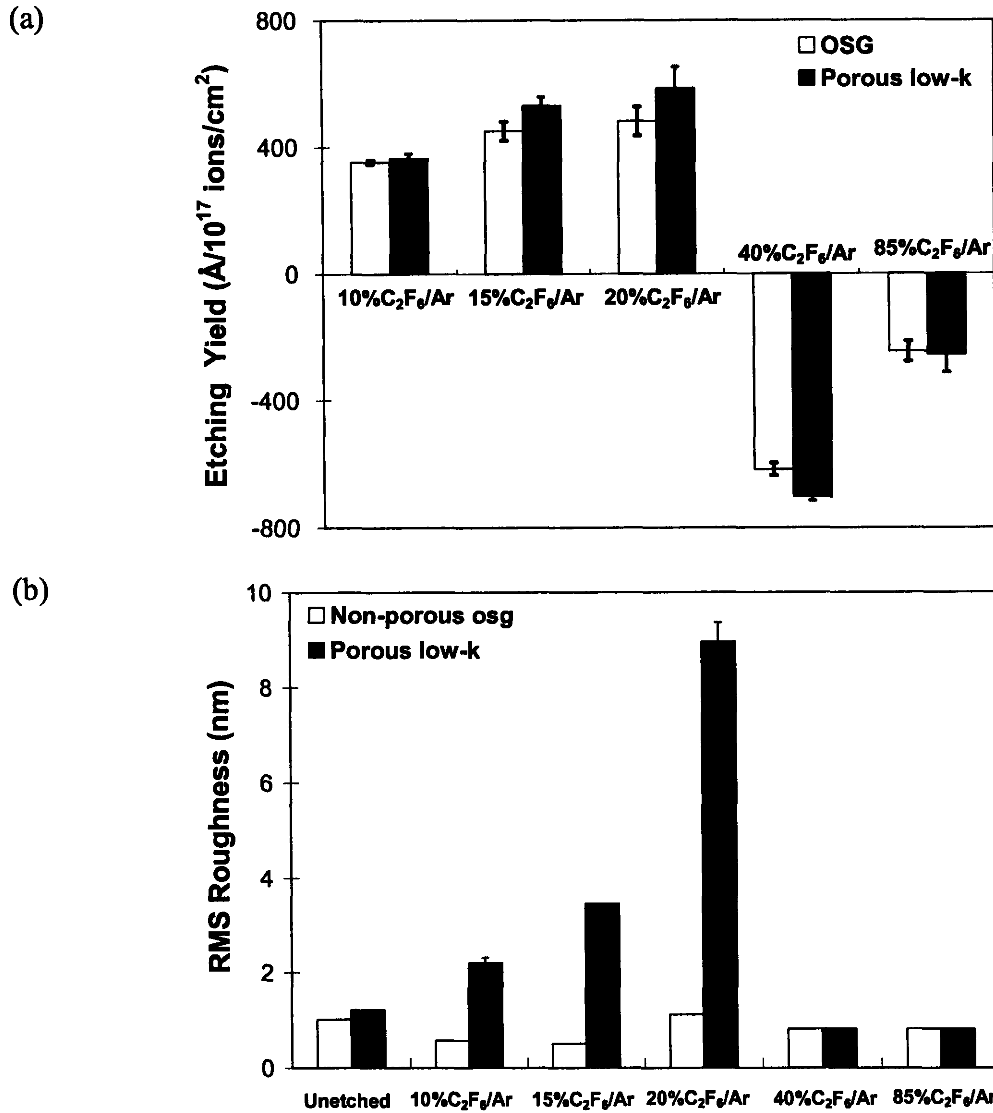

Figure 6-8 The impact of plasma polymerization capability on (a) etching rate and (b) surface roughness after etching in C_2F_6/Ar plasma at normal impingement angle. Plasma etching conditions: total flow rate 5 sccm, beam source pressure 10 mtorr, RF source power 350 W, ion fluence 5.0×10^{17} ions/cm^2, and ion energy level 370 eV (equivalently, DC bias 350 V).

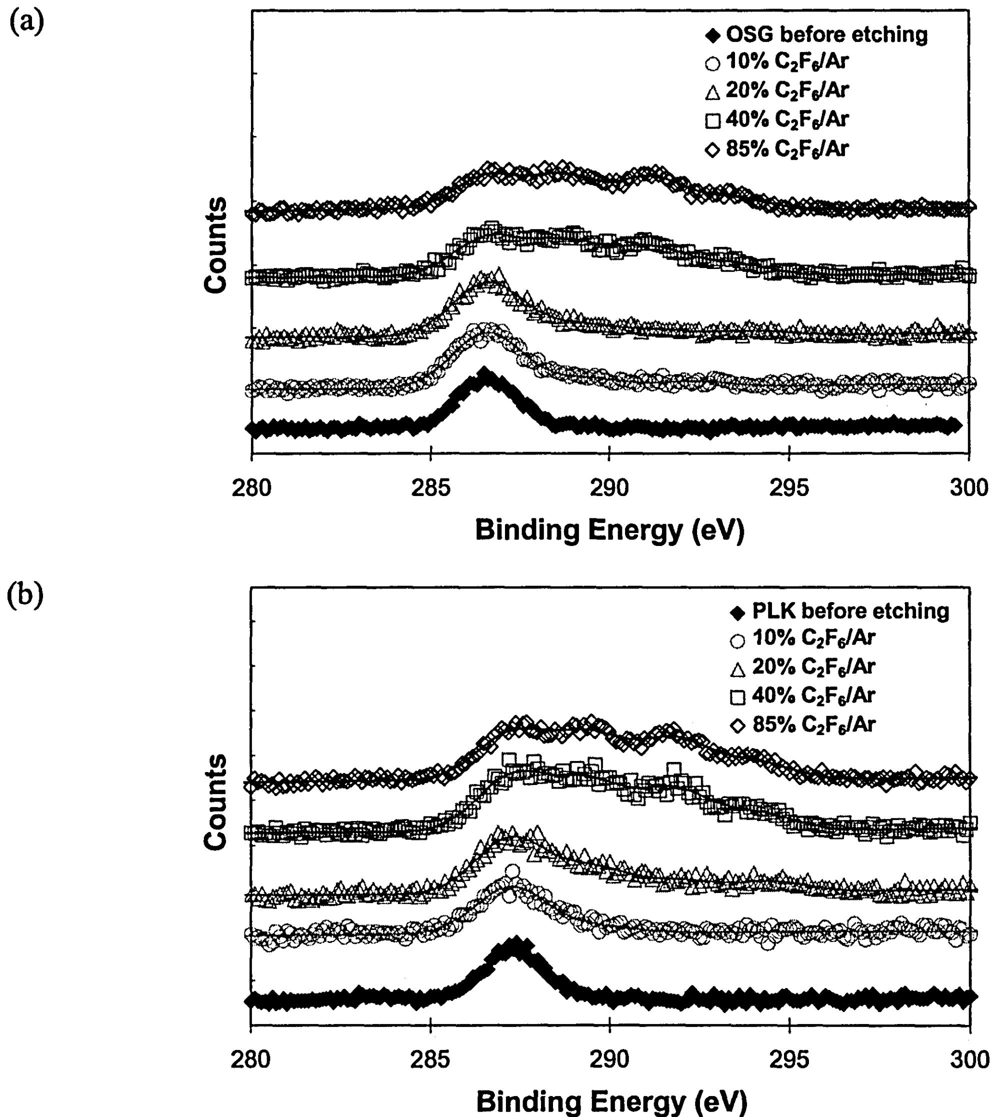

Figure 6-9 XPS C(1s) signals of (a) OSG and (b) porous low-k films before and after etching in C_2F_6/Ar plasma as a function of C_2F_6 molar percentage in the mixed feed gas at normal angle. Plasma etching conditions: total flow rate 5 sccm, beam source pressure 10 mtorr, RF source power 350 W, ion fluence 5.0×10^{17} ions/cm^2, and ion energy level 370 eV (equivalently, DC bias 350 V).

Another contribution to the etching rate variation is the impact of the C_2F_6 percentage on fluorocarbon neutral concentrations in the plasma. Generally speaking, fluorocarbon neutral concentrations become higher with the increase of C_2F_6 percentage, as demonstrated in Figure 6-10. Higher neutral concentration levels in the plasma phase typically enhance the adsorption of fluorocarbon neutrals on the substrate surface and tend to result in thicker fluorocarbon film on the film surface. This argument has already been

proved by experiments and molecular dynamics simulation[28,30]. My etching rate measurement also supports this argument. For instance, the etching kinetics go from net etching to net deposition when the percentage of C_2F_6 increases from 20% to 40%.

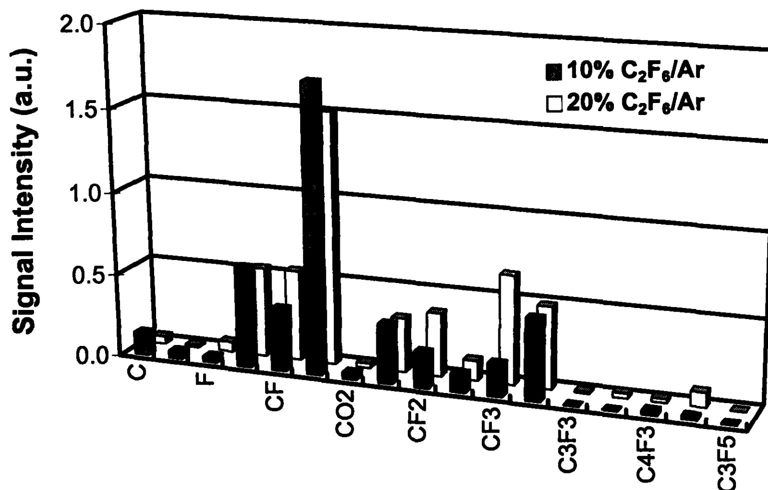

Figure 6-10 The plasma neutral spectrums of 10% C_2F_6/Ar and 20% C_2F_6/Ar plasmas. In both cases, the plasma running conditions are: total gas flow rate 5 sccm, beam source pressure ~10 mtorr, RF source power of 350 W.

The evolution of surface roughness of these two films with the percentage of C_2F_6 shows totally different trends. Solid OSG film surface after etching is independent of the C_2F_6 percentage and always remains smooth. In contrast, the roughening of porous low-k films can be divided into three regimes according to the polymerization capability of the plasma: net deposition regime, "clean" etching regime and local polymer deposition regime. The surface remains smooth after etching in the net deposition regime. For instance, the RMS roughness of porous low-k film is about 1.0 nm after etching in 40% C_2F_6/Ar plasma. In the "clean" etching regime, the plasma polymerization effects are trivial and surface after etching becomes moderately rougher. Etching of porous low-k film in 10% C_2F_6/Ar plasma falls into this regime where the RMS roughness after etching is 2.2 nm. In the local polymer deposition regime, the surface becomes much rougher after etching. The etching of porous low-k film in 20% C_2F_6/Ar plasma (RMS values goes up from 1.2 nm before etching to 9.0 nm) is an example of this regime.

6.7 Local Polymer Deposition Induced Micro-masking Roughening Mechanism

The surface roughening of low-k films during etching in fluorocarbon plasmas can be explained by a polymerization-induced micro-masking mechanism, which is shown schematically in Figure 6-11. The porous structure in the substrate plays a critical role in the film roughening evolution. The pores at the near surface region in the substrate allow the deposition of fluorocarbon polymers within the protected recesses of the pores, which are shielded from ion bombardment. Consequently, local polymer-rich regions form on the surface. It is commonly observed that fluorocarbon rich surfaces etch more slowly than oxide rich surfaces during exposure to the same plasma fluxes. Under the condition of high selectivity, it has been observed that polymer is deposited on the fluorocarbon surfaces while etching occurs on the oxide surfaces. Under these particular conditions, it is believed that that the polymer-rich regions grow while the OSG-rich regions etch. With time, the polymer-rich regions form micro-masks that induce roughening.

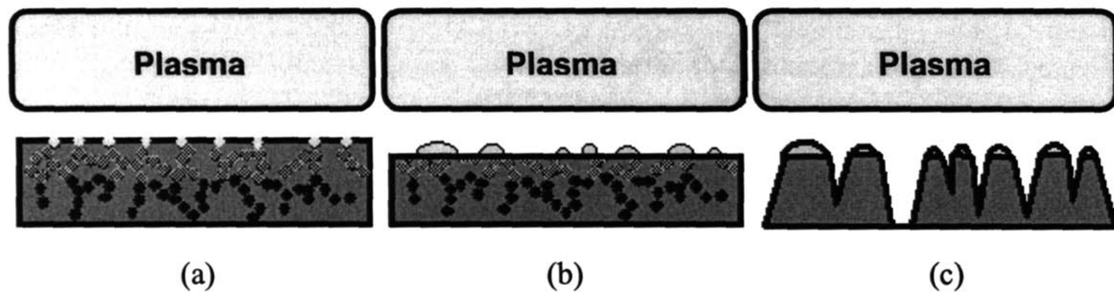

Figure 6-11 Pore filling seeds micromask formation on porous low-k film. (a) The polymer fills into the pores; (b) Simultaneous etching of the porous low-k film forms polymer micromasks even under conditions of high ion bombardment; (c) Selectivity between the deposited polymer and the substrate roughens the surface.

The surface roughness evolution of solid OSG is very different with porous low-k film because of the absence of a porous structure in the substrate. Only a very thin layer/amount of polymer forms on the surface of solid OSG in the net etching regime. The polymer deposition inhomogeneity is not significant to trigger the formation of polymer-rich and OSG-rich regions to roughen the surface.

This proposed polymer deposition induced micro-masking roughening mechanism explains the experimental results. First, it demonstrates why porous low-k film becomes rougher when the etching time is longer while solid OSG doesn't become rougher after

etching in 20% C_2F_6/Ar plasma, as shown in Figure 6-3 and Figure 6-4. Since the etching kinetics in 20% C_2F_6/Ar plasma is in the local polymer deposition regime as mentioned in Chapter 6.6, the inhomogeneity caused by local polymer deposition becomes more significant when the etching time is longer and, consequently, the surface becomes rougher after etching. In contrast, the amount of polymer accumulated on the surface of solid OSG is small and doesn't change with etching time because of the absence of pores; the surface remains smooth after etching for different time scales. Second, this micro-masking mechanism explains why the roughening of porous low-k films can be divided into three regimes according to the polymerization capability of the plasma. A fairly thick layer of polymer is deposited on the substrate surface when net deposition is prevalent on both films; the micro-masking roughening mechanism is not in effect, the surface of both films remains smooth after etching, and the RMS roughness values are almost identical to each other. Minor polymer deposits on the substrate surface in the "clean" etching regime; the micro-masking mechanism, if it exists, is not very important. Interestingly, slightly more polymer is accumulated on the porous low-k film surface and the surface after etching becomes moderately rougher. Appropriate amounts of polymer are retained on the porous low-k film, which makes the micro-masking mechanism very significant and leads to a much rougher surface after etching. Similarly, the totally different roughness evolution trend between solid OSG and porous low-k films is caused by the porous structure. Third, the roughening of both films as a function of ion bombardment energies is also consistent with this micro-masking mechanism. It has been mentioned in Figure 6-6(b) that the roughness of porous low-k film scales with ion energy, while for solid OSG it does not. Interestingly, the roughness of porous low-k film after etching in the net etching regime is mainly related to the amount of film removed, as indicated in Figure 6-12. This is because the polymer deposition induced inhomogeneity on porous low-k substrate is more significant after more material is removed according to the micro-masking mechanism. This argument is again not applied to solid OSG film because of the absence of porous structure in the substrate; consequently, the surface remains smooth no matter how much material is removed.

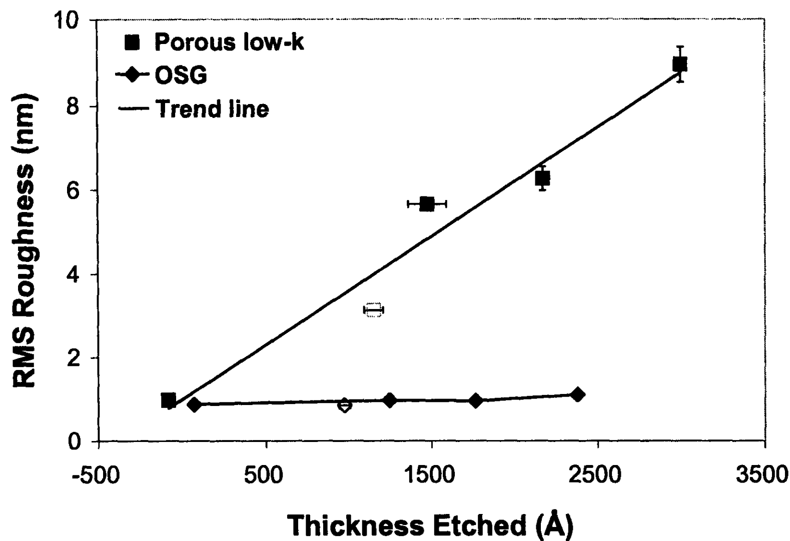

Figure 6-12 The variation of surface roughness of (♦,◊) solid OSG and (■, □) porous low-k films after processing in 20% C_2F_6/Ar plasma at normal impingement angle. Plasma etching conditions: total flow rate 5 sccm, beam source pressure 10 mtorr, RF source power 350 W; ion fluence 5.0×10^{17} ions/cm^2 for close symbols and 2.0×10^{17} ions/cm^2 for open symbols.

6.8 Surface Roughening during Etching at Grazing Angles

Surface kinetics of low-k film etching at a grazing angle can be achieved by adjusting the angle between the ion impingement direction and surface normal, which is defined as off-normal angle. Figure 6-13 gives the surface topography evolution of OSG and porous low-k films after etching at a grazing angle in C_2F_6/Ar plasma chemistry. The ion dosage levels are measured at normal angle and corrected to the corresponding view factor at 75° off-normal angle. Most surprisingly, a striation structure parallel to the ion beam impingement direction emerges. The striation structure on the porous low-k film is more significant than that on the solid OSG film.

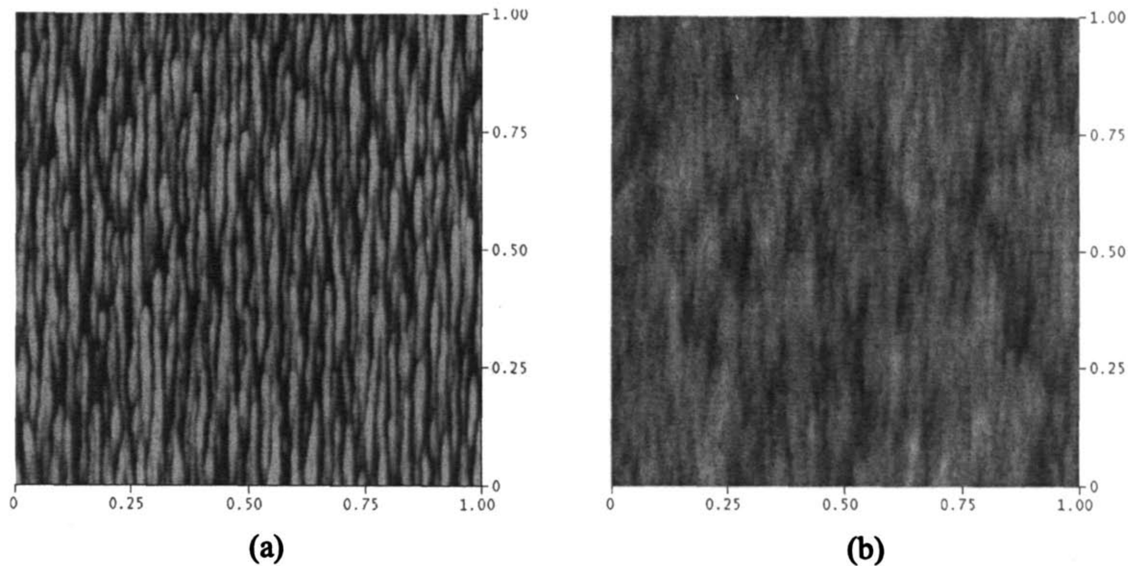

Figure 6-13 The surface roughness of (a) porous low-k films and (b) solid OSG films after etching in 20% C_2F_6/Ar plasma beam at 75° off-normal angle. The beam direction is parallel to the striation structure and is from bottom to top. Plasma etching conditions: total flow rate 5 sccm, beam source pressure 10 mtorr, RF source power 350 W, ion energy is 340 eV. The vertical scale is 20 nm for both AFM images and RMS roughness is 2.7 nm for porous low-k and 0.5 nm for solid OSG film. The real ion fluence is 1.3×10^{17} ions/cm^2, which is measured at normal impingement angle and corrected to the view factor at 75° off-normal angle.

A possible explanation of the striation formation on the substrate during etching at glancing angle is related to the shadowing effects. As is well known, the substrate surface is not perfectly smooth; indeed, there are some micro-size cones, pyramids, or ridges on the surface. These micro-structures might show some shadowing effect at the initial stage of the etching, as shown in Figure 6-14. Due to the very glancing angle formed by the beam ions, areas of the surface directly behind a protrusion receive no flux. Consequently, this portion of the surface could not be etched during etching and, therefore, some specific shadowing structure formed and will be propagated along the beam direction. Finally, the striation structure forms on the surface.

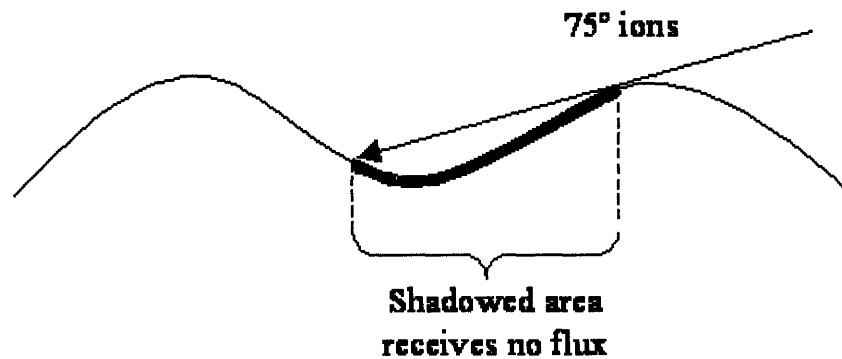

Figure 6-14 The schematic of "shadowed" sample area with near- glancing ions at 75°. Due to the very glancing angle formed by the beam ions, areas of the surface directly behind a protrusion receive no flux. This occurs when the angle formed by the surface normal and incident ion direction exceeds 90°.

There is a good way to check if the proposed shadowing effect is reasonable or not. As has been mentioned previously, uniform polymerization will be prevalent when the DC-bias level is low enough for the etching of porous low-k film at normal angle in 20% C_2F_6/Ar plasma chemistry. Net polymerization can also be achieved for the etching of porous low-k film in C_2F_6/Ar chemistry at glancing angle (off-normal angle is 75°); the AFM image of the etching under this condition is shown in Figure 6-15. Most importantly, the shadowing effect is not possible because of net polymerization. As an impact, the striation structure is quenched and isotropic roughness results. Additionally, the RMS roughness of the substrate after etching becomes smoother compared to the pre-etched porous low-k film.

Although polymerization can quench the striation structure, it is not crucial for the origin of the striation formation, at least under these conditions. Figure 6-16 gives the surface topography evolution of porous low-k after sputtering in pure Ar chemistry with real ion fluence level of 1.5×10^{17} ions/cm^2. As can be observed from the AFM images, the striation structure is developed at glancing angle using only Ar sputtering, which does not have any polymerization capability. As a result, the polymerization effect is not the key factor for striation formation when etching at grazing angle. Additionally, this striation structure can also be formed on solid substrates, as discussed in Chapter 4.

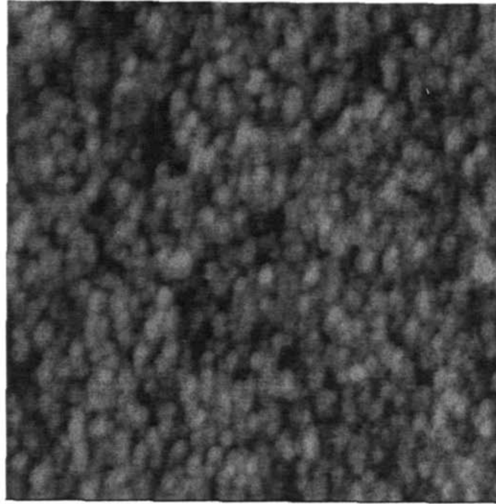

Figure 6-15 The AFM image of porous low-k film after etching at grazing 75° off-normal angle in 20% C_2F_6/Ar plasma in the beam chamber system. 110 eV ions were used (DC bias level 100 V) and the vertical scale of the image is 10 nm. The surface topography after etching is very smooth and no striation structure is available. The RMS roughness is 0.8 nm.

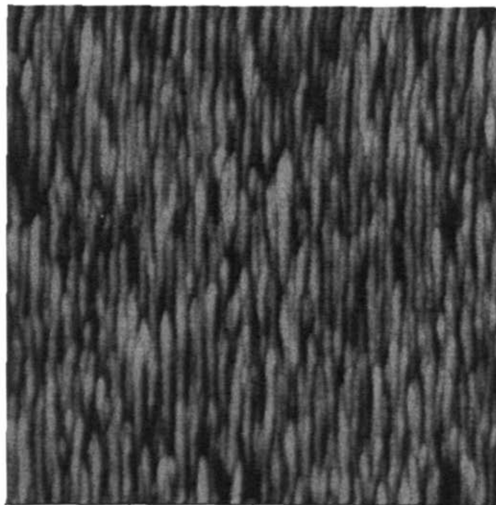

Figure 6-16 The surface topography of porous low-k after sputtering in pure Ar chemistry at 75° off-normal angle with real ion fluence level 1.5×10^{17} ions/cm^2. The ion energy level is about 340 eV and the vertical scale is 20 nm. The RMS roughness after etching is 2.3 nm.

6.9 Conclusions

A plasma beam chamber system has been used to characterize surface roughening of low-k films in fluorocarbon beams. A polymerization-induced micro-masking

mechanism was proposed to explain the surface roughening of porous low-k films. The porous structure in the substrate plays a critical role in the film roughening evolution. Pores at the near surface enhance the fluorocarbon thin film, which is not necessarily continuous. Polymeric deposition etches more slowly under fluorocarbon plasma exposure and forms micro-masks that induce roughening. On the contrary, only a very thin layer/amount of polymer forms on the surface of solid OSG in the net etching regime under the plasma running condition in this work. Therefore, the polymer deposition induced inhomogeneity is not significant enough to roughen the surface. This local polymer deposition induced micro-masking mechanism explains the surface roughness evolution of porous low-k and solid OSG films as a function of etching time, ion bombardment energies, and the plasma polymerization capabilities.

6.10 References

[1] Y. N. Chen, R. Myricks, M. Decker, J. Liu, and G. S. Higashi, Ieee Electron Device Letters 24, 295-297 (2003).

[2] C. H. Diaz, H. J. Tao, Y. C. Ku, A. Yen, and K. Young, Ieee Electron Device Letters 22, 287-289 (2001).

[3] D. J. Norris, A. G. Cullis, S. H. Olsen, A. G. O'Neill, and J. Zhang, in *Microscopy of Semiconducting Materials 2003* (2003), p. 389-392.

[4] A. Yamaguchi, H. Fukuda, H. Kawada, and T. Iizumi, Journal of Photopolymer Science and Technology 16, 387-393 (2003).

[5] R. H. Havemann and J. A. Hutchby, Proceedings of the Ieee 89, 586-601 (2001).

[6] K. Maex, M. R. Baklanov, D. Shamiryan, F. Iacopi, S. H. Brongersma, and Z. S. Yanovitskaya, Journal of Applied Physics 93, 8793-8841 (2003).

[7] L. L. Chapelon, V. Arnal, M. Broekaart, L. G. Gosset, J. Vitiello, and J. Torres, Microelectronic Engineering 76, 1-7 (2004).

[8] M. Fayolle, G. Passemard, O. Louveau, F. Fusalba, and J. Cluzel, Microelectronic Engineering 70, 255-266 (2003).

[9] B. D. Lee, Y. H. Park, Y. T. Hwang, W. Oh, J. Yoon, and M. Ree, Nature Materials 4, 147-U26 (2005).

[10] B. Z. Li, T. D. Sullivan, T. C. Lee, and D. Badami, Microelectronics Reliability 44, 365-380 (2004).

[11] M. Morgen, E. T. Ryan, J. H. Zhao, C. Hu, T. H. Cho, and P. S. Ho, Annual Review of Materials Science 30, 645-680 (2000).

[12] A. M. Padovani, L. Rhodes, L. Riester, G. Lohman, B. Tsuie, J. Conner, S. A. B. Allen, and P. A. Kohl, Electrochemical and Solid State Letters 4, F25-F28 (2001).

[13] K. N. Tu, Journal of Applied Physics 94, 5451-5473 (2003).

[14] D. Eon, V. Raballand, G. Cartry, M. C. Peignon-Fernandez, and C. Cardinaud, European Physical Journal-Applied Physics 28, 331-337 (2004).

[15] S. W. Hwang, G. R. Lee, J. H. Min, S. H. Moon, Y. C. Kim, H. K. Ryu, Y. S. Cho, and J. W. Kim, Japanese Journal of Applied Physics Part 1-Regular Papers Short Notes & Review Papers 41, 5782-5786 (2002).

[16] N. Posseme, T. Chevolleau, O. Joubert, and L. Vallier, Journal of Vacuum Science & Technology B 21, 2432-2440 (2003).

[17] T. Standaert, E. A. Joseph, G. S. Oehrlein, A. Jain, W. N. Gill, P. C. Wayner, and J. L. Plawsky, Journal of Vacuum Science & Technology a-Vacuum Surfaces and Films 18, 2742-2748 (2000).

[18] S. A. Vitale, H. Chae, and H. H. Sawin, Journal of Vacuum Science & Technology A 18, 2770-2778 (2000).

[19] S. A. Vitale and H. H. Sawin, Journal of Vacuum Science & Technology a-Vacuum Surfaces and Films 20, 651-660 (2002).

[20] D. Shamiryan, M. R. Baklanov, S. Vanhaelemeersch, and K. Maex, Journal of Vacuum Science & Technology B 20, 1923-1928 (2002).

[21] H. Nagai, S. Takashima, M. Hiramatsu, M. Hori, and T. Goto, Journal of Applied Physics 91, 2615-2621 (2002).

[22] J. N. Sun, Y. F. Hu, W. E. Frieze, W. Chen, and D. W. Gidley, Journal of the Electrochemical Society 150, F97-F101 (2003).

[23] Y. S. Zheng, Y. J. Su, B. Yu, and P. D. Foo, Microelectronics Reliability 43, 1311-1316 (2003).

[24] D. L. Goldfarb, A. P. Mahorowala, G. M. Gallatin, K. E. Petrillo, K. Temple, M. Angelopoulos, S. Rasgon, H. H. Sawin, S. D. Allen, M. C. Lawson, and R. W. Kwong, Journal of Vacuum Science & Technology B 22, 647-653 (2004).

[25] S. A. Rasgon, Ph.D. Thesis, Massachusetts Institute of Technology, 2005.

[26] J. H. Scofield, Journal of Electron Spectroscopy and Related Phenomena 8, 129-137 (1976).

[27] M. Schaepkens and G. S. Oehrlein, Journal of the Electrochemical Society 148, C211-C221 (2001).

[28] T. Standaert, C. Hedlund, E. A. Joseph, G. S. Oehrlein, and T. J. Dalton, Journal of Vacuum Science & Technology A 22, 53-60 (2004).

[29] L. Zheng, L. Ling, X. F. Hua, G. S. Oehrlein, and E. A. Hudson, Journal of Vacuum Science & Technology A 23, 634-642 (2005).

[30] J. J. Vegh, D. Humbird, and D. B. Graves, Journal of Vacuum Science & Technology A 23, 1598-1604 (2005).

[31] H. H. Sawin, (unpublished).

[32] C. R. Eddy, D. Leonhardt, S. R. Douglass, B. D. Thoms, V. A. Shamamian, and J. E. Butler, Journal of Vacuum Science & Technology a-Vacuum Surfaces and Films 17, 38-51 (1999).

[33] M. J. Barela, H. M. Anderson, and G. S. Oehrlein, Journal of Vacuum Science & Technology A 23, 408-416 (2005).

[34] A. N. Goyette, Y. C. Wang, M. Misakian, and J. K. Olthoff, Journal of Vacuum Science & Technology A 18, 2785-2790 (2000).

Chapter 7. Statistical Analysis of Plasma-etched Surfaces: Power Spectral Density and Geostatistical Methods

The power spectral density (PSD) and geostatistical semivariogram analyses were applied to analyze the surface topography of etched surfaces. These two methods are advantageous since both vertical and lateral information of a given surface were used, unlike the root mean squared (RMS) roughness where only the vertical height variation was considered. It was demonstrated that the spatial variation of horizontal structures on etched surfaces can be characterized quantitatively with the assistance of these two statistical methods. In particular, the PSD analysis showed that the AFM tip filtering effects became important beyond a critical spatial frequency. Furthermore, the average length of the striation structures along the directions parallel or perpendicular to the streaks could be quantified using geostatistical semivariogram method. In addition, the average periodicity along X direction (perpendicular to the streaks) from these two methods was consistent, indicating that these two statistical methods were reliable for surface roughness analysis on the etched surfaces.

7.1 Introduction

As the feature key dimension continues shrinking down to sub-100 nm regime, feature surface roughening becomes more and more important because it might affect the device performance significantly. At the front end side, the sidewall roughness present in the final etched gate can affect the implant profile of the source and drain regions of the transistor, consequently, change the effective gate length. Charge carrier mobility can also be degraded via electron scattering[1]. On the back end, sidewall roughness can degrade the resolution of contacts, interfere with the deposition of conformal liner materials, and potentially lead to short circuits between adjacent metal lines or contacts[2,3].

Quantification of the surface roughness on the etched feature surfaces requires an instrument that can capture the structures at nanometer scale. AFM is one of the most efficient tools applied due to its wide range of lateral measurements. Generally, an AFM working at tapping mode has a lateral resolution of 10 nm and a vertical noise level about 0.1 nm. The methods of interpreting the AFM images, however, are diverse and some

useful information might be ignored during data processing depending upon the specific methods selected. In the literature[4-7], Root-Mean-Squared (RMS) roughness is the most commonly used statistical method to characterize the roughness level on the etched feature surfaces. Regardless its popularity, only vertical height information is used to estimate the RMS roughness level and all of the horizontal information is ignored. Therefore, the anisotropy and spatial variation on the etched surfaces shown in previous chapters can not be measured and compared using this method. Even worse, it has been demonstrated that two images with exactly the same RMS roughness level may have totally different surface topography[8]. Furthermore, the effects of anisotropy (such as the spatial variation) on device properties have been proved in the literature [9-11]. Consequently, statistical methods that include both the vertical information and lateral characteristics should be applied to the analysis of the AFM images in order to interpret the etched surfaces accurately and faithfully.

Power Spectral Density (PSD) method, that converts the information contained in the AFM image from spatial domain to frequency domain, is one of the statistical methods that use both the vertical and lateral information. Most importantly, it allows analyzing the roughness at different spatial frequencies. However, it is not straightforward to capture the spatial variation (such as the striation structures in Chapter 4) in this method.

In geostatistics, semivariance analysis is applied to analyze the landscape topography variation over a broad length scale, from meters to thousands of kilometers. Without any further modification, this statistical method can be used to analyze the etched surfaces over the range of nanometers to a few microns. Very excitingly, both the spatial periodicity and the structure length can be interpreted quantitatively when using this method.

In this chapter, the PSD and semivariance statistical methods were applied to analyze the etched surfaces under different conditions. In particular, the sensitivity of the RMS roughness to the spatial frequency was quantified using PSD method; the variation of striation periodicity (perpendicular to the striation direction) and length of the streaks (parallel to the striation direction) were analyzed by semivariance method. Moreover, the

impact of processing conditions, such as the etching time, on the development of striation structures was discussed.

7.2 Theory

7.2.1 Power Spectral Density Analysis

The PSD analysis is often used to represent the spatial frequency content of the surface roughness in the literature, which describes two aspects of the surface roughness such as the height variation over vertical and lateral dimensions. For this reason, PSD method represents a surface much better than RMS roughness. In principle, obtaining the PSD from measured surface profile data (e.g. AFM images) is straightforward. Using Fourier transformation, the surface cross section data profile can be decomposed into sinusoids of different frequency which sum to the original surface profile. The one-dimensional PSD can be estimated by taking the square of the Fourier transformation of the surface profile. Assuming the cross section data profile along a specific direction on a given AFM image is $h(x)$, the 1D PSD can be calculated as [12]

$$P_{1D}(f) = \lim_{L\to\infty}\left|\int_{-\frac{L}{2}}^{\frac{L}{2}} h(x)e^{-i2\pi xf}dx\right|^2, \tag{7-1}$$

where L represents the scan size at the specific direction during AFM measurement, and f is the frequency of the sinusoidal waves.

In my AFM measurements, only a finite number of values of h(x) were measured at equidistant points, x_k, separated by a distance of Δx. Consequently, the 1D PSD at the spatial frequency $f_j = j\Delta f$ can be approximated by[12]

$$P_{1D}(f_j) = \frac{\Delta x}{N}\left|\sum_{k=1}^{N} h(x_k)\exp(-i2\pi jk/N)\right|^2, \tag{7-2}$$

where $j = 1,2,...\frac{N}{2}$. Δf is the frequency difference of two adjacent sinusoidal waves which is always taken as unity, therefore, it is not shown in the equation above.

According to Parseval's theorem in Fourier Theory[13], the power of a signal represented by a function of $h(x)$ is the same whether estimated in signal space or frequency (transform) space. For this reason, the RMS surface roughness can be calculated from either spatial domain or frequency domain. Consequently[14],

$$\delta^2 = \sum_{j=1}^{N/2} P_{1D}(f_j)\Delta f, \tag{7-3}$$

where δ is the RMS roughness.

Encouragingly, the sensitivity of RMS roughness on frequency f_j can be easily analyzed based upon equation (7-3). Indeed, the contribution of a given frequency f_j to the RMS roughness can be described as

$$\delta_{f_j}^2 = P_{1D}(f_j). \tag{7-4}$$

It seems really promising to apply the PSD analysis on a given AFM image to explore the surface roughness in both vertical and lateral dimensions. In particular, the RMS roughness sensitivity to a specific spatial frequency can be studied. Moreover, PSD analysis is also a powerful tool to remove the AFM artifacts of a given AFM image, such as the acoustic noise, as reported by Fang et al.[15]. Furthermore, PSD analysis is helpful to determine the effect of AFM tip size and image scan size[15]. In current research, the image scan size is 1 μm × 1 μm, and a surface will always be measured by at least two different sharp tips with a tip radius less than 10 nm. Therefore, the effects of these two factors were always kept at the minimal levels.

7.2.2 Geostatistical Analysis

In geostatistics, spatial patterns are usually described in terms of dissimilarity between observations as a function of the separation distance (lag distance). The average dissimilarity between data separated by a lag vector h is quantified as semivariogram, $\gamma(h)$. Mathematically, $\gamma(h)$ is calculated as half of the average squared difference between the compoments of each data pair[16-18],

$$\gamma(h) = \frac{1}{2N(h)} \sum \left[z(x) - z(x+h)\right]^2, \tag{7-5}$$

where $N(h)$ is the number of data pairs of lag vector h.

Essentially, semivariogram analysis examines the contribution of the average variance of all pairs of points that are separated by a specific lag distance to the total sample variance. Specifically, adjacent objects are compared first, then every other object, then every third and so on. The lag vector h ranges from 1(adjacency) to a maximum of one-half of the spatial size of the data set since larger lags eliminate points from the analysis.

It is a principle in geography that nearby points on a surface are more closely related than those widely separated. Consequently, in a typical plot of semivariogram as a function of lag vector h, the semivariogram usually increase from a theoretical Y intercept of zero, and level off at the maximum semivariance (the sill), which occurs at and beyond a particular lag distance (the range). The range identifies the distance beyond which data pairs no longer exhibit spatial autocorrelation.

Figure 7-1 and Figure 7-2 show the typical semivariogram plots on a surface. For an isotropic surface, as shown in Figure 7-1, the semivariogram increases with the lag distance until the critical lag distance (range, *a*), beyond which the semivariogram is leveled off at the maximum semivariance (sill, *C*). The numerical values of *a* and *C* can be estimated by fitting the semivariance experimental data with semivariogram models. One of the most commonly used models is the spherical model[16,19], as shown in equation (7-6),

$$\gamma(h) = \begin{cases} \frac{3}{2}C\left(\frac{h}{a}\right) - \frac{1}{2}C\left(\frac{h}{a}\right)^3, & h \le a \\ C, & h \ge a \end{cases} \tag{7-6}$$

where a is the range, C is the sill, and h is the lag distance.

On an anisotropic surface with a series of parallel streaks, the semivariogram across the parallel streaks shows similar characteristics, but has waviness structure at the leveled-off regime where the semivariance oscillates around the mean sill value, as shown in Figure 7-2. The lag distance to the first minimum after the first maximum, defined as parameter *mindist*[20], provides a way to measure the average spacing between parallel streaks on the surface. This is extremely useful since it provides a possible systematic way

to quantify the striation structure on the etched surfaces at grazing ion bombardment angles, as shown in previous chapters.

As has been mentioned previously, semivariogram analysis is often applied to analyze the landscape topography variation over a broad length scale, from meters to thousands of kilometers. Without any further modification, this statistical method can be used to analyze the etched surfaces over the range of nanometers to a few microns. The resulting AFM image of an specific etched surface is essentially a 2-dimensional plot of the height information at different X and Y locations, noted as $z(x_i, y_i)$. By performing semivariogram analysis at desired directions (X or Y), the spatial variation of the surface at each direction can be investigated following the same strategy developed in geostatistics.

One may argue that spatial autocorrelation analysis can be applied to estimate the average spacing of the striation structures on the surface, rather than using the semivariogram method adopted from geostatistics. The autocorrelation function (ACF) between series related measurements is defined as[21],

$$r_k = r(z(x_t), z(x_{t+k})) = \frac{\sum (z(x_t) - \bar{z})(z(x_{t+k}) - \bar{z})}{\sum (z(x_t) - \bar{z})^2}, \tag{7-7}$$

where r_k denotes the ACF, and $\bar{z}$ represents the mean height of all the data points under investigation.

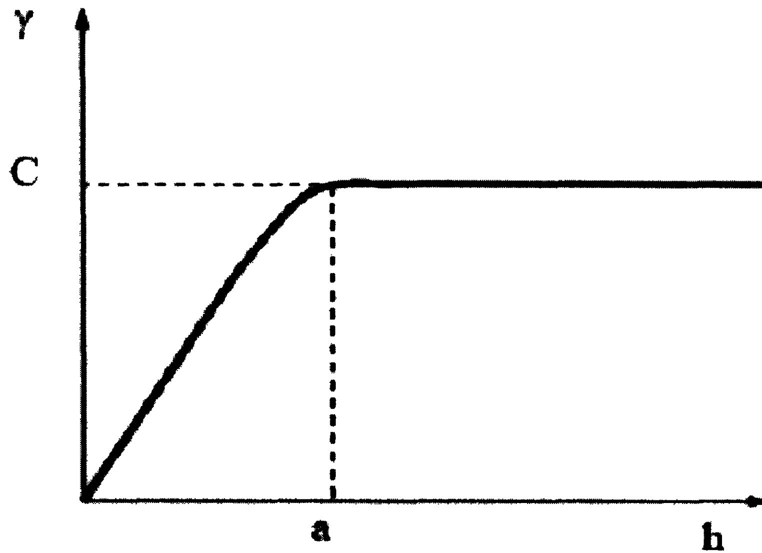

Figure 7-1 Ideal semivariogram on an isotropic surface where the sill (C) and the range (a) are shown.

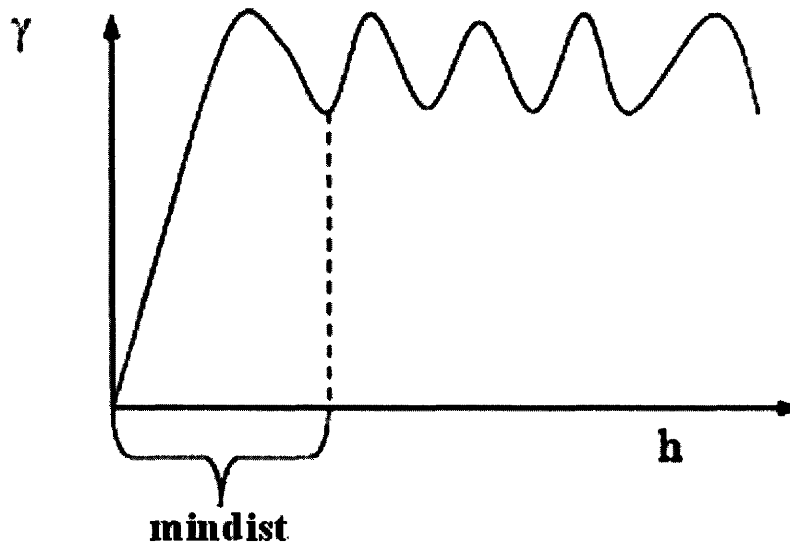

Figure 7-2 Semivariogram of a anisotropic surface where a series of parallel streaks exist, taken in the direction across the streaks. The lag distance to the first minimum (mindist) can be interpreted as the average spacing of the ridges.

In fact, autocorrelation and semivariogram are two different statistical methods based upon the same concepts. Semivariogram analysis describes the dissimilarity between data separated by a lag distance, h. On the contrary, autocorrelation analysis quantifies the correlation (similarity) between two data points separated by a lag distance, h. Therefore, within the range (a), the ACF decreases while the semivariogram function

increases with the lag distance. Beyond the critical range (*a*), there is no autocorrelation between two data points in which I am interested, therefore, the ACF is around 0. Similarly, the semivariogram function is leveled off at the maximum semivariogram. Consequently, identical conclusions would be resulted when appling these two methods to the same surface. Figure 7-3 describes the ACF (dashed line) and the semivariogram (solid line) as a function of the lag distance across the striation structure. Not surprisingly, the range derived from both methods is around 85-90 nm. Within this range, the semivariogram increases and the ACF decreases with the lag distance.

(a)

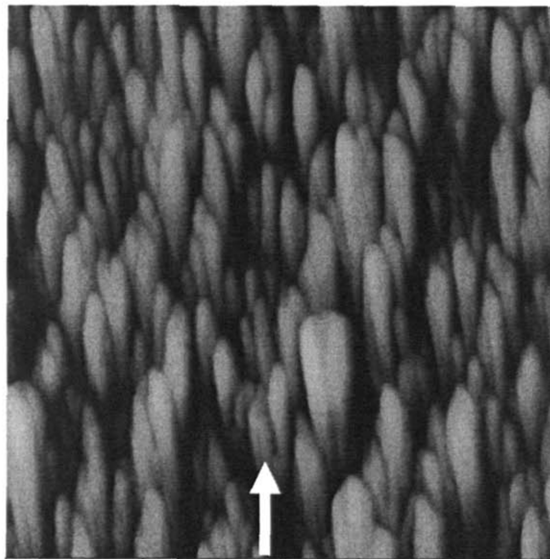

(b)

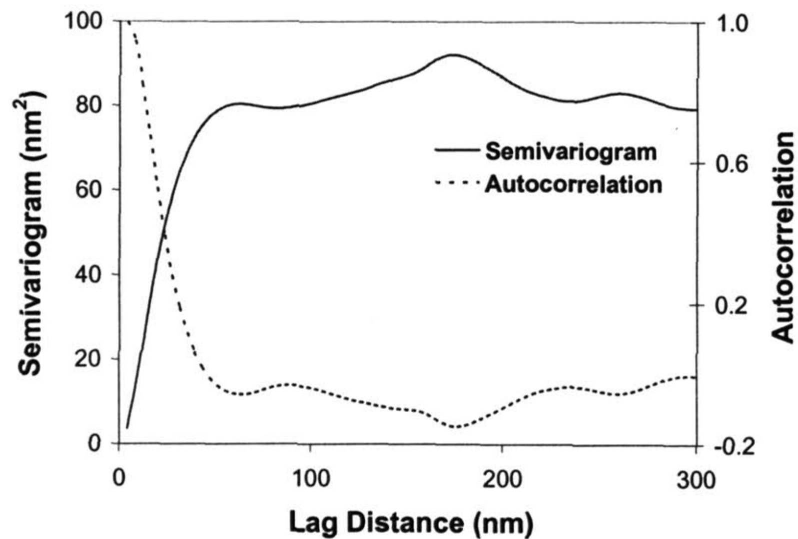

Figure 7-3 Comparison between the autocorrelation and semivariogram analysis on the sputtered coral film in Ar plasma at 75° ion bombardment off-normal angle.

7.3 Results and Discussion

7.3.1 Impact of Etching Time on the Striation Structure

As has been demonstrated in Figure 4-10 in Chapter 4, the RMS roughness of coral and thermal silicon dioxide films after etching at grazing angles increased with the film thickness etched, or equivalently, the etching time. It turns out that not only the RMS roughness increases with the etching time, but also the striation structure development along the ion bombardment direction varies significantly with the increase of etching time, as demonstrated in Figure 7-4.

Since RMS roughness only considers the vertical height information, the striation structure along the lateral dimension on the surface could not be captured in RMS roughness level. In order to demonstrate that the spatial variation of the striation structure can be characterized quantitatively, the PSD and geostatistical semivariogram analyses were performed on the AFM images of coral films sputtered in argon plasma for different etching time levels at 75° off-normal angle.

Figure 7-5 summarizes the 1D PSD functions of coral films before and after sputtering in argon plasma, along the direction perpendicular to the streaks. Obviously, the PSD values are much higher at lower spatial frequencies in all cases. Consequently, one can conclude that the RMS roughness is much more sensitive to the structures at lower spatial frequencies, as demonstrated in equation (7-4). Moreover, for all of the three etching time levels, the PSD values on etched coral surfaces keep at relatively constant levels until reaching a critical spatial frequency (f_c), followed by a constant-sloped region where the PSD value decreases quickly with the spatial frequency.

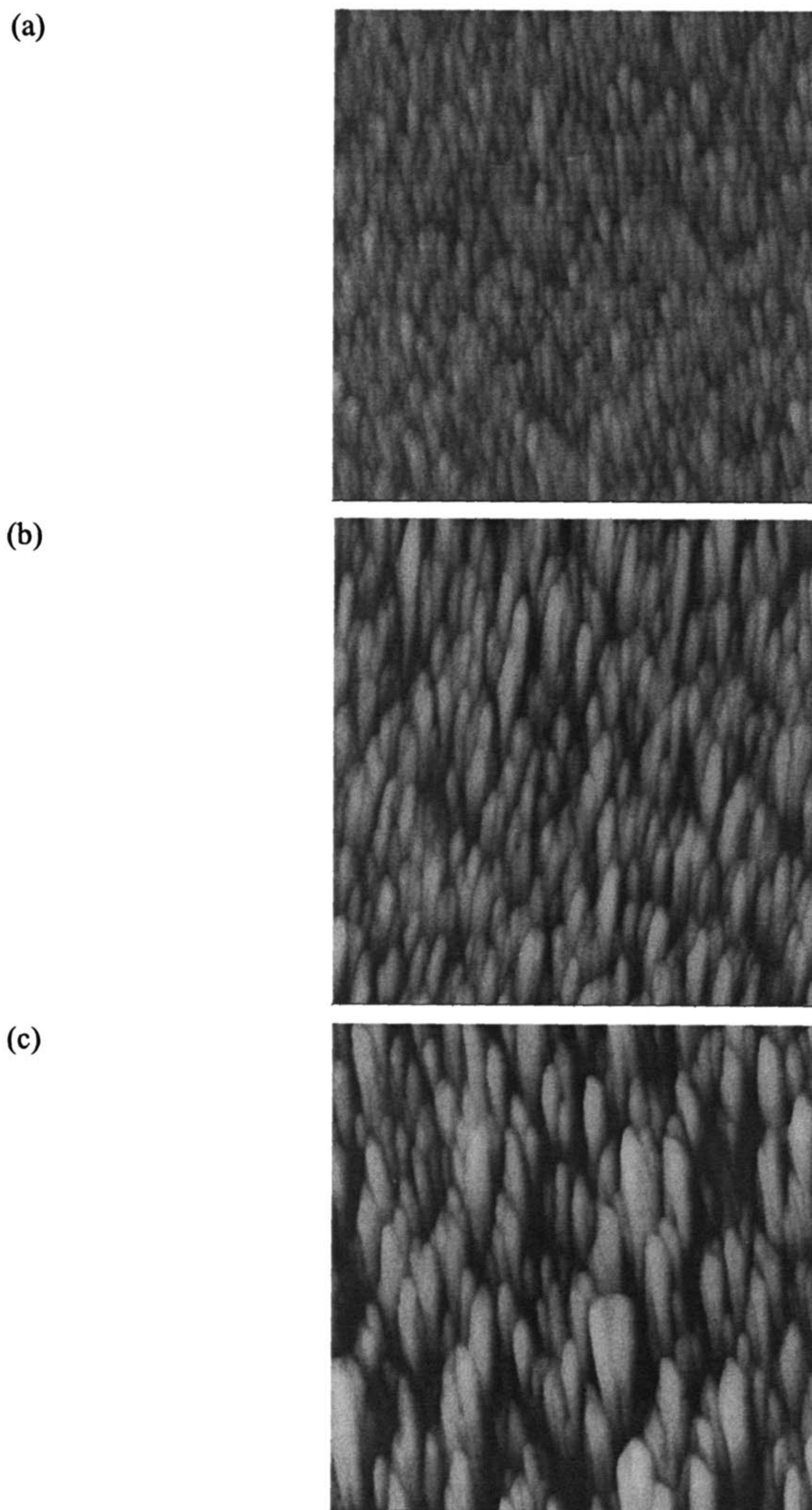

Figure 7-4 The AFM images of coral film, after sputtering in argon plasma for different ion fluence levels at 75° ion bombardment off-normal angle. In all cases, the vertical range is 50 nm. The ion fluence levels are: (a) 1.0×10^{17}, (b) 2.0×10^{17}, and (c) 3.5×10^{17} ions/cm^2.

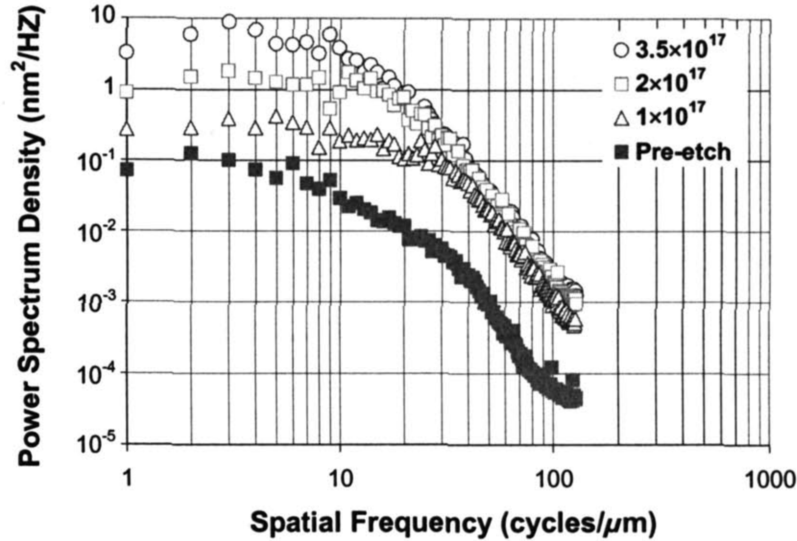

Figure 7-5 The PSD analysis of coral film, along the X direction perpendicular to the streaks, after sputtering in argon plasma for different ion fluence levels at 75° ion bombardment off-normal angle.

The constant slope regimes of the PSD shown in Figure 7-5 indicates self-similar roughness scaling [22,23], a concept used extensively to describe fractal surfaces. Essentially, an object can be self-similar if it is formed by parts that are similar to the whole[24]. For a fractal surface, the fractal dimension D_s, is related to the power spectral density of the surface PSD[22]

$$PSD(f) = \frac{c\eta^{2D_s-3}}{f^{7-2D_s}}, \tag{7-8}$$

where c and η represent the magnitude of the PSD, and the denominator describes the power-law in the fractal regime (the constant-sloped region in Figure 7-5). Therefore, the fractal dimension of a surface can be estimated from the slope (k) of the PSD in the constant-sloped region. In general, D_s ranges from 2 for a perfectly flat surface to 3 for a fully dense three-dimensional object. Therefore, the slope (k) of the constant-sloped region should be between -1 and -3 in order to meet the requirement for D_s. In practice, however, the constant-sloped region might have slopes greater than -3, implying that the high-frequency roughness does not significantly increase the surface area, or equivalently, does not increase the surface roughness obviously. In the current work, the slope (k) of all of the three etched surfaces shown in Figure 7-5 is the same, with a numerical value of -3.7,

indicating that the roughness of the surfaces beyond the critical spatial frequency (f_c) scaled similarly regardless of the size of the streaks.

It is also believed that the AFM tip filtering effect is an important reason causing the fast decrease in the sloped region. Goldfarb et al.[25] introduced a mathematical estimation of the critical frequency (f_c) beyond which the AFM tip filtering effects existed. At the critical spatial frequency, the following relationship is true,

$$\frac{A}{2}\left(\frac{2\pi x}{P_c}\right)^2 = \left(\frac{x^2}{2R}\right), \tag{7-9}$$

where A represents the average amplitude of the surface cross section along the desired direction, P_c denotes the period of the sinusoidal wave at the critical spatial frequency, and R is the AFM tip radius. In particular, the expression on the left side describes the local curvature of the sinusoidal wave, and the expression on the right side represents the local curvature captured by the AFM tip. Physically, equation (7-9) describes that the local curvature measured by the AFM tip is identical to the real surface locally at the critical frequency f_c. Since the scan size of the AFM measurement at the desired directions (X or Y) is 1000 nm, equation (7-8) can be rewritten as

$$f_c = \frac{1000}{2\pi\sqrt{AR}}. \tag{7-10}$$

For the AFM tips involved in current research (Veeco Probes, model RTESP), the tip radius was usually no more than 10 nm. To make it simplified, it was assumed conservatively that the tip radius R was 10 nm. Table 7-1 summarizes the estimation of the critical frequency at different etching time levels, from both the PSD analysis and equation (7-10). It was found that the numerical values of f_c from these two different methods are consistent at all the ion fluence levels. For this reason, it was straightforward to conclude that the AFM tip filtering effect happens at the very beginning of the constant-sloped region. In addition, since the AFM tip filtering effects become significant at the beginning of the constant-sloped region, it is believed that these constant-sloped region of the PSD on etched surfaces is caused by both the self-similarity behavior of fractal surfaces and the AFM tip filtering effects.

Table 7-1 Estimation of the critical spatial frequency beyond which the tip filtering effects exist.

Ion fluence (ions/cm^2)	Amplitude A (nm)	f_c from PSD analysis (cycles/μm)	f_c from equation (7-10) (cycles/μm)
1.0×10^{17}	4-5	26-30	23-25
2.0×10^{17}	8-10	14-17	16-18
3.5×10^{17}	15-18	10-13	12-13
No-etch	1.5-2	--	36-41

It is also noticed that the PSD function of the un-etched surface has quite different characteristics compared to those on etched surfaces, as shown in Figure 7-5. First of all, for the sloped region, there are two different slopes (-1.6, and -3.6, respectively), with a transition frequency (f_t) at around 40 cycles/μm. Not surprisingly, the numerical value of this transition frequency is consistent with the critical frequency (f_c) estimated from equation (7-10), as shown in Table 7-1. Therefore, I believe that the first constant-sloped region (10-40 cycles/μm) is mainly due to self-similarity behavior of fractal surfaces. On the other hand, the second constant-sloped region might be due to both of the self-similarity behavior and the AFM tip filtering effects. In addition, in the sloped region, the magnitude of the PSD values on the un-etched surface is much smaller than on etched surfaces, while at frequency-independent region the difference is not so significant. Based upon equation (7-3) and (7-4), it is therefore concluded that the roughness at high frequencies on pre-etched surface contributes less to the total roughness compared to the etched surfaces.

In order to quantitatively characterize the striation structure developed on the etched surfaces, semivariogram analysis was applied along the directions both perpendicular and parallel to the direction of the streaks, and the results are shown in Figure 7-6 and Figure 7-8, respectively.

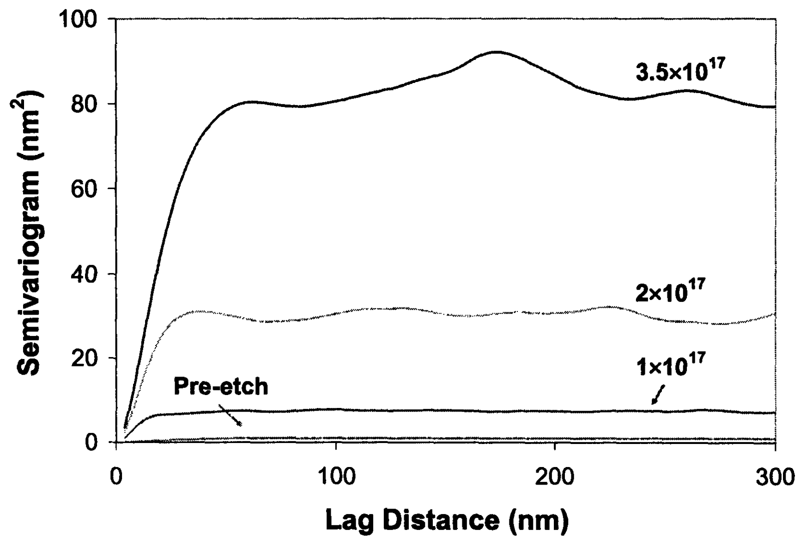

Figure 7-6 The impact of etching time on the semivariogram along the X direction, perpendicular to the striation structure, for coral film after sputtering in argon plasma for different ion fluence levels.

Clearly, the semivariogram function has oscillating characteristics around the mean 'sill' after the range (mindist), along the direction (X direction) perpendicular to the streaks, as demonstrated in Figure 7-6. This makes sense since the surface contains a series of parallel streaks perpendicular to the X direction. More specifically, the lag distance to the first minimum after the first maximum can be interpreted as the average period of the streaks (striation periodicity) along X direction. Figure 7-7 describes the average striation periodicity as a function of the ion fluence level reaching the surface, estimated by both the geostatistical method and the PSD analysis based upon the critical frequency f_c showed in Table 7-1. Not surprisingly, the striation periodicity along X direction increases with longer etching time (or equivalently, the ion fluence reaching the surface), which is consistent with the qualitative observation on the AFM images. Additionally, the average striation periodicity estimated by PSD analysis shows excellent consistency to the observation from the semivariogram geostatistical analysis, which suggests that both of these two statistical methods are helpful to quantify the spatial variation of the striation structure on etched surfaces. Semivariogram analysis, however, is slightly advantageous compared to the PSD method, since it is more straightforward to get the information on the spatial variation of the streaks.

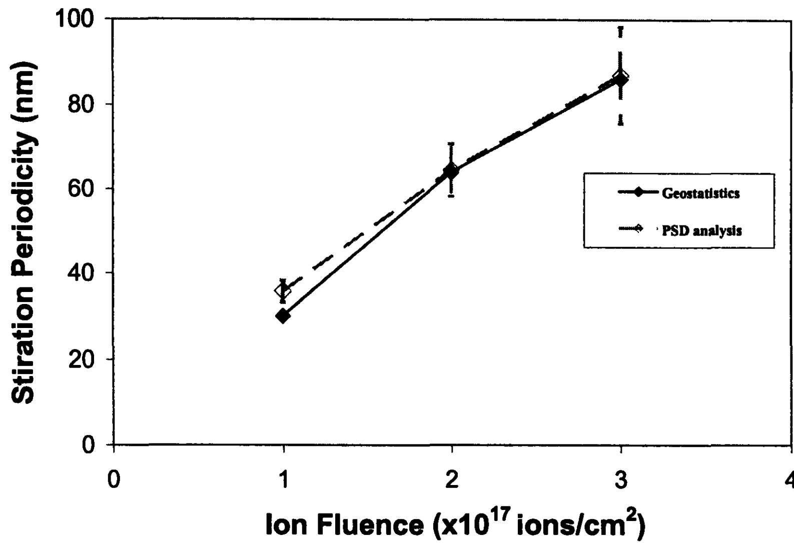

Figure 7-7 The impact of etching time on the average striation periodicity along the X direction, perpendicular to the striation structure, for coral film after sputtering in argon plasma for different ion fluence levels.

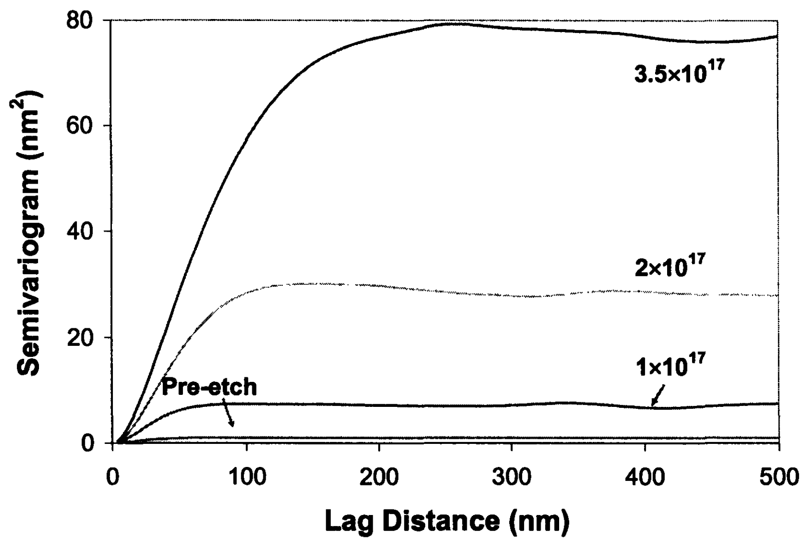

Figure 7-8 The impact of etching time on the semivariogram along the Y direction, parallel to the striation structure, for coral film after sputtering in argon plasma for different ion fluence levels.

The Semivariogram plots along the direction (Y direction) parallel to the streaks, as shown in Figure 7-8, show slightly different behavior, compared with those in the perpendicular direction to the streaks shown in Figure 7-6. Essentially, the semivariogram plots along Y direction increase linearly within the range, then are leveled off at the

maximum value (sill) beyond the range. This behavior is similar to the semivariogram function taken on an isotropic surface. This isotropic behavior along the *Y* direction is reasonable since the striation structures show no specific patterning along *Y* direction, based upon the qualitative observation on the AFM images. Moreover, the range (a) represents the average striation length along *Y* direction. Using the spherical model commonly used in geostatistical semivariogram analysis, the numerical value of the range can be fitted. Therefore, the impact of etching time on the striation length along *Y* direction can be easily quantified, as shown in Figure 7-9. Obviously, the striation length along *Y* direction increases almost linearly with increasing etching time, which is consistent with the observation on the AFM images.

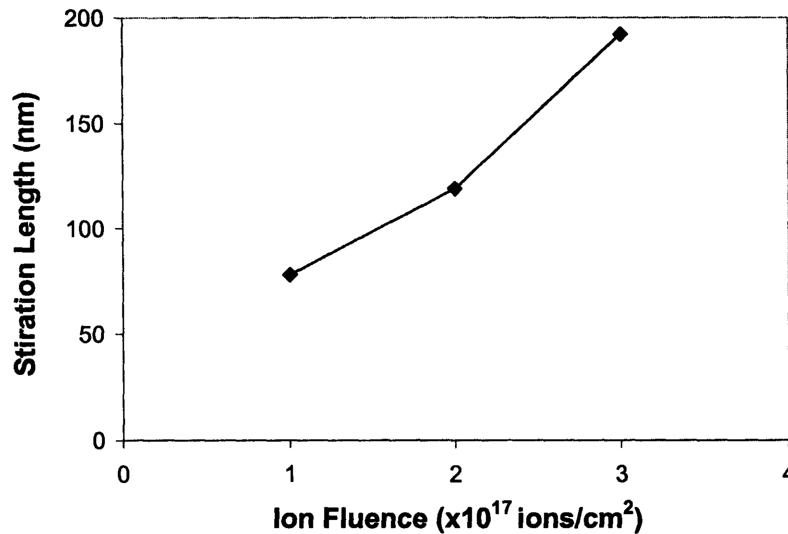

Figure 7-9 The impact of etching time on the average striation length along the Y direction, parallel to the striation structure, for coral film after sputtering in argon plasma for different ion fluence levels.

So far, it has been demonstrated that the etching time has significant impact not only on the RMS surface roughness but also on the spatial variation of the striations, of the etched coral surfaces in argon plasma at 75° off-normal angle. Encouragingly, this impact can be understood quantitatively by applying PSD and geostatistical semivariogram analyses on the AFM images.

7.3.2 Impact of Ion Bombardment Angle on the Striation Structure

As demonstrated in Chapter 4, the striation structure during etching process at grazing angle was influenced by both the etching time and the ion bombardment off-normal angle. Figure 7-10 shows that the AFM images for coral film after sputtering in argon plasma at 75° and 82° off-normal angles, respectively. Obviously, the striation structures are quite different under these two different ion bombardment angles, after receiving approximately the same ion fluence. In particular, the striation length along Y direction (parallel to the streaks) is longer at 82° off-normal angle than at 75° off-normal angle. Additionally, at 82° off-normal angle, the average periodicity of the streaks along X direction (perpendicular to the streaks) is slightly smaller than that at 75° off-normal angle. In short, the striation structures at 82° off-normal angle are more anisotropic. In this section, geostatistical semivariogram analysis is applied to quantify the phenomena described above.

Figure 7-11 and Figure 7-12 show the geostatistical semivariogram analyses on the etched coral film at 75° and 82° off-normal angles along the directions perpendicular and parallel to the streaks, respectively. Along X direction (perpendicular to the streaks), the semivariogram functions (Figure 7-11) show oscillating behavior around the mean sill (C) beyond the range (a) for both ion bombardment off-normal angles, consistent with the observation in the previous section. In particular, based upon the lag distance to the first minimum after the first maximum shown in Figure 7-11, the average striation periodicity along X direction at 82° off-normal angle (35 nm) is smaller than that (64 nm) at 75 ° off-normal angle, as shown in Table 7-2.

(a)

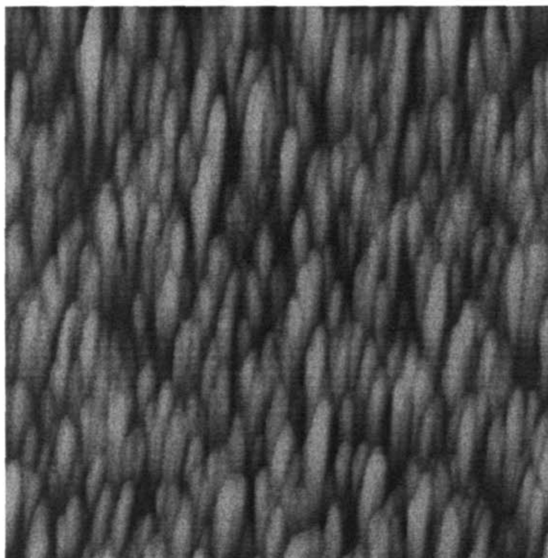

(b)

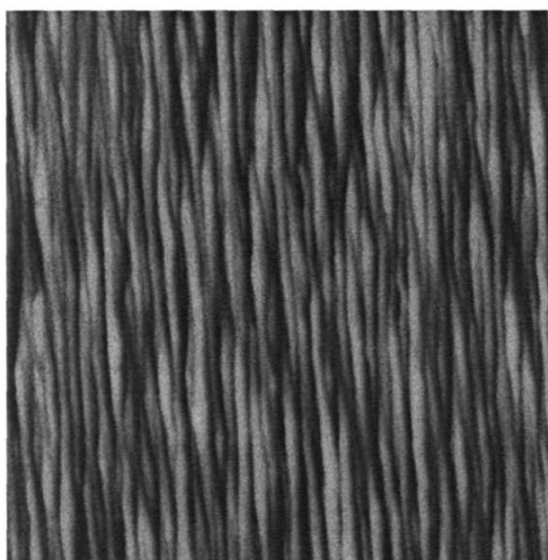

Figure 7-10 The AFM images of coral film, after sputtering in argon plasma for two different ion bombardment off-normal angles. The vertical range is (a) 50 nm and (b) 30 nm. The ion bombardment off-normal angles are (a) 75°, and (b) 82°.

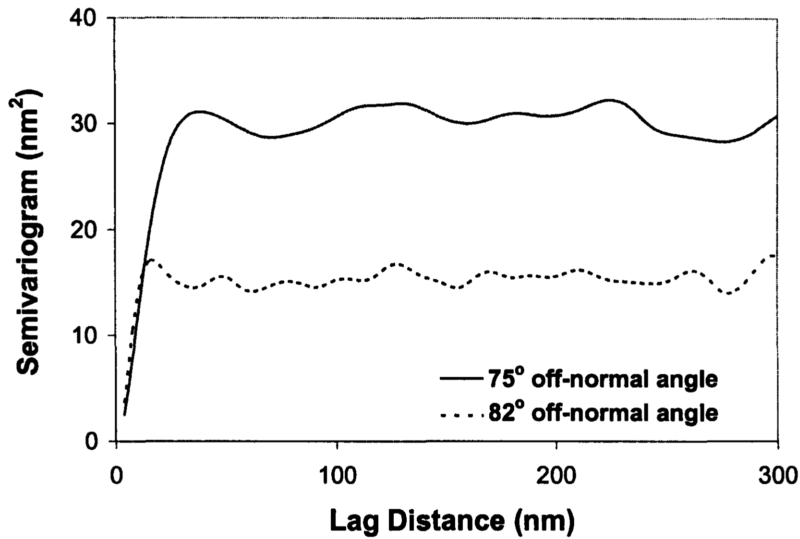

Figure 7-11 The impact of ion bombardment off-normal angle on the semivariogram along the X direction, perpendicular to the striation structure, for coral film after sputtering in argon plasma.

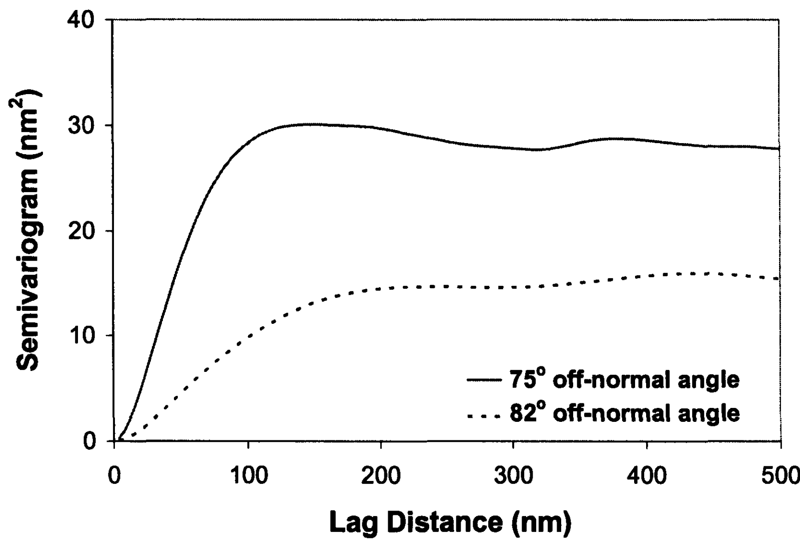

Figure 7-12 The impact of ion bombardment off-normal angle on the semivariogram along the Y direction, parallel to the striation structure, for coral film after sputtering in argon plasma.

Consistently, the semivariogram plots along *Y* direction (parallel to the streaks, shown in Figure 7-12) show no oscillating behavior beyond the range (C) for both ion bombardment angles. Based upon the spherical model fitting, the average striation length along *Y* direction at each ion bombardment off-normal angle was predicted, and the

results are summarized in Table 7-3. As expected, the striation length along Y direction is much higher at 82° off-normal angle (226 nm) than that at 75° off-normal angle (119 nm).

Clearly, the anisotropy of the etched surfaces increased when increasing the ion bombardment off-normal angle from 75 ° to 82 ° off-normal angle. In my analysis, the anisotropy on the surface can be defined as,

$$Anisotropy = \frac{striation\ length}{striation\ periodicity}. \tag{7-11}$$

Since the striation length (Y direction) and the striation periodicity (X direction) have already been summarized in Table 7-2 and Table 7-3, the anisotropy at each ion bombardment off-normal angle can be estimated easily. The anisotropy values at 75° and 82° off-normal angles are 1.9 and 6.5, respectively.

Table 7-2 The impact of ion bombardment off-normal angle on the average striation periodicity along the X direction, perpendicular to the striation structure, for coral film after sputtering in argon plasma.

Off-normal angle (°)	Average periodicity (nm)
75°	64
82°	35

Table 7-3 The impact of ion bombardment off-normal angle on the average striation length along the Y direction, parallel to the striation structure, for coral film after sputtering in argon plasma.

Off-normal angle (°)	Average length (nm)
75°	119
82°	226

7.4 Conclusions

The RMS roughness is not a comprehensive representation of the surface roughness on the etched surfaces since only vertical height information on the AFM images is used. In order to include the surface roughness along the lateral dimension, the power spectral density (PSD) and geostatistical semivariogram methods were introduced to analyze the surface roughness on coral film after sputtering in argon plasma at grazing ion

bombardment angles. It has been demonstrated that both of these two statistical methods were capable to quantify the striation structures on the etched surfaces. In particular, the PSD analysis showed that the AFM tip filtering effects became important beyond a critical spatial frequency. Moreover, the average length of the striation structures along the directions parallel or perpendicular to the streaks could be quantified using geostatistical semivariogram method. In addition, the average periodicity along X direction (perpendicular to the streaks) from these two methods was consistent, indicating that these two statistical methods were reliable for surface roughness analysis on the etched surfaces.

7.5 References

1. A. Pirovano, A. L. Lacaita, G. Ghidini, and G. Tallarida, Ieee Electron Device Letters 21, 34-36 (2000).
2. A. E. Kaloyeros and E. Eisenbraun, Annual Review of Materials Science 30, 363-385 (2000).
3. B. Z. Li, T. D. Sullivan, T. C. Lee, and D. Badami, Microelectronics Reliability 44, 365-380 (2004).
4. B. Kim, S. Kim, and B. T. Lee, Journal of Vacuum Science & Technology B 22, 2467-2472 (2004).
5. A. P. Mahorowala, K. Babich, Q. Lin, D. R. Medeiros, K. Petrillo, J. Simons, M. Angelopoulos, R. Sooriyakumaran, D. Hofer, G. W. Reynolds, and J. W. Taylor, Journal of Vacuum Science & Technology a-Vacuum Surfaces and Films 18, 1411-1419 (2000).
6. L. Ling, X. Hua, X. Li, G. S. Oehrlein, E. A. Hudson, P. Lazzeri, and M. Anderle, Journal of Vacuum Science & Technology B 22, 2594-2603 (2004).
7. Y. P. Yin, S. Rasgon, and H. H. Sawin, Journal of Vacuum Science & Technology B 24, 2360-2371 (2006).
8. S. J. Fang, W. Chen, T. Yamanaka, and C. R. Helms, Applied Physics Letters 68, 2837-2839 (1996).
9. S. D. Kim, H. Wada, and J. C. S. Woo, Ieee Transactions on Semiconductor Manufacturing 17, 192-200 (2004).
10. A. Asenov, A. R. Brown, J. H. Davies, S. Kaya, and G. Slavcheva, Ieee Transactions on Electron Devices 50, 1837-1852 (2003).
11. A. Asenov, S. Kaya, and A. R. Brown, Ieee Transactions on Electron Devices 50, 1254-1260 (2003).
12. E. Marx, I. J. Malik, Y. E. Strausser, T. Bristow, N. Poduje, and J. C. Stover, Journal of Vacuum Science & Technology B 20, 31-41 (2002).

[13] H. J. Weaver, *Theory of discrete and continuous Fourier analysis* (Wiley, New York, 1989).

[14] J. M. Elson and J. M. Bennett, Applied Optics 34, 201-208 (1995).

[15] S. J. Fang, S. Haplepete, W. Chen, C. R. Helms, and H. Edwards, Journal of Applied Physics 82, 5891-5898 (1997).

[16] P. Goovaerts, Biology and Fertility of Soils 27, 315-334 (1998).

[17] J. E. Meisel and M. G. Turner, Landscape Ecology 13, 347-362 (1998).

[18] U. C. Herzfeld and C. A. Higginson, Computers & Geosciences 22, 35-& (1996).

[19] X. D. Jian, R. A. Olea, and Y. S. Yu, Computers & Geosciences 22, 387-397 (1996).

[20] U. C. Herzfeld, H. Mayer, W. Feller, and M. Mimler, in *Annals of Glaciology, Vol 30, 2000*; *Vol. 30* (2000), p. 235-242.

[21] G. E. P. Box, J. S. Hunter, and W. G. Hunter, *Statistics for experimenters : design, innovation, and discovery*, 2nd ed. (Wiley-Interscience, Hoboken, N.J., 2005).

[22] C. J. Buchko, K. M. Kozloff, and D. C. Martin, Biomaterials 22, 1289-1300 (2001).

[23] A. E. Lita and J. E. Sanchez, Journal of Applied Physics 85, 876-882 (1999).

[24] A.-L. Barabási and H. E. Stanley, *Fractal concepts in surface growth* (Press Syndicate of the University of Cambridge, New York, NY, USA, 1995).

[25] D. L. Goldfarb, A. P. Mahorowala, G. M. Gallatin, K. E. Petrillo, K. Temple, M. Angelopoulos, S. Rasgon, H. H. Sawin, S. D. Allen, M. C. Lawson, and R. W. Kwong, Journal of Vacuum Science & Technology B 22, 647-653 (2004).

Chapter 8. Conclusions and Recommendations for Future Work

8.1 Conclusions

Plasma etching processes often roughen the feature sidewalls and form anisotropic striations. As the feature key dimension continues shrinking below the 100 nm regime, roughness becomes more and more important in nanostructures and nanodevices because it does not scale down with the dimensions of the devices. A clear understanding of the origin and control of sidewall roughening is extremely critical. In particular, at the front end, variations in line width at the gate level can adversely impact the electrical performance of the device; at the back end, feature sidewall roughness of the dielectric materials might degrade the resolution of contacts, interfere with the deposition of conformal liner materials, and make the process integration challengeable.

A new, inductively coupled plasma beam source was set up and well characterized to study this sidewall roughening. This apparatus allowed the exposure of a sample to a realistic ion and neutral flux, of any desired plasma chemistry, while allowing independent control of the ion bombardment energy and incident angle. By rotating blank samples to a near-glancing angle, a sidewall can be simulated. In this way, the etching behavior on real feature sidewalls was investigated by etching blank films at grazing ion bombardment angles.

The angular etching yields of polysilicon and dielectric materials in Ar, Cl_2/Ar, and C_4F_8/Ar plasma beams were studied as a function of ion bombardment energy, ion bombardment angle, etching time, plasma pressure, and plasma composition. Interestingly, the effective neutral-to-ion flux ratio was the primary factor influencing the etching yield. A typical sputtering angular yield curve, with a peak around 60° off-normal angle, was formed at non-saturated etching regime, while the ion-enhanced-etching angular yield curve was observed in the saturated etching regime. Additionally, local polymer deposition effect, if existed, was not important in term of the angular etching yields evolution in current work.

In Ar plasma, various films stayed smooth after etching at normal angle while became rougher at grazing angles. Specifically, the striation structure formed at grazing

angles could be either parallel or transverse to the beam impingement direction. Encouragingly, the sputtering caused roughening at different off-normal angles could be qualitatively explained by combining the corresponding angular dependent etching yield curves.

In fluorocarbon plasmas, the roughening of thermal silicon dioxide and low-k coral films at grazing ion bombardment angles depended on both the etching kinetics and the etching chemistry. In particular, the surface became roughened when the etching process was physical-sputtering like (at low neutral-to-ion flux ratios), even though the polymer deposition effect was trivial; when the etching kinetics was dominated by ion-enhanced etching (at high neutral-to-ion flux ratios), the roughening was mainly caused by the local polymer deposition effects. Moreover, surfaces could be etched without roughening at intermediate neutral-to-ion flux ratios and/or with the addition of oxygen to the discharge. The oxygen addition broadened the region over which etching without roughening could be performed.

Additionally, the local-polymer-deposition induced micro-masking mechanism was proposed to explain the surface roughening of porous low-k films. Porous structure in the substrate played a critical role in the film roughening evolution. This phenomenon could be interpreted by the concept of pore filling with polymeric deposition that etched more slowly under fluorocarbon plasma exposure. Later on, the polymer formed micro-masks that induced roughening. Although scaled with the ion bombardment energy, the roughness level of porous low-k film etched in C_2F_6 plasma was mainly related to the film thickness removed; no similar trend was observed on non-porous OSG films under the same etching conditions.

In short, to minimize the feature surface roughening in plasma etching at grazing ion bombardment angles, it was critical to control the physical sputtering component in order to minimize the ion scattering caused ion channeling effects. At the same time, selecting appropriate etching chemistries was decisive to control the local polymer deposition content on the surface, consequently, the local polymer deposition induced roughening was trivial.

Last, it was demonstrated that the RMS roughness was not a comprehensive representation of the surface roughness on the etched surfaces since only vertical height information on the AFM images was used. In order to include the surface roughness along the lateral dimension, both the power spectral density (PSD) and geostatistical semivariogram methods were introduced to analyze the topography of etched surfaces. It has been proven that both of these two statistical methods were capable to quantify the striation structures on the etched surfaces. In particular, the PSD analysis indicated that the AFM tip filtering effects became important beyond a critical spatial frequency. While the spatial variations of the streaks could be quantified using geostatistical semivariogram method. Moreover, the average periodicity along X direction (perpendicular to the streaks) from these two methods was consistent.

8.2 Future Work

It has been demonstrated that the sidewall roughening of photoresist layer is one of the key factors influencing the sidewall roughness of patterned features due to top LER effects (or, equivalently templating effects)[1,2]. In current research, however, only some preliminary work was done on a conventional chemical positive tone photoresist (Shipley SPR 700)[3]. The properties of real photoresists used in sub 100 nm technologies, such as 65 nm node, might be quite different from those of the conventional resists. For instance, compared to the conventional resists, the etching resistance of real photoresists is smaller, and the required film thickness is also much thinner. For this reason, the etching kinetics and surface roughening on real photoresists should be characterized carefully in order to have a thorough understanding of the origin and evolution of feature sidewall roughening in plasma etching.

At the front end, polysilicon gate materials are heavily n-doped, and partially silicided or metalized in the real processing conditions. Therefore, in the future, it will be necessary to characterize the etching of heavily doped polysilicon since its etching behavior might be quite different from that of intrinsic undoped polysilicon. In particular, the kinetics in $HBr/Cl_2/CF_4$ chemistries is worth to investigate.

At the back end, it has been demonstrated that porous structures in dielectric materials are important for the development of surface roughening in plasma etching,

especially in fluorocarbon plasmas. The influence of pore size and the connectivity of pores on roughening needs to be studied in the future in order to fully understand the pore effects.

When applying the geostatistical method to analyze the surface roughening on etched surfaces, only 1-Dimensional analysis along specific directions (perpendicular or parallel to the striation structures) was performed. In the future, 2-Dimensional geostatistical analysis on etched surfaces should be done so that the correlation of the streaks at different directions can be investigated.

8.3 References

[1] S. A. Rasgon, Ph.D. Thesis, Massachusetts Institute of Technology, 2005.

[2] E. Gogolides, V. Constantoudis, G. P. Patsis, and A. Tserepi, Microelectronic Engineering 83, 1067-1072 (2006).

[3] Y. P. Yin, H. H. Sawin, SRC Diverable, Task ID: 1009.002 (2005).

Appendix - Mechanical Drawings

The mechanical drawings of this plasma beam reactor are included in this section. The drawings that have been shown elsewhere were not included. Please refer to Stacy Rasgon's PhD thesis for the mechanical drawing of the ion energy analyzer and the ion flux analyzer.

The drawings are arranged in the following order:

1. Plasma beam reactor assembly (page 186)
2. Main chamber and the extended chamber ring (page 187 - 197)
3. Mass Spec chamber and the beam source bottom (page 198 - 209)
4. Liners inside of the chamber (page 210 - 215)
5. Sample holder (page 216- 223)
6. filament neutralization. (page 224 - 226)

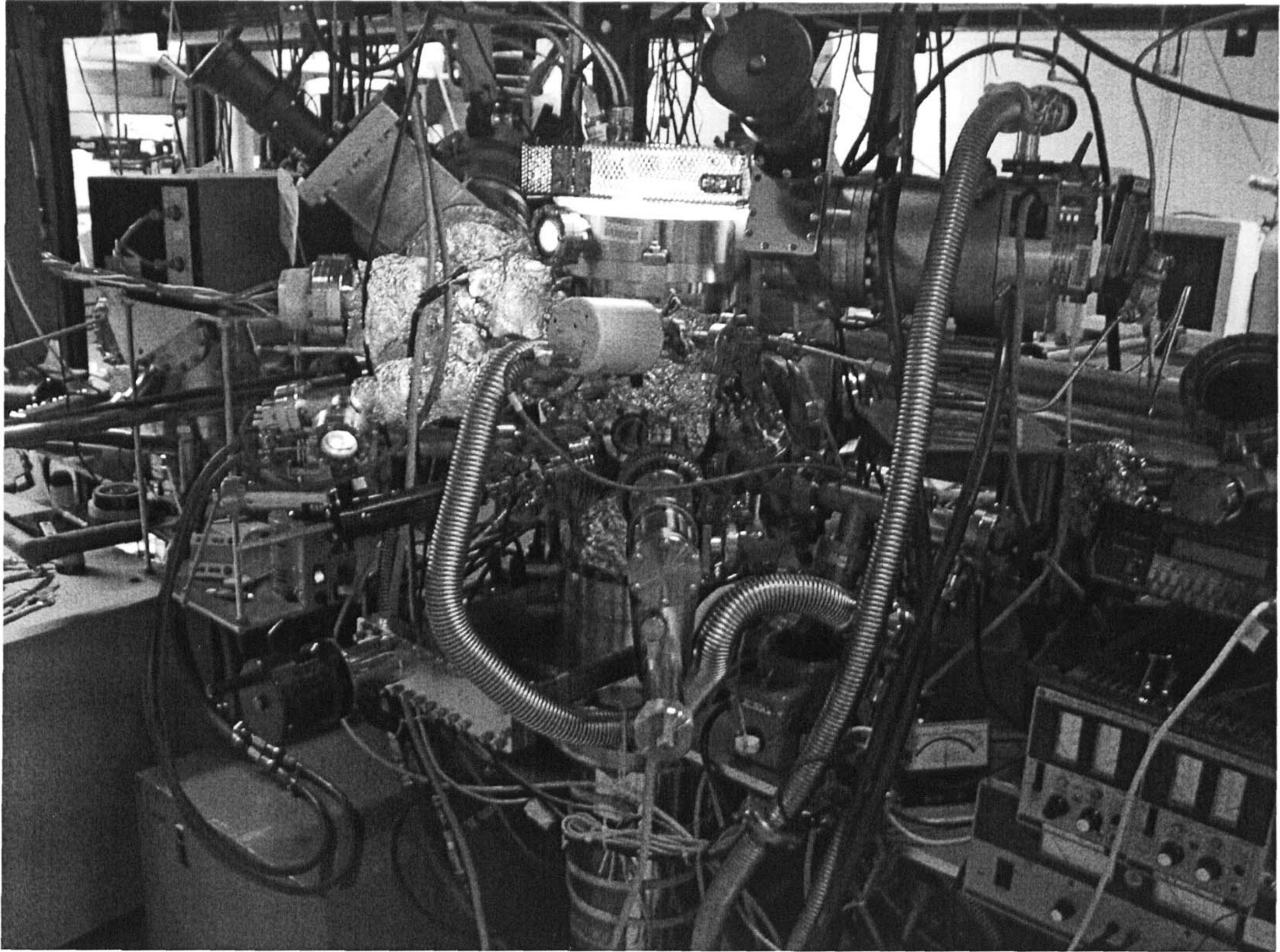

Main Chamber Description

Port #	Termination	Tube OD (in)	Focal point	Focal length (in)	Azimuthal Angle (degree)	Polar angle (degree)
1	2.75" OD flange, clearance holes	1.5	A	5.0	270	90
2	2.75" OD flange, clearance holes	1.5	A	7.0	315	90
3	4.62" OD flange, clearance holes	3.0	A	7.0	0	90
4	2.75" OD flange, clearance holes	1.5	A	7.0	45	90
5	2.75" OD flange, clearance holes	1.5	A	5.0	90	90
6	6" OD flange, clearance holes	4.0	A	6.0	180	90
7	2.75" OD flange, tapped holes	1.5	A	5.5	30	70
8	6" OD flange, clearance holes	4.0	B	6.5	315	90
9	1.33" OD flange, clearance holes	0.75	B	5.0	90	90

Note:

1. As shown in the drawing, the main chamber's xy reference plane lies at the base (coincident with the bottom surface of the 10" OD bottom flange).
2. The z axis is the 8" OD tube's center line.
3. Focal point A, (0,0,6.75)
   Focal point B, (0,0,13)
4. The Leak-Check slots of the ports are vertical unless otherwise indicated.
5. All flanges are nonrotatable.
6. Port 3 and Port 7 are viewports.

Yunpeng Yin
MIT
7/30/03

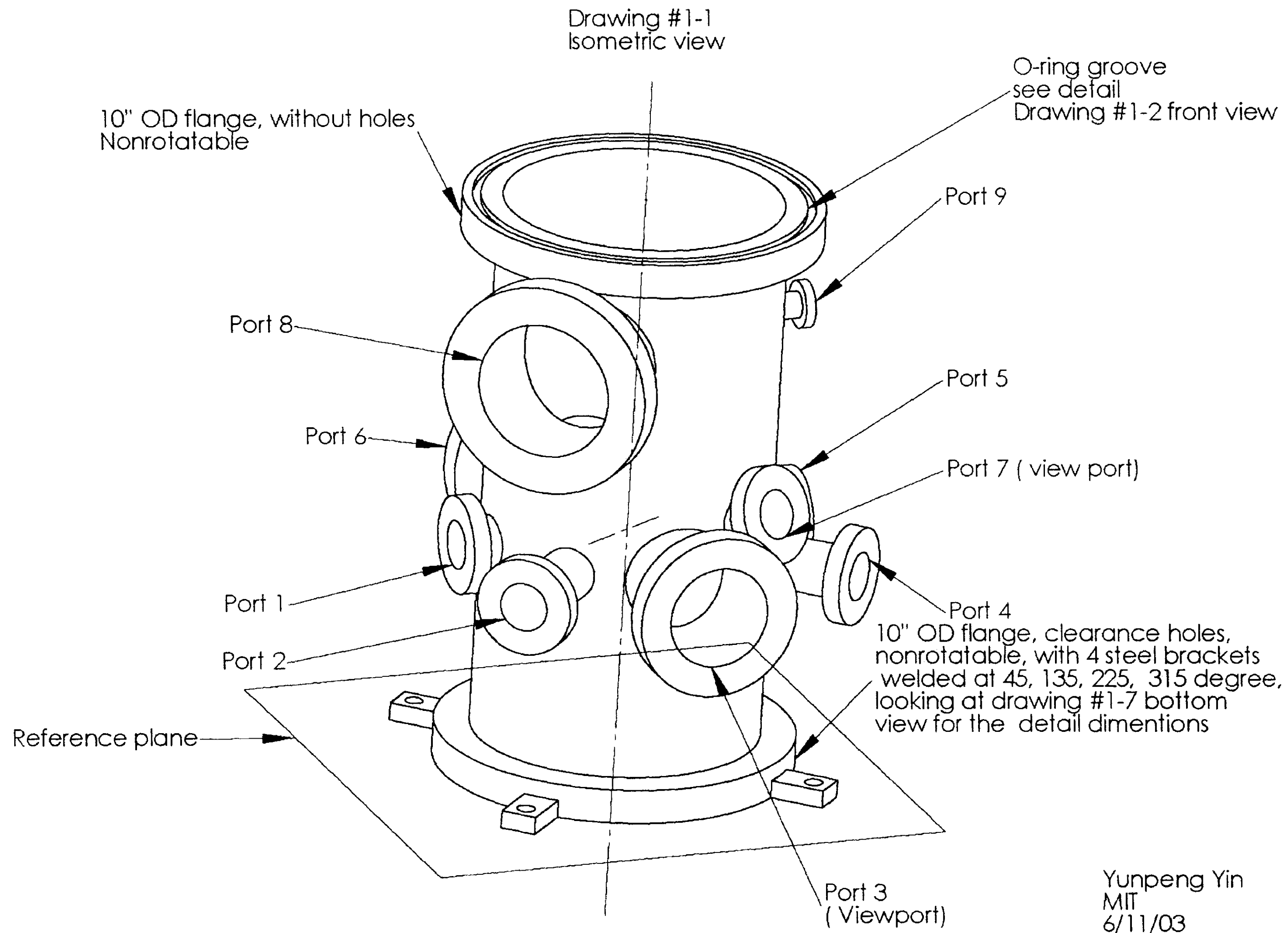
Drawing #1-1
Isometric view
O-ring groove
see detail
Drawing #1-2 front view
10" OD flange, without holes
Nonrotatable
Port 9
Port 8
Port 5
Port 6
Port 7 (view port)
Port 1
Port 4
10" OD flange, clearance holes,
nonrotatable, with 4 steel brackets
welded at 45, 135, 225, 315 degree,
looking at drawing #1-7 bottom
view for the detail dimentions
Port 2
Reference plane
Port 3
(Viewport)
Yunpeng Yin
MIT
6/11/03

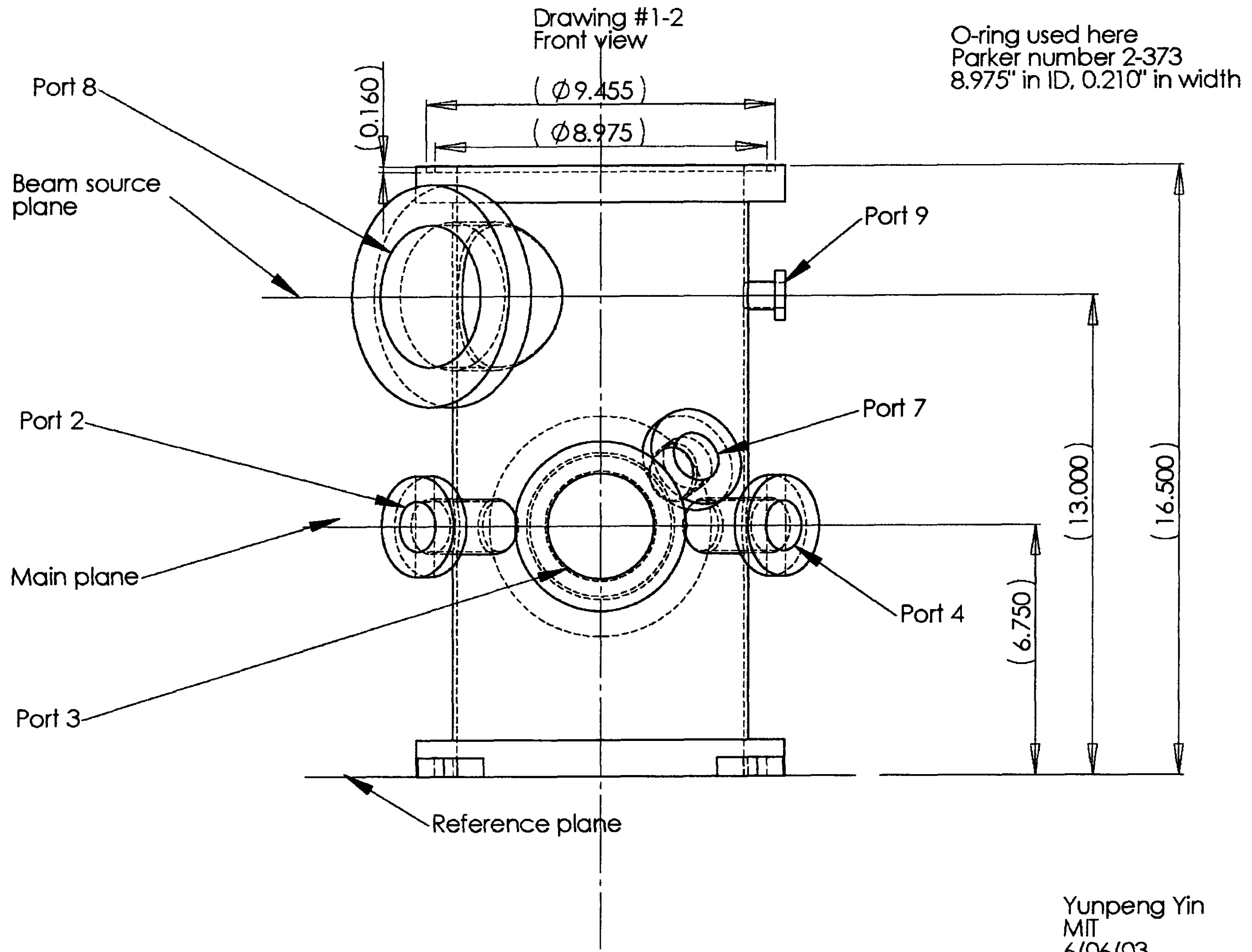
Drawing #1-2
Front view
O-ring used here
Parker number 2-373
8.975" in ID, 0.210" in width
Port 8
(0.160)
(Ø9.455)
(Ø8.975)
Beam source
plane
Port 9
Port 7
Port 2
Main plane
Port 4
Port 3
(13.000)
(16.500)
(6.750)
Reference plane
Yunpeng Yin
MIT
6/06/03

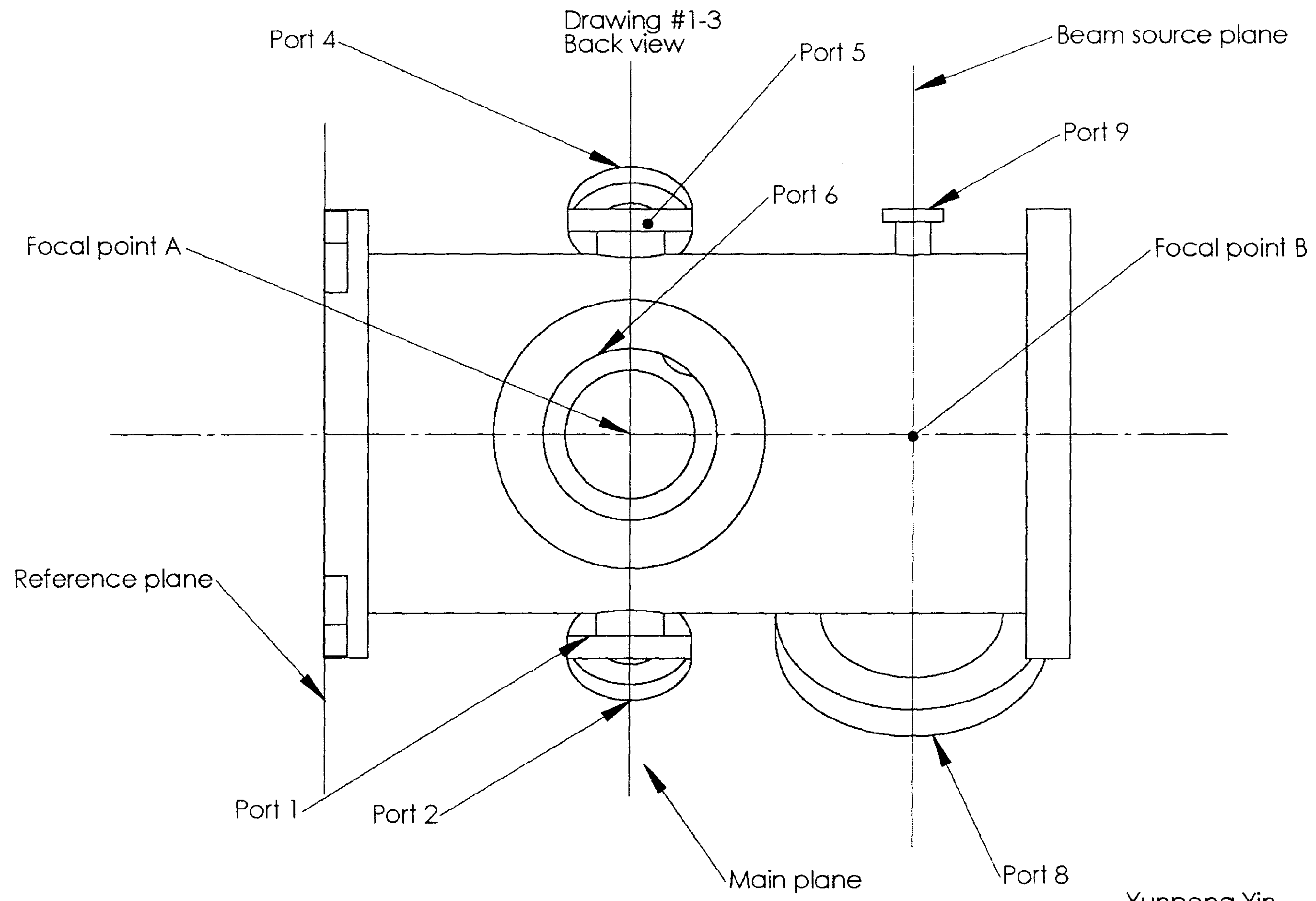

Drawing #1-3
Back view
Port 4
Port 5
Beam source plane
Port 9
Port 6
Focal point A
Focal point B
Reference plane
Port 1
Port 2
Main plane
Port 8
Yunpeng Yin
MIT
6/06/03

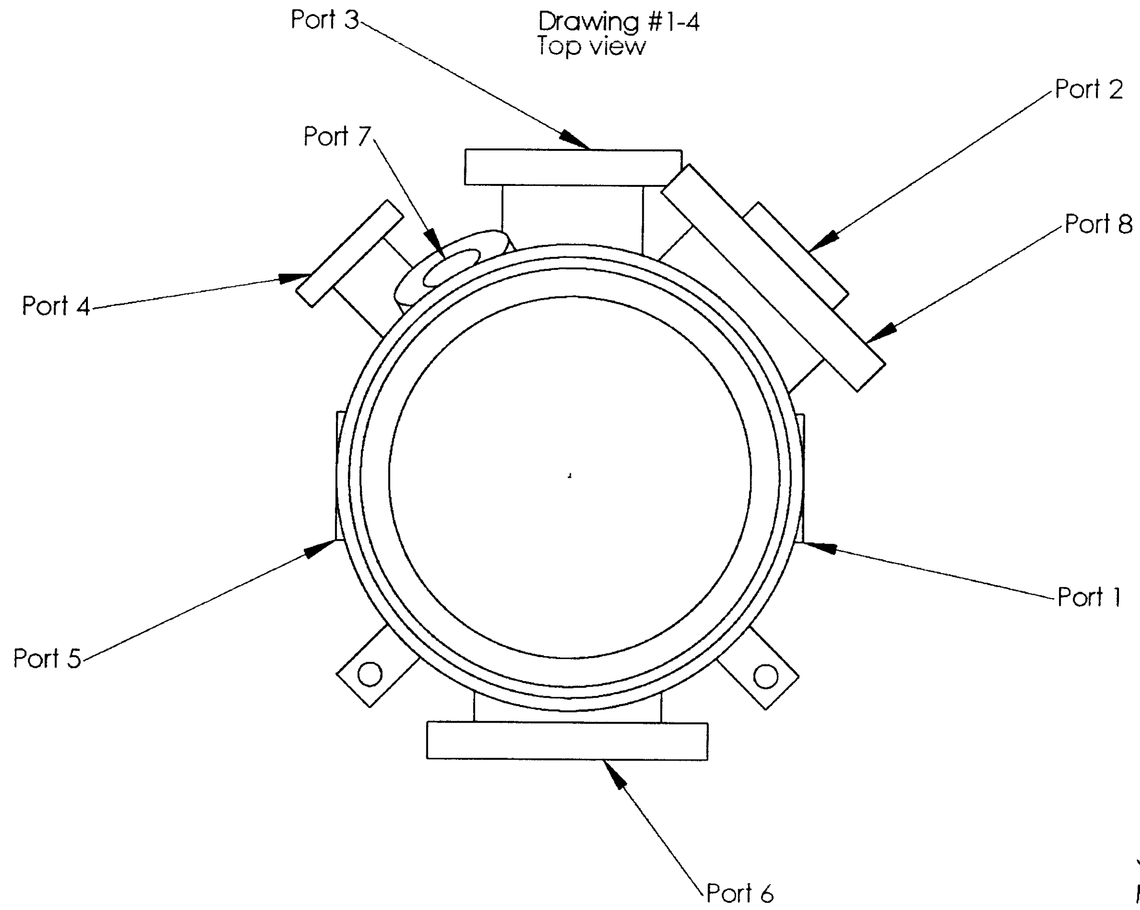
Drawing #1-4
Top view
Port 3
Port 7
Port 2
Port 8
Port 4
Port 5
Port 1
Port 6
Yunpeng Yin
MIT
6/06/03

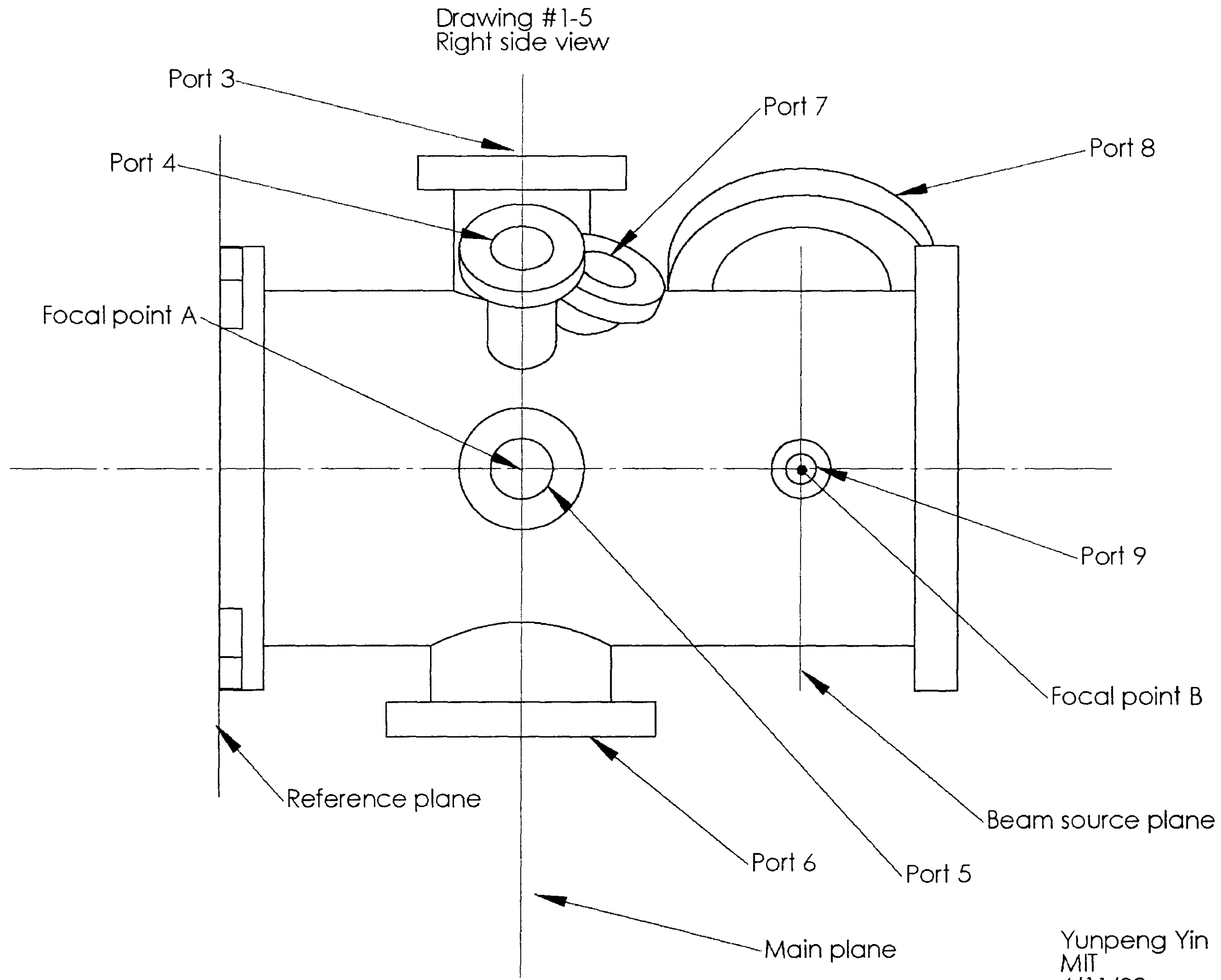
Drawing #1-5
Right side view
Port 3
Port 7
Port 8
Port 4
Focal point A
Port 9
Focal point B
Reference plane
Beam source plane
Port 6
Port 5
Main plane
Yunpeng Yin
MIT
6/11/03

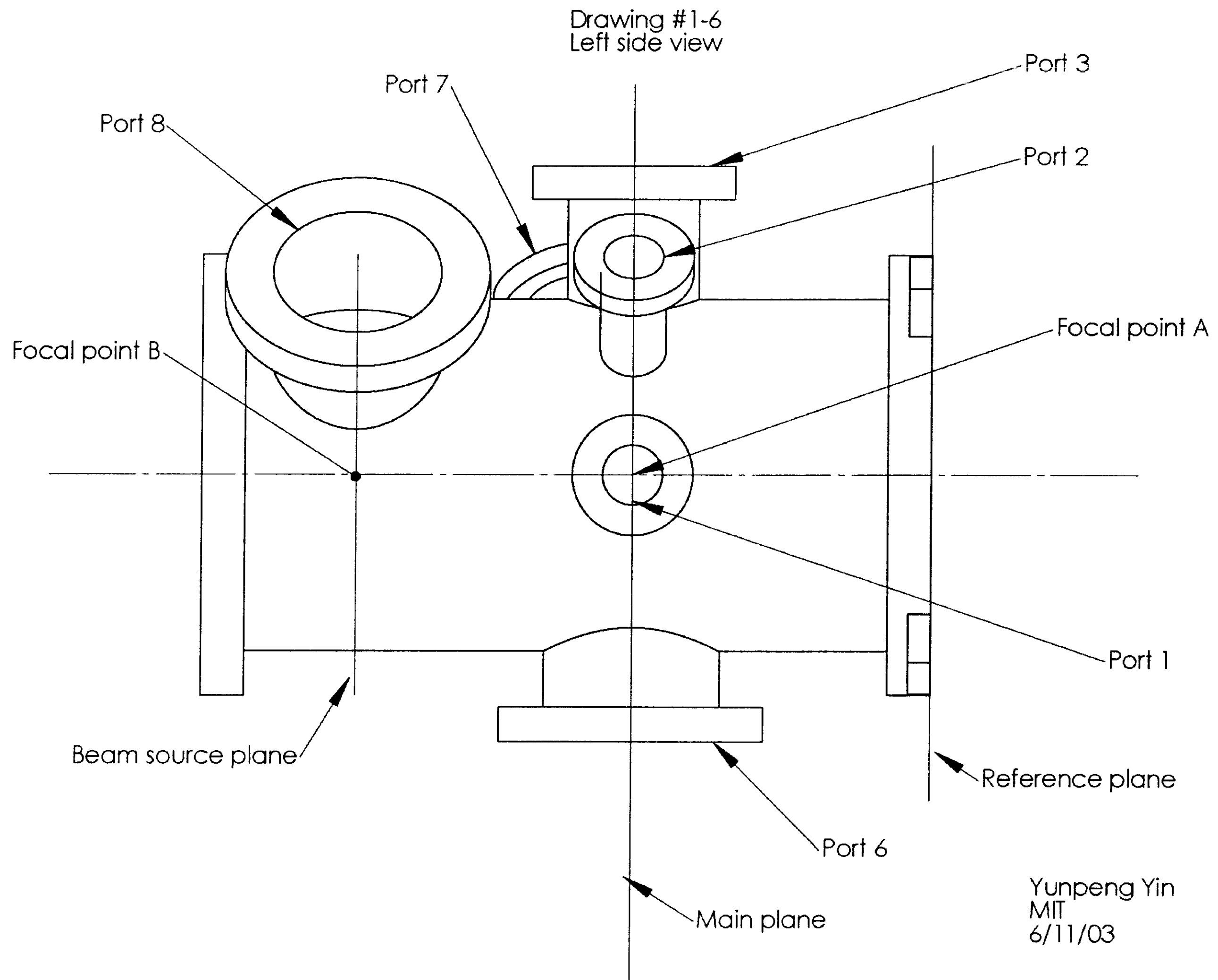
Drawing #1-6
Left side view
Port 3
Port 7
Port 8
Port 2
Focal point A
Focal point B
Port 1
Beam source plane
Reference plane
Port 6
Main plane
Yunpeng Yin
MIT
6/11/03

Drawing #1-7
Bottom view

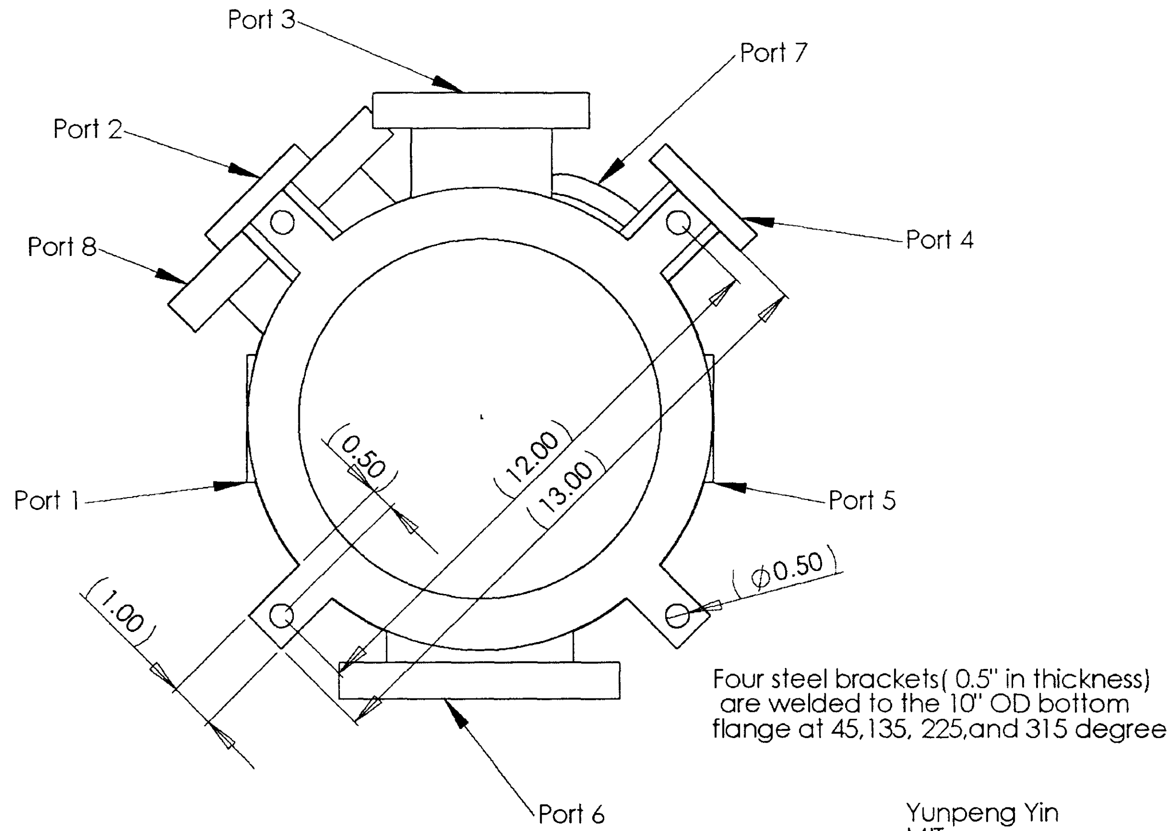

Yunpeng Yin
MIT
6/11/03

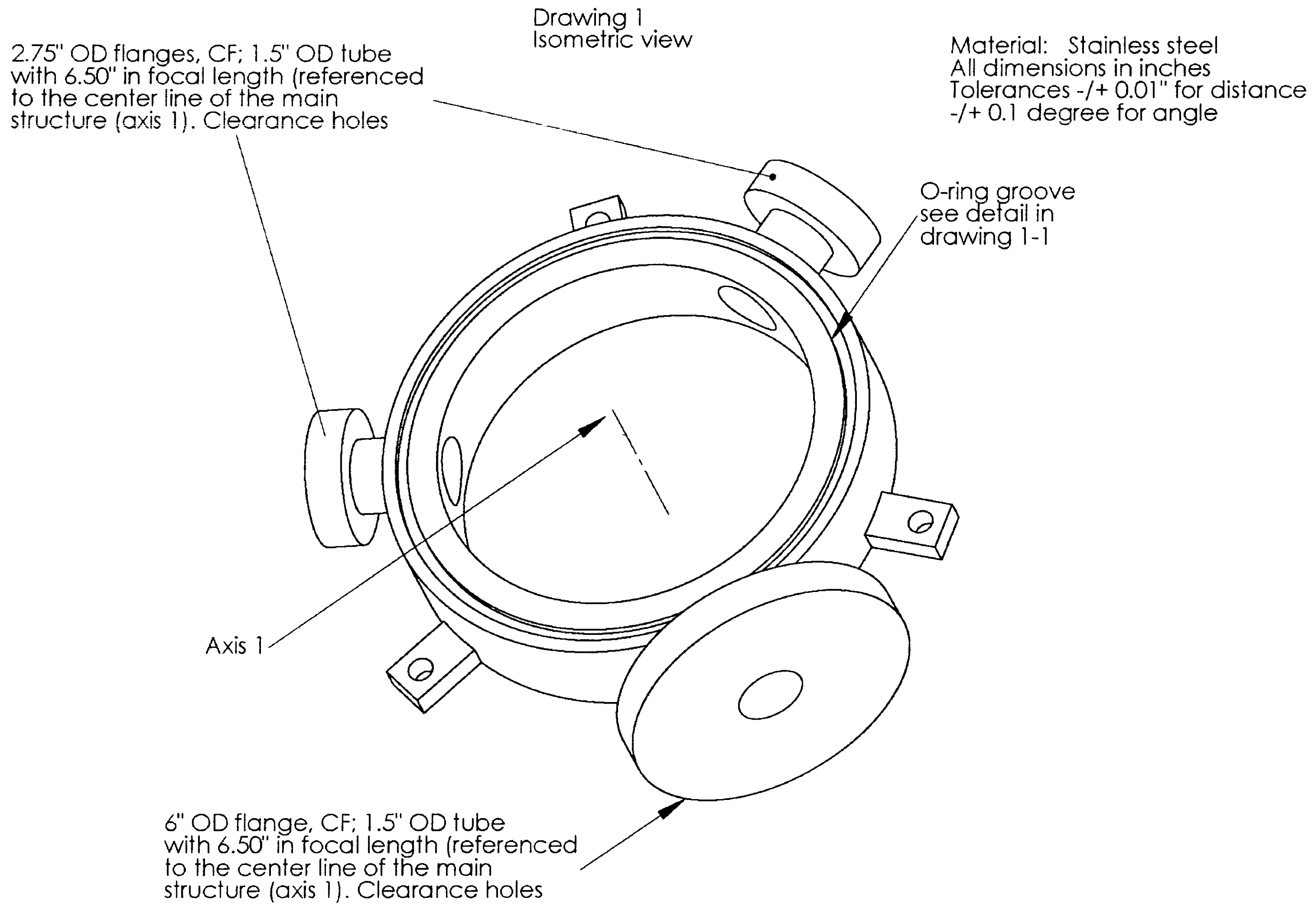

Yunpeng Yin
05/22/05

Drawing 1-1
Frong view

Material: Stainless steel
All dimensions in inches
Tolerances -/+ 0.01" for distance
-/+ 0.1 degree for angle

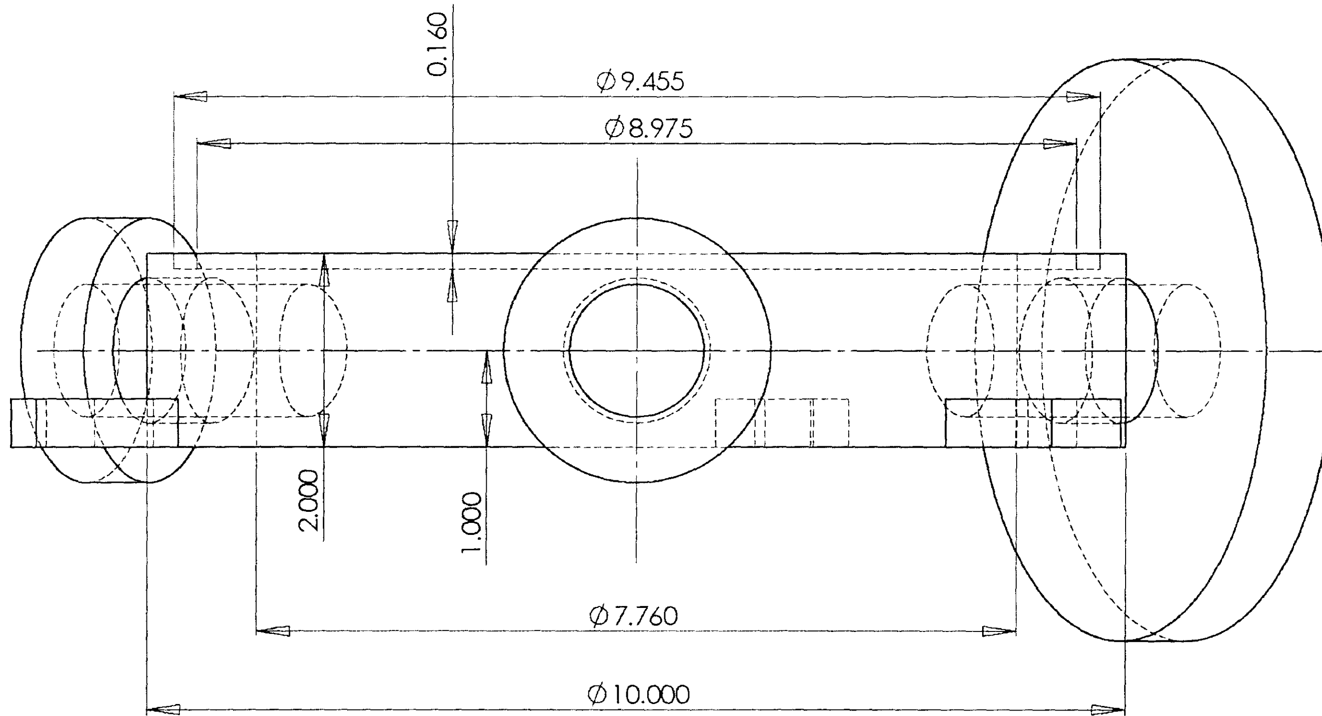

Shown here are dimensions of the main disc and the O-ring groove

Yunpeng Yin
05/22/05

Drawing 1-2
Top view

Material: Stainless steel
All dimensions in inches
Tolerances -/+ 0.01" for distance
-/+ 0.1 degree for angle

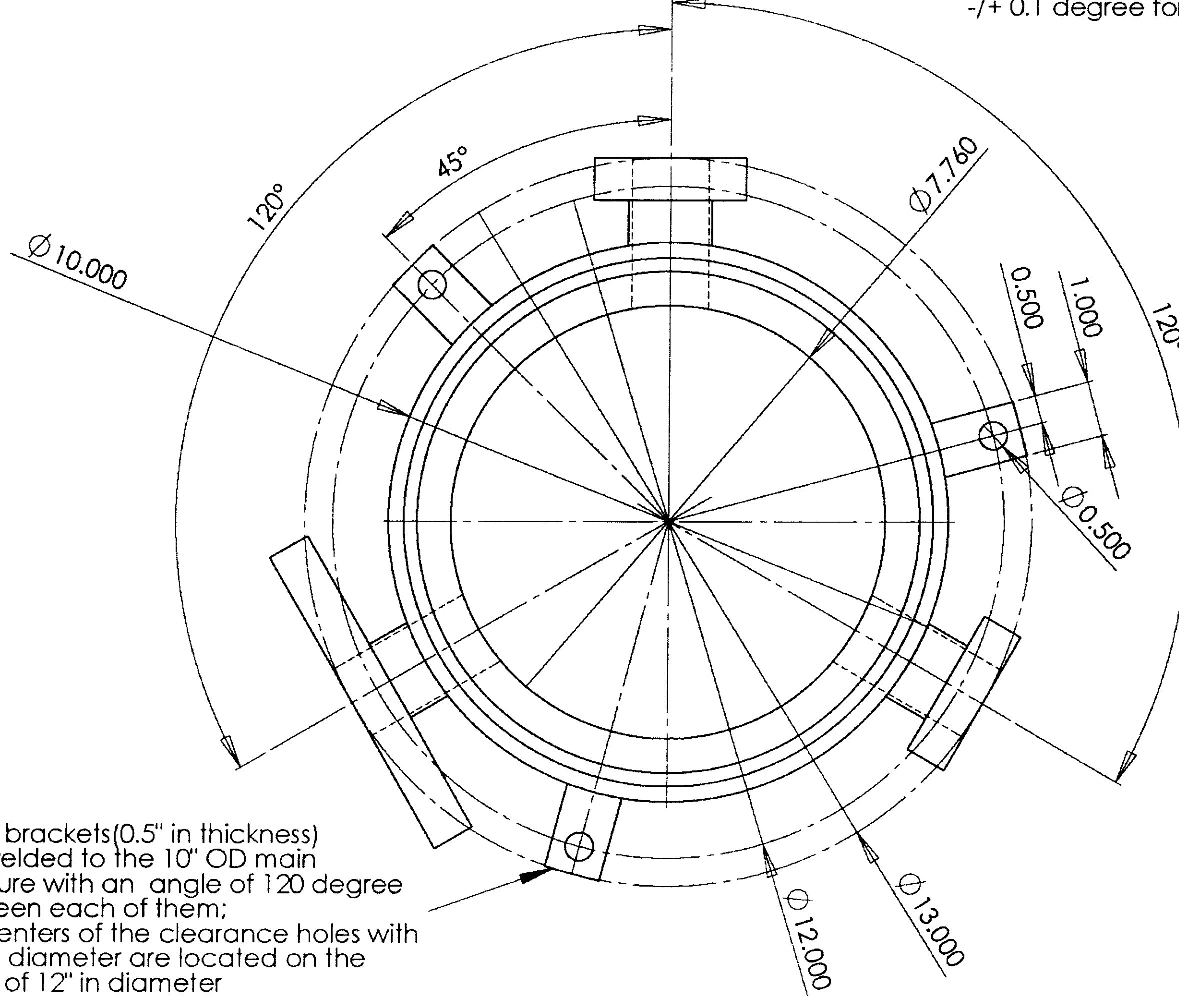

Three brackets(0.5" in thickness)
are welded to the 10" OD main
structure with an angle of 120 degree
between each of them;
The centers of the clearance holes with
0.5" in diameter are located on the
circle of 12" in diameter

Yunpeng Yin
05/22/05

Drawing #2
Left side view of beam source and main chamber

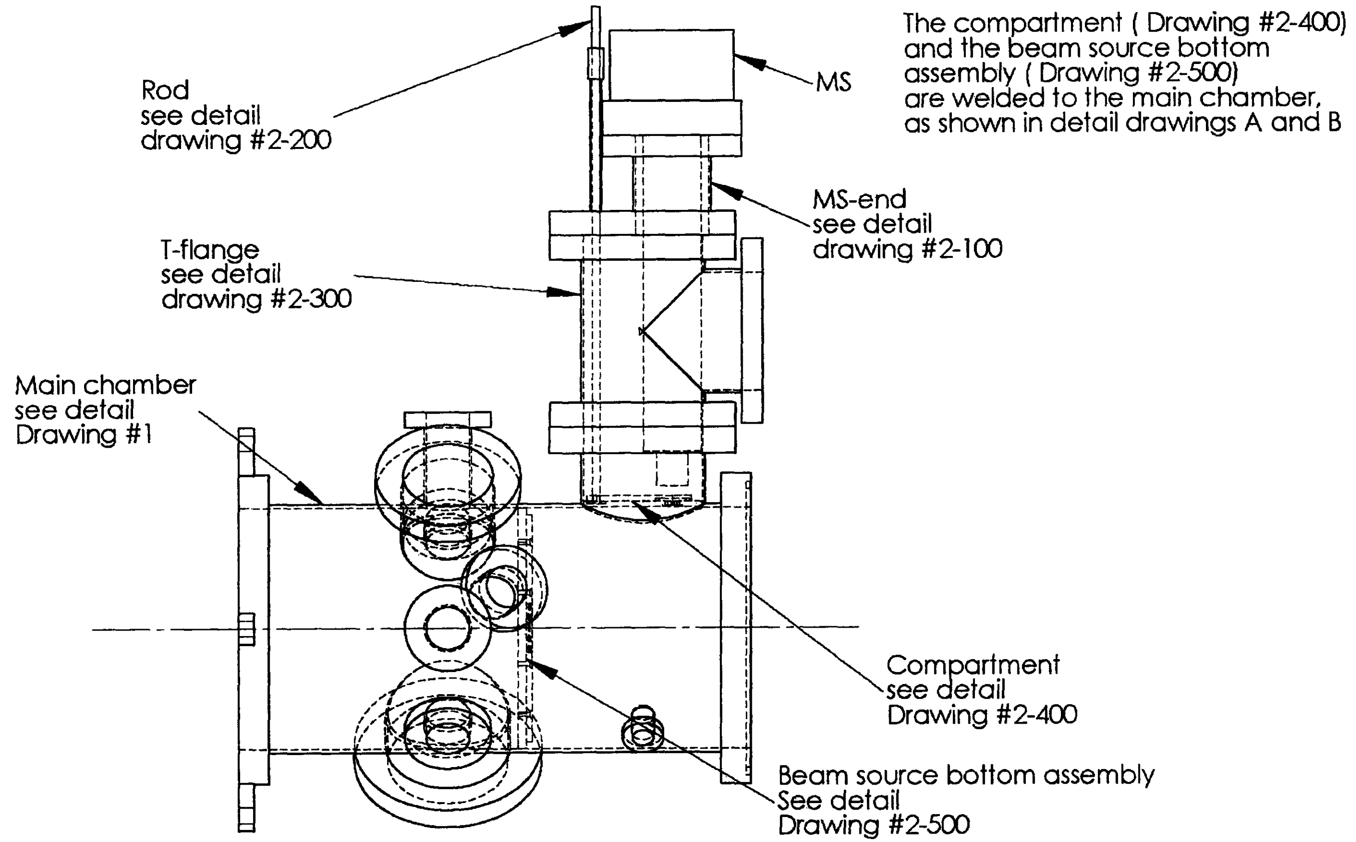

Yunpeng Yin
MIT
6/11/03

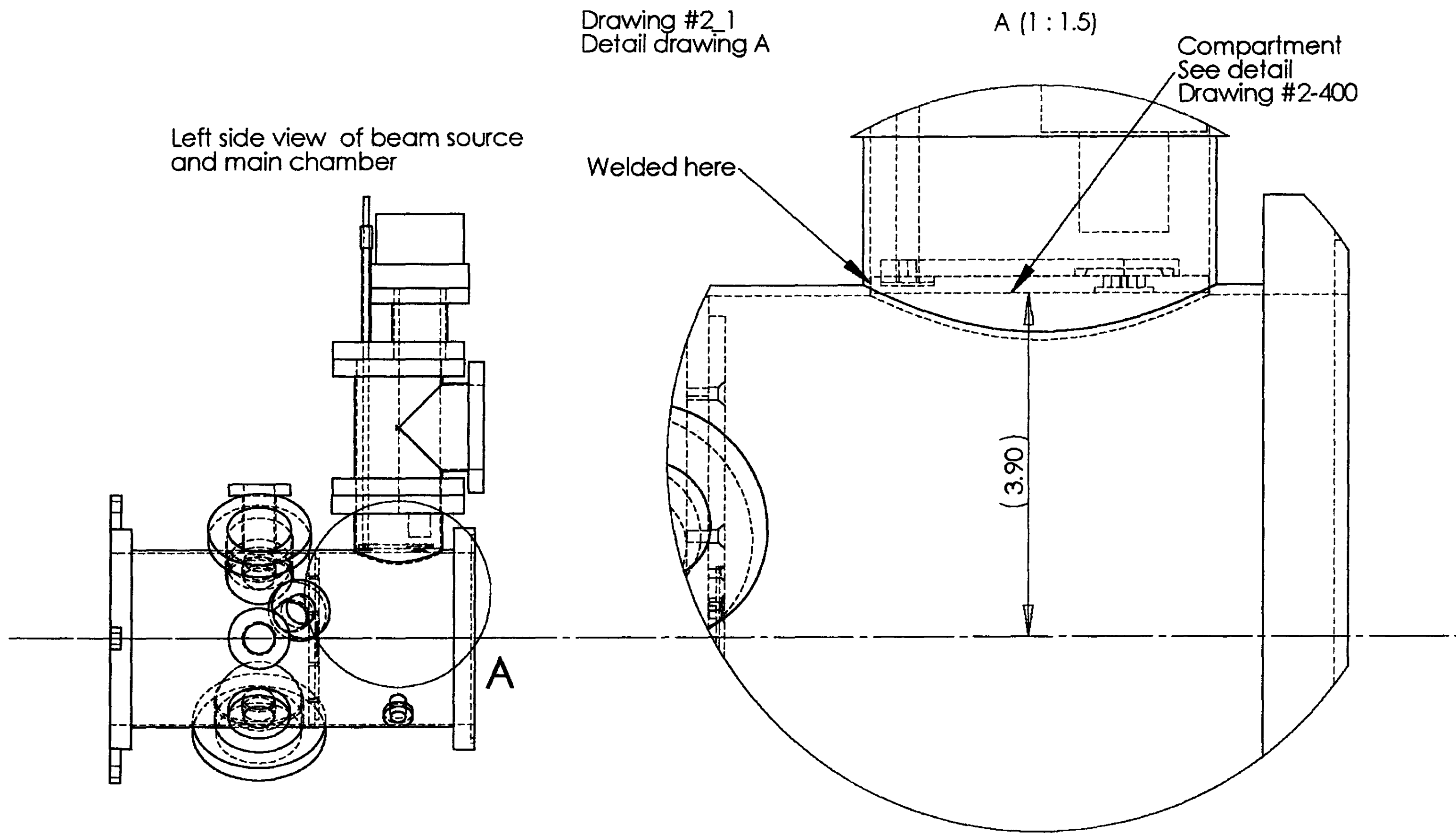

Yunpeng Yin
MIT
6/11/03

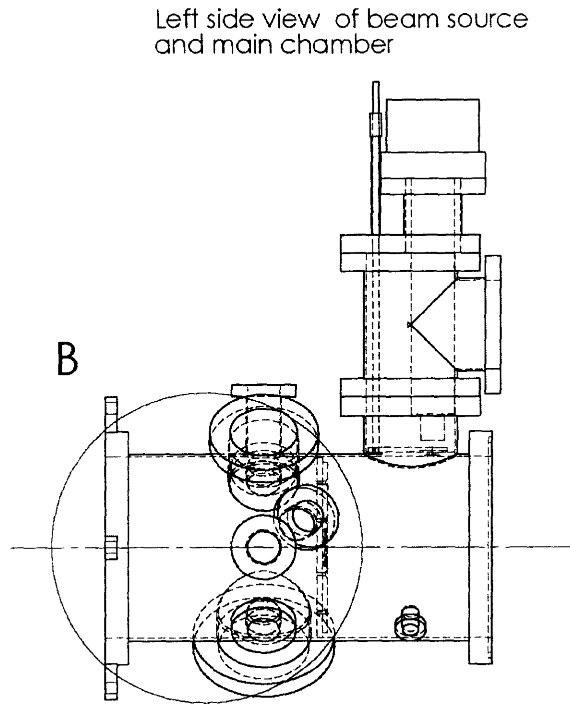

Drawing #2-2
Detail drawing B

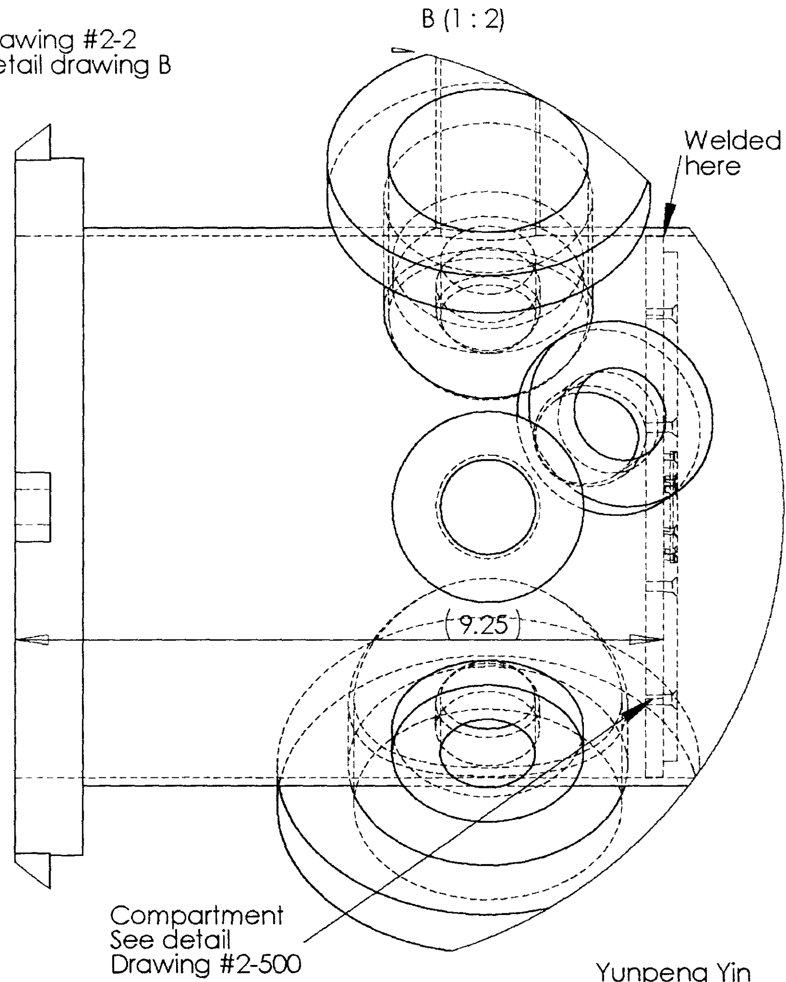

Yunpeng Yin
MIT
7/30/03

Material:
Stainless steel

Yunpeng Yin
MIT
6/03/03

All Leak-Check slots are vertical

Drawing #2-100

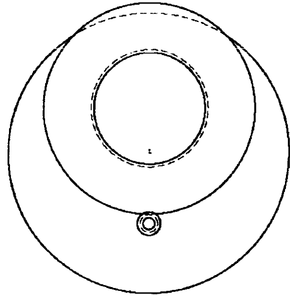

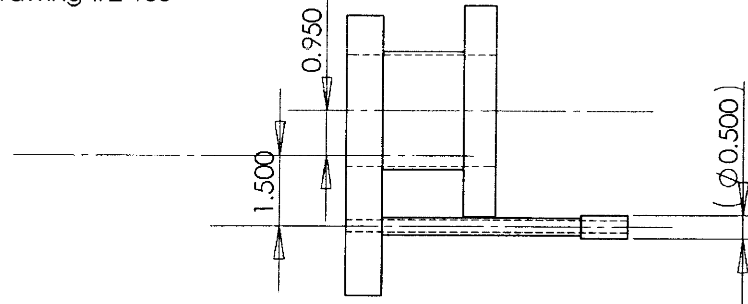

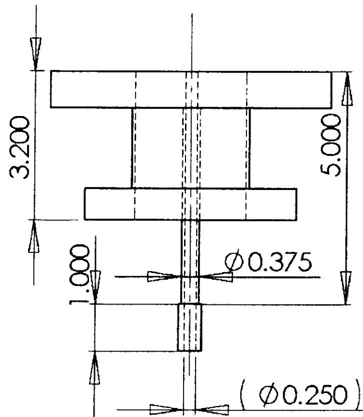

4.5" OD flange,CF
2.5" OD tube
Nonrotatable
tapped

6.0" OD flange,CF
Nonrotatable,
Clearance holes

Compression fitting
with the rod

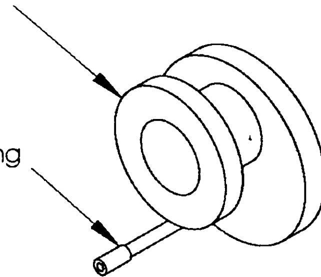

Drawing #2-200
Partially threaded rod

threaded for 10-32

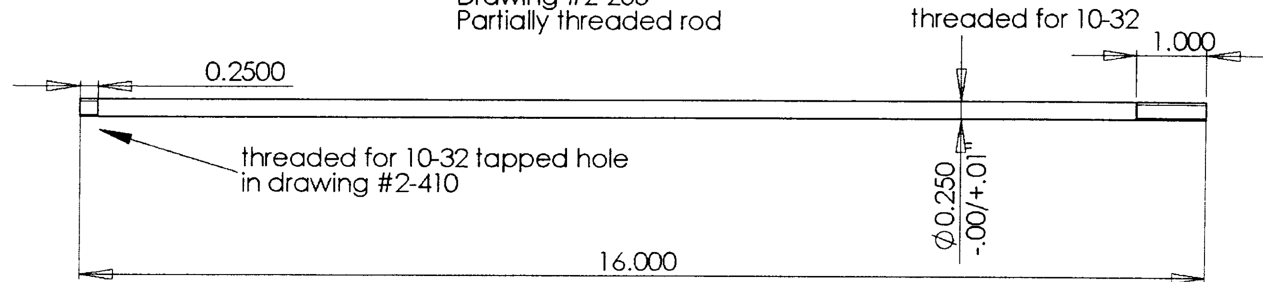

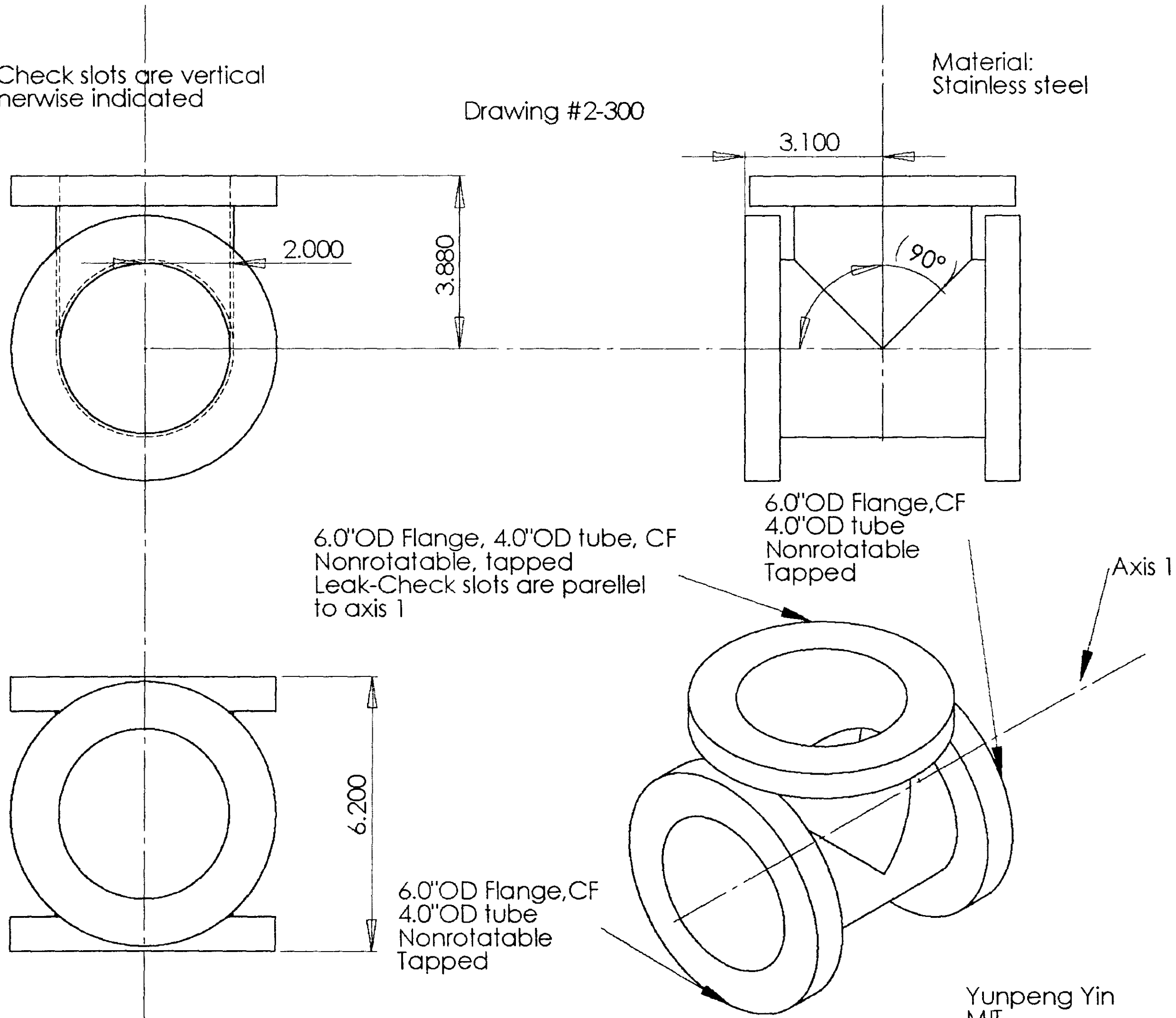
All Leak-Check slots are vertical
unless otherwise indicated
Drawing #2-300
Material:
Stainless steel
3.100
2.000
3.880
90°
6.200
6.0"OD Flange, 4.0"OD tube, CF
Nonrotatable, tapped
Leak-Check slots are parellel
to axis 1
6.0"OD Flange,CF
4.0"OD tube
Nonrotatable
Tapped
Axis 1
6.0"OD Flange,CF
4.0"OD tube
Nonrotatable
Tapped
Yunpeng Yin
MIT
7/24/03

Drawing #2-400

Isometric View

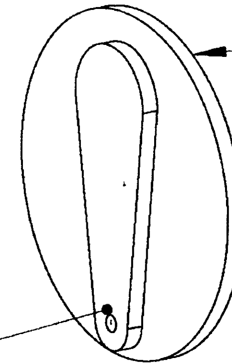

compartment end
see detail
drawing #2-420

grid shutter
see detail
drawing #2-410

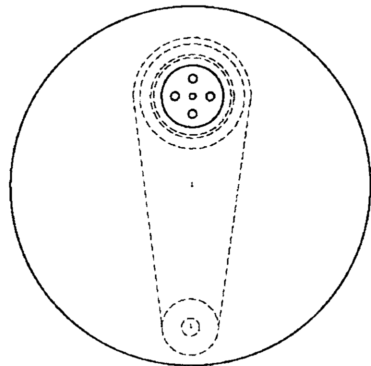

Yunpeng Yin
MIT
7/24/03

Drawing #2-410

Material:
Stainless steel

Tapped thru hole for 10-32,
which should be perpendicular
to make tight o-ring(Parker # 2-118) seal

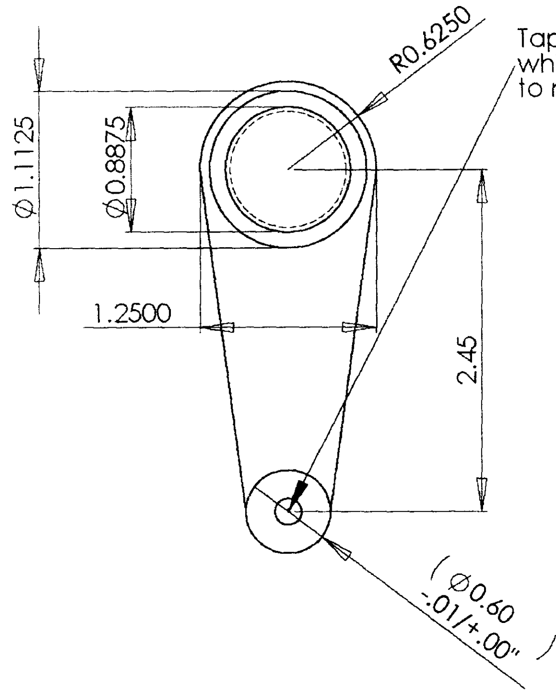

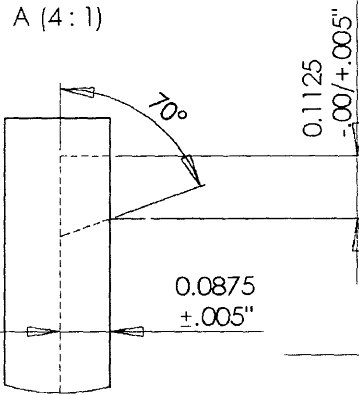

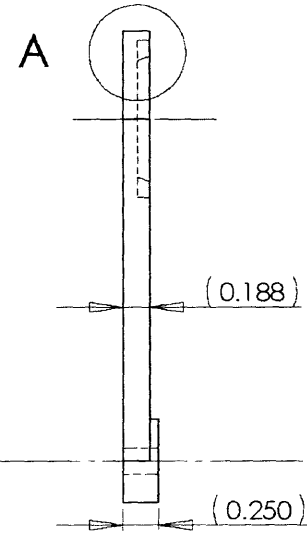

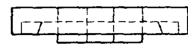

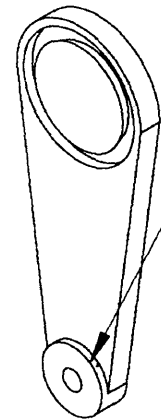

this small 0.6" diameter disc of
thickness 0.0625" is welded onto the
shutter

All dimensions in inches
Tolerances -/+ 0.01" for distance
-/+ 0.1 degree for angle
Unless otherwise indicated

Yunpeng Yin
MIT
7/30/03

Material:
Stainless steel

Drawing #2-420

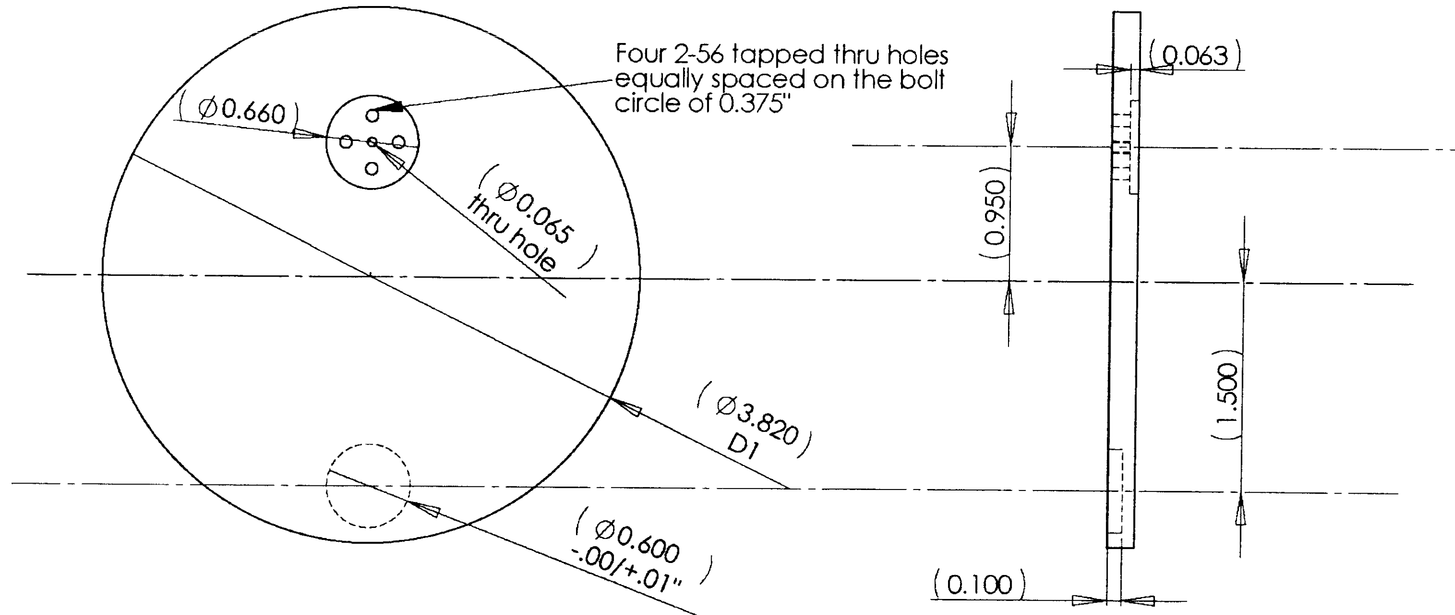

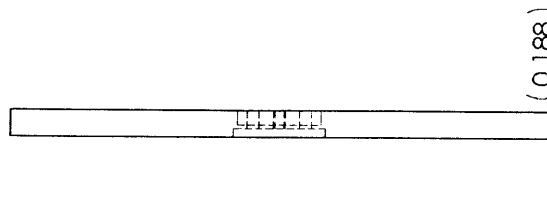

Dimension D1 can not be larger than the inner diameter of the 4" OD tube (see port 8 in drawing# 1)

Yunpeng Yin
MIT
7/24/03

Drawing #2-500

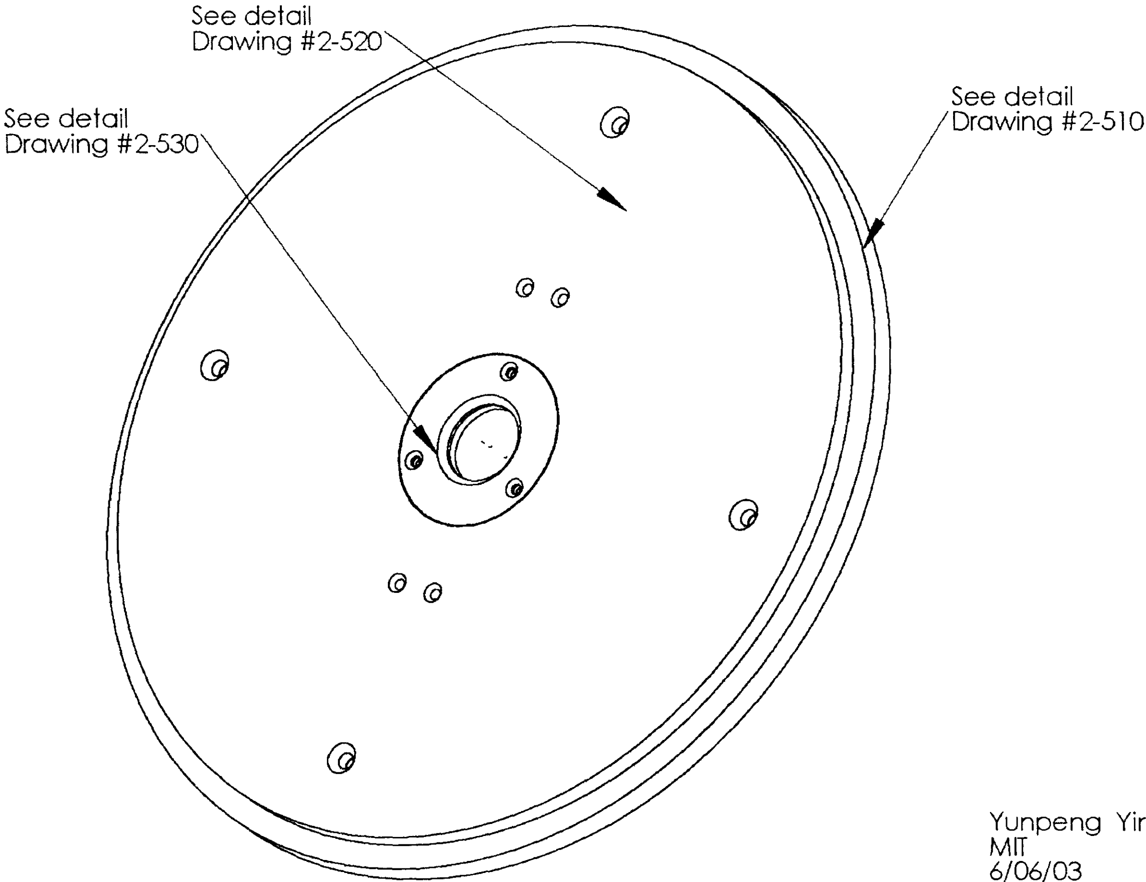

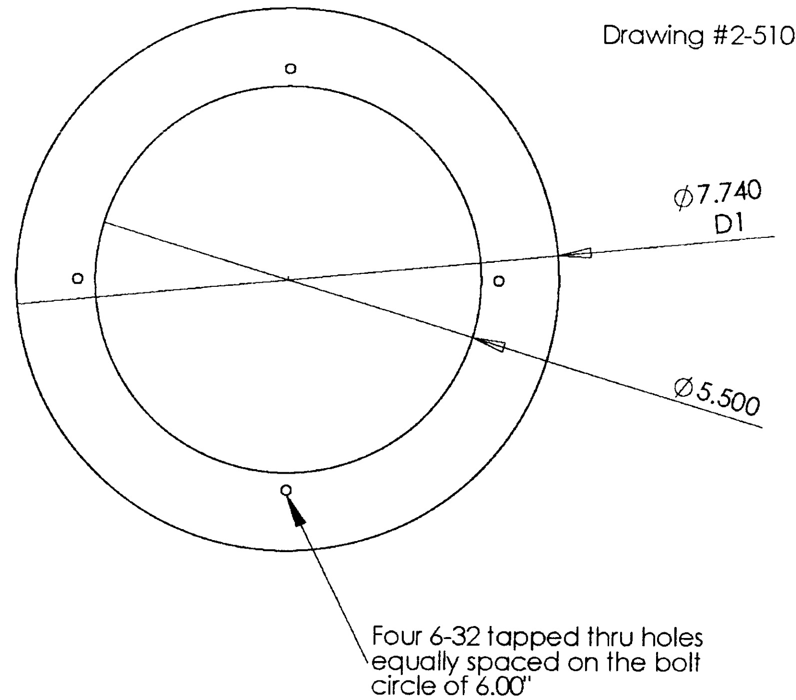

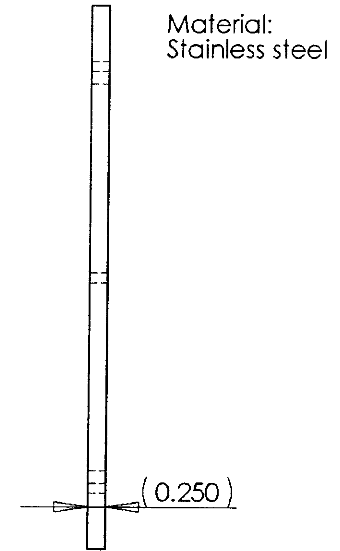

Dimension D1 can not be larger than the inner diameter of the 8" OD tube in the main chamber, so that we can weld it to the inner surface of the main chamber

Yunpeng Yin
MIT
6/11/03

Drawing #2-520

Material:
Stainless steel

Three 2-56 tapped thru holes equally spaced on the bolt circle of 1.30"

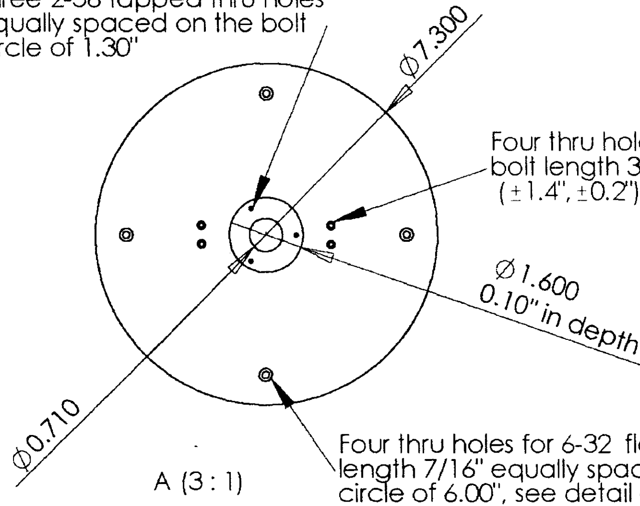

Four thru holes for 2-56 flat bolts of bolt length 3/4", whose coordinates are (±1.4", ±0.2"), see detail drawing B

Four thru holes for 6-32 flat bolts of bolt length 7/16" equally spaced on the bolt circle of 6.00", see detail drawing A

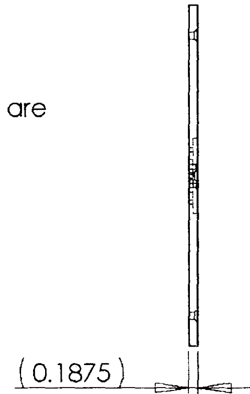

A (3 : 1)

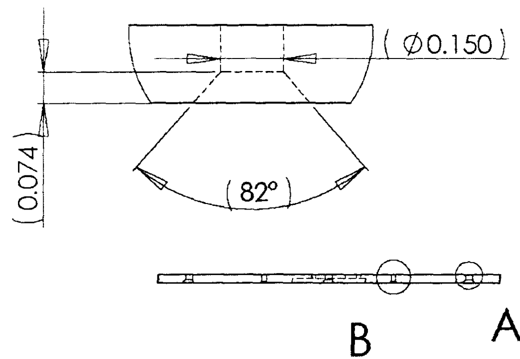

B (4 : 1)

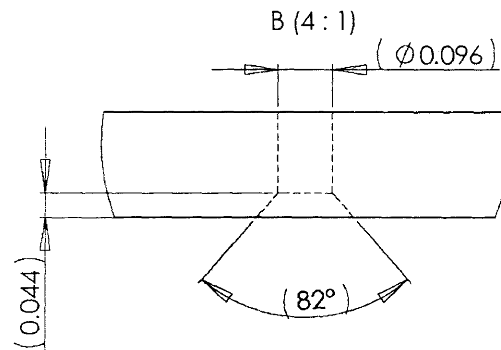

Yunpeng Yin
MIT
6/03/03

Drawing #2-530

Material:
Stainless steel

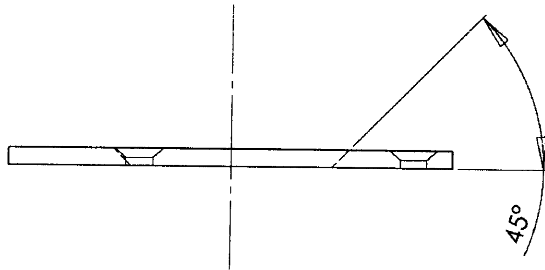

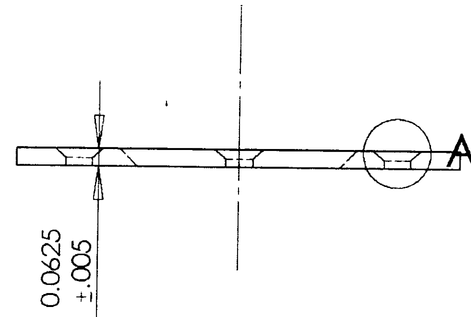

Three thru holes for 2-56 flat bolts of bolt length 5/16" equally spaced on the bolt circle of 1.30", see detail drawing A

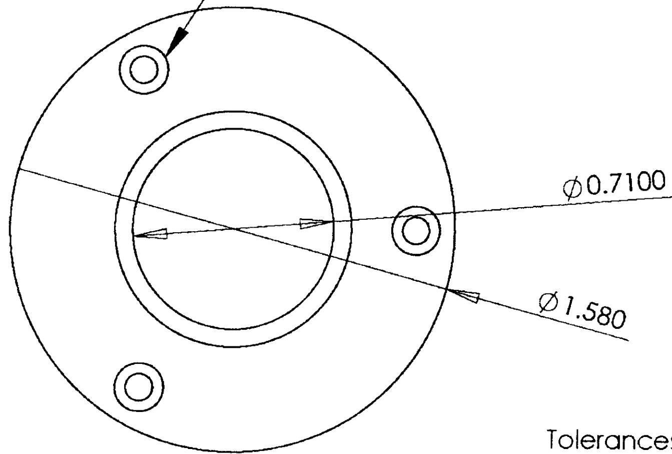

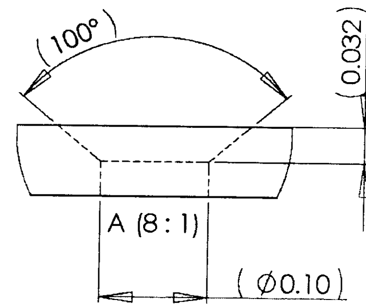

Tolerances -/+ 0.01" for distance
-/+ 0.1 degree for angle
Unless otherwise indicated

Yunpeng Yin
MIT
6/5/03

Insulator assembly drawing

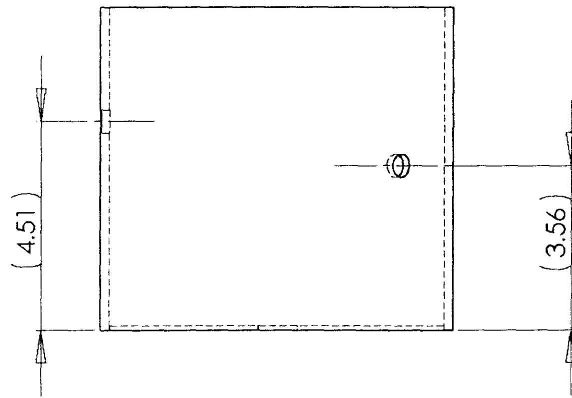

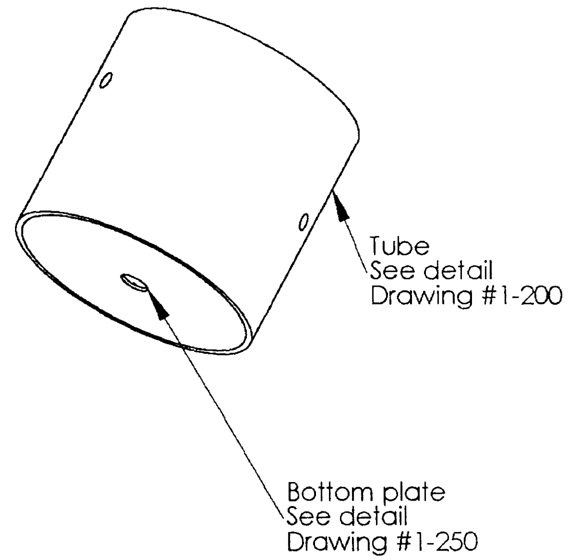

Tolerances -/+0.01" for distance
-/+0.1 degree for angle
unless otherwise indicated

Drawing #1-250 is fused onto
the bottom of drawing #1-200

Yunpeng Yin
MIT
6/9/03

Drawing #1-200

Material:
Alumina/quartz

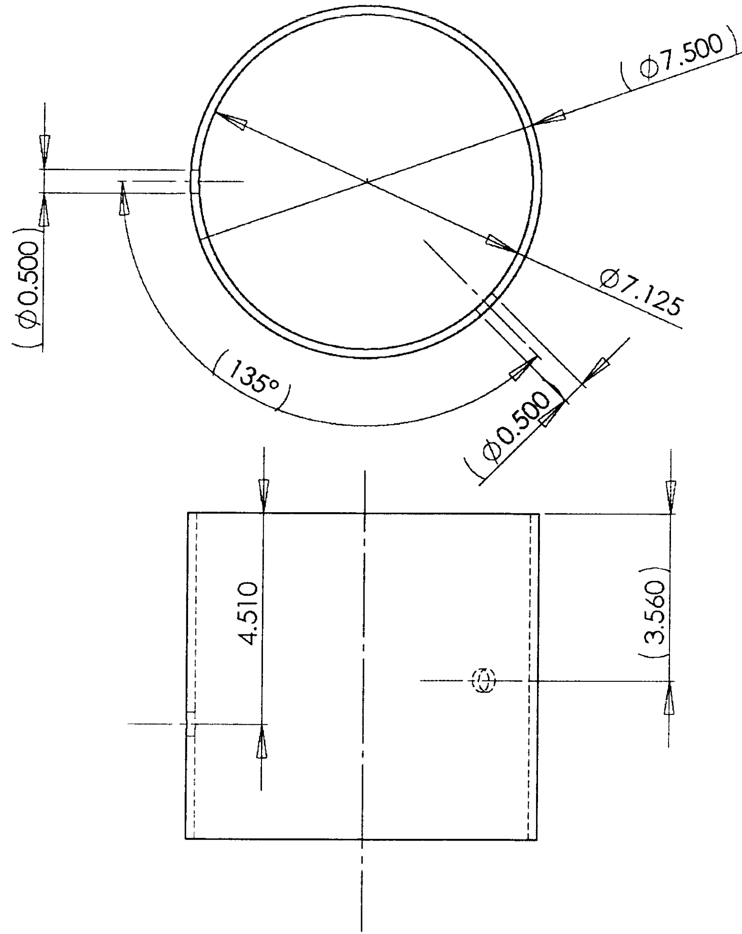

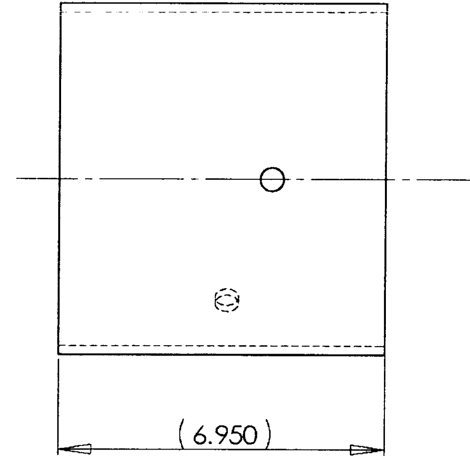

Yunpeng Yin
MIT
6/09/03

Drawing #1-250

Material:
Alumina/quartz

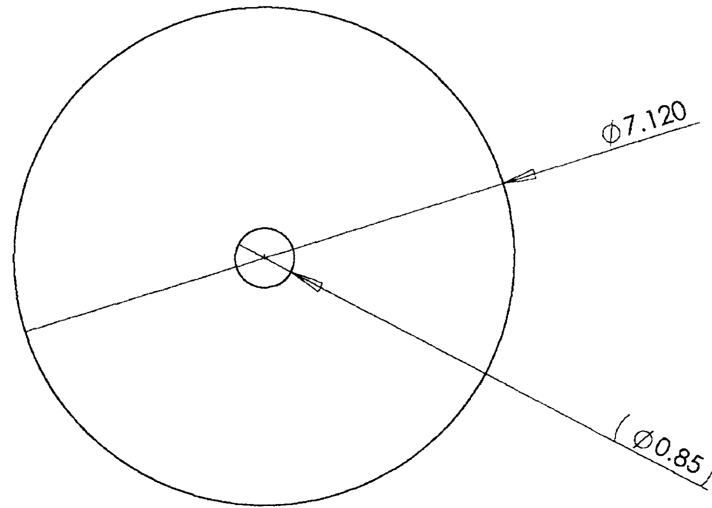

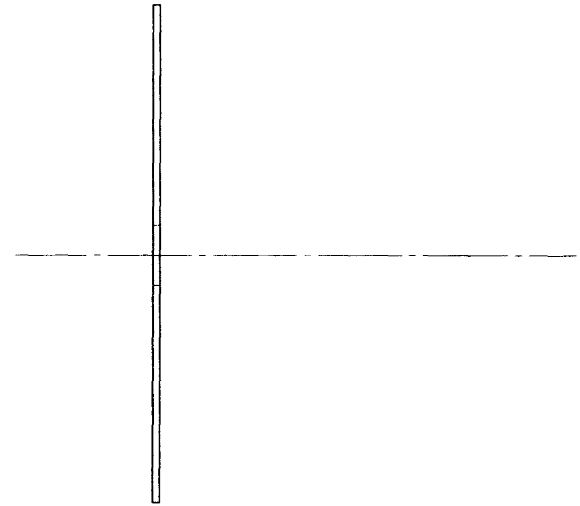

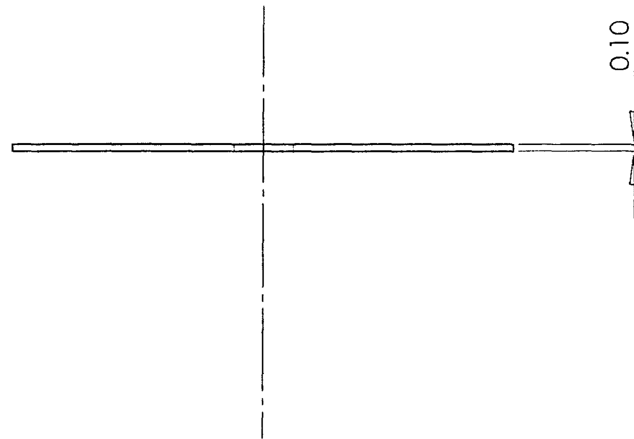

Yunpeng Yin
MIT
6/09/03

Drawing #1-300_1
Top plate

Material:
Alumina/quartz

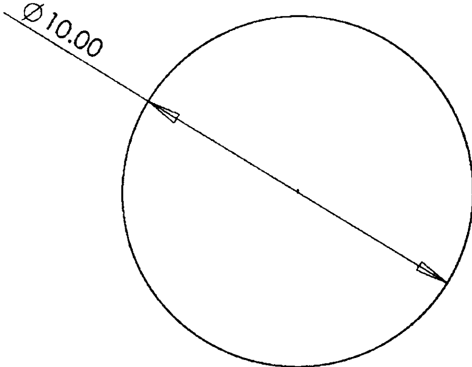

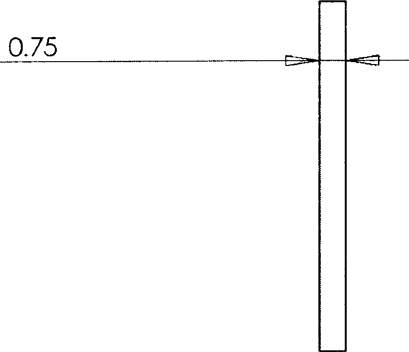

Tolerances -/+ 0.01" for distance
-/+ 0.1 degree for angle
Unless otherwise indicated

Yunpeng Yin
MIT
6/02/03

Drawing 2
Isometric view

Material: Quartz
All dimensions in inches
Tolerances -/+ 0.01" for distance
-/+ 0.1 degree for angle

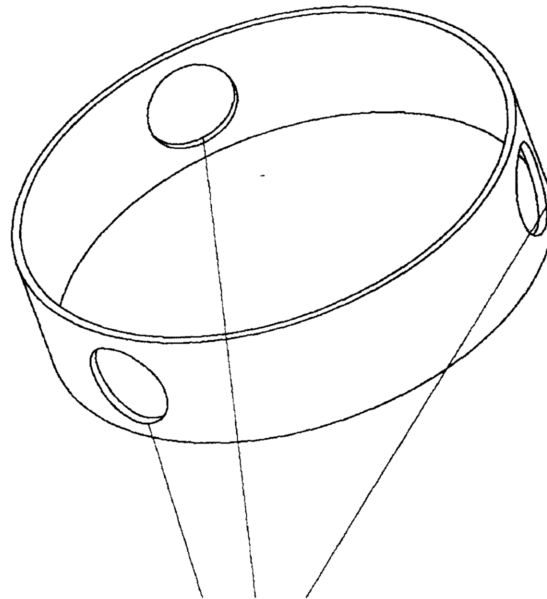

Three holes with 1.37" in diameter
See detail in Drawing 2_1

Yunpeng Yin
06/02/05

Drawing 2_1
3D view

Material: quartz
All dimensions in inches
Tolerances -/+ 0.01" for distance
-/+ 0.1 degree for angle

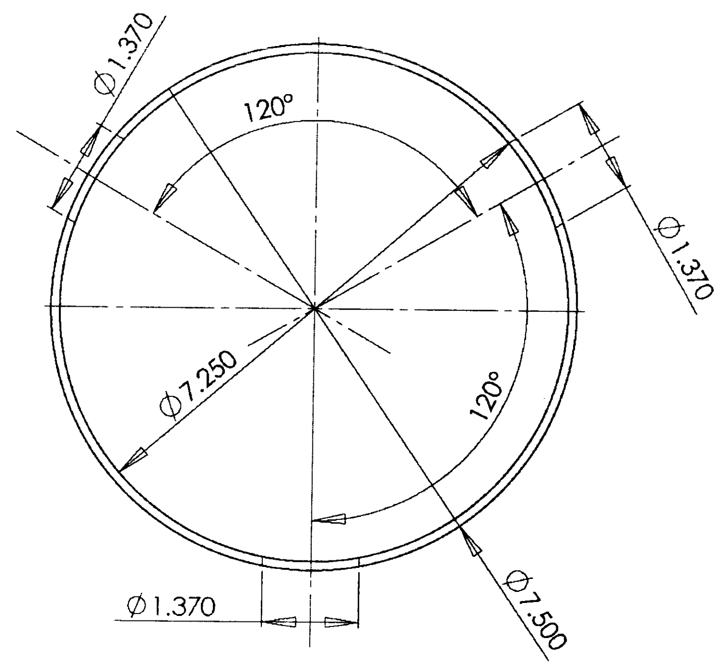

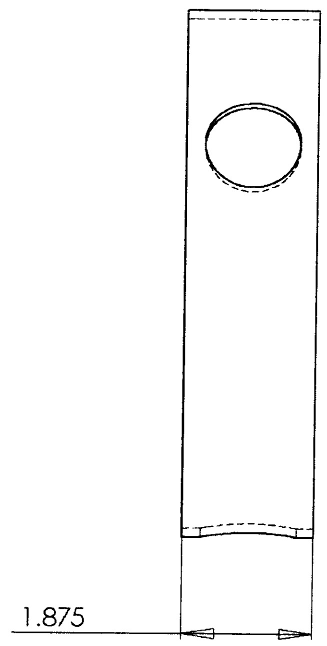

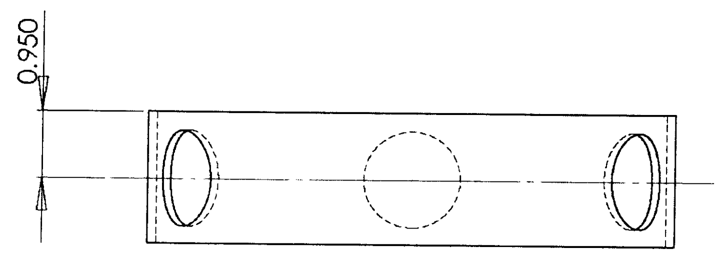

Yunpeng Yin
06/02/05

Drawing #4

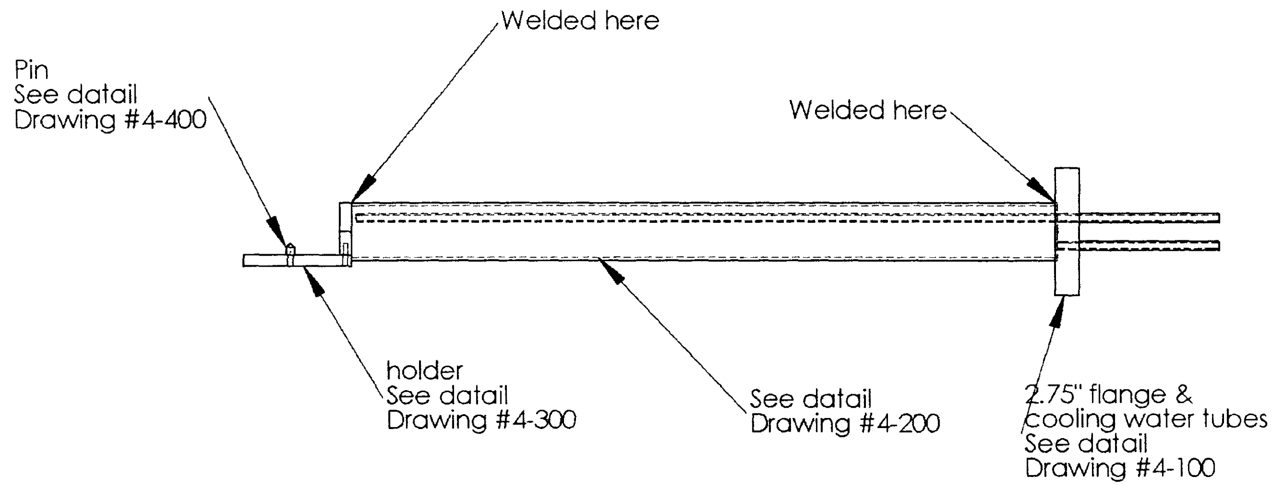

Drawing #4-200 and the 2.75" OD flange are coaxial

Yunpeng Yin
MIT
6/02/03

Drawing #4-100
2.75" flange & cooling water tubes

Material:
Stainless steel

2.75" OD flange
See detail from drawing #4-110

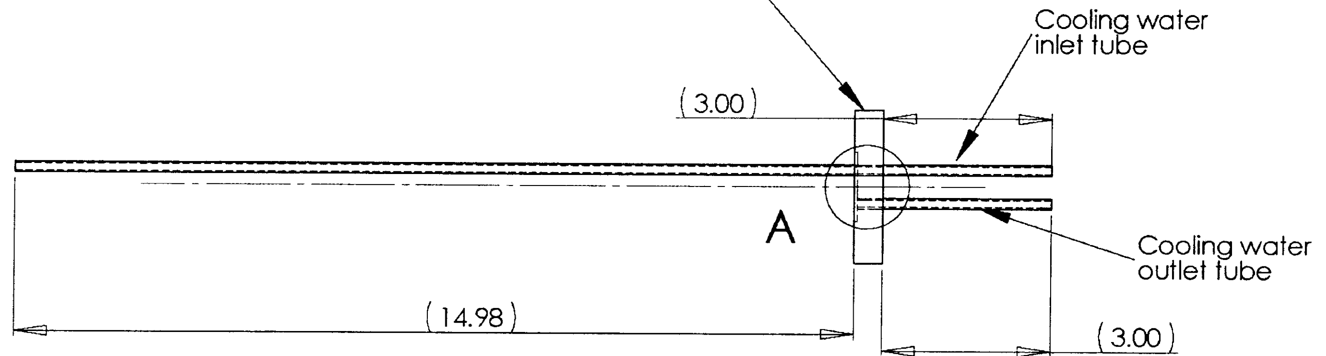

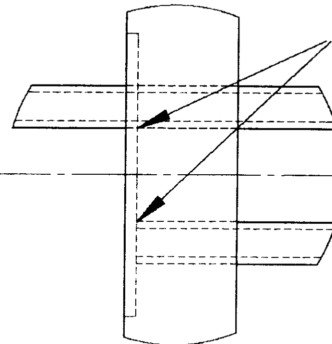

Cooling water tubes are welded to the 2.75" OD flange

A (4 : 2.5)

All cooling water tubes are 0.1875" in OD, and 0.1250" in ID
Length: cooling water inlet tube, 18.48"
cooling water outlet tube, 3.45"

Yunpeng Yin
MIT
6/09/03

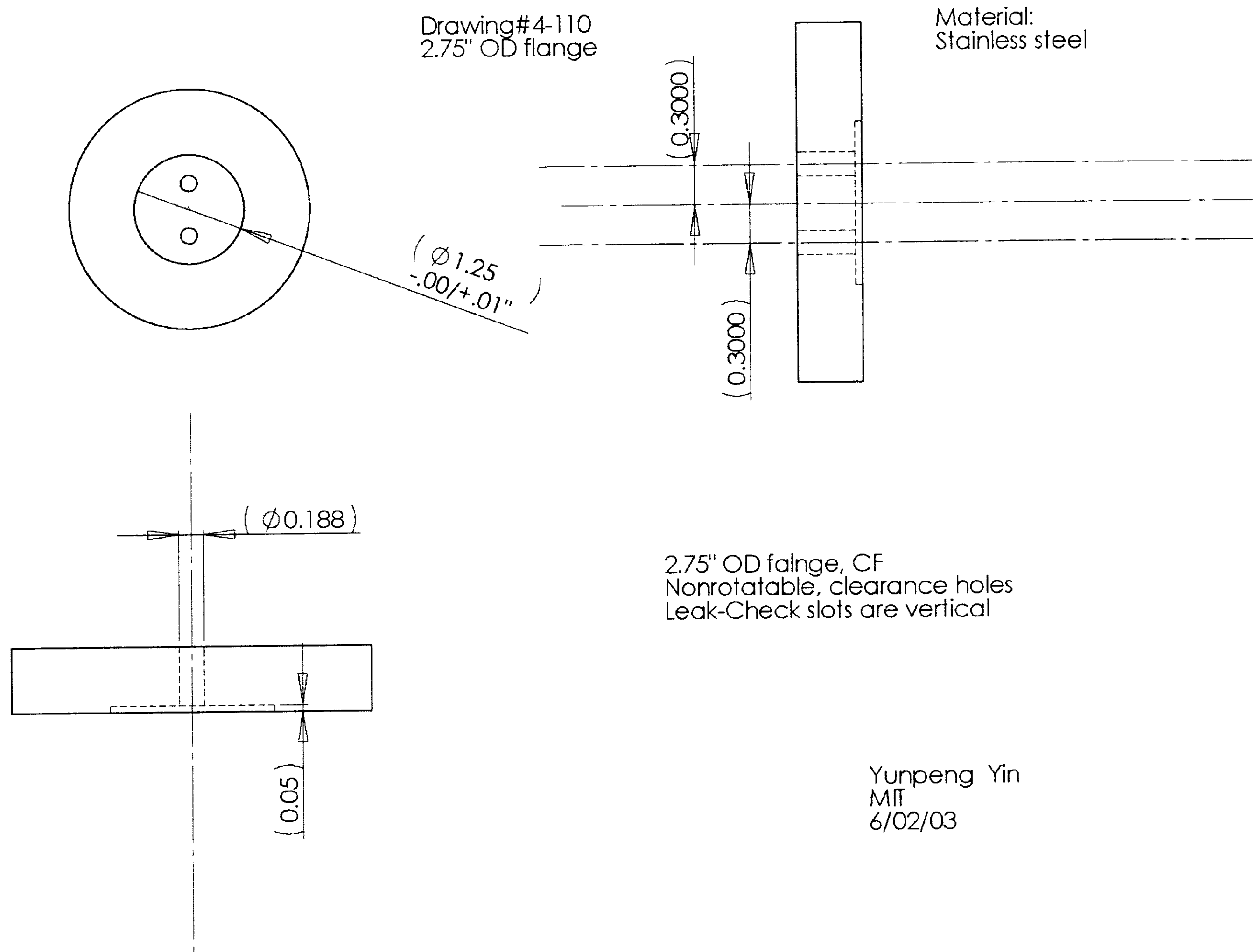
Drawing#4-110
2.75" OD flange
Material:
Stainless steel
(0.3000)
(0.3000)
(Ø1.25
-.00/+.01")
(Ø0.188)
(0.05)
2.75" OD falnge, CF
Nonrotatable, clearance holes
Leak-Check slots are vertical
Yunpeng Yin
MIT
6/02/03

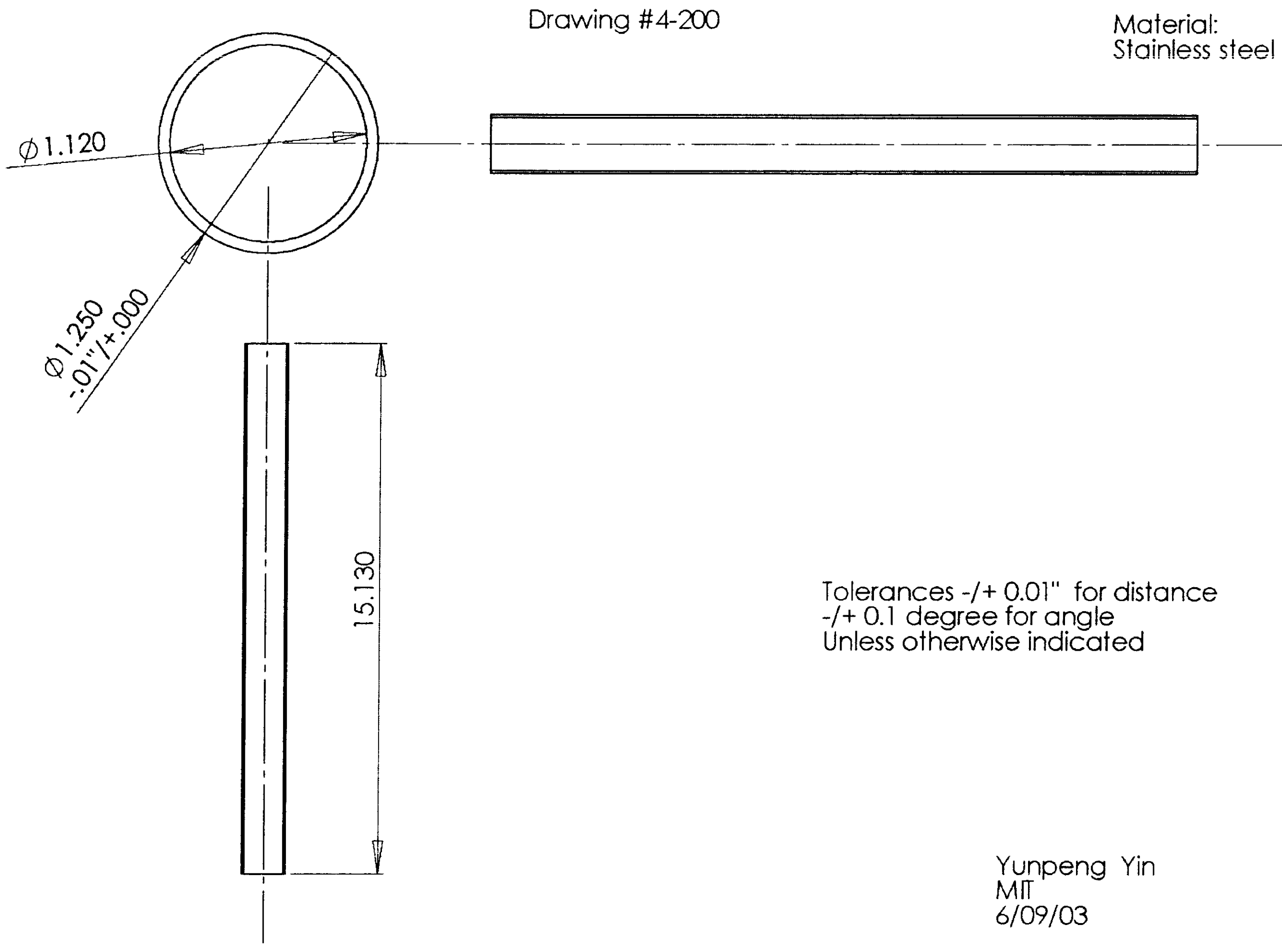
Drawing #4-200
Material:
Stainless steel
∅1.120
∅1.250
-.01"/+.000
15.130
Tolerances -/+ 0.01" for distance
-/+ 0.1 degree for angle
Unless otherwise indicated
Yunpeng Yin
MIT
6/09/03

Drawing #4-300

Material:
Stainless steel

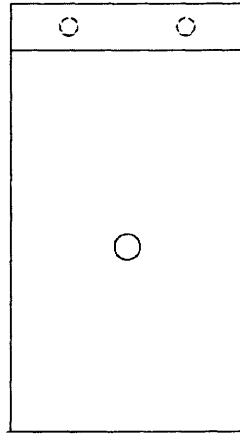

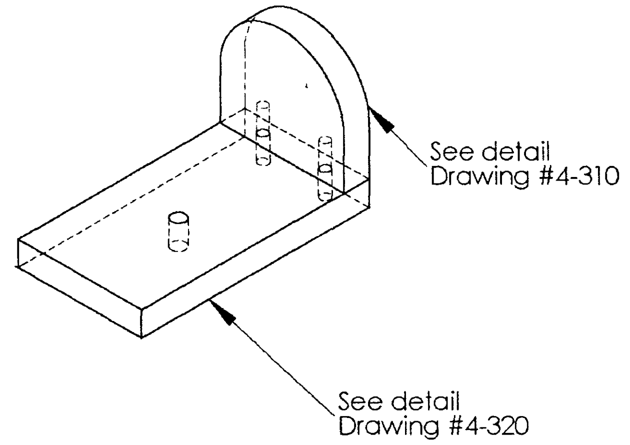

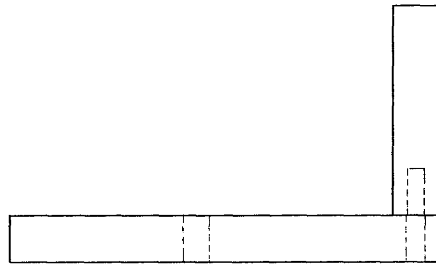

Yunpeng Yin
MIT
5/27/03

Drawing #4-310

Material:
Stainless steel

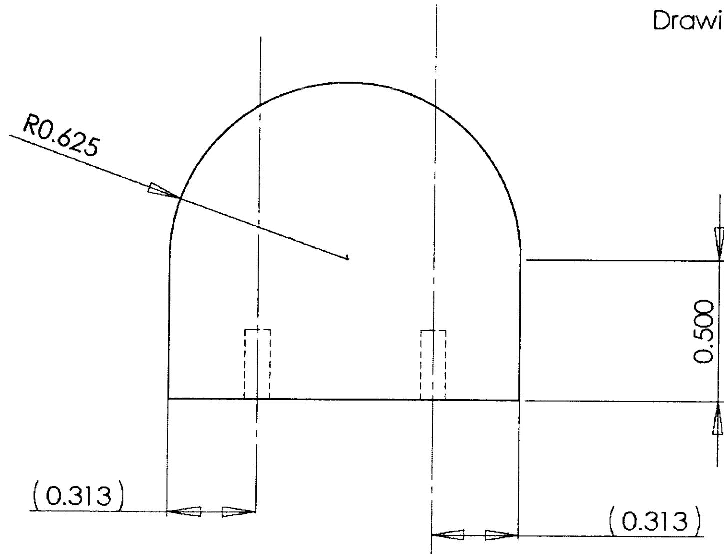

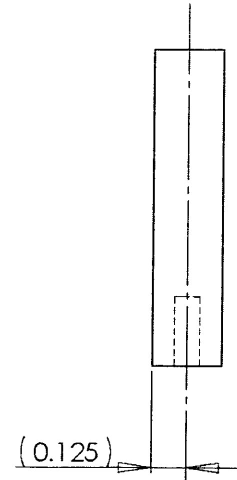

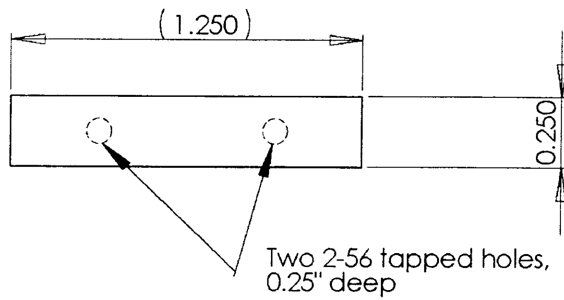

Tolerances -/+ 0.01" for distance
-/+ 0.1 degree for angle
Unless otherwise indicated

Yunpeng Yin
MIT
5/27/03

Drawing #4-320

Material:
Stainless steel

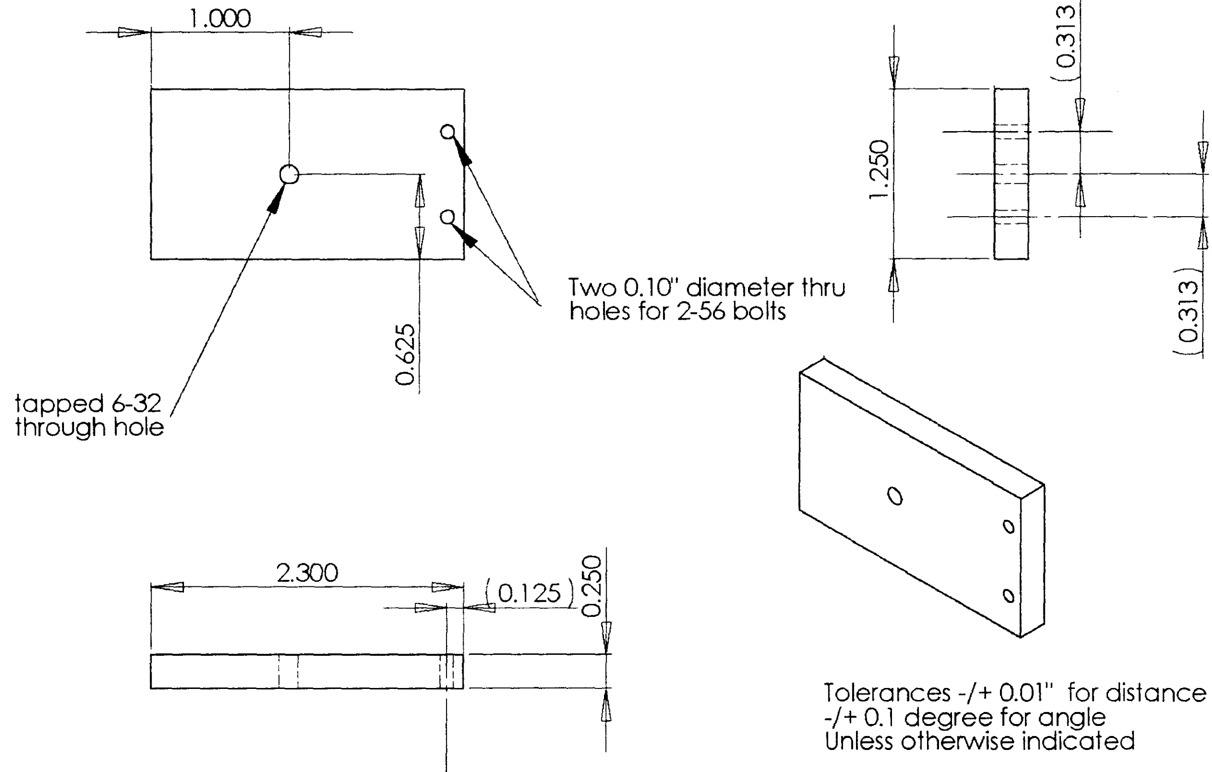

Yunpeng Yin
MIT
6/09/03

Drawing #4-400

Material:
Stainless steel

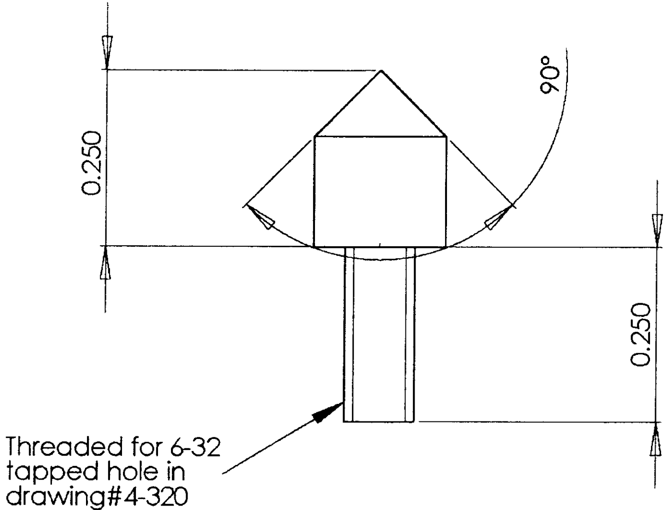

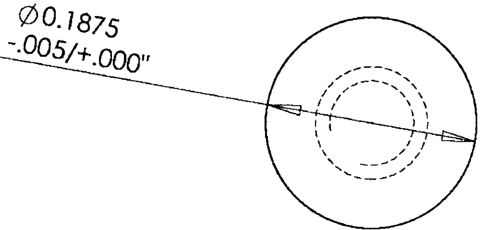

Tolerances -/+ 0.01" for distance
-/+ 0.1 degree for angle
Unless otherwise indicated

Yunpeng Yin
MIT
5/27/03

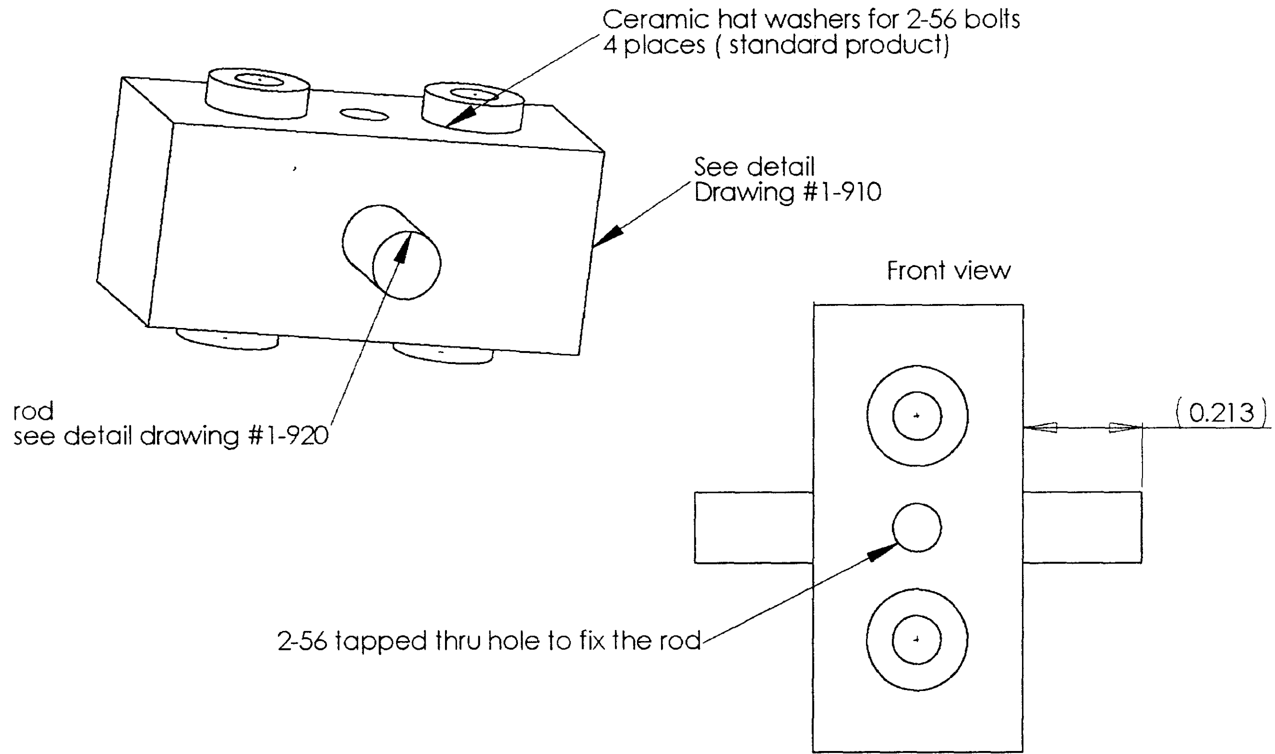
Drawing #1-900
This Assembly is used to fix Filament to
the bottom surface of the assembly
drawing #2-500
Ceramic hat washers for 2-56 bolts
4 places (standard product)
See detail
Drawing #1-910
Front view
(0.213)
rod
see detail drawing #1-920
2-56 tapped thru hole to fix the rod
Yunpeng Yin
MIT
6/02/03

Drawing #1-900 ceramic hat washer

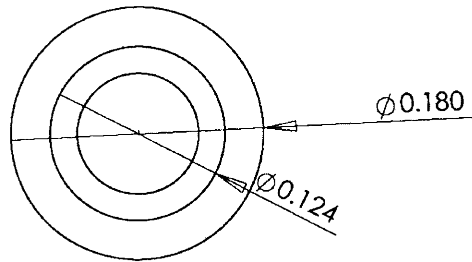

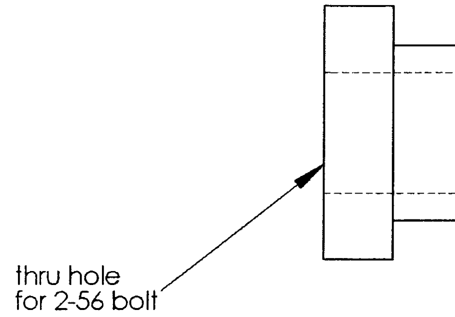

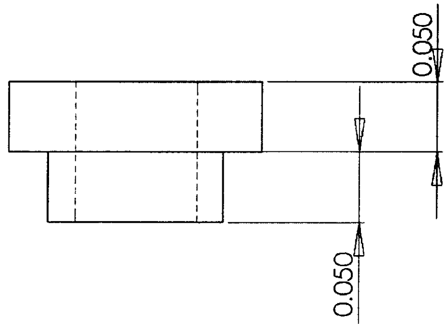

Tolerances -/+ 0.005" for distance
-/+ 0.1 degree for angle
Unless otherwise indicated

Yunpeng Yin
MIT

6/02/03

Material:
Stainless steel

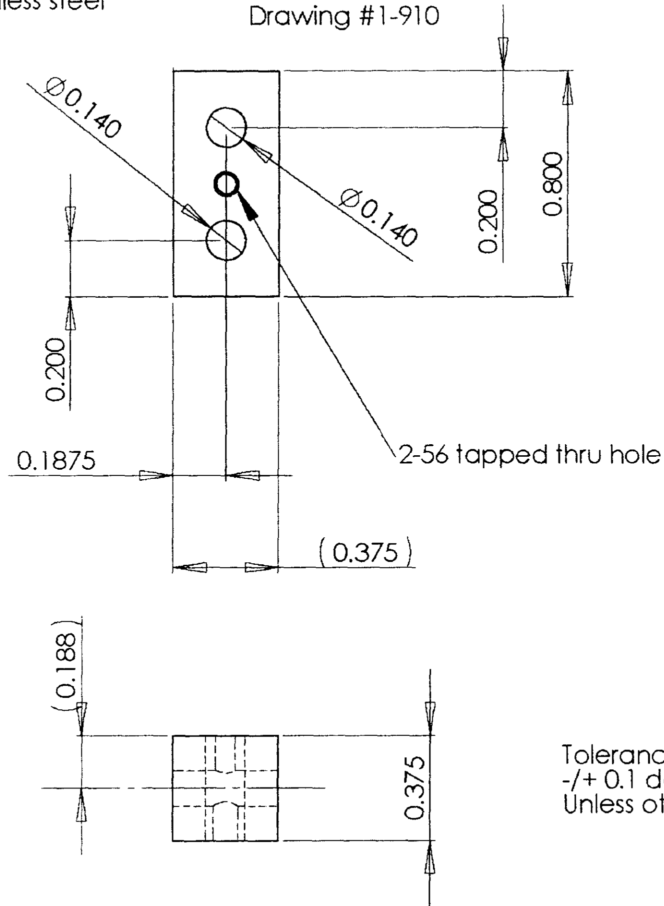

Tolerances -/+ 0.01" for distance
-/+ 0.1 degree for angle
Unless otherwise indicated

Drawing #1-920

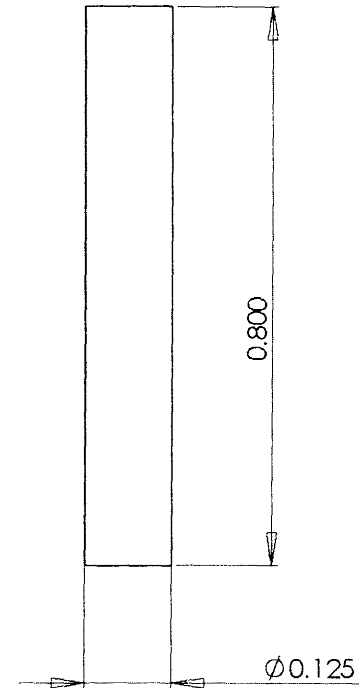

Yunpeng Yin
MIT
5/28/03